CALIFORNIA INSTITUTE OF TECHNOLOGY

EARTHQUAKE ENGINEERING RESEARCH LABORATORY

POST - ELASTIC DYNAMIC RESPONSE OF MILD STEEL STRUCTURES

by

Robert D. Hanson

A report on research conducted under a grant from the National Science Foundation

Pasadena, California

June 1965

POST-ELASTIC DYNAMIC RESPONSE OF MILD STEEL STRUCTURES

Thesis by

Robert Duane Hanson

In Partial Fulfillment of the Requirements
For the Degree of
Doctor of Philosophy

California Institute of Technology
Pasadena, California
1965
(Submitted May 4, 1965)

ACKNOWLEDGEMENTS

The author wishes to thank Professors G. W. Housner and D. E. Hudson for their guidance and assistance in the preparation of this work.

The force generators were made available by the Division of Architecture of the State of California. The cost of the experimental structure and auxiliary expenses were defrayed by a grant from the National Science Foundation.

The author is further indebted to the Ford Foundation for the Ford Foundation Faculty Fellowships received and to the California Institute of Technology for the scholarships and assistantships granted.

ABSTRACT

The current philosophy of earthquake resistant design is that a structure should be able to withstand an extremely strong motion earthquake without collapsing, even though a certain amount of damage is incurred. To make such a design requires a knowledge of the dynamic behavior of structures under large amplitude vibrations. The objective of the work reported here was to investigate the dynamic frequency response characteristics of a mild steel structure vibrating in the plastic range. Comparisons were made of the static, the dynamic, and the theoretical responses of the yielding structure.

The behavior of single-story structures having structural steel columns was investigated experimentally by means of horizontally applied forces generated by a shaking machine. The experimentally determined dynamic response showed the decrease in resonant frequency for increases in deflection amplitude which is characteristic of a "softening spring" type of nonlinearity. Ultraharmonic response was also observed. Under steady-state oscillations the fraction of equivalent viscous damping varied from 0.0016 at small, elastic deflections to 0.089 at large, plastic deflections. Structural deterioration was observed in both the static and dynamic experiments with a recovery of strength occurring between tests. A completely stable hysteretic loop was not attained at large deflection amplitudes, and the hysteresis loop did not become completely stable until the deflection amplitude was reduced to almost the initial yield value. However, the change in the hysteretic loop per cycle for the large

deflections was small enough to permit assuming that a steady-state dynamic condition existed over a limited number of cycles.

Discrepancies between the theoretical and the experimental virgin force-deflection curves were found and these are shown to be the result of simplifying approximations introduced in the structural analysis. It was found that the resonant vibrational amplitude of the structure can be predicted within 20%, and the resonant natural frequency within 2-1/2%, on the basis of the static virgin force-deflection curve. For large, plastic deflections at an excitation frequency of 3 cps, it was found that the differences between the dynamic and the static hysteresis loops were less than the changes in the static loops resulting from the deterioration caused by repeated cycles of loading.

TABLE OF CONTENTS

I. INTRODUCTION

Analysis of the stresses and deformations developed in a structure by externally generated oscillations is an important problem for the engineer and one which has received extensive research and investigation. The response of a structure whose base is subjected to earthquake motion is a special case of the general structural dynamics problem. The relationship of the earthquake vibration problem to the general vibration problem is discussed in detail in Chapter II.

The ground motion of an earthquake is caused by compressional and shear waves generated from a rupture of stressed rock and slip along an earthquake fault. For a strong motion earthquake, which is of interest for the design of engineering structures, the time history of the acceleration of the ground appears to be a random function over the "strong motion" portion of the earthquake, which may be some 30 seconds in duration for very large earthquakes.

A logical approach to the analysis and design of earthquake resistant structures is the response spectrum technique.[1-4]* By this method the maximum response of a linear, viscously damped single-degree-of-freedom oscillator is determined by an analog or digital computer for a given earthquake. The response spectrum presents the maximum response expressed as a function of the

*The superscripts refer to the list of references near the end of the thesis.

natural period and the fraction of critical damping. Since no two earthquakes are identical, any future earthquake cannot be expected to duplicate the response spectrum of a previous earthquake. For this reason, Housner[5] has determined the average velocity spectrum for the normalized spectra for eight components of the four strongest ground motions yet recorded (1959). The average velocity spectra consist of a set of normalized curves which can be used to estimate the response of a single-degree-of-freedom structure. Using normal mode analysis as described in reference (5), the velocity spectrum approach can also be applied to multistory buildings.

Employing the current ultimate strength design methods, it is expected that the response of a structure to small or moderate earthquakes will remain within the elastic range. For an extremely large earthquake, the structure is expected to yield, but not collapse. Therefore, for large earthquakes the nonlinearities associated with yielding must be considered. Since the response spectrum approach has been developed for linear structures, a nonlinear structure is usually transformed to an equivalent linear system before the method is used. Housner,[5, 6, 7] Blume,[8] Berg,[9] Veletsos and Newmark,[10] Hudson,[11] and others have examined the yielding structure problem by approximate and exact analyses. The exact analyses are not in a form which can be applied at the present time in a structural design and the approximate approaches must be applied conservatively because of the lack of sufficient

data on the cyclic static and dynamic characteristics of engineering materials loaded into yielding.

The material requirements for a structure normally subjected to reversed loading cycles, e. g. , a machine or airplane, differ from those required by a building subject to earthquake excitation. The number of reversed loading cycles for a machine in its design life-time may be more than a million, but for an earthquake excited structure designed according to the above philosophy the number of high stress cycles might range from zero to a few hundred.

For a low number of loading cycles, a high design stress can be used without anticipating a fatigue failure even though at these high stress levels the material characteristics change during the loading cycles. A knowledge of the nature of these changes is important because they imply that the experimental results cannot be duplicated with the same structure. Because of the importance of this point in outlining an experimental program, it will be discussed in more detail.

The changes in the hysteretic force-deflection relationship caused by successive cycles of testing can be described by the changes in two independent parameters. These parameters, defined in figure 1. 1, are the area of the hysteresis loop, A, and the slope of the major axis, θ. Benham and Ford[12] have presented a comprehensive study of these two parameters for reversed and repeated load cycling and strain cycling of axially loaded mild steel specimens. Although cycling between fixed loads and cycling between fixed strains

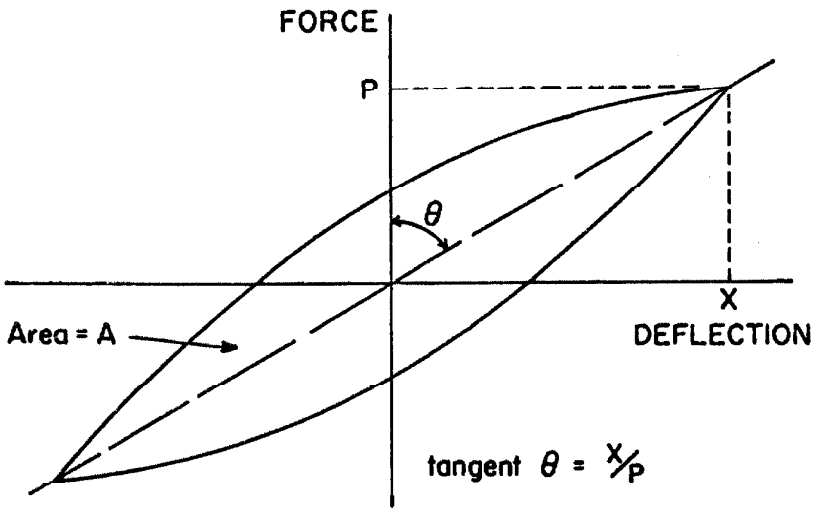

FIG. 1.1 HYSTERESIS LOOP PARAMETERS

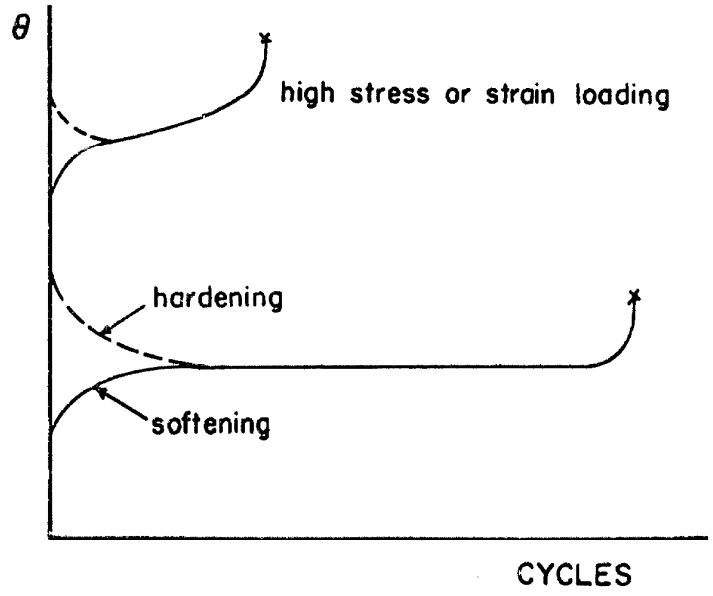

FIG. 1.2 VARIATION OF θ WITH THE NUMBER OF REPEATED CYCLES

produce different numerical values of θ as a function of the number of cycles, the general character is similar. During load cycling the load limits are held constant, and a tendency for the metal to harden or soften is shown by the variation of the deflection limits. When the material softens the total deflection-range increases and vice versa when material hardening occurs. Prominent changes occur rapidly in the loop during the first 10 to 20 percent of the life and thereafter θ remains relatively stable until the approach of failure when θ increases rapidly. At high strains or loads the stable region is very short or non-existent. These properties are indicated in figure 1. 2 with A having characteristics similar to θ for load limited cycling and 1/A having characteristics similar to θ for strain limited cycling. It should be noted that the experimental results reported by Benham and Ford[12] were obtained at frequencies of 5 to 15 cycles per minute. Also, the tests were continuous from the initial cycle until failure. The material strain ageing which would occur with intermittent testing would influence the results. Other experimenters have tested low cycle fatigue for stress or strain conditions such as rotating bending,[13] plain bending,[14] and axial or shear with bending.[15]

A number of static tests into the yielding range of full-scale mild steel frames and beams have been made. In most of these tests the load was increased until failure of the structure, or the load was applied alternatingly, but very few reversed cyclic tests have been made. The Commentary on Plastic Design in Steel[16]

gives some of these test results and has references to many of the others. Jacobsen[17] reviews thirteen references dealing with reversed cyclic loading beyond the normal elastic conditions of joints, wood frames, built-up beams, and concrete frames which are not concerned with the number of cycles to failure. Medearis and Young[18] have reported tests of nailed plywood panels subjected to reversed static cyclic loads. Again the number of cycles to failure have not been reported. The plywood panels were designed to be equivalent to partition shear walls currently being used in single-story school buildings. The above work[17] has considered the possible energy absorption of joints in steel but has not considered the energy absorption by yielding of the main steel members. A much more difficult problem is presented by the post-elastic response of reinforced concrete structures. C. P. Siess at the University of Illinois has been supervising work on static bending tests of reinforced concrete members to failure which has included some reversed loading tests. These test reports have been published in the Civil Engineering Studies, Structural Research Series of the University of Illinois.

The purpose of the research reported in this thesis was three-fold. First, to determine the actual dynamic response of a yielding structure. To date the dynamic structural response had only been predicted analytically by assuming various hysteretic force-deflection relationships, e. g. , elasto-plastic and bilinear. Second, to compare dynamic response with corresponding static measurements

to determine the validity of using static measurements to predict dynamic response. Third, to determine the energy absorbed by the mild steel frame vibrating in the plastic range because of its significance in earthquake resistant design of buildings.

II. GENERAL VIBRATION PROBLEM

The purpose of this chapter is to establish the relationships between linear and nonlinear vibration response so that the nonlinear system can be approximated by an appropriate linear system. The vibrational analysis presented will make clear the nature of the linear earthquake response problems and will indicate some of the special features of nonlinear vibrations that are pertinent to the nonlinear earthquake response problem.

First, linear vibrational analysis will be reviewed for a general forcing function, and then the response will be given for sinusoidal, random, and earthquake forcing functions. From this the relationship between earthquake excitation analysis and the usual vibrational analysis can be seen.

Second, the nonlinear problem will be discussed with a description of some nonlinear phenomena. A definition of an appropriate equivalent linear system for earthquake resistant design procedures will conclude the chapter.

A. Linear Problem

1. General Forcing Function

1a. Single-degree-of-freedom system. The equation of motion of the single-degree-of-freedom viscously damped linear structure shown in figure 2.1 is

$$m\ddot{x} + c\dot{x} + kx = F \qquad (2.1)$$

where the dot indicates differentiation with respect to time, t, and

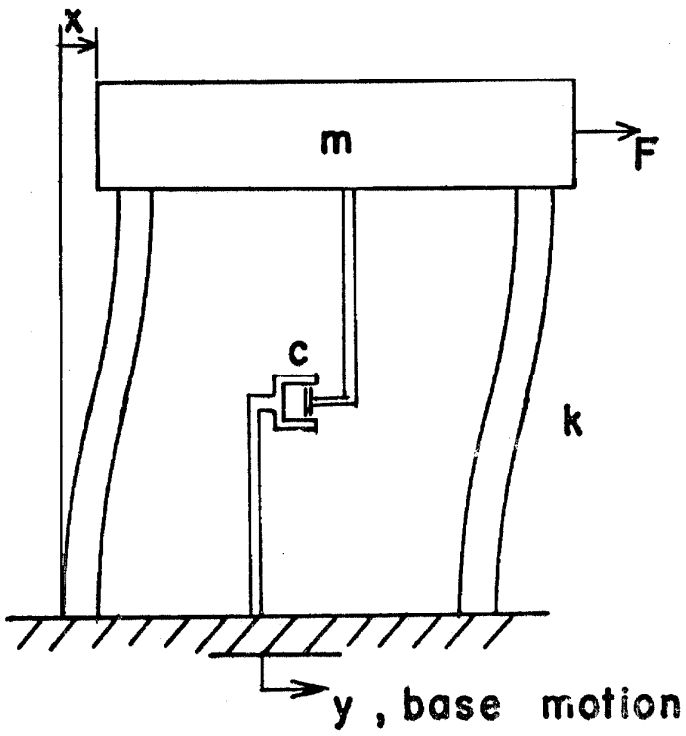

FIG. 2.1 LINEAR SINGLE-DEGREE-of-FREEDOM SYSTEM

where m, c and k are constant with respect to time and F is expressed as a function of time. As is well known, the complete solution to equation 2.1 consists of the superposition of the homogeneous solution and the particular solution:

$$x(t) = e^{-n\omega_n t}\left[A \sin \omega_d t + B \cos \omega_d t\right] + \int_0^t \frac{F(\tau)e^{-n\omega_n(t-\tau)}}{m\,\omega_d} \sin \omega_d(t-\tau)\, d\tau \qquad (2.2)$$

where n is the fraction of critical damping, $n = \frac{c}{2\sqrt{km}}$, $\omega_n^2 = \frac{k}{m}$ and $\omega_d = \sqrt{1-n^2}\,\omega_n$. ω_n is the undamped natural frequency of the system shown in figure 2.1 and the constants A and B are evaluated from the conditions at t = 0.

For the undamped case, n = c = 0, equation 2.2 reduces to

$$x(t) = A \sin \omega_n t + B \cos \omega_n t + \int_0^t \frac{F(\tau)}{m\,\omega_n} \sin \omega_n(t-\tau)\, d\tau \qquad (2.3)$$

Since undamped motion is difficult to realize in a building, the damped motion will be used as the general case.

Another common forcing function is caused by an acceleration, $\ddot{y}$, of the base of the structure. The equation of motion for this case is

$$m(\ddot{x} + \ddot{y}) + c\dot{x} + kx = 0 \qquad (2.4)$$

or

$$m\ddot{x} + c\dot{x} + kx = -m\ddot{y} \qquad (2.5)$$

By comparing equations 2.1 and 2.5, the solution of equation 2.5 is seen to be given by equation 2.2 with the substitution of $-m\ddot{y}(\tau)$

for $F(\tau)$.

1b. Multiple-degree-of-freedom system. In this section the discussion will be limited to passive systems possessing distinct natural frequencies, which insures that the set of equations of motion can be transformed into a symmetrical set of equations. Analysis of the more general problem has been discussed by Caughey and O'Kelly.[19, 20]

Using the notation of figure 2. 2, where the displacements x_i are measured relative to the base, in matrix notation the equation of motion comparable to equation 2. 1 is

$$\left[M\right]\left\{\ddot{x}\right\} + \left[C\right]\left\{\dot{x}\right\} + \left[K\right]\left\{x\right\} = \left\{F\right\} \qquad (2.6)$$

The mass matrix $\left[M\right]$ is a diagonal matrix with positive real elements. Since the dashpots and stiffnesses are real linear elements, $c_{ij} = c_{ji}$ and $k_{ij} = k_{ji}$, or in other words, $\left[C\right]$ and $\left[K\right]$ are symmetric. As an aid to understanding equation 2.6 the equation of motion for the i^{th} mass will be expanded from the i^{th} row of equation 2. 6.

$$m_i \ddot{x}_i + c_{il}\dot{x}_1 + \ldots + c_{ij}\dot{x}_j + \ldots + c_{in}\dot{x}_n + k_{il}x_1 + \ldots + k_{in}x_n = F_i \qquad (2.7)$$

The mode shapes and undamped natural frequencies are found from the classical homogeneous problem

$$\left[M\right]\left\{\ddot{x}\right\} + \left[K\right]\left\{x\right\} = 0 \qquad (2.8)$$

Let

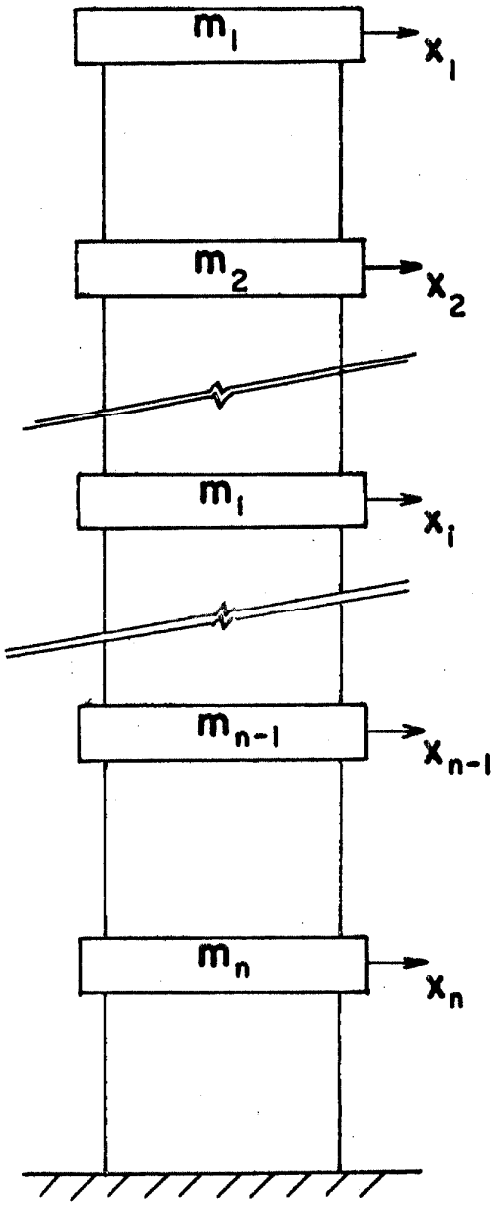

FIG. 2.2 LINEAR MULTIPLE-DEGREE-OF-FREEDOM SYSTEM

$$\{x\} = [M]^{-1/2} \{\xi\} \tag{2.9}$$

Then substituting and premultiplying by $[M]^{-1/2}$, equation 2.8 becomes

$$[M]^{-1/2}[M]\,[M]^{-1/2}\{\ddot{\xi}\} + [M]^{-1/2}[K][M]^{-1/2}\{\xi\} = 0 \tag{2.10}$$

or

$$[I]\{\ddot{\xi}\} + [K^*]\{\xi\} = 0 \tag{2.11}$$

It can be shown that $[K^*]$ is symmetric and therefore, a unique orthogonal transformation matrix exists which will diagonalize $[K^*]$ provided that the eigenvalues are distinct. Let this matrix be $[\theta]$ such that

$$[\theta]^T[\theta] = [I] \tag{2.12}$$

and

$$\{\xi\} = [\theta]\{\epsilon\} \tag{2.13}$$

Applying this relation to equation 2.11 and premultiplying by $[\theta]^T$, there results

$$[I]\{\ddot{\epsilon}\} + [\theta]^T[K^*][\theta]\{\epsilon\} = 0$$

or

$$[I]\{\ddot{\epsilon}\} + [\omega^2]\{\epsilon\} = 0 \tag{2.14}$$

Since the columns of $[\theta]$ are the eigenvectors of the system of equation 2.11, the eigenvectors of the original problem, equation 2.8, are found to be

$$[\Psi] = [M]^{-1/2}[\theta] \tag{2.15}$$

The columns of $[\Psi]$ are the normal modes of the original system. It can be shown that

$$\{\psi^i\}^T[M]\{\psi^j\} = 0 \qquad i \neq j \tag{2.16}$$

and

$$\{\psi^i\}^T [K] \{\psi^j\} = 0 \qquad i \neq j$$

and also

$$\{\psi^i\}^T [M] \{\psi^i\} = 1 \tag{2.17}$$

and

$$\{\psi^i\} [K] \{\psi^i\} = \omega_i^2$$

It has been shown[19] that if $[C]$ and $[K]$ are to be simultaneously reduced to diagonal form by the same transformation, then the necessary and sufficient condition is that $[C^*][K^*] = [K^*][C^*]$ where $[M]^{-1/2}[C][M]^{-1/2} = [C^*]$ and $[M]^{-1/2}[K][M]^{-1/2} = [K^*]$. By assuming the commutability of $[C^*]$ and $[K^*]$, equation 2.6 can be completely uncoupled by the transformation $[\Psi]$. Let

$$\{x\} = [\Psi]\{\epsilon\} \tag{2.18}$$

Substituting this expression into equation 2.6 and premultiplying by $[\Psi]^T$ yields

$$[\Psi]^T[M][\Psi]\{\ddot{\epsilon}\} + [\Psi]^T[C][\Psi]\{\dot{\epsilon}\} + [\Psi]^T[K][\Psi]\{\epsilon\} = [\Psi]^T\{F\} \tag{2.19}$$

or

$$[I]\{\ddot{\epsilon}\} + [D]\{\dot{\epsilon}\} + [\omega^2]\{\epsilon\} = \{P\} = [\Psi]^T\{F\} \tag{2.20}$$

where $[D]$ is a diagonal matrix. The equation of motion for the i^{th} row of equation 2.20 in expanded form becomes

$$\ddot{\epsilon}_i + d_i \dot{\epsilon}_i + \omega_i^2 \epsilon_i = P_i \tag{2.21}$$

The solution for each of the ϵ_i's is the same as described for the single-degree-of-freedom system. For example, if the steady-state solution of equation 2.6 for a periodic forcing function is desired where

$$P_3 = F(t)$$
$$P_i = 0 \qquad \text{for all } i \neq 3 \tag{2.22}$$

and x(t) is the response of the single-degree-of-freedom system to F(t), equations 2.2 and 2.21, then

$$\{x\} = [\Psi] \begin{Bmatrix} 0 \\ 0 \\ \epsilon_3 \\ 0 \\ 0 \end{Bmatrix} = \{\psi^3\}\, x(t) \tag{2.23}$$

which is a pure normal mode. For any other forcing function the approach is the same except in the general case $\{x\}$ becomes a weighted sum of all the normal modes where the ϵ_i's as calculated from equation 2.21 are the weighting functions. Account must be taken of the phase angle of the mode response since the chance that all the phase angles are the same is remote.

For a base acceleration, $\ddot{y}$, equation 2.6 becomes

$$[M]\{\ddot{x}\} + [C]\{\dot{x}\} + [K]\{x\} = -[M]\{\ddot{y}\} \tag{2.24}$$

where $\{\ddot{y}\}$ equals $\ddot{y}$ times a vector whose elements are all unity. Substituting equation 2.18 and premultiplying by $\{\psi^r\}^T$, equation 2.24 becomes

$$\{\psi^r\}^T[M][\Psi]\{\ddot{\epsilon}\} + \{\psi^r\}^T[C][\Psi]\{\dot{\epsilon}\} + \{\psi^r\}^T[K][\Psi]\{\epsilon\} = -\{\psi^r\}^T[M]\{\ddot{y}\} \tag{2.25}$$

Applying the conditions of equations 2.16 and 2.17 and similar results for $[C]$, equation 2.25 reduces to

$$\ddot{\epsilon}_r + d_r \dot{\epsilon}_r + \omega_r^2 \epsilon_r = \sum_{j=1}^{N} \psi_j^r \ddot{y} m_j \qquad (2.26)$$

from which together with equation 2.2 for zero initial conditions yields

$$\epsilon_r = \int_0^t \frac{e^{-\frac{1}{2} d_r (t-\tau)}}{\omega_{rd}} \sin \omega_{rd}(t-\tau) \sum_{j=1}^{N} \psi_j^r \ddot{y}(\tau) m_j \, d\tau \qquad (2.27)$$

or

$$\epsilon_r = \frac{\sum_{j=1}^{N} \psi_j^r m_j}{\omega_{rd}} \int_0^t \ddot{y}(\tau) e^{-\frac{1}{2} d_r (t-\tau)} \sin \omega_{rd}(t-\tau) \, d\tau$$

where ω_{rd} is the damped natural frequency of the r^{th} mode. The final solution $\{x\}$ can be found from equation 2.18 when all the ϵ_r's are known.

2. Sinusoidal Force

One of the most important response conditions in practice is the steady-state motion of a mass caused by a harmonic forcing function, $F(t) = F_o \sin \omega t$. The steady-state solution to equations 2.1 or 2.2 in this case is

$$x(t) = \frac{F_o/k}{\sqrt{\left\{1 - \left(\frac{\omega}{\omega_n}\right)^2\right\}^2 + 4n^2\left(\frac{\omega}{\omega_n}\right)^2}} \sin(\omega t - \phi) \qquad (2.28)$$

where ϕ is defined by

$$\tan \phi = \frac{2n \frac{\omega}{\omega_n}}{1 - \left(\frac{\omega}{\omega_n}\right)^2} \qquad (2.29)$$

It can be seen that the amplitude of the motion of the mass is dependent upon the ratio of the forced frequency to the natural frequency and upon the fraction of critical damping.

The restoring force or the force transmitted by the spring and damper is

$$R(x) = F(t) - m\ddot{x} = c\dot{x} + kx \tag{2.30}$$

Letting the amplitude of equation 2.28 equal A, the restoring force becomes

$$R(x) = 2n\,\omega_n m\omega\, A\cos(\omega t - \phi) + kA\sin(\omega t - \phi) \tag{2.31}$$

with $x = A\sin(\omega t - \phi)$. The ellipse shown in figure 2.3 is the result of plotting equation 2.31 versus x. The force width at zero displacement equals $4n(\omega / \omega_n)A\,k$ or $2c\omega A$.

Similarly for the periodic forcing function $P\,\omega^2 \sin\omega t$, equation 2.28 becomes

$$x(t) = \frac{P\,\omega^2/k}{\sqrt{\left[1-\left(\frac{\omega}{\omega_n}\right)^2\right]^2 + 4n^2\left(\frac{\omega}{\omega_n}\right)^2}}\sin(\omega t - \phi) \tag{2.32}$$

where ϕ is defined by equation 2.29. A major difference between equations 2.28 and 2.32 is that for increasing damping the maximum response according to equation 2.28 occurs at decreasing values of ω / ω_n less than unity while the maximum response according to equation 2.32 occurs at increasing values of ω / ω_n greater than unity.

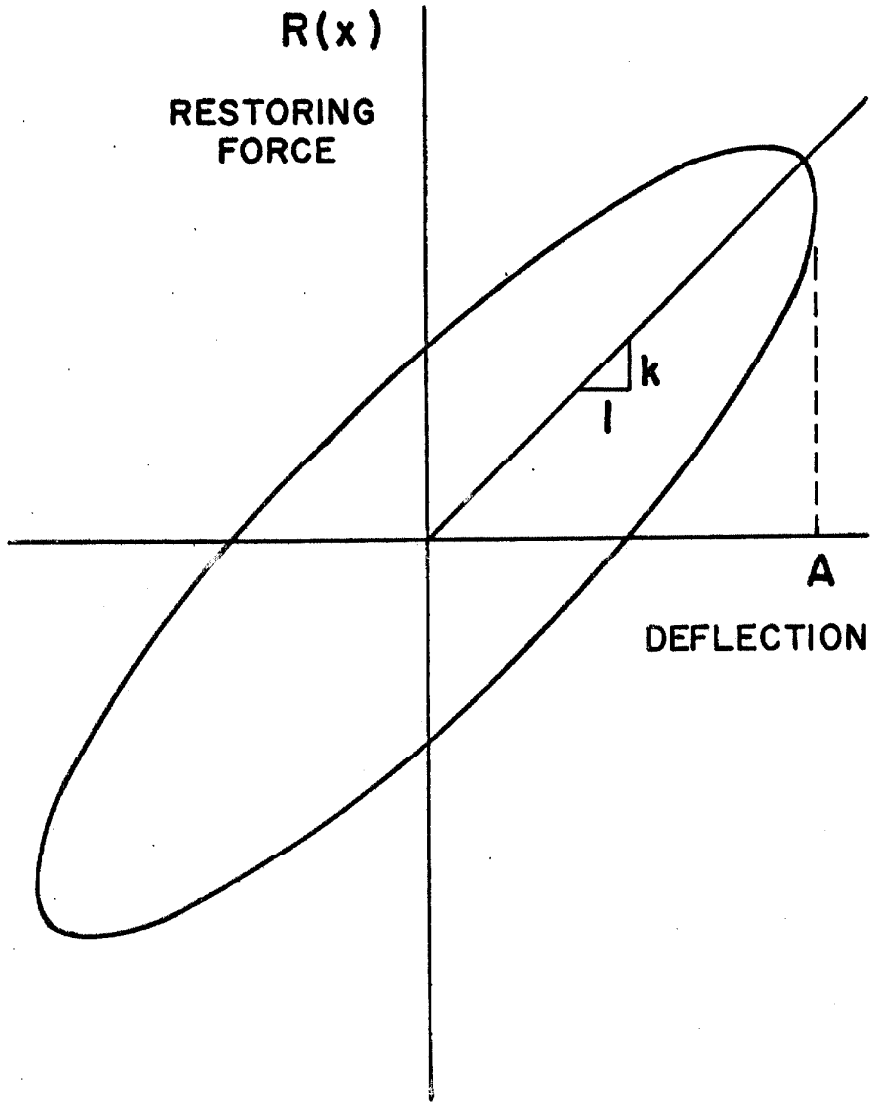

FIG. 2.3 RESTORING FORCE vs. DEFLECTION FOR VISCOUS DAMPING

3. Random Force

Recently many vibration problems have arisen in which the excitation is a random function. Two examples of such random excitation are the rough burning of the rockets of a ballistic missile and the ground motion of earthquakes.

Since a random vibration is not deterministic (i. e., repeated experiments do not produce identical results), a statistical description of the vibration records must be made. The theory of random processes has been available in the literature for over 15 years.[21, 22] Some of the important properties of the response of linear systems are: i) if the excitation is a stationary random process, then the response is also a stationary random process; ii) if the excitation has a zero mean value, then the response also has a zero mean value; and iii) if the excitation is ergodic, then the response is also ergodic.

Definitions of some of the common terms of random vibration theory will first be presented and then the number of response cycles of x exceeding a certain level x_1 will be determined for a specified random excitation. If the first order probability density is defined as p(x), the mean or expected value of x is

$$E\left[x\right] = \int_{-\infty}^{\infty} x\, p(x)\, dx \qquad (2.33)$$

and the mean square value of x is

$$E\left[x^2\right] = \int_{-\infty}^{\infty} x^2\, p(x)\, dx \qquad (2.34)$$

An important statistical parameter is the variance of x; mathematically it is

$$\sigma^2 = E\left[(x-E\left[x\right])^2\right] = E\left[x^2\right] - (E\left[x\right])^2 \qquad (2.35)$$

It follows from equation 2.35 that for the special case where the mean of x is zero, the variance of x is equal to the mean square value of x. For a stationary random process, the autocorrelation function, $R(\tau)$, is a function only of the time difference as

$$R(\tau) = E\left[x(t)\, x(t-\tau)\right] \qquad (2.36)$$

The power spectral density, $S(\omega)$, of a stationary random process is

$$S(\omega) = \frac{1}{2\pi} \int_{-\infty}^{\infty} R(\tau)\, e^{-i\omega\tau}\, d\tau \qquad (2.37)$$

The power spectral density of a real process is an even nonnegative function of ω whose area is equal to the mean square value of x, i.e.,

$$E\left[x^2\right] = \int_{-\infty}^{\infty} S(\omega)\, d\omega \qquad (2.38)$$

The first order probability density function p(x) of a normal or Gaussian process is described by

$$p(x) = \frac{1}{\sigma\sqrt{2\pi}} \exp\left(-\frac{(x-E\left[x\right])^2}{2\sigma^2}\right) \qquad (2.39)$$

where σ is defined by equation 2.35. It is assumed that $\ddot{y}$ is a zero mean stationary random base acceleration of the structure in figure 2.1 with an ideal white noise spectrum, i.e., uniform power

spectral density S_o. Then the mean square value of the response x can be shown[21] to be

$$\sigma^2 = E\left[x^2\right] = \frac{\pi}{2} \frac{S_o}{n\ \omega_n^3} \tag{2.40}$$

In addition, if the response is a normal or Gaussian process, then the number of peaks per unit time in which the absolute value of the response x exceeds a given absolute value response x_1 is given by[22]

$$M_{x_1} = \frac{\omega_n}{\pi} \exp\left(\frac{-x_1^2}{2\sigma^2}\right) \tag{2.41}$$

An estimate of the damage to a structure can be made from equations 2.40 and 2.41 if the damage-deflection relationship of the structure is known and an estimate of the excitation time is made. This solution is not exact because usually the actual conditions do not meet all of the characteristics of the assumed ideal excitation.

4. Earthquake Excitation

The difficulty in applying the above analysis lies in determining the random characteristics of earthquake ground acceleration. Some of these complications have been avoided in the past by approaching the analysis in a different manner.

The most accurate method of computing the response of a structure to an earthquake excitation is to make an analog or digital computation. In this case, each structure in question is subjected to the base acceleration caused by the earthquake and the particular response characteristics of the structure are computed.

The velocity response spectrum is a convenient and informative method of characterizing the earthquake ground motion, and some of its basic principles will now be presented. The maximum velocity response spectrum, S_v, is defined as:

$$S_v = \left[\int_0^t \ddot{y}(\tau)\, e^{-\omega_n n(t-\tau)} \sin \omega_n (t-\tau)\, d\tau \right]_{max} \qquad (2.42)$$

For a single-degree-of-freedom system, figure 2.1 and equation 2.2, with zero initial conditions and assuming $\sqrt{1-n^2} \approx 1$, it has been shown[23] that S_v very closely describes the maximum of the envelope of the relative velocity response. In dynamic problems where the excitation differs widely from earthquakes, the accuracy of the approximations in arriving at S_v should be checked.

Having S_v, the maximum relative velocity of the structure during the earthquake, the maximum relative deflection and maximum absolute acceleration of the structure during the earthquake are given approximately by

$$\text{relative Deflection, } S_d = \frac{1}{\omega_n} S_v$$

and

$$\text{absolute Acceleration, } S_a = \omega_n S_v \qquad (2.43)$$

An interesting property of S_v is that, on the average, the maximum energy per unit mass is equal to $\frac{1}{2} S_v^2$.

The Fourier transform of the base acceleration is

$$F(\omega) = \int_0^T \ddot{y}(\tau) e^{-i\omega\tau}\, d\tau \qquad (2.44)$$

where T is taken as the duration of the earthquake. The Fourier amplitude spectrum is given by the square root of the sum of the squares of the real and imaginary parts of $F(\omega)$. Evaluation of equation 2. 44, to give the Fourier amplitude spectrum, shows that it is equal to the amplitude of the relative velocity at time T for the case of zero damping. Thus, as a function of ω, the undamped velocity response at the end of the earthquake is equal to the Fourier amplitude of the earthquake acceleration.

The maximum velocity response spectrum values for an earthquake record are determined and plotted for the c/m and the k/m values of interest either by analog or digital methods. Since it is not expected that a future earthquake will duplicate a past earthquake, Housner and Jennings[24] have developed eight pseudo-earthquake accelerograms which are samples of stationary, Gaussian, random processes with the same power spectral density found from the average of the undamped velocity spectra of recorded ground accelerations. These pseudo-earthquake accelerograms can be used for analysis and design of structures. A length of record of 30 seconds was arbitrarily selected.

Applying the velocity response spectrum techniques to multistory buildings requires the determination of the characteristic frequencies, the corresponding mode shapes of the system, and the damping in each mode. Thus, equation 2. 27 is evaluated for each value of r using the established velocity response spectrum curves. The solution from equation 2. 18 in this case assumes that each

vibration mode reaches its maximum value at the same time, which is improbable. Merchant[25] investigated this problem for various methods of mode combination.

B. Nonlinear Problem

Although many structures can be adequately described by linear analysis, in certain cases nonlinear equations are required to describe the physical situation accurately. Most nonlinear equations in structural analysis cannot be solved exactly; however, two examples of nonlinear systems which do have exact solutions are the pendulum moving with large motions and the piece-wise-linear stiffness systems. The primary functions of this section will be to give a brief description of some nonlinear phenomena which are not observed in the linear case and to establish an equivalent linear system to approximate the nonlinear response.

One method of attacking a specific nonlinear vibration problem is to first determine an approximate analytical solution. From the approximate solution the important variables of the problem can be determined, and a solution can be made with the aid of an analog or digital computer. The analog solution could be important in that certain nonlinear phenomena may be observed which were obscured by the approximate analytical technique. Important points brought out by analog analysis then can be examined in more detail using the digital computer.

An important difference between linear and nonlinear analysis

exists. For the linear case, when a particular motion satisfies the equation of motion, this is a sufficient condition that this motion can exist. However, for the nonlinear case, the stability of the particular motion must be established before it can be said that the motion can exist. Periodic solutions of the nonlinear problem are usually assumed.

Nonlinear Phenomena

For a viscously damped system where the nonlinearity only occurs in the stiffness, frequency response curves similar to those shown in figure 2. 4 can be expected. As was mentioned above, the mathematically possible responses must be checked to insure stability. In figure 2. 4 the regions of unstable response are marked to indicate that any response in these regions cannot be sustained; so the actual response must be either on the upper or lower branch of the response curve. It can be seen, therefore, that response jumps can occur for very small changes in the excitation frequency.

It can be shown[26] that the structure will respond at its natural frequency when excited at a frequency of 1/3, 1/5, 1/7, ... , of its natural frequency. This is termed ultraharmonic or superharmonic response. Also, if the initial conditions of the motion are properly established, a natural frequency response can be observed when the excitation frequency is 3, 5, 7, ..., times the natural frequency. This is termed subharmonic response.

The frequency response relationship for a viscously damped system with the nonlinearity only in the stiffness was given in

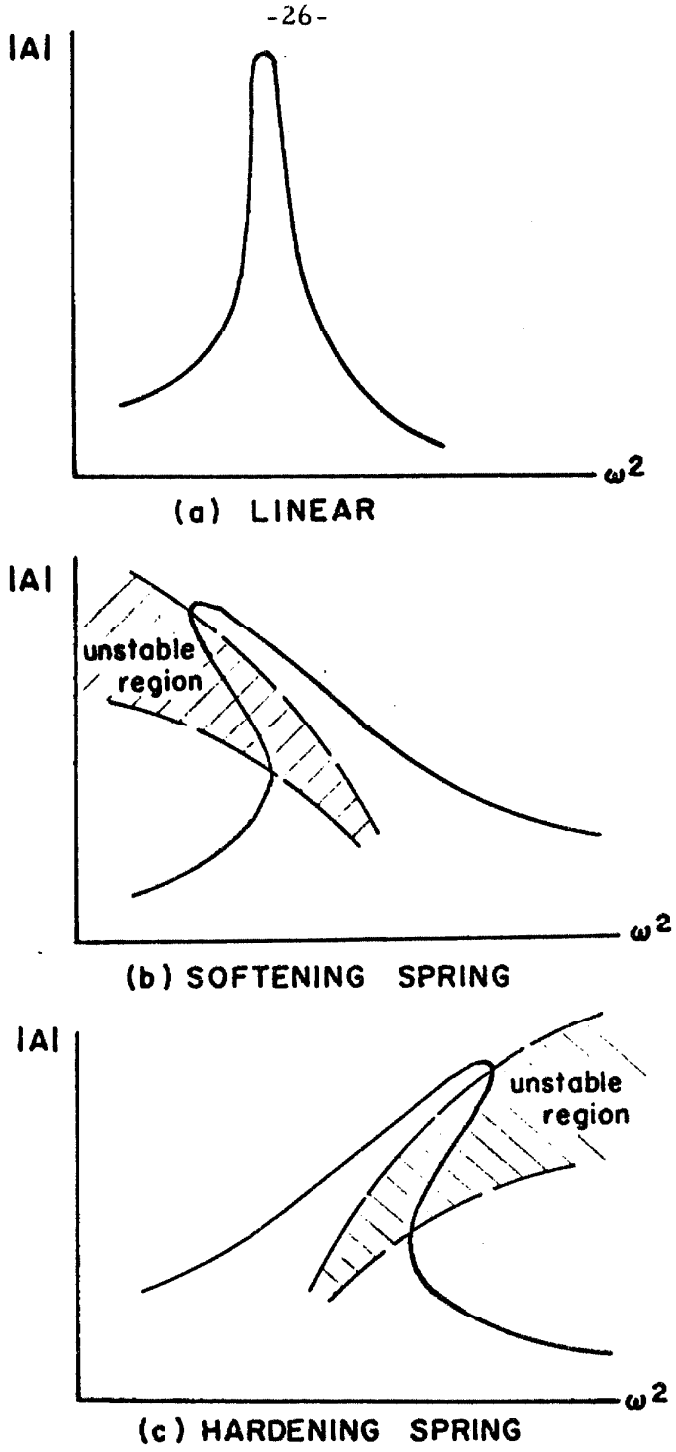

FIG. 2.4 FREQUENCY RESPONSE CURVES

figure 2. 4. The frequency response for an elasto-plastic hysteretic force-deflection relation and no viscous damping, as determined by Caughey,[27] is given in figure 2. 5. A similar curve for a more complex hysteretic force-deflection relation established by Jennings[28] is given in figure 2. 6. The curves of figures 2. 5 and 2. 6 bear a remarkable resemblance to the curves of figure 2. 4 with the exception that the instability regions do not normally exist for the hysteretic force-deflection type of nonlinearity.[27] Iwan[29] has shown, however, a specific case of a hysteretic force-deflection system which does have an instability region. Substitution of an equivalent viscous damping and a nonlinear spring stiffness for either of the hysteretic systems gives good steady-state response results as long as the discussion is restricted to frequencies where the behavior is predominantly fundamental.[30]

The linear viscous damping system's force-deflection curve was given in figure 2. 3 and two types of hysteretic force-deflection curves are shown in figures 2. 5 and 2. 6. The hysteretic force-deflection curves are theoretical approximations to the actual curves for structures. These theoretical curves and the corresponding frequency response curves are based on the assumption that the force-deflection relationship for the structure is continually retraced during steady-state motion. It is not convenient to consider time variation of the force-deflection relationship in the present theoretical approximations of the hysteretic structural behavior although it is known to exist. It is a purpose of this research to

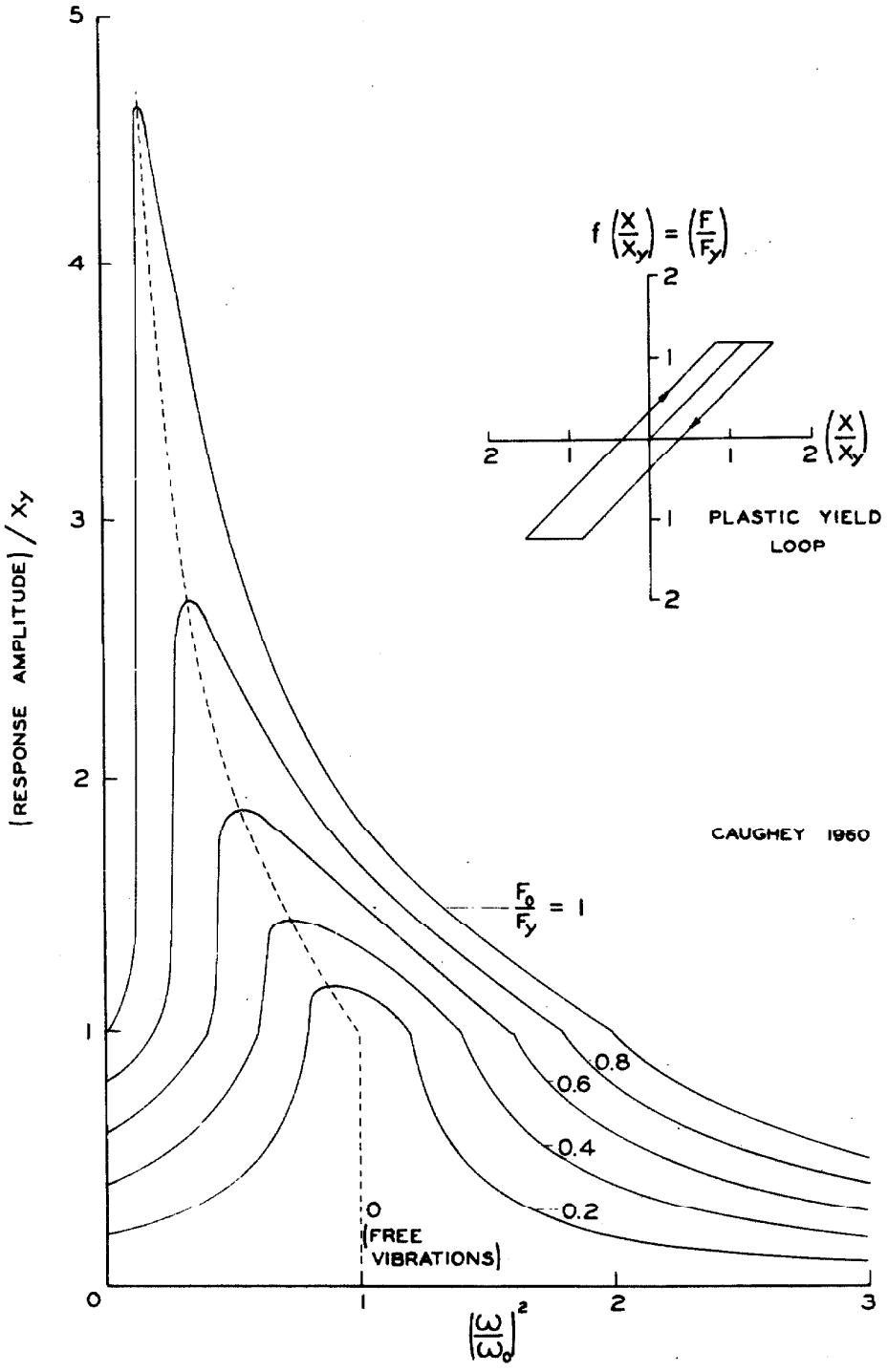

FIG. 2.5 HYSTERESIS TYPE RESONANCE CURVES

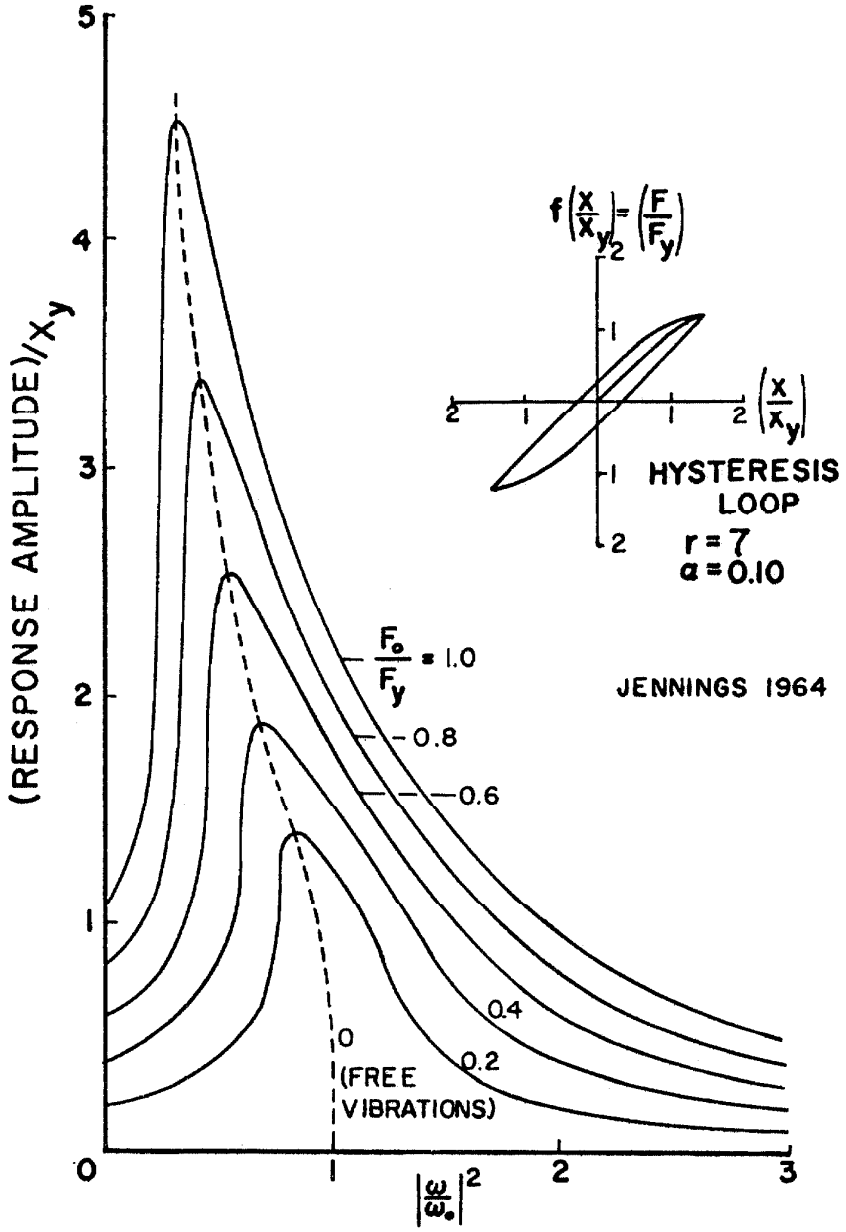

FIG. 2.6 HYSTERESIS TYPE RESONANCE CURVES

determine the relationship between the static and dynamic force-deflection curves to assist in the theoretical prediction of the dynamic response of structures.

Most nonlinear analytical solutions are limited to periodic responses which are dependent upon relatively small nonlinearities. *It is fortunate (or unfortunate depending on your point of view) that* the nonlinear phenomena also occur for small nonlinearities.

An appropriate linear system to approximate the nonlinear system will be established by two important properties of the frequency response curve. The two properties are the resonant amplitude and the excitation frequency at resonance. These two important characteristics of the response curve will be treated separately. The equivalent linear system will be defined as:

$$m\ddot{x} + \bar{c}\dot{x} + kx = F \qquad (2.45)$$

where $k/m = \omega_n^2$ and $\bar{c}$ is considered as a function of the amplitude of motion only. The resonant frequency of the nonlinear system ω_p / ω_n, is also a function only of the amplitude of motion. The advantages of this formulation of the equivalent linear system for earthquake analysis and design have been expressed by Hudson. [11]

III. EXPERIMENTAL STRUCTURE

A. Introduction

This chapter reviews the design process evolving from the basic objectives of the investigation and the design limitations to the final structural design. Designs of one- and two-story structures were made, but only the details of the single-story structures used in the experiments are presented.

A restatement of the three basic objectives in studying a yielding structure follows: First, measurements of the dynamic response characteristics are desired. Second, a comparison of the dynamic, static, and theoretical results is needed to determine the probable success in predicting dynamic response. Finally, the energy absorbed by the experimental structure is wanted for possible application to earthquake resistant design of buildings.

Testing of actual buildings into the yielding range might give results directly applicable to earthquake resistant building design. However, controllable forces large enough to excite the structure into this range is a necessary requirement which currently cannot be met for most multistory buildings. In actual buildings the source of the damping and stiffnesses cannot be accurately identified because of the interaction of the structural and nonstructural components. Initial damaging test cycles may eliminate a majority of the nonstructural components' participation in the following cycles or at the very least will modify the nature of their participation. The effect of these nonstructural components on the building's response to a strong

motion earthquake would have to be resolved in order to interpret the test results. These experimental investigations could only be made with buildings to be demolished since the tests by necessity would make the buildings unusable.

In a full-scale experimental building the effect of the non-structural components could be controlled or eliminated. However, even if the nonstructural components are eliminated, the analysis of the structure is still complicated by the nature of the joints of the structure and a precise analysis of the experimental results would be extremely difficult. Furthermore, the problem of supplying the large forces for this test is still not solved.

A laboratory scale building has several advantages over a full-scale structure; the most important being that the available static forces are almost limitless and only the type and magnitude of the dynamic forces would be a limit on the design of the structure. Four new force generators have been recently developed[31, 32] which produce a sinusoidal force in any horizontal direction.* To generate the horizontal force, two equal eccentric weights are counter-rotated in a horizontal plane at a fixed frequency. This type of force generation is not new, but the amplidyne control system is much more

---

* The force generators are owned by the State of California, Division of Architecture, and have been used for testing several full-scale structures such as steel frame and reinforced concrete frame buildings, earth dams, concrete towers, and rocket test stands.

accurate than the controls of previous systems. The frequency of the rotating eccentric weights can be controlled to within 1/300 cps. Also, the four force generators can be operated simultaneously from one control panel at any desired phase relationship between the generators. Obviously, the two most commonly used relationships are with the generators in phase (i. e., sinusoidal forces in the same direction) or 180 degrees out of phase (i. e., forces in opposite directions which will give a pure torsional force). The generators have an effective frequency range from slightly below one cps to about nine cps. Each generator can produce a force amplitude of 800 lbs. at one cps and is limited to 5000 lbs. maximum. Each unit is driven with a 1-1/2 horsepower D. C. motor. In addition to the obvious limitation upon energy absorption that this power source imposes (it must also provide for friction, wind losses and efficiency), there is also the limitation of the torque capacity of the motor. The required torque is dependent upon the motion of the structure and because of this instability may be introduced. Because the experiments reported here provided the first opportunity to investigate the effect of the torque limitation upon the stability of the frequency control, the problem of torque limitation is discussed in Appendix I.

B. General Description

1. Design Limitations and Considerations

The final designs of the experimental structures were governed by a number of independent objectives and limitations, some of which

are important in obtaining a proper perspective of the final structure. Since dynamic investigations of the type reported here have not been made previously, there was no background of experience to assist in designing the experiment. The theoretical analysis developed by Jennings[28] (see Chapter V of this thesis) was used as a guideline in the design to anticipate dynamic response amplitudes and energy absorption of the structure. The reason for using this approach was that previous work done in the area of dynamic hysteresis response (reported in Chapter I) showed that this assumed hysteresis force-deflection relationship most nearly fitted the expected force-deflection relationship of the experimental structure.

Tests of full size elements or structures have a great advantage over tests of scale model structures, because they eliminate the problem of scale effects. Any results obtained from full-scale tests can be applied in practice almost directly, whereas, scale model tests possibly have different scaling factors for different applications of interest. On this basis it was hoped to use full size elements under known loading conditions. A single-degree-of-freedom system with material yielding sections was selected for the experimental investigation, because it is the simplest nonlinear system to analyze.

Since the available static forces were almost limitless, the type and magnitude of the available dynamic force was the only limit upon the design of the structure. Using the force generators described above, the horizontally directed force led to a structural design consisting of a rigid mass supporting one or two force

generators on four columns. The columns acting as the spring of the single-degree-of-freedom system were the sections to be investigated. The design of these columns was restricted by the frequency range of the force generators, the energy available from the 1-1/2 horsepower motors, the torque capacity of the force generators, a limit on the maximum weight of the structure, and a specified test deflection of two to four times the initial yield deflection.

Using theoretical dynamic constants of $a = 0.10$ and $r = 7$ (see Chapter V) for design purposes, various rolled structural steel sections were analyzed for a maximum deflection of four times the yield deflection. Since the maximum power available from two force generators at an assumed efficiency of 50 percent eliminated all structural sections that are used as columns in normal building construction, a special model column had to be designed. Attempting to keep the structural analysis as simple as possible, it was decided that the effect of the end connections should be minimized as much as possible. This meant that the high stresses should occur at a relatively simple section located away from the connection. Dynamic tests of various types of structural connections, such as bolted, welded and riveted, are important but they were considered an extra complication to be avoided in this investigation.

The smallest rigid floor area which would support two force generators and still permit continuation of the columns for additional story heights was selected. The floors were made extremely rigid relative to the columns so that the floor could be

considered as a rigid mass without joint rotations, see figure 3.1 for the dimensions of the floor. All nonstructural components were eliminated from the experimental structure.

Equation 2.1 expresses the equation of motion for a single-story structure for small vibrations within the elastic range. Since the hysteresis type of nonlinearity produces frequency response relationships similar to the "softening spring" without the unstable region, shown in figure 2.6, the undamped natural frequency at small vibrations was established slightly higher than the desired test resonant frequency.

The limited maximum weight of this small rigid floor, the available frequency range of the dynamic force, and a limit on the maximum deflection of the structure (torque limit of the force generators) limited the column stiffness within a specified range. This, together with the problem of making the end connections so that the columns would be tested and not the connections, led to a non-uniform column section which utilized a hot rolled structural steel test section.

Since a two-story structure was ultimately desired, the clearances required to place a force generator on the lower floor established a minimum second-story column height. The analytical development for the column stiffnesses and the natural frequencies follows.

The single-story structure has three independent natural frequencies and vibration motions which are translation about the

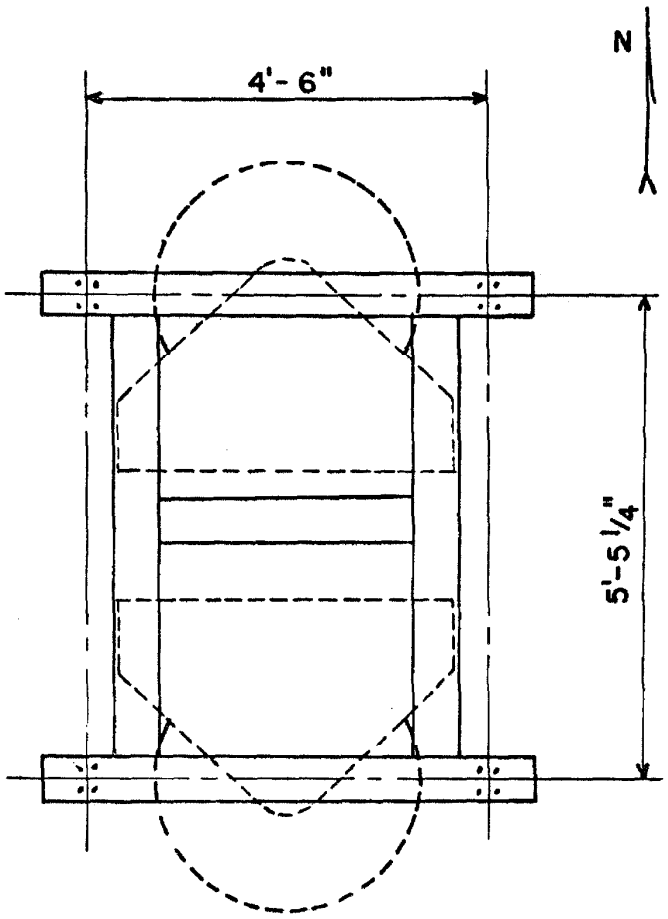

FIG. 3.1 RIGID FLOOR PLAN

two principle axes and torsion. For a two-story structure the number of independent motions is raised to six.

If the two masses of the structure are set equal, then $[M]$ and $[K]$ become

$$[M] = \begin{bmatrix} m_1 & 0 \\ 0 & m_1 \end{bmatrix} \tag{3.1}$$

$$[K] = \begin{bmatrix} k_1 & -k_1 \\ -k_1 & (k_1+k_2) \end{bmatrix} \tag{3.2}$$

where k_1 and k_2 are the stiffness values as indicated in figure 3.2. Both k_1 and k_2 are nonlinear for large displacements. Letting $\omega_1^2 = k_1/m_1$ and $\kappa = (1 + (k_2/k_1))$, substitution of equations 3.1 and 3.2 into equation 2.8 gives for small displacements

$$\begin{bmatrix} 1 & 0 \\ 0 & 1 \end{bmatrix} \begin{pmatrix} \ddot{x}_1 \\ \ddot{x}_2 \end{pmatrix} + \omega_1^2 \begin{bmatrix} 1 & -1 \\ -1 & \kappa \end{bmatrix} \begin{pmatrix} x_1 \\ x_2 \end{pmatrix} = 0 \tag{3.3}$$

The roots of the characteristic equation obtained by setting $x = Ae^{\lambda t}$ are $\lambda_1 = i\gamma\omega_1$ and $\lambda_2 = i\delta\omega_1$ (3.4)

where

$$\gamma = \sqrt{\frac{1+\kappa}{2} - \frac{\kappa^2-2\kappa+5}{4}}$$

and (3.5)

$$\delta = \sqrt{\frac{1+\kappa}{2} + \frac{\kappa^2-2\kappa+5}{4}}$$

λ_1 and λ_2 are the small vibration undamped natural frequencies of the first and second modes respectively. $\lambda_2/\lambda_1 = \delta/\gamma$ gives

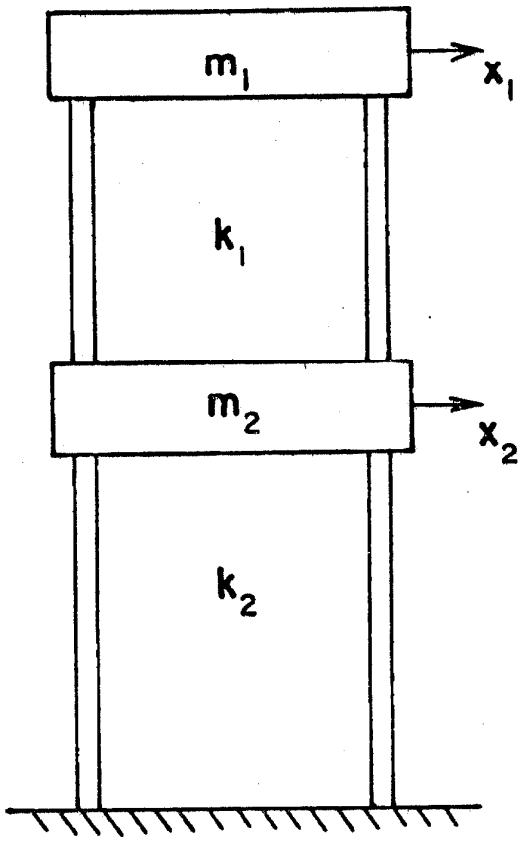

FIG. 3.2 TWO STORY EXPERIMENTAL STRUCTURE

the ratio of the free small vibration natural frequencies in the two modes of vibration. γ , δ and δ/γ are plotted with respect to k_2/k_1 in figure 3. 3. The mode shapes associated with these frequencies are

$$\left|\psi^1\right| = \frac{1}{\sqrt{\gamma^4-2\gamma^2+2}} \begin{pmatrix} 1 \\ 1-\gamma^2 \end{pmatrix}$$

and (3. 6)

$$\left|\psi^2\right| = \frac{1}{\sqrt{\delta^4-2\,\delta^2+2}} \begin{pmatrix} 1 \\ 1-\delta^2 \end{pmatrix}$$

where

$$\left|x\right| = \left[\left|\psi^1\right| \quad \left|\psi^2\right|\right] \left|\epsilon\right| \tag{2. 18}$$

and $\left|\epsilon\right|$ is the solution of

$$\begin{bmatrix} 1 & 0 \\ 0 & 1 \end{bmatrix} \left|\ddot{\epsilon}\right| + \left[\Psi\right]^T \left[C\right] \left[\Psi\right] \left|\dot{\epsilon}\right| + \begin{bmatrix} \lambda_1^2 & 0 \\ 0 & \lambda_2^2 \end{bmatrix} \left|\epsilon\right| = \left[\Psi\right]^T \left|F\right| \tag{2. 19}$$

It should be remembered that the coefficient of $\left|\dot{\epsilon}\right|$ is a diagonal matrix for the conditions described in Chapter II.

For small nonlinearities, the mode shapes may be expected to be similar to the linear case; but the similarity may not hold if only one of the story heights has a nonlinear stiffness relationship.

2. Description

The experimental structure was erected on its own reinforced concrete foundation (7' - 6" x 6'- 6" x 1'- 0") placed on virgin soil about 16 feet below original ground level. Details of the foundation and anchorage of the one inch steel base plates are given in figure 3. 4.

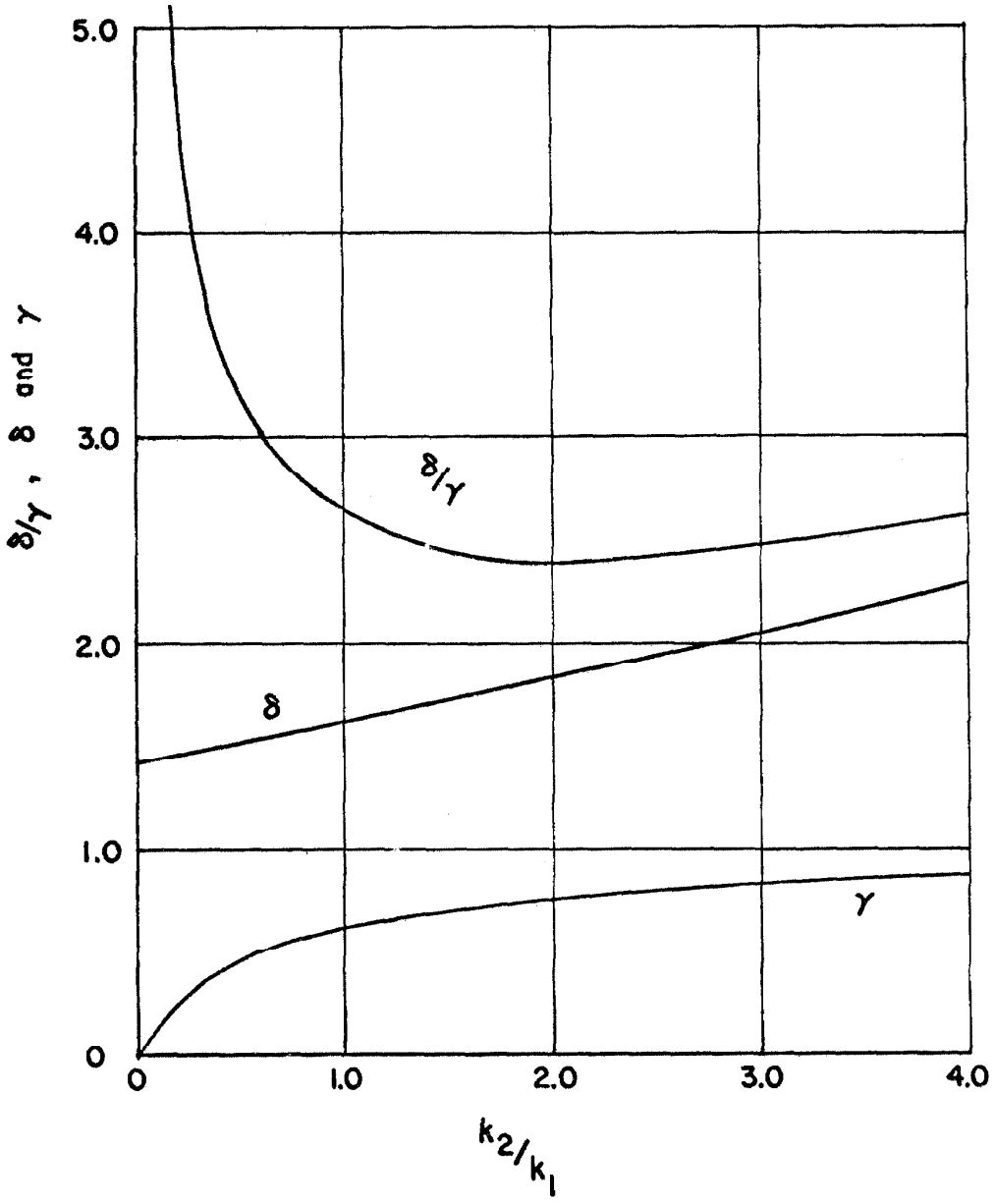

FIG. 3.3 NATURAL FREQUENCIES AND THEIR RATIO FOR A TWO STORY STRUCTURE

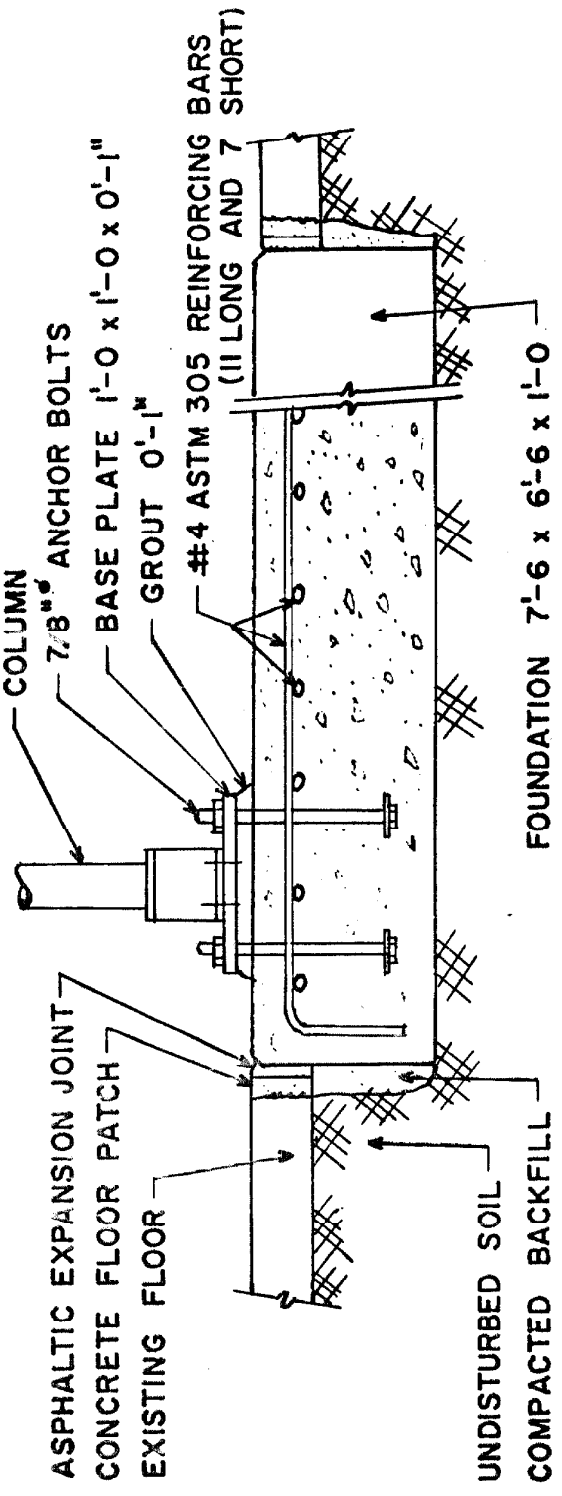

FIG 3.4 FOUNDATION AND BASE PLATE DETAIL

This foundation is isolated from the existing floor-on-grade by asphalt impregnated expansion strips. The mass of the foundation and the stiffness of the underlying soil were sufficiently great compared to the mass and stiffness of the test structure so that the foundation could be treated as immovable.

A two ton capacity overhead traveling crane simplified the erection of the structure and the handling of the equipment. A clear overhead space of 13 feet is currently available for the structure with a maximum of 20 feet if an existing steel stair is temporarily removed. With the steel stair removed, a second two ton capacity overhead crane could be utilized. With this overhead clearance a multistory experimental structure could be erected easily.

C. Details of Structures Investigated

The experimental structures were all single-story with structural differences occurring only in the columns. The first column design (long column) was established so that the structure could be forced in either, or both, of its major directions and in torsion. Figure 3. 5 shows the column. The detail dimensions are given in Table III-1 together with the dimensions of the other columns. While experimenting with this set of columns in the strong (N-S) direction, it was observed that the structure did not move purely in translation. It was suspected that the major reasons for this were the closeness of the natural frequencies in the weak, strong, and torsional directions together with the natural tendency of the

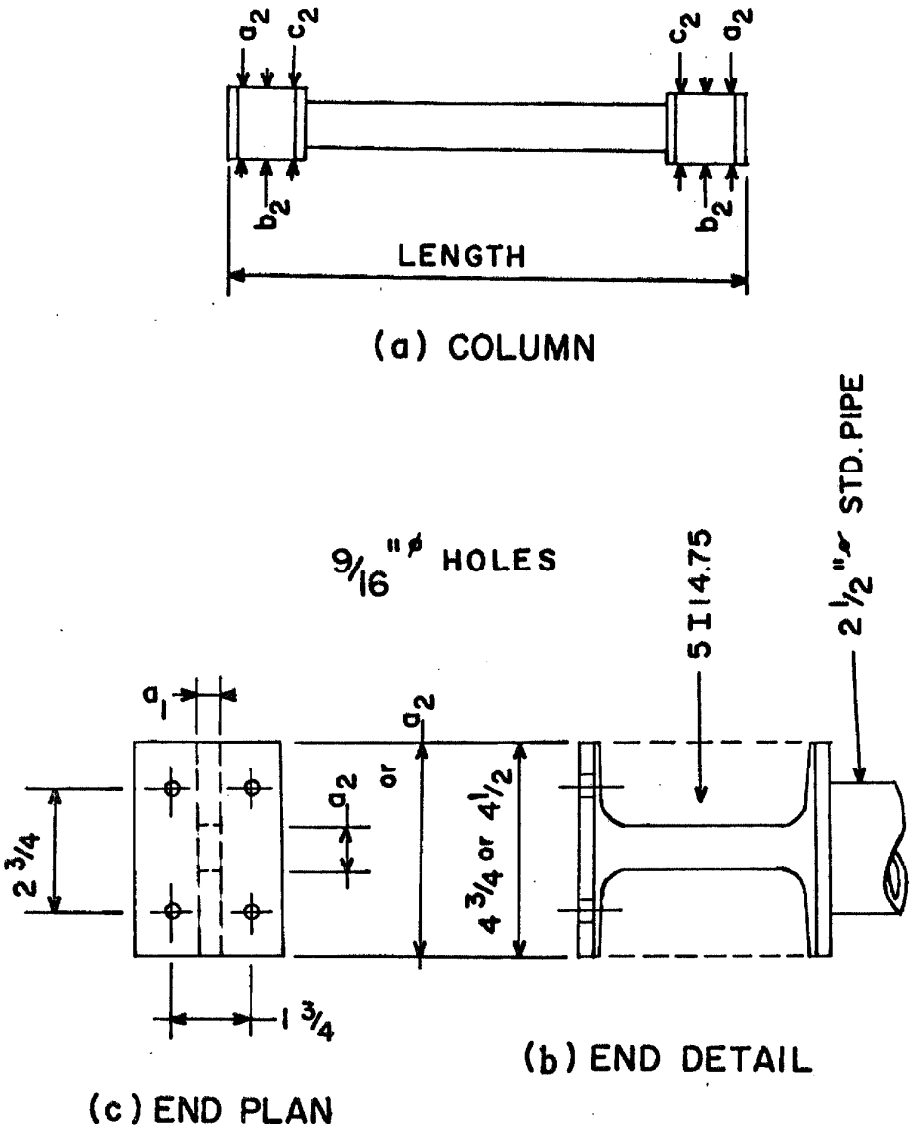

FIG. 3.5 EXPERIMENTAL COLUMN DETAILS

Table III-1

Column Dimensions
(inches)

Column	a_1	b_1	c_1	a_2	b_2	c_2	Length
COLUMN LI							
NE Top	0.496	0.497	0.496	1.002	1.001	1.001	30.06
Bottom	0.496	0.497	0.500	1.001	1.001	1.001	
SE Top	0.497	0.499	0.496	1.001	0.999	0.996	30.06
Bottom	0.497	0.499	0.497	1.004	1.002	1.000	
SW Top	0.496	0.496	0.496	1.004	1.003	1.001	30.06
Bottom	0.498	0.497	0.498	1.001	1.000	1.000	
NW Top	0.496	0.498	0.496	1.005	1.005	1.003	30.06
Bottom	0.496	0.496	0.496	1.003	1.002	0.999	
COLUMN SI							
NE Top	0.497	0.496	0.496	4.568	4.573	4.588	24.88
Bottom	0.498	0.497	0.495	4.561	4.559	4.566	
SE Top	0.497	0.495	0.495	4.534	4.528	4.526	24.93
Bottom	0.499	0.497	0.496	4.524	4.516	4.514	
SW Top	0.499	0.498	0.498	4.499	4.493	4.490	24.91
Bottom	0.499	0.498	0.498	4.491	4.488	4.488	
NW Top	0.496	0.496	0.496	4.530	4.530	4.533	24.88
Bottom	0.498	0.498	0.497	4.425	4.428	4.435	
COLUMN SII							
NE Top	0.498	0.498	0.497	4.517	4.520	4.528	24.93
Bottom	0.490	0.487	0.488	4.491	4.491	4.488	
SE Top	0.497	0.496	0.496	4.554	4.549	4.543	24.93
Bottom	0.489	0.487	0.487	4.499	4.497	4.494	
SW Top	0.498	0.498	0.496	4.503	4.503	4.503	24.91
Bottom	0.488	0.489	0.489	4.507	4.502	4.498	
NW Top	0.496	0.496	0.496	4.517	4.520	4.519	24.93
Bottom	0.488	0.486	0.487	4.510	4.512	4.505	
COLUMN SIII							
NE Top	0.498	0.496	0.497	4.569	4.562	4.557	24.88
Bottom	0.498	0.498	0.496	4.509	4.507	4.506	
SE Top	0.498	0.498	0.498	4.501	4.493	4.494	24.88
Bottom	0.490	0.488	0.488	4.507	4.503	4.501	
SW Top	0.498	0.497	0.496	4.510	4.511	4.513	24.88
Bottom	0.499	0.498	0.497	4.508	4.510	4.515	
NW Top	0.490	0.487	0.487	4.508	4.510	4.512	24.88
Bottom	0.489	0.487	0.489	4.481	4.481	4.485	

structure to move in the direction of the least resistance. To eliminate these effects, the second design (short column) was established so that the natural frequencies were well separated with only the weak (E-W) direction frequency falling into the frequency range of the force generators. This column is also shown in figure 3.5 and its dimensions are given in Table III-1.

The largest possible range in natural frequencies with a given column section was obtained by allowing for a large change in the mass of the rigid floor of the structure. This was done by leaving the entire center panels of the floor open for the lowest mass and by filling these panels with lead weights to increase the mass. The weight of the floor frame was 786 pounds and the maximum amount of lead which could be added between the flanges of the frame was 9560 pounds. Figure 3.1 shows this rigid floor frame which was made of 10 WF 29 steel sections with full penetration butt welds at all junctions. The top and bottom surfaces of the completed floor were milled so that the two surfaces were plane and parallel. This permits continuing the columns for the next story height from the top of the floor. The webs of the 10 WF 29 beams were braced at each column position with four 3/8 inch web stiffener plates.

The objectives of the design were met satisfactorily. The end conditions were very favorable in that the material under high stress did not occur directly at the connection, in fact, the effect of the connections on the experimental results was minimal. Using

columns which were not truly full-scale columns as used in building construction was unavoidable. However, the test sections were standard rolled sections of the same material used in building construction, which lead to the minimization of any scaling factors as far as material effects were concerned.

The structure as investigated had a total weight of 3238 pounds independent of the weight of the force generators. The sources of this weight are listed in Table III-2. In addition to this weight the rigid floor supported either none, one, or two force generators plus

Table III-2

Rigid Floor Weight

item	weight (pounds)
Rigid Frame	786
1/3 of column weight	23
Lead Pigs	2310
Lead Support System	119
Total	3238

eccentric weights depending upon the test conditions. Force generator No. 1 weighs 800 pounds and force generator No. 4 weighs 645 pounds. The maximum total weight of the structure was 4683 pounds exclusive of the eccentric weights. The lead weight consisted of lead pigs varying in weight between 69 and 115 pounds each. The lead pigs were wedged together and against the rigid frame in order to eliminate any translation or rotation of the weights.

The columns were connected to the rigid frame and base plate with four 1/2 inch diameter high-strength steel bolts. The proof load of the bolts is 12,050 pounds and beveled washers were used because

of the sloping flange of the 5 I 14. 75 column end sections. The column to frame bolts were torque tightened to 65 foot-pounds and the column to base plate bolts to 50 foot-pounds. The suggested torque to develop the ASTM 325 proof load is 100 foot-pounds.

The material of the 5 I 14. 75 beam used for column sets SI, SII, and SIII was chemically and mechanically analyzed. These tests and their results are reported in Appendix II.

All the column end sections were covered with a brittle lacquer to give a visual indication of maximum strain regions of the columns during the experiments. The brittle lacquer was used for an overall qualitative indication of strain while a pair of post-elastic strain gages were used on each column set to give quantitative strain values.

IV. EXPERIMENTAL INVESTIGATION

The experiments performed on the structures described in Chapter III and the results of these investigations are reported in this chapter. Although the column sets LI, SI, SII, and SIII were studied in sequence with a new column set started after failure of the previous set, the results are generally not reported in chronological sequence. The chronological summary of the experiments is reported in Appendix III.

The results are divided into three groups; dynamic response, static results, and dynamic hysteresis curves. The dynamic response group has many types of results reported, e. g. , frequency response, free vibrations, equivalent viscous damping, ultraharmonics, etc.

Some of the results are presented in several ways to facilitate comparison. However, the overall discussion of these comparisons is reserved to Chapter V.

A. Experimental Procedure

Several different variations of the following procedures were actually used in the program, but these variations were only small changes of the basic procedures given here. The instruments used and their accuracy are described in Appendix I.

1. Dynamic Procedure

The basic data recorded for each test were three accelerations, one displacement, one strain measurement, and the phase pulse of the generated force. The accelerometers were given a static ± 1 g calibration by rotating the accelerometer through plus and minus 90

degrees from the balanced position and recording the output. The accelerometers were bolted to milled steel blocks, figure 4.1, which simplified this accurate calibration. The displacement was measured by a linear variable differential transformer (LVDT) which was calibrated by moving the core through several measured deflections. These calibration deflections were measured with a dial indicator connected to the core rod and were measured to ± 0.0003 inch. The calibration of the strain gages was established by the "calibrate" button of the amplifier or by a known external change in resistance applied to the strain gage bridge.

The deflection of the frame was measured at the center of a side by placing the LVDT either at the top or bottom flange of the rigid floor. The positions of the accelerometers were varied somewhat from test to test, but one accelerometer was usually placed over each column on the static forcing side of the structure (i.e., the north side or the west side of the structure). The third accelerometer usually was placed at approximately midspan of a side or over one of the other columns.

While using one force generator, the force pulse occurred when the top bucket of the force generator was east of center. For East-West excitation, the force pulse corresponds to a maximum force amplitude in the easterly direction. For North-South excitation, the force pulse corresponds to the zero force amplitude preceding a force in the northerly direction. While using two force generators, the force pulse occurred when the top bucket of the force generators

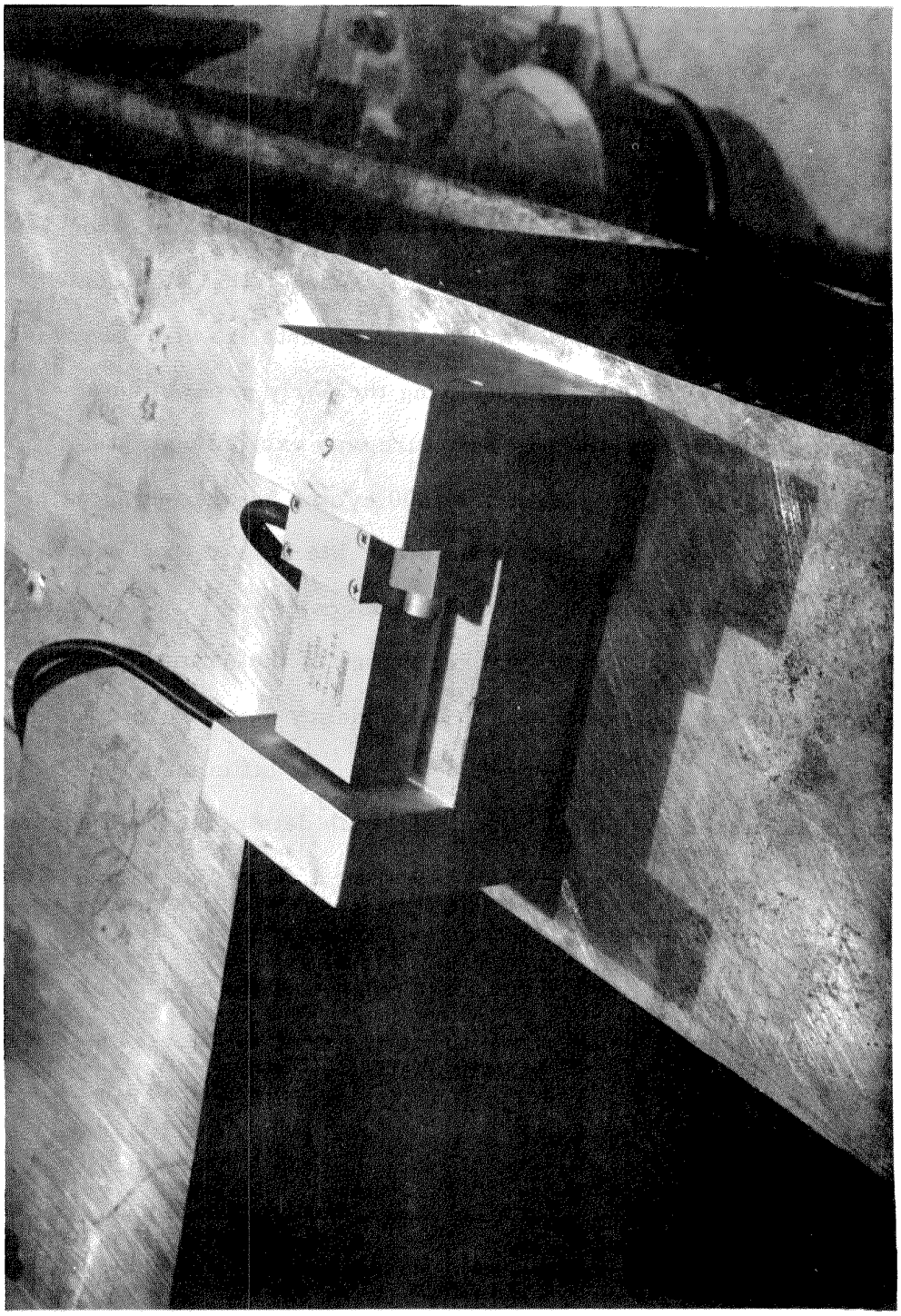

FIG. 4.1 ACCELEROMETER MOUNTED IN A MILLED STEEL BLOCK

were west of center. Therefore, the East-West excitation force pulse corresponds to a maximum force amplitude in the westerly direction for two the force generators.

The experimental sequence for a given force amplitude consisted of a one hour warm-up for the equipment, initial calibration, data taking and final calibration. From the initial tests, it was observed that the structure changed rapidly during the early experiments. Therefore, in several tests, the structure was excited near its resonant frequency for approximately 800 cycles before taking data. Typical test data were obtained as follows. Starting at the lowest frequency which generated a reasonable response level, the frequency was increased in steps through the resonance of the structure until a minimum response was reached. The frequency steps were not of constant size, but varied in order to obtain most efficiently the maximum amount of significant data. At each data point the frequency was held constant until the structure reached a steady state condition.* After the minimum response condition was reached, the frequency was decreased in steps until the initial frequency was reached. This double tracing of the frequency response curve of the structure completed a set of data. A check of the transducer calibration completed the experiment.

---

* The importance of maintaining a steady-state condition is well documented in the literature, e. g., references 33, 34 and 35.

The double tracing of the frequency response curve described above was carried out only for small deflections of column LI because the properties of the structure changed during testing and the peak response changed. This was observed even in the case of small deflections.

Some of the experiments for dynamic hysteresis data consisted of only a few data points at preselected frequencies.

2. Static Procedure

The calibration of the load cell in terms of the number of lines at a given db setting corresponding to a given number of pounds was established for a particular amplifier and galvanometer by applying a known load to the cell. A corresponding reading of the "calibrate" deflection was also noted, so that future checks of the load cell did not require a full recalibration. The known load calibration was performed several times during the year of experimenting to insure a stable load cell calibration. The calibration did not change during this time.

The dial indicators were located at each column of the loading side and were positioned at the bottom flange of the rigid floor. Initial dial readings were taken. The balanced and calibrated load cell was connected between the forcing system and the structure at center span. In some of the static tests the column strain was measured by the same strain gage bridge used in dynamic tests and was recorded simultaneously with the imposed load.

Data were taken while the structure was forced through several cycles of predetermined deflection ranges. At each data point, the two dial indicators were read and the load cell and strain gage readings were recorded. Data were usually taken for two equal maximum deflection cycles before changing to a different deflection range. While taking data from a test cycle, the zero load position was recorded periodically in order to monitor the drift of the zero position. As was noted in the discussion on accuracy, this drift decreases with time; but since the time intervals between measurements are relatively short and the drift small, a linear change in drift between the two check values was assumed on the basis that the time between data points was constant. These assumptions are sufficiently accurate. After completing the tests of two or three successive different deflection series, the load cell was freed from the structure and "calibrated", and the final deflection and strain readings were taken.

B. Test Results

As will be seen in the following section, the previous testing history of the structure has an effect upon the results of a particular experiment. Therefore, a complete chronological list of all the structural experiments is given in Appendix III for which the reference notation is A3. aa where the A3 refers to Appendix III and the aa to the number of the test listed. It should be noted that the static and dynamic tests were run alternatively even though the results are reported in groups.

1. Dynamic Response Tests

1a. Evidence of structural damage. First, the frequency-response curves have an altered shape with successive testing, all other factors being held constant. Second, a structural failure of the columns occurred within a limited number of test cycles which indicates an early deterioration consistent with the endurance properties of the material. This will be discussed further in the section on fatigue in Chapter V.

The altered shape of the frequency-response curve can be best illustrated by actual data. Figures 4. 2 and 4. 3 show typical frequency-response curves for LI (N-S) by forces with increasing frequency steps followed immediately thereafter with decreasing frequency steps. Again, the A3. aa numbers refer to specific experiments as listed chronologically in Appendix III. Another example showing this change in the structure caused by progressive testing is given in figure 4. 4. In this figure, both frequency response curves are determined with increasing frequency steps of the same force amplitude. The only cause for the difference between these two curves is the structural changes effected by the experimentation which occurred between the tests for the curves. By using the test identification numbers for each curve, Appendix III will give the experiments which occurred between the tests plotted in figure 4. 4.

1b. Recorded data. Although three acceleration readings, a strain reading, and for small deflections a LVDT reading were taken simultaneously, only one of the acceleration readings was used

FIG. 4.2 FREQUENCY RESPONSE OF LI (N-S)

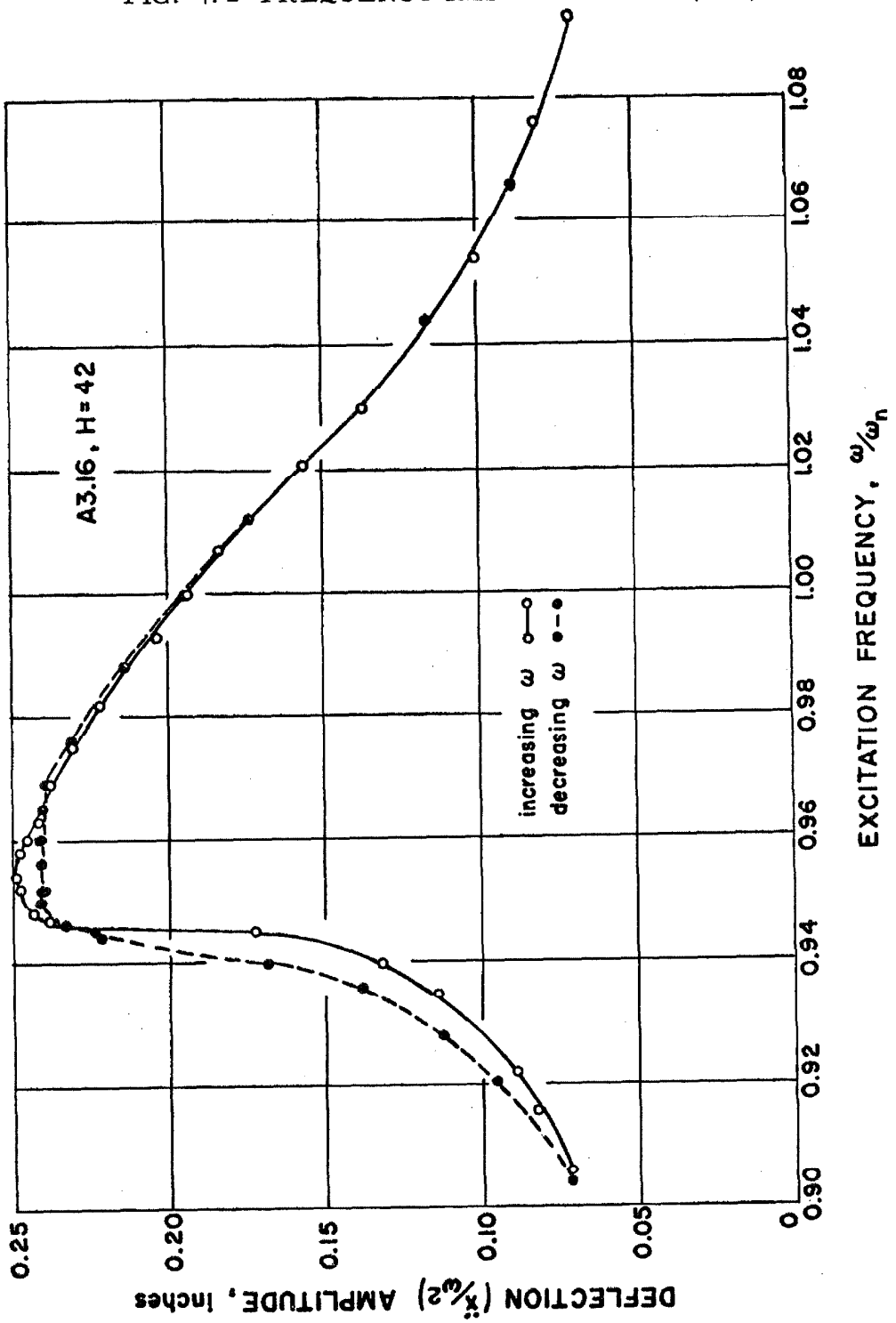

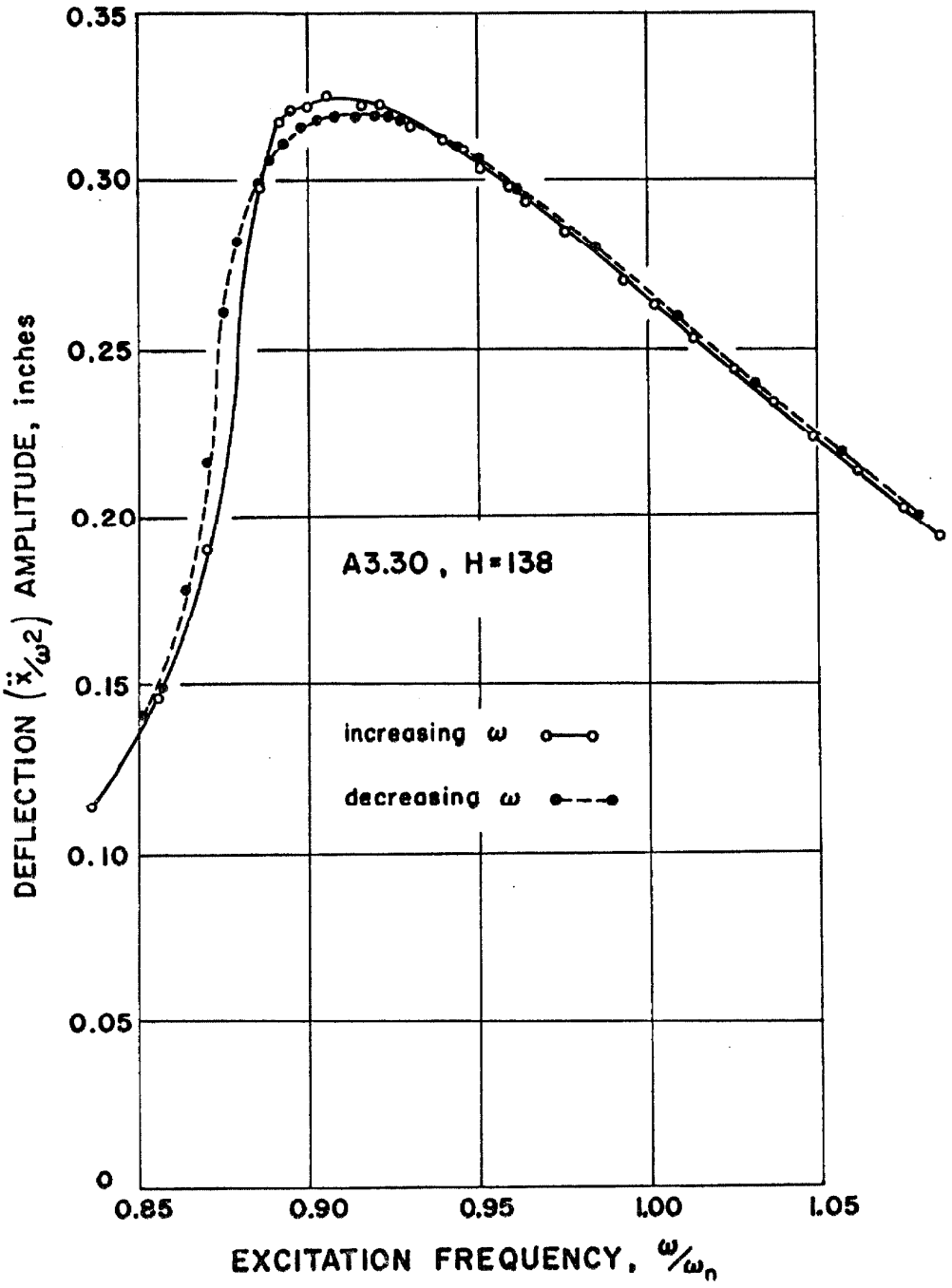

FIG. 4.3 FREQUENCY RESPONSE OF LI (N-S)

FIG. 4.4 FREQUENCY RESPONSE OF LI (N-S)

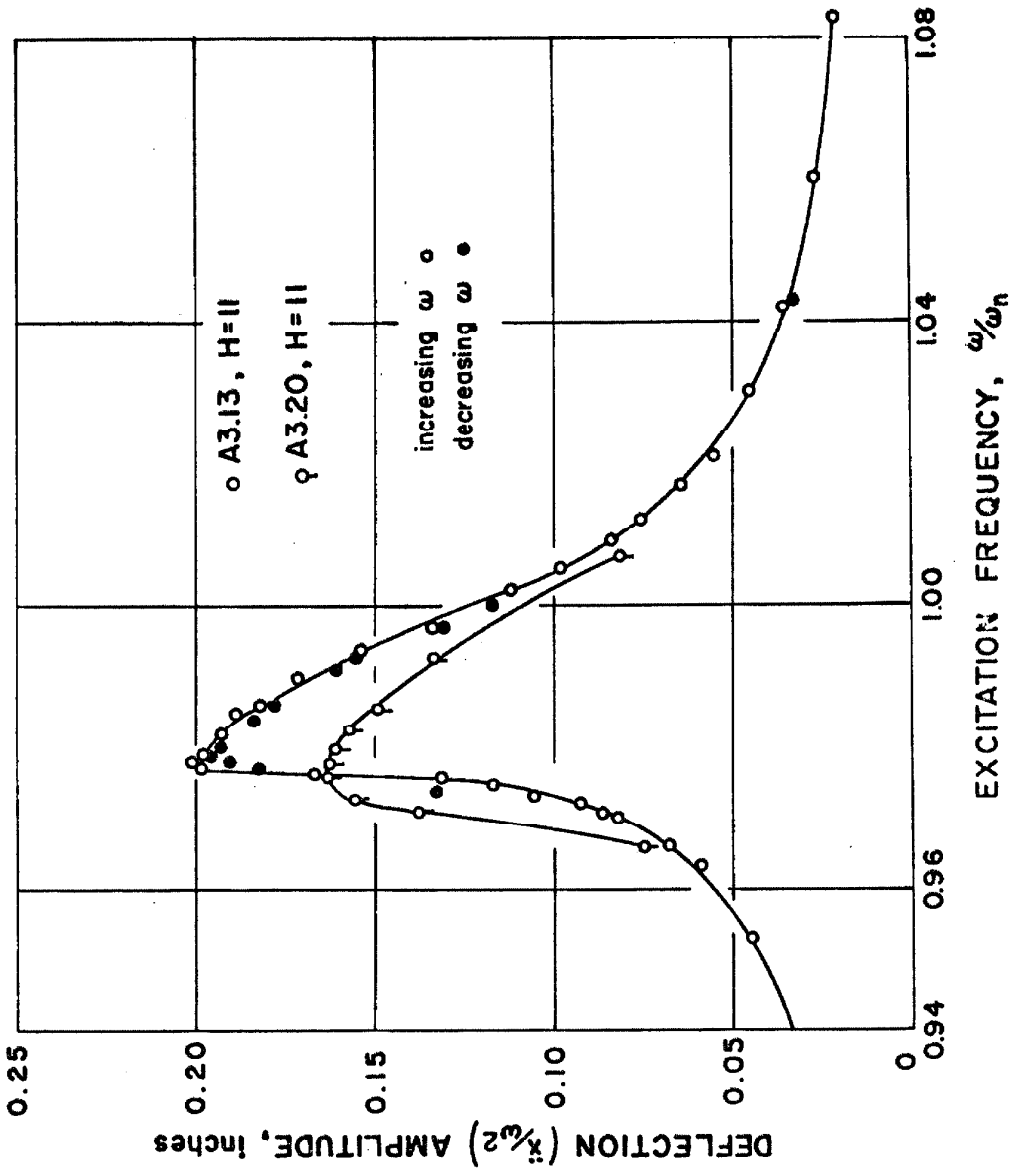

for data reduction unless the strain data were also wanted for a specific reason. There was a periodic cross checking between the accelerometers to be sure that any one of the readings would be representative of all readings. The greatest discrepancy in this approach occurred when testing columns LI in the North-South (strong) direction. In this case the east columns had a deflection about 20% greater than the west columns and, therefore, the average of the east and west accelerations was used and compared with the LVDT reading at midspan. The average accelerations reduced to deflections agreed within the predicted error with the LVDT readings. In this case, the motion was not purely translational as assumed, but there was also a torsional component. In analyzing the motion of the floor as a rigid body with the translational acceleration

$$\ddot{x} = \ddot{x}_o \sin \omega t$$

and the torsional acceleration

$$\ddot{\theta} = \ddot{\theta}_o \sin(\omega t + \phi),$$

it was found for a specific case that the resulting force per column in the weak (E-W) direction amounted to about 11 pounds compared to about 200 pounds in the strong (N-S) direction. The resulting eccentricity of the gravity center of the mass of the frame relative to the column resistance centroid was about 1. 5 inches. The effect of this small eccentricity is pronounced because the resulting forces required to maintain equilibrium acted in the most flexible direction, normal to the direction desired. It was primarily this action which dictated that the subsequent column design should act in only one

direction. In this manner, the weakest direction could be tested and the secondary effects caused by eccentricities and other factors would be minimized.

1c. Normalization of the data. The data has been normalized before presentation so that the several different tests can be compared. The peak to peak acceleration is divided by $2\omega^2$, where ω is the circular frequency of the forced motion in radians per second. This normalized "acceleration" has units of deflection in inches. It approximates, but is not exactly equal to the maximum deflection of the structure because the acceleration is not purely sinusoidal. However, since the acceleration is not very different from a sinusoid at any time, the normalized "acceleration" can be taken as the maximum deflections of the structure for all practical purposes and will henceforth be used in that way.

The frequency scale is normalized by dividing the excitation frequency by the natural frequency of the virgin structure determined by the original free vibrations.

The amplitude in pounds of the sinusoidal force is identified by H. The determination of the force amplitude is as follows. The force amplitude

$$F_o = Bf^2 \qquad (4.1)$$

where B is defined in Appendix I with values given in Appendix III for each test and f is the excitation frequency in cps. The natural frequency of the structure as defined in the preceding paragraph is f_n. Then

$$F_o = Bf_n^2 \left(\frac{f}{f_n}\right)^2 = H\left(\frac{f}{f_n}\right)^2 = H\left(\frac{\omega}{\omega_n}\right)^2 \qquad (4.2)$$

where

$$H = B f_n^2. \qquad (4.3)$$

1d. Free vibrations. The natural frequencies listed in Table IV-1 are used in the normalized frequency determination by the relation

$$f_{nt} = f_n \sqrt{\frac{W_n}{W}} \qquad (4.4)$$

where f_{nt} is the natural frequency to be used for normalization of that test, f_n and W_n are the natural frequency and effective weight of the structure given in Table IV-1 and W is the effective weight of the structure under test conditions.

The free vibration data for LI and SIII were taken with the Sanborn recorder which has a one second time pulse based on the 60 cps line current. Thus, the accuracy of the measured frequency is determined by the measuring error which was less than ± 0.1%. The

TABLE IV-1

Free Vibration Natural Frequencies

Column	Test	Experimental f_n (cps)	W_n (lbs.)	Theoretical Eqn. 5.32 (cps)
LI (E-W)	A3.2	1.56	3238	--
LI (N-S)	A3.2	3.16	3238	3.19
SI (E-W)	A3.34	3.78	4038	3.79
SII (E-W)	A3.45	3.68	4220	3.70
SIII (E-W)	A3.55	3.525	4683	3.51

free vibration data for SI and SII were taken with the light beam

recording oscillograph in which the time spacing of the time lines is a variable function of the temperature of the oscillograph. In this case, the time base was established by checking the time line spacing with the force generator speed as measured by a 0.1% digital counter during the following forced vibration test.

1e. Frequency-response results. All the frequency-response test curves will be given, with the exception of the few tests of SII with one force generator, for which the force generator torque limitation was reached.

For column LI, figure 4.5(a) shows the result of the initial dynamic tests and gives the relative position of the torsional natural frequency to the N-S natural frequency. In figure 4.5(b), an enlarged scale of the response peak is given to show the changes in the response of the structure with additional testing even at this low stress level. It can be seen that the response seems to reach a relatively stable relationship at a maximum deflection ($\ddot{x} / \omega^2$) amplitude of 0.195 inch. Figures 4.6 and 4.7 show the differences in structural response as the horizontal force increments are increased and decreased respectively. There are two important items to note:

i) Response amplitudes in the latter tests are substantially below those of the original tests for equal horizontal forces, with the exception of the response to the largest force amplitude;

ii) The pronounced changes in response with repeated testing at the same force amplitude shown in figure 4.6 has almost completely disappeared for the results in figure 4.7.

FIG. 4.5 FREQUENCY RESPONSE OF LI (N-S)

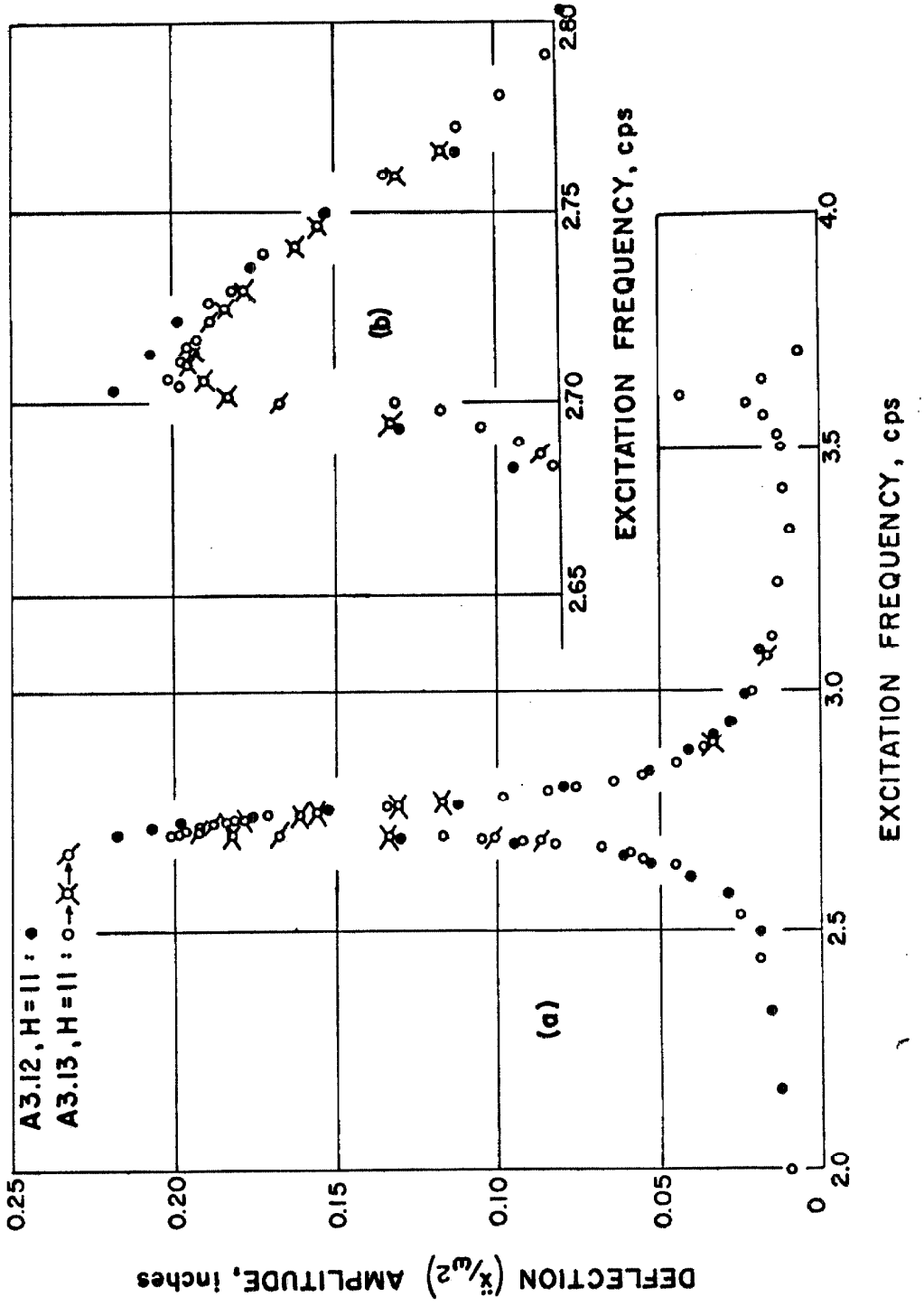

FIG. 4.6 FREQUENCY RESPONSE OF LI (N-S)

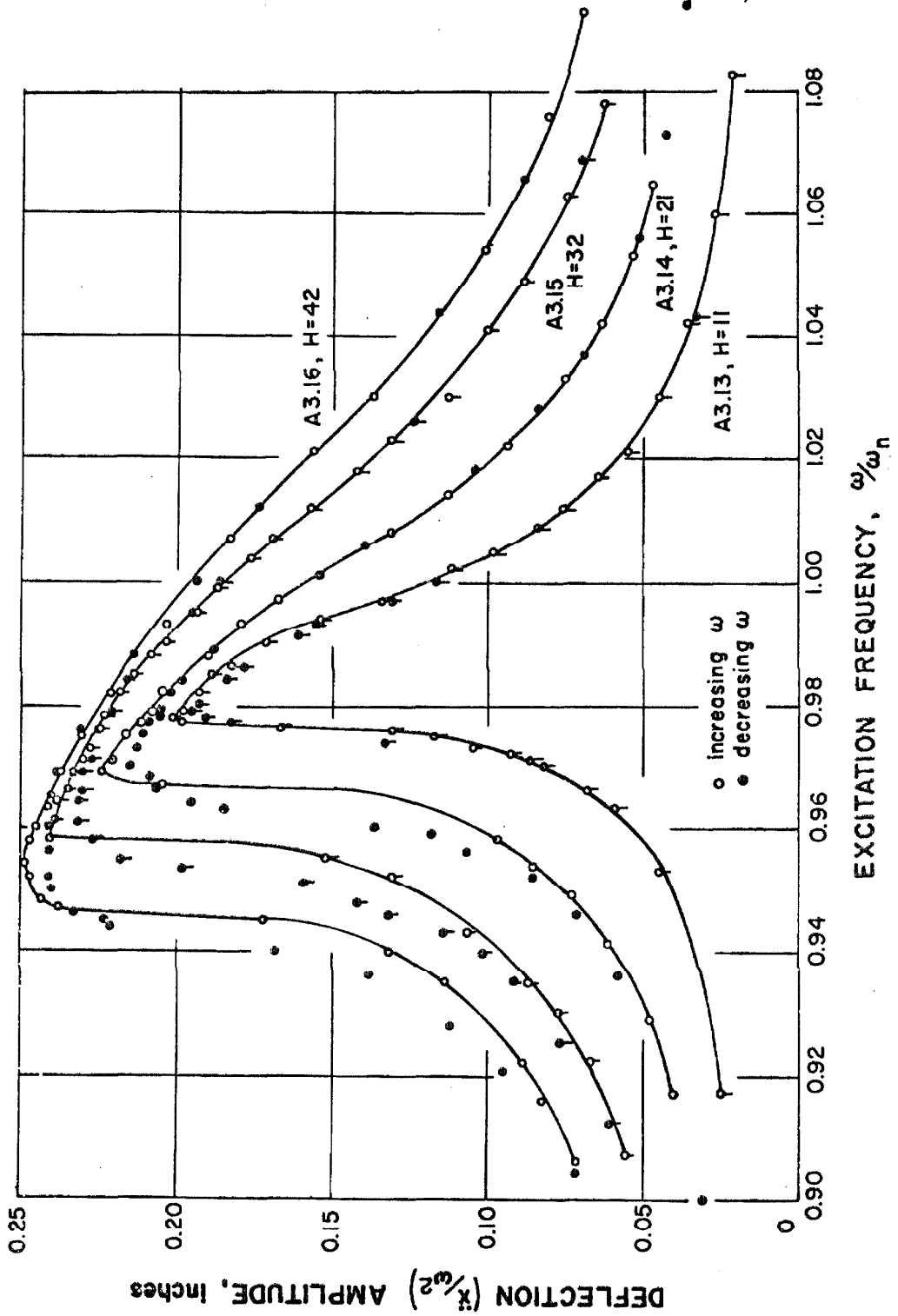

FIG. 4.7 FREQUENCY RESPONSE OF LI (N-S)

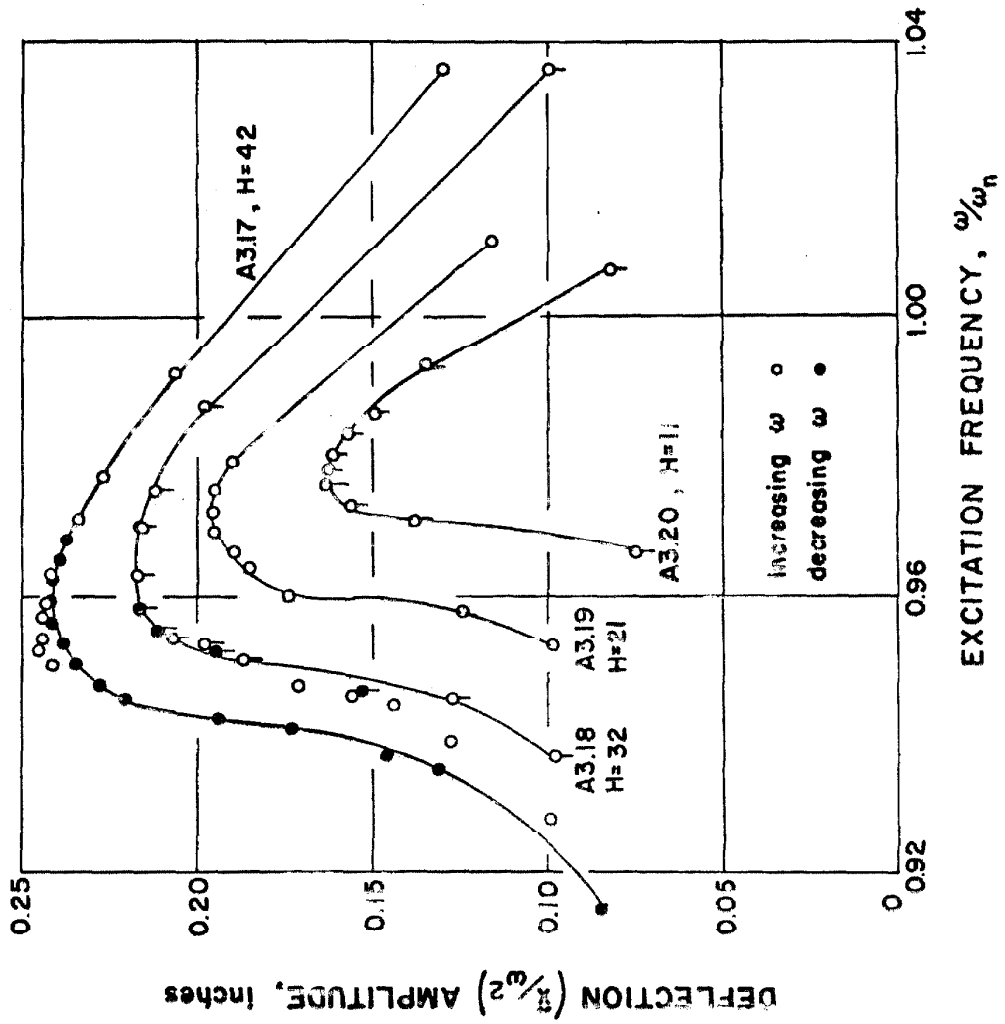

Two additional response curves are given in figure 4. 8 in which the first curve, A3. 24, repeats a previously used force amplitude and the second corresponds to a slightly larger force. Figure 4. 9 completes the response curves obtained from column LI (N-S). These curves were obtained from increasing force amplitudes, therefore, they correspond to figure 4. 6 rather than figure 4. 7. As expected, the decrease in frequency associated with the peak response is characteristic of a softening spring type of non-linear system.

The response curves for columns SI and SII are given in figure 4. 10. Retracing of the response curves was not done because of the relatively short expected endurance life. The changes in the response of the structure because of testing will be illustrated for these columns in the sections on static and dynamic hysteresis curves. Again, the softening spring type of non-linearity occurred as expected.

1f. Dynamic response at failure. A detailed study of the structural response in the regions approaching, during and after failure is of interest as a possible means of investigating structural damage in real structures.

Column LI failure was noticed while testing in the N-S direction by observing an increasing torsional component of the structure's motion. Upon inspection of the columns, a crack through the brittle lacquer coating was observed at the bottom fillet of the northeast column. This crack was not believed to be across the entire cross-section. Since all the dynamic tests until this time were in the N-S direction and because the stability of the force generators under

FIG. 4.8 FREQUENCY RESPONSE OF LI (N-S)

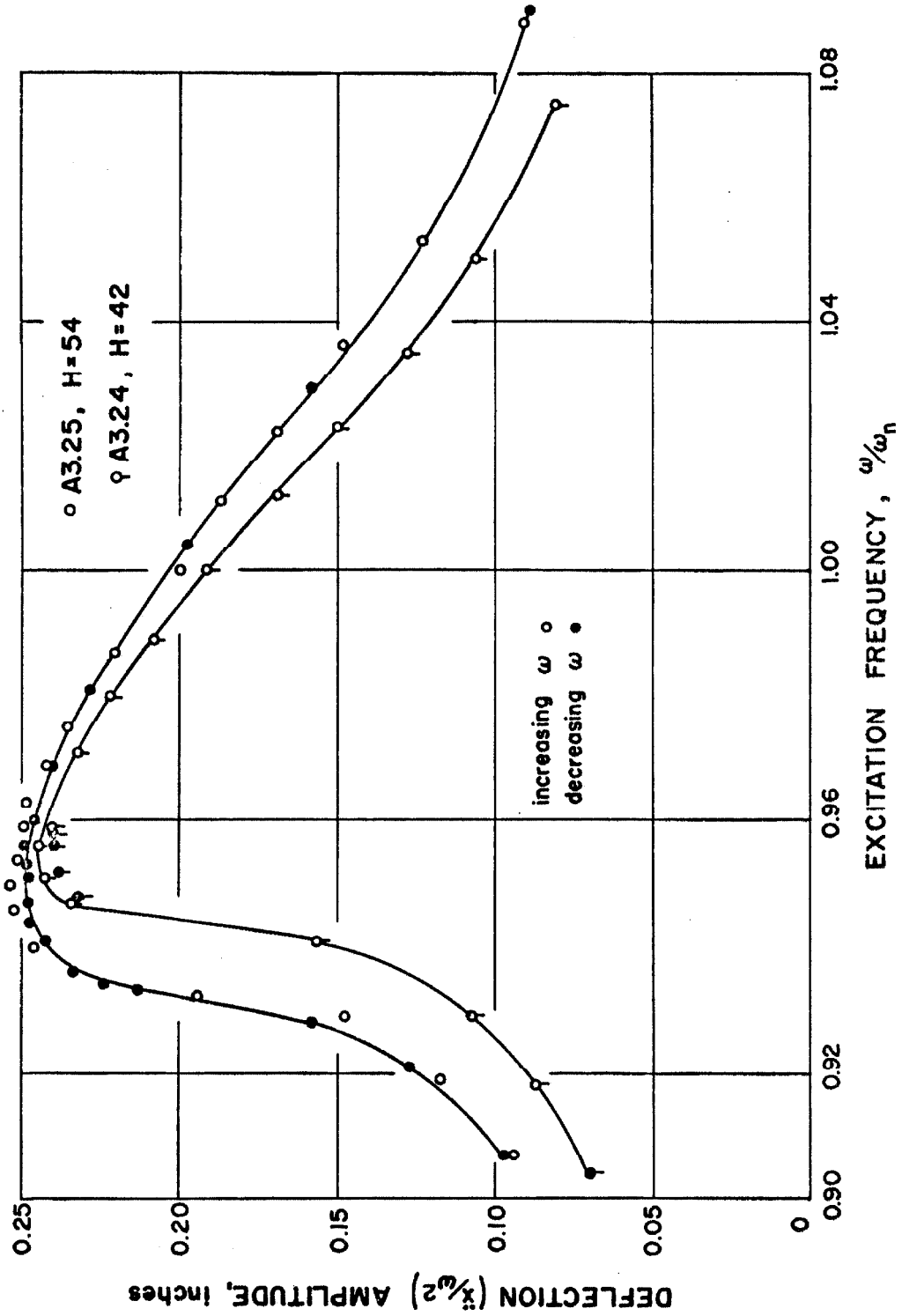

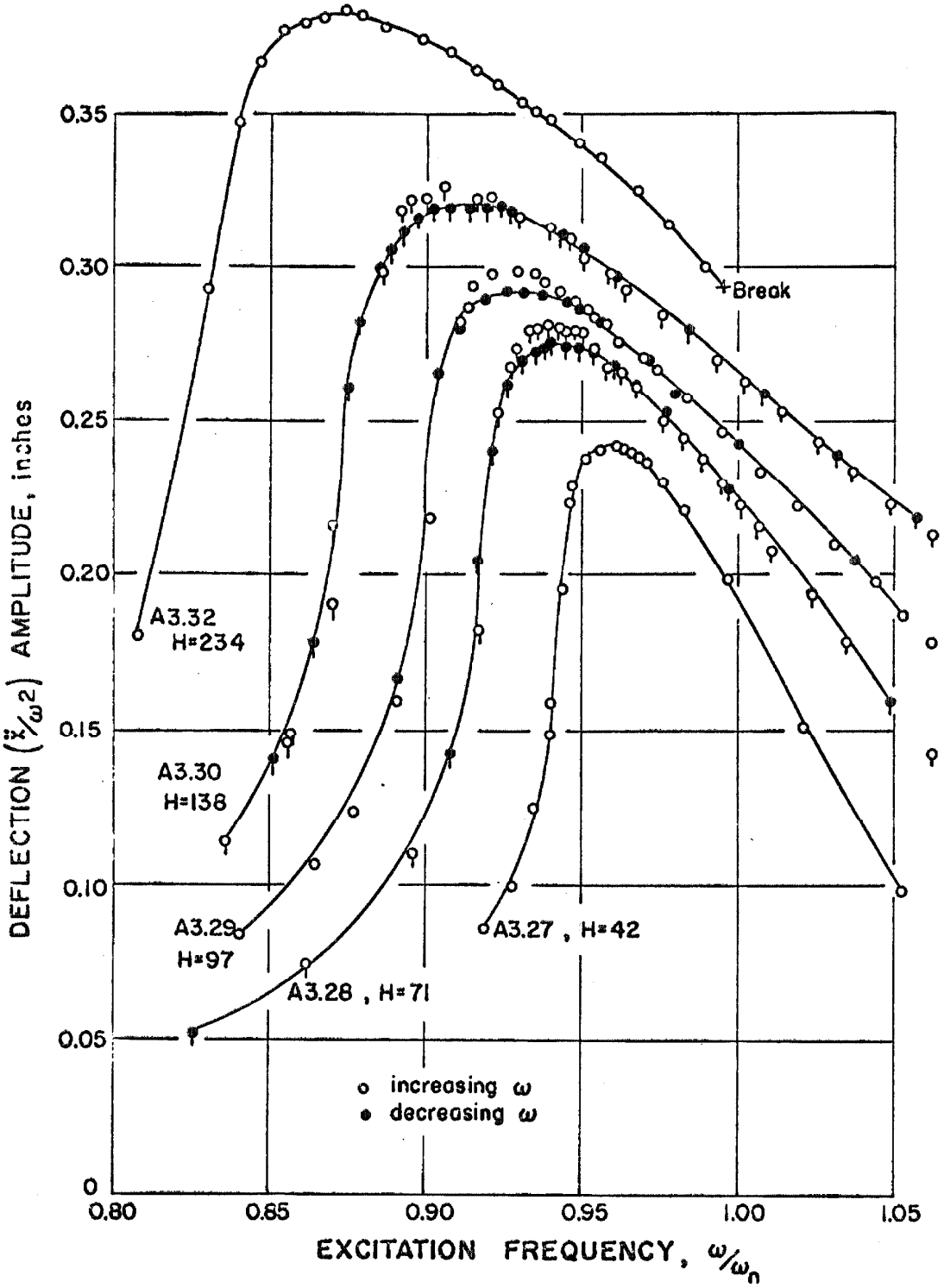

FIG. 4.9 FREQUENCY RESPONSE OF LI(N-S)

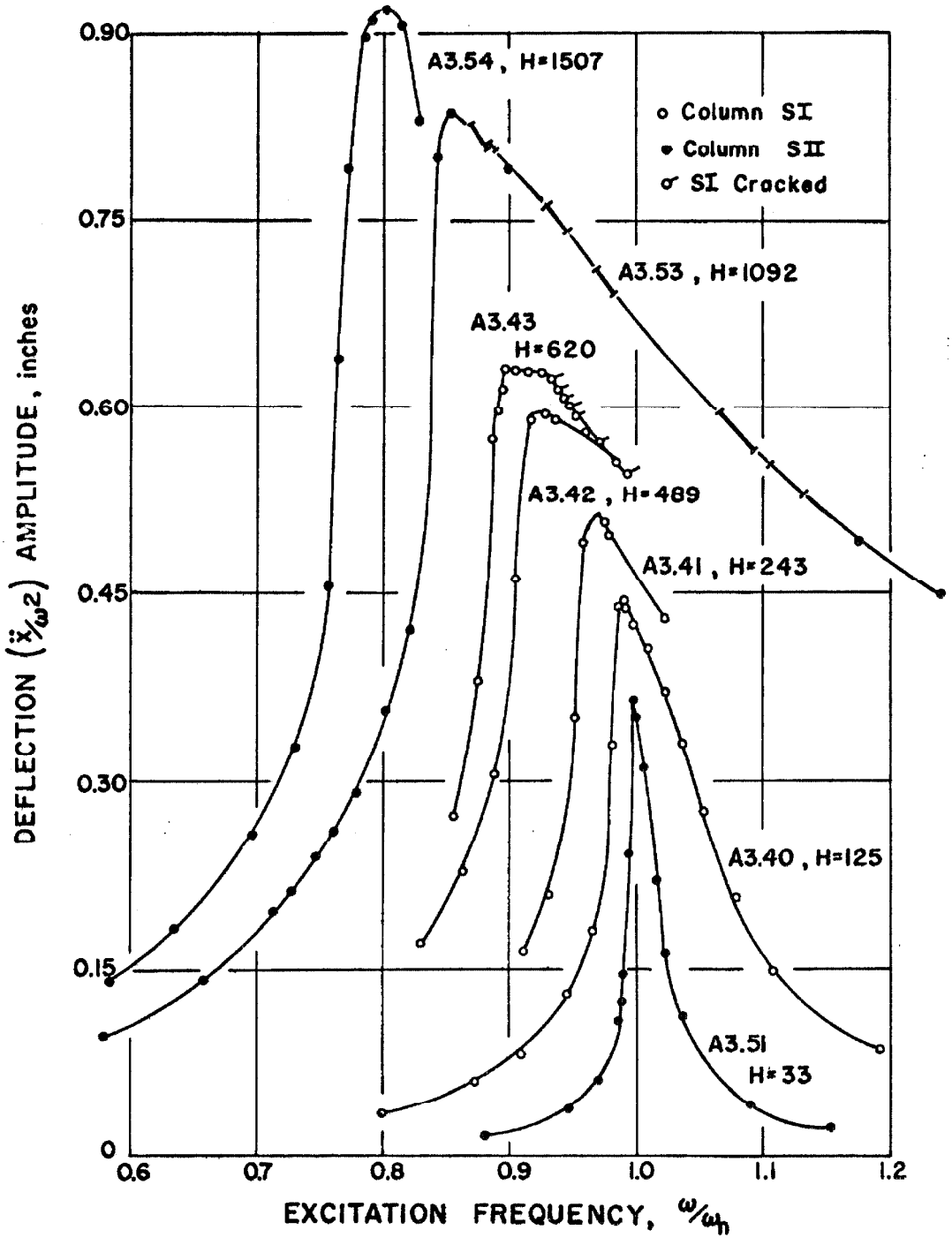

FIG. 4.10 FREQUENCY RESPONSE OF SI AND SII

large deflections was unknown, it was decided to test this failed column set in the E-W direction. The E-W direction was the weak direction of the structure and it was found that torsion was not a serious problem in exciting translational motion in the weak direction even with one column less stiff than the other three. At this point it was decided that the next test columns would be designed to be tested in only the weak direction. Figure 4.11 gives the response curves for the tests in the weak direction of LI. The characteristic of the response curves crossing other response curves at lower force amplitudes indicates that the stiffness of the structure has decreased due to continual weakening of the cracked section. The final break occurred at a frequency of about one cycle per second and the entire frame slowly and smoothly collapsed until it was supported by the emergency timber cribbing below. Figure 4.12(a) and (b) show the structure in its timber supported position. It seems that the surest method to determine if a structure has been damaged is to check the existing natural frequencies with the original frequencies and if no observable change occurs, to determine any change in the position of the centroid of the structural stiffness.

Because restoring the collapsed structure to testing condition involved a considerable effort and because little could be learned from a complete collapse, all further tests were halted before complete collapse. Figure 4.13 shows the last two tests of column SI. In this case, the column failure in the test A3.43 was not realized by observation of the columns or by plotting the acceleration response

FIG. 4.11 FREQUENCY RESPONSE OF LI (E-W) BROKEN

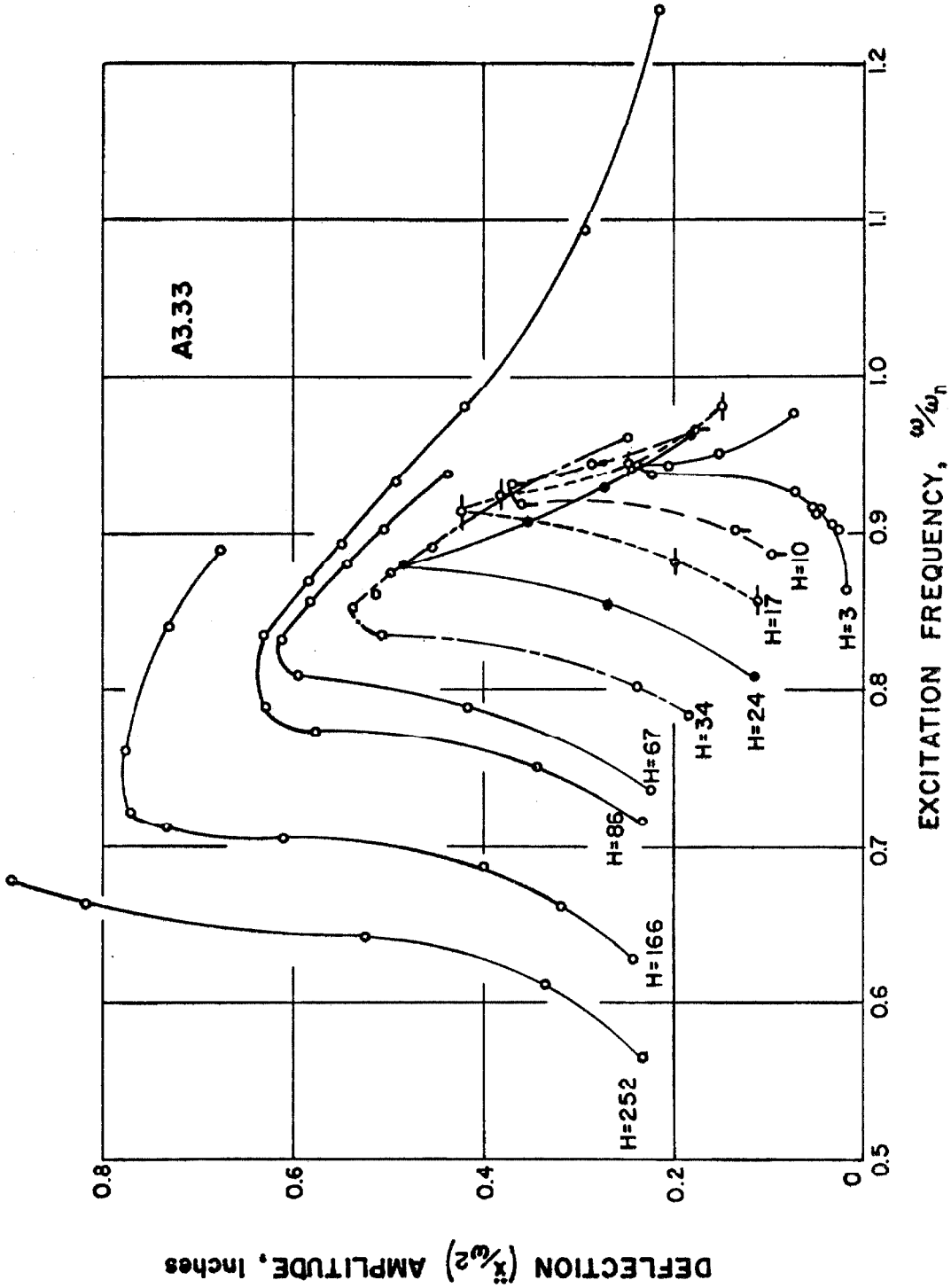

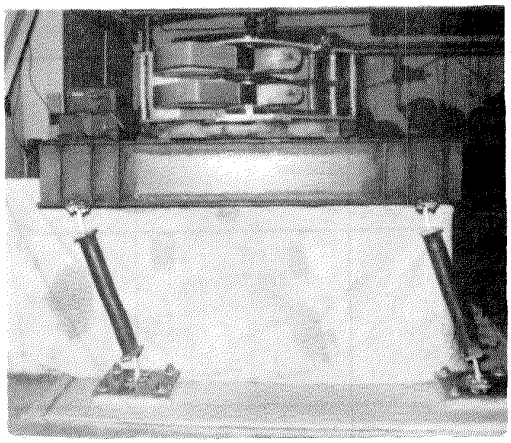

(a) Elevation Looking North

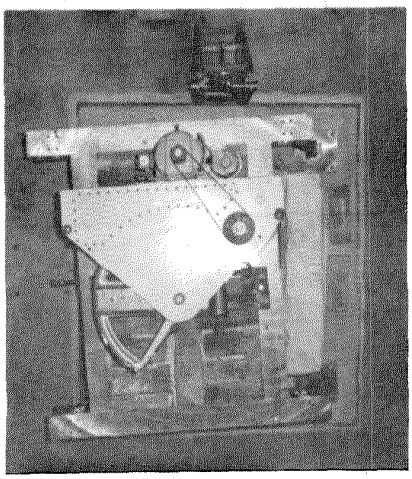

(b) Plan (North ↑)

FIG. 4.12 COLLAPSED LI STRUCTUR E

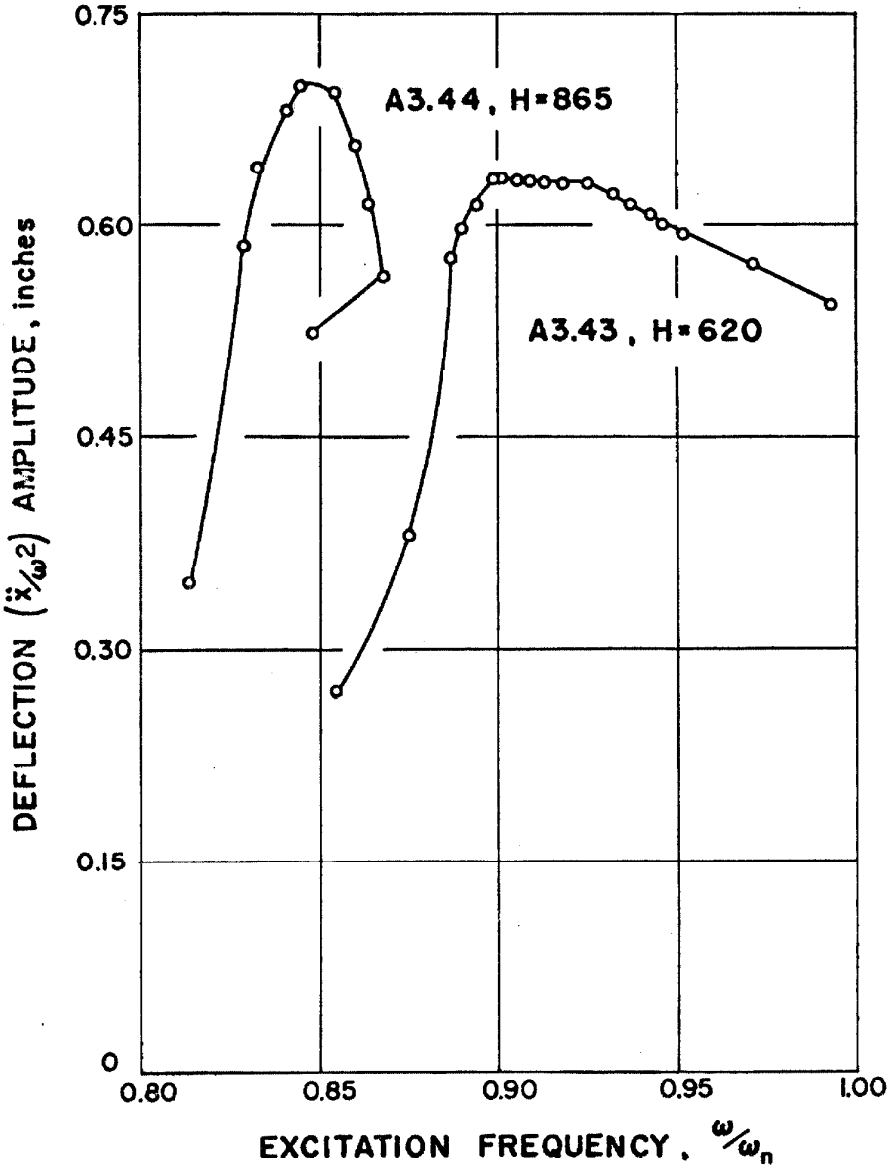

FIG. 4.13 FREQUENCY RESPONSE OF SI AT FAILURE

curve. The failure became obvious in test A3.44 because of a very rapid decrease in acceleration and deflection response with an increase in frequency. The cause of the rapid decrease in the response is the decrease in the natural frequency of the structure, i.e., ω / ω_n increases without change in ω.

The failure was less discernable in column SII, in fact, the last test, A3.54, was continued until completion even though the failure was suspected. The original acccleration data is included with the deflection ($\ddot{x} / \omega^2$) in figure 4.14 to show the type of acceleration response obtained and also to show the data reduction of the non-constant frequency of test A3.53. This changing frequency was eliminated by a slight adjustment of the force generator control.

1g. Equivalent viscous damping; Forced vibration definition.

Many methods of obtaining the equivalent viscous damping of a structure with their specific advantages have been ably presented elsewhere[11, 36, 37]. The development of the approach felt most suitable for the current discussion is based on the equivalent linearization of the equation by specifying that the energy dissipated by the original and the linearized systems near resonance is the same per cycle for the same maximum deflections. This can be done using the equivalent linear system of equation 2.45.

Since the structural response is a steady-state motion, the deflection is periodic in ω and can be expressed by the Fourier expansion

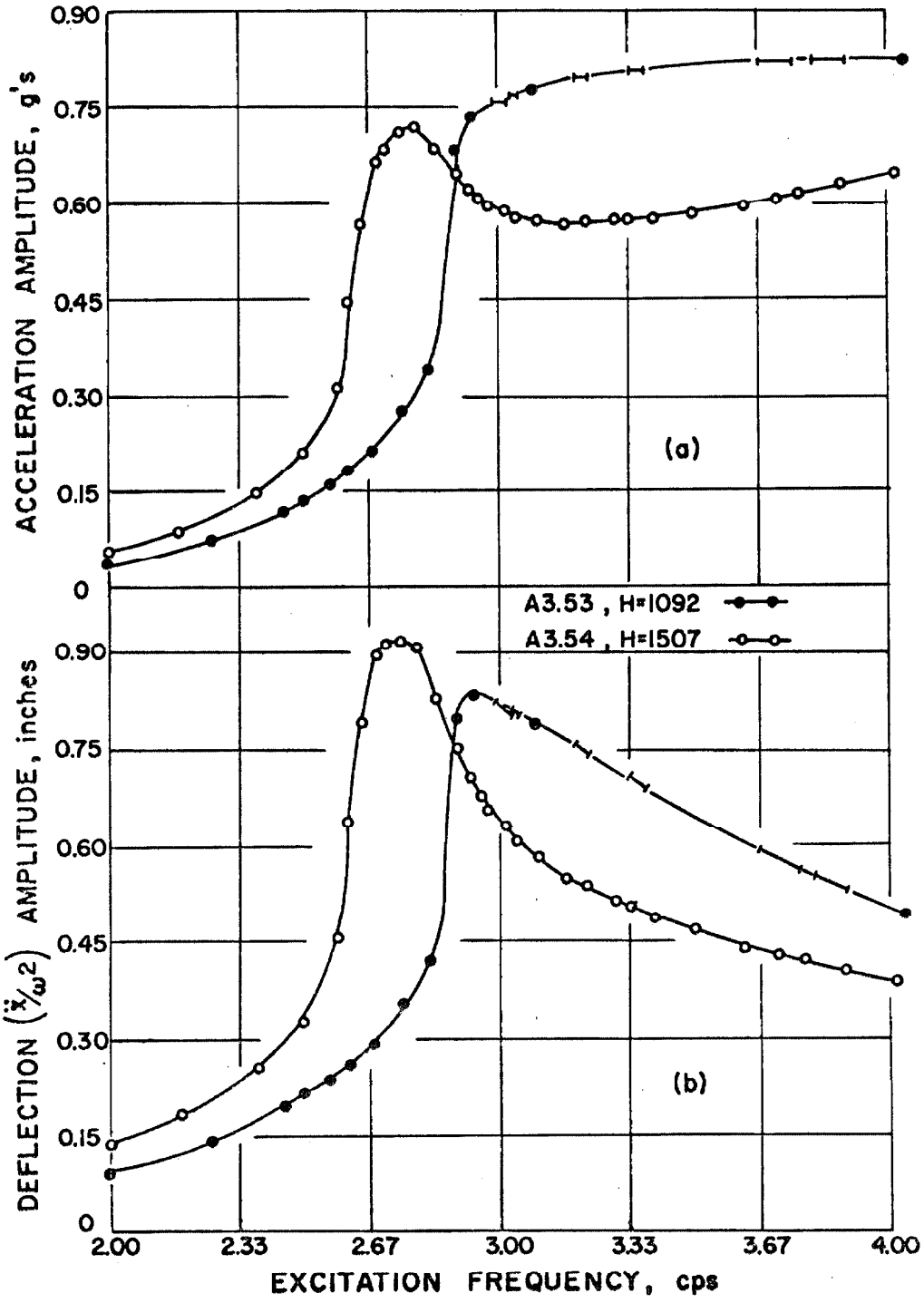

FIG. 4.14 FREQUENCY RESPONSE OF SII AT FAILURE

$$x(t) = \sum_{m=1}^{\infty} A_m \sin(m\omega t - \phi_m) \tag{4.5}$$

where A_m is the amplitude and ϕ_m is the phase angle of the m^{th} term of the series. The energy input per cycle to the structure by the sinusoidal force can be expressed by

$$\oint F\dot{x}dt = \int_0^{2\pi/\omega} B\left(\frac{\omega}{2\pi}\right)^2 \sin\omega t \left[\sum_{m=1}^{\infty} A_m(m\omega)\cos(m\omega t - \phi_m)\right]dt \tag{4.6}$$

where the force amplitude is defined in equation 4.1. The interchange of the summation and integration operations is valid in this case so equation 4.6 can be evaluated using the orthogonality of the trigonometric functions to obtain

$$\text{Energy Input} = B\left(\frac{\omega}{2\pi}\right)^2 \pi A_1 \sin\phi_1 \tag{4.7}$$

Since the deflections are almost sinusoidal, A_1 will be taken as approximately equal to the deflection ($\ddot{x}/\omega^2$) amplitude, A. The energy dissipated per cycle by the equivalent viscous damping for sinusoidal motion at resonance is

$$\text{Energy Dissipated} = \bar{c}\, A^2 \pi\, \omega_n \tag{4.8}$$

where A is the amplitude of the sinusoidal deflection and $\bar{c}$ is the equivalent viscous damping. Critical viscous damping will be defined as

$$c_c = 2\sqrt{Km} = 2\sqrt{\frac{KW}{g}} \tag{4.9}$$

where K is the column stiffness of the structure for small

deflections and m is the mass of the structure. C(A) will be defined as

$$C(A) = \left|\frac{\omega_p}{\omega_n}\right|^2 \tag{4.10}$$

where ω_p is the frequency at the maximum response of the nonlinear structure and ω_n is the small deflection natural frequency. Equating the energy dissipated to the energy input yields

$$\frac{\bar{c}}{c_c} = n_{eq} = \frac{B\left(\frac{\omega}{2\pi}\right)^2 \pi A_1 \sin\phi_1}{A_1^2 \pi \omega_n 2\sqrt{\frac{KW}{g}}} \tag{4.11}$$

Remembering that

$$\omega_n = \sqrt{\frac{Kg}{W}} \tag{4.12}$$

and using g = 386 inches/second^2, equation 4.11 becomes

$$n_{eq} = 4.88\left(\frac{B}{W}\right)\frac{\sin\phi}{A}\left|\frac{\omega}{\omega_n}\right|^2 \tag{4.13}$$

where B is defined by equation A1.8 in Appendix I, W is in pounds, A_1=A is in inches, and $\phi_1 = \phi$. In order to calculate the experimental fraction of critical damping by equation 4.13, $\sin\phi$ must be calculated from the experimentally determined ϕ. Since the frequency response curves have a different shape for the linear and nonlinear cases, the equivalent viscous damping as defined by equation 4.13 is meaningful only near the peak response.

Free vibration definition. For free vibration studies, the equivalent viscous damping is calculated from the decrease in acceleration amplitude over a given number of cycles. Because the

damping is small, the fraction of critical damping can be taken as

$$n_{eq} = \frac{1}{2\pi}\left(\frac{\Delta\ddot{x}_{mean}}{\ddot{x}_{mean}}\right) \quad \text{or} \quad \frac{1}{2\pi}\left(\frac{\Delta x_{mean}}{x_{mean}}\right) \tag{4.14}$$

The fraction of critical damping values for the peak displacements and the free vibration tests can be found in the chronological record of Appendix III.

Determination of the fraction of critical damping. For forced vibration experiments the error in the fraction of critical damping is proportional to the error in ϕ. The importance of phase shift accuracy made it necessary to make a special study of the phase shifts in the instrumentation system, as reported in Appendix I.

The calculated values of n_{eq} for the maximum deflections of the tests of LI (N-S) are plotted in figure 4.15. The n_{eq} values for SI, SII, and SIII are plotted in figure 4.16. The n_{eq} values plotted in figures 4.15 and 4.16 were calculated from data taken near the resonance of the structure. This satisfied the condition of nonlinear-linear equivalence, and also minimized the error associated with ϕ because the phase lag at resonance was approximately 90 degrees.

The area of the force-deflection hysteresis loop is equal to the amount of energy absorbed by the structure. This fact can be used as one method of comparing the static and dynamic response. The dynamic energy dissipated per cycle near resonance has been calculated for columns SI, SII, and SIII by means of equation 4.7 and are plotted in figure 4.17.

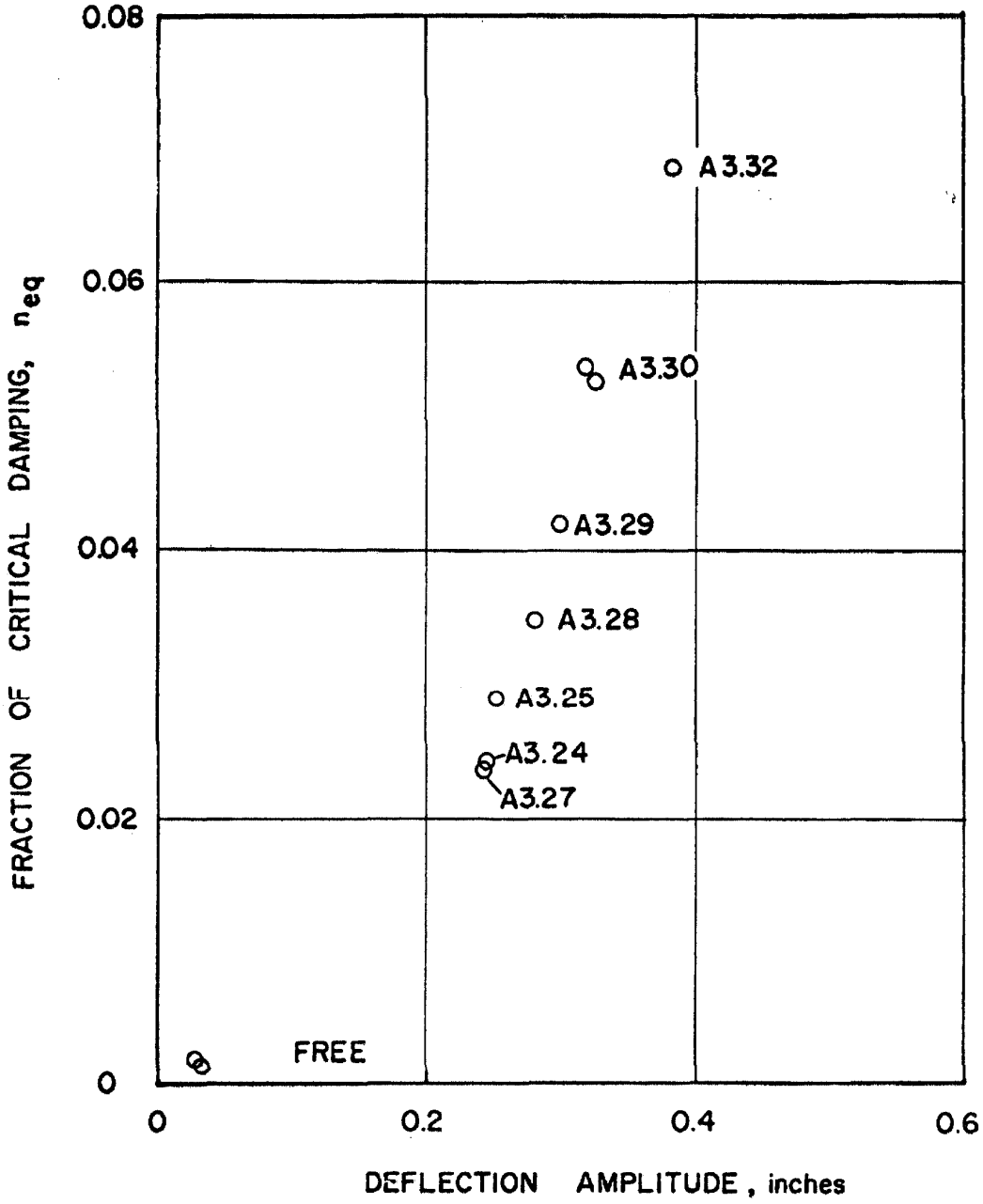

FIG. 4.15 EQUIVALENT VISCOUS DAMPING OF LI (N-S)

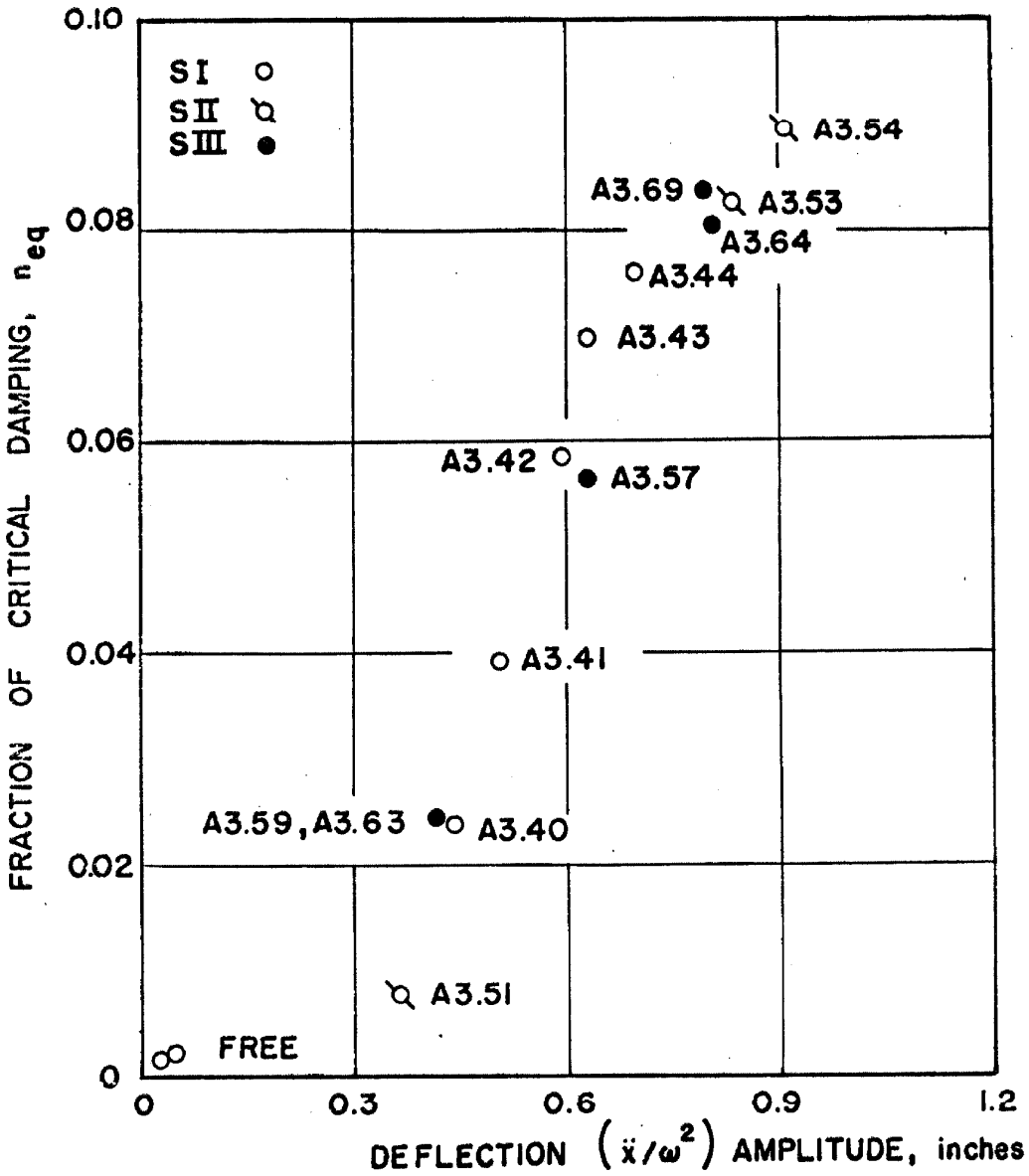

FIG. 4.16 EQUIVALENT VISCOUS DAMPING OF SI, SII AND SIII

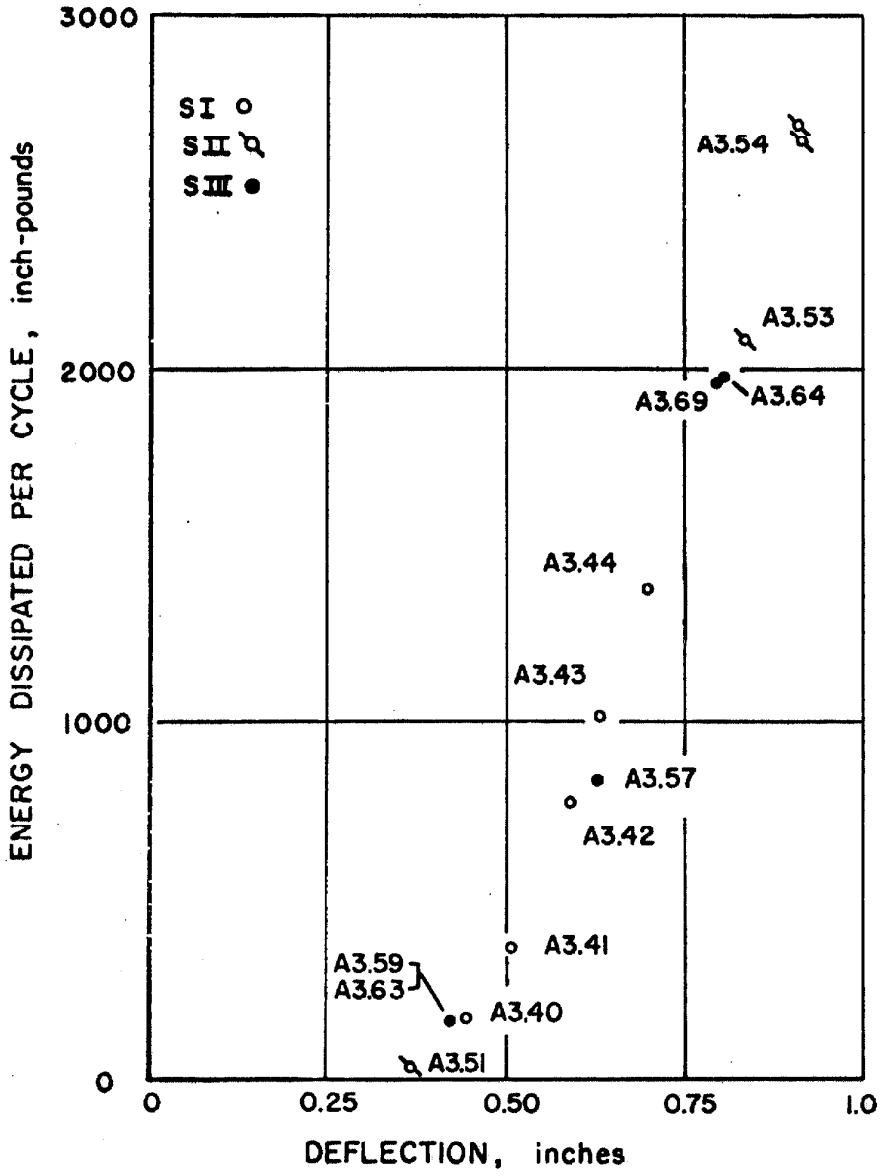

FIG. 4.17 ENERGY DISSIPATED PER CYCLE FOR SI, SII AND SIII

1h. Ultraharmonic response of the experimental structure. The existence of ultraharmonic response of this nonlinear system was not unexpected. The existence of higher frequency components superimposed upon the basic response at the excitation frequency was occasionally encountered, and such test runs called for special interpretation. The experiments in which this action was most noticeable were with columns SII and SIII. The reason for this was that the two force generators were arranged so the force from each was almost three feet on each side of the center of the column stiffness. Thus, any mismatch of forces from the two generators would produce a large torque on the structure. The ultraharmonics of the torsional natural frequency are in the range of the translational testing frequencies.

Figure 4.18 shows the ultraharmonic torsional response superimposed upon the translational response at the excitation frequency of 2.867 cps for test A3.51. The data recorded in figure 4.18 for motion in the east-west direction are: (channels from left to right), (a) the floor acceleration at the mid-span east edge of the floor, (b) floor acceleration at the northwest column, (c) floor acceleration at the southwest column, (d) strain in the northwest column top, (see Table III-1 for column SII) and (e) the force pulse from force generator No. 1. The acceleration traces are all recorded at approximately the same calibration condition so that they may be compared directly.

The single amplitude translational acceleration is about

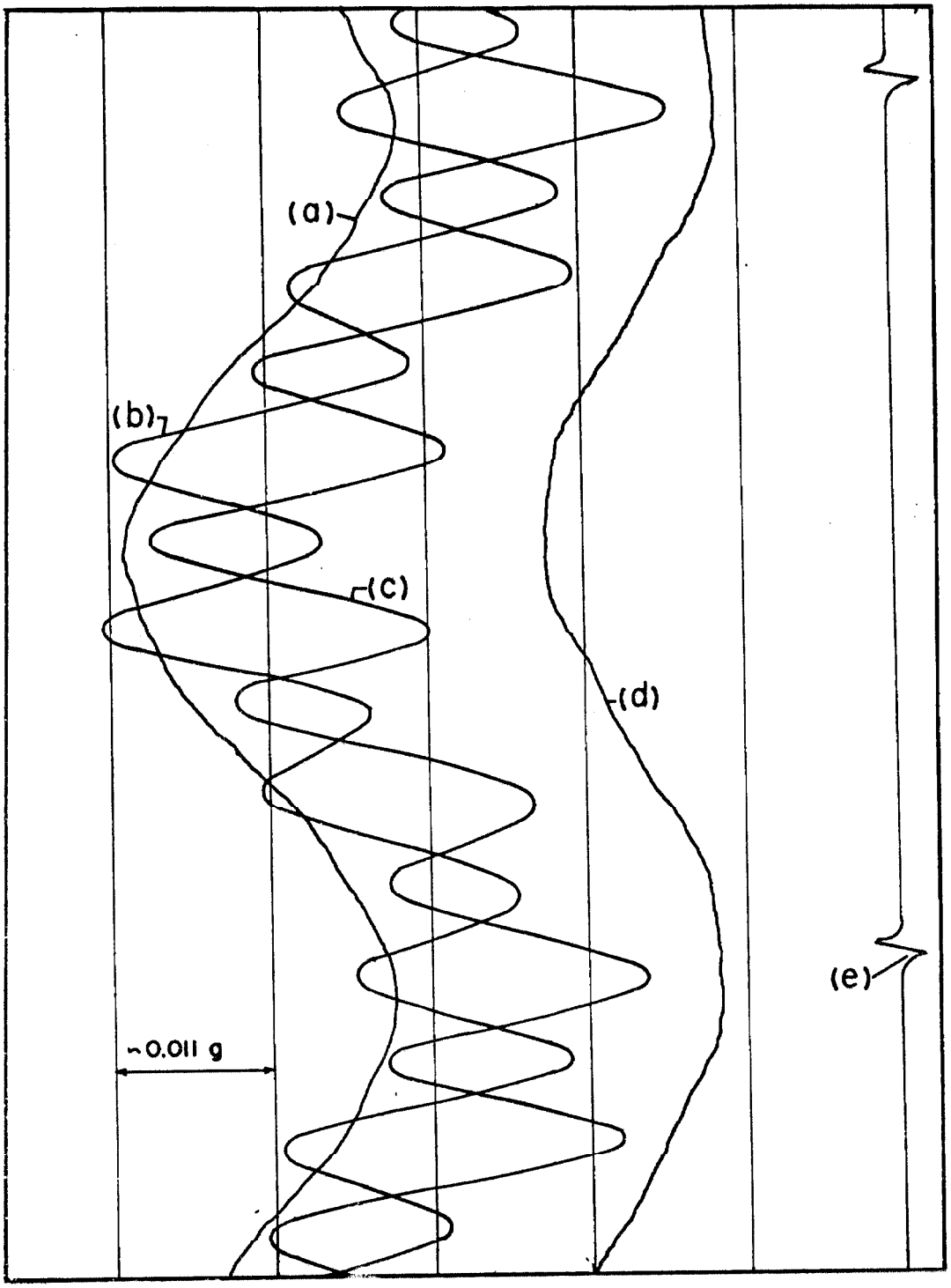

FIG. 4.18 TRACING OF ORIGINAL RECORD

3. 72 inches/second^2 calculated from the mid-east accelerometer and the average single amplitude torsional acceleration superimposed on the translational acceleration is about 0. 11 radians/second^2 calculated from the southwest and northwest column accelerometers.

The important thing to note in figure 4. 18 is that the torsional motion has exactly five cycles for every one cycle of translational motion or force generation. It was expected that the ultraharmonics would occur at 1/3, 1/5, 1/7, ... of the torsional natural frequency.

li. Structural "demagnetization". It was noted that the residual deflection after a static test was substantially reduced by the following dynamic test. The two cases for which data were taken are static test A3. 58 which gave a residual deflection of 0. 052 inch east and dynamic test A3. 59 resulted in a change in equilibrium position of about 0. 050 inch west. Also, static test A3. 60 had a residual deflection of 0. 078 inch west while dynamic tests A3. 63 and A3. 64 resulted in an equilibrium position change of 0. 063 inch west. The greater portion of the remaining 0. 015 inch of the second example was probably recovered in dynamic test A3. 62 in which the shift in equilibrium position was not measured.

2. Static Results

The static experiments are reported in chronological sequence without mentioning the occurrence of any intervening dynamic or free vibration studies. After all of the static tests are reported, various significant cycles will be replotted in a single figure to facilitate

comparison. The basic static data was obtained by a strain gage type load cell.

2a. Column LI. The static force data in the east-west direction of column set LI were taken with a low capacity laboratory developed force gage and a SR_4 strain indicator. The characteristics of this gage can be judged by the hysteresis curve for a tension calibration given in Appendix I. For test A3. 1 all the data points lie within the estimated error of a straight line whose slope gives a stiffness of 795 pounds per inch. The result of test A3. 3 plotted in figure 4. 19 shows the beginning of a definite hysteresis force-deflection relationship for the structure. Figure 4. 20 has tests A3. 4 and A3. 8 plotted where the zero deflection of test A3. 8 was shifted to the east 0. 112 inch to account for the residual deflection of test A3. 4. Test A3. 10 plotted in figure 4. 21 completes the static experiments of column LI (E-W). Because of the hysteresis of the force gage the area of the force-deflection diagrams plotted in figures 4. 19 to 4. 21 is larger than the true area for the structure but the difference is not a very large percentage of the total area for the larger loops. The static tests in the east-west direction were cycled by equal force levels, whereas, all the following static studies were cycled at equal deflection values.

At this stage of the investigation, a more accurate and more convenient load cell was obtained. The first static study of LI (N-S) was A3. 21 and the result is progressively plotted in figures 4. 22, 4. 23 and 4. 24. Figure 4. 22 gives the first one and three quarters

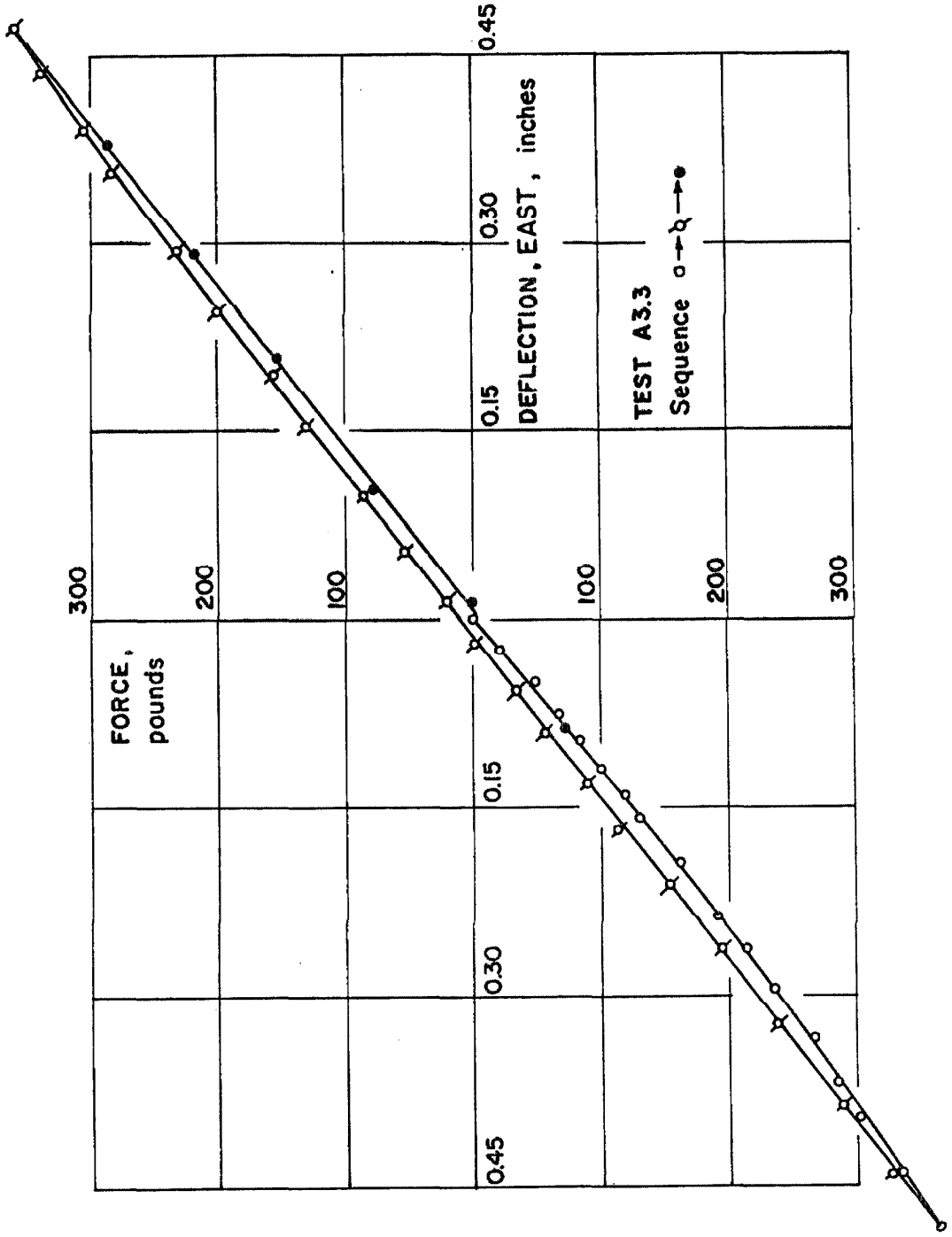

FIG. 4.19 STATIC TEST OF LI (E-W)

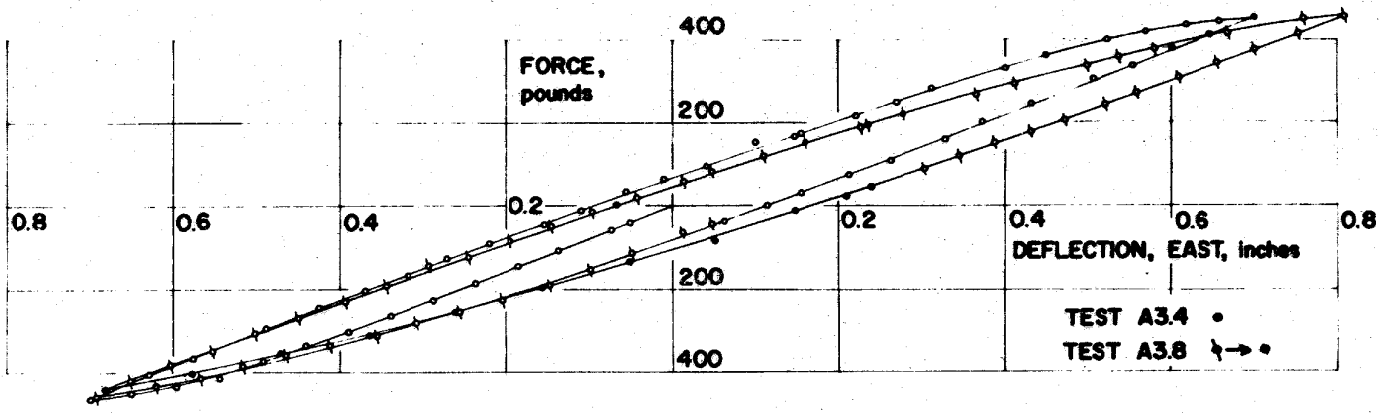

FIG. 4.20 STATIC FORCE-DEFLECTION CURVES, LI (E-W)

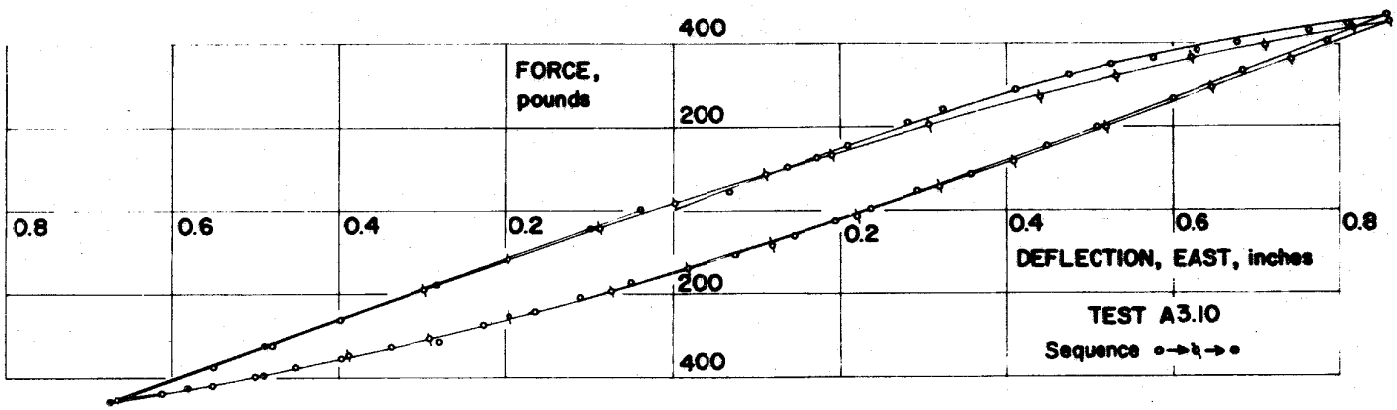

FIG. 4.21 STATIC FORCE-DEFLECTION CURVES, LI (E-W)

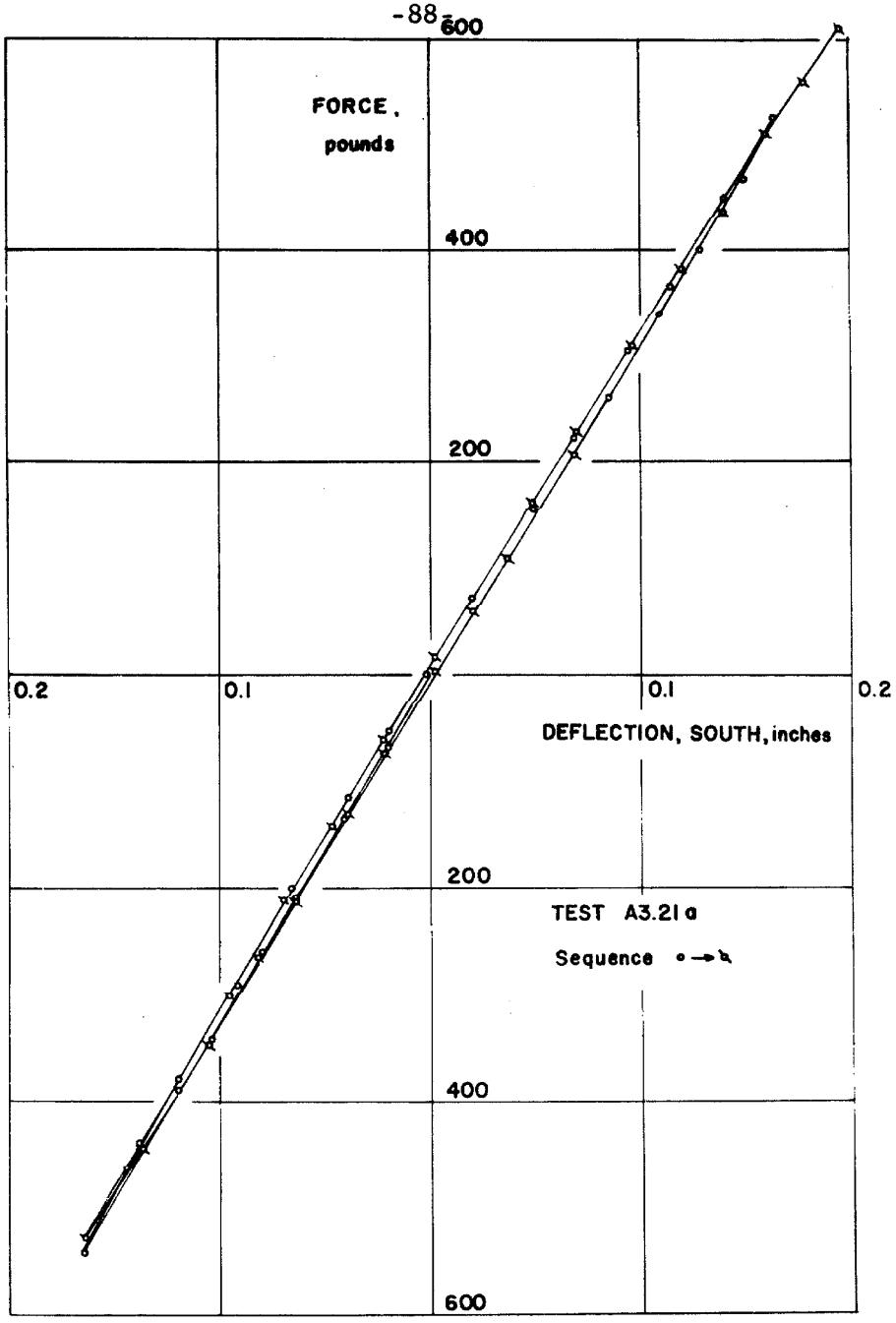

FIG. 4.22 STATIC FORCE-DEFLECTION OF LI (N-S)

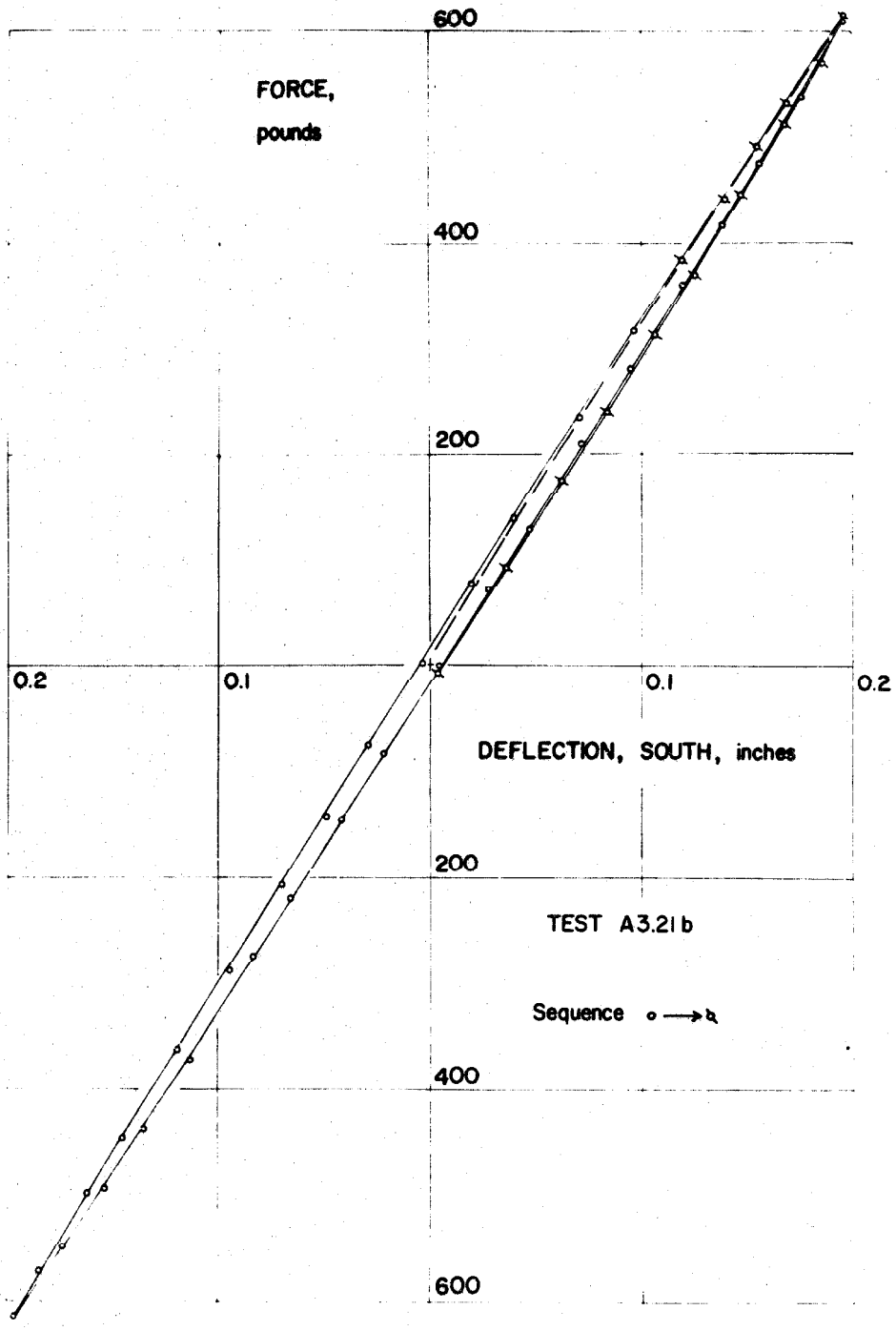

FIG. 4.23 STATIC FORCE-DEFLECTION, LI (N-S)

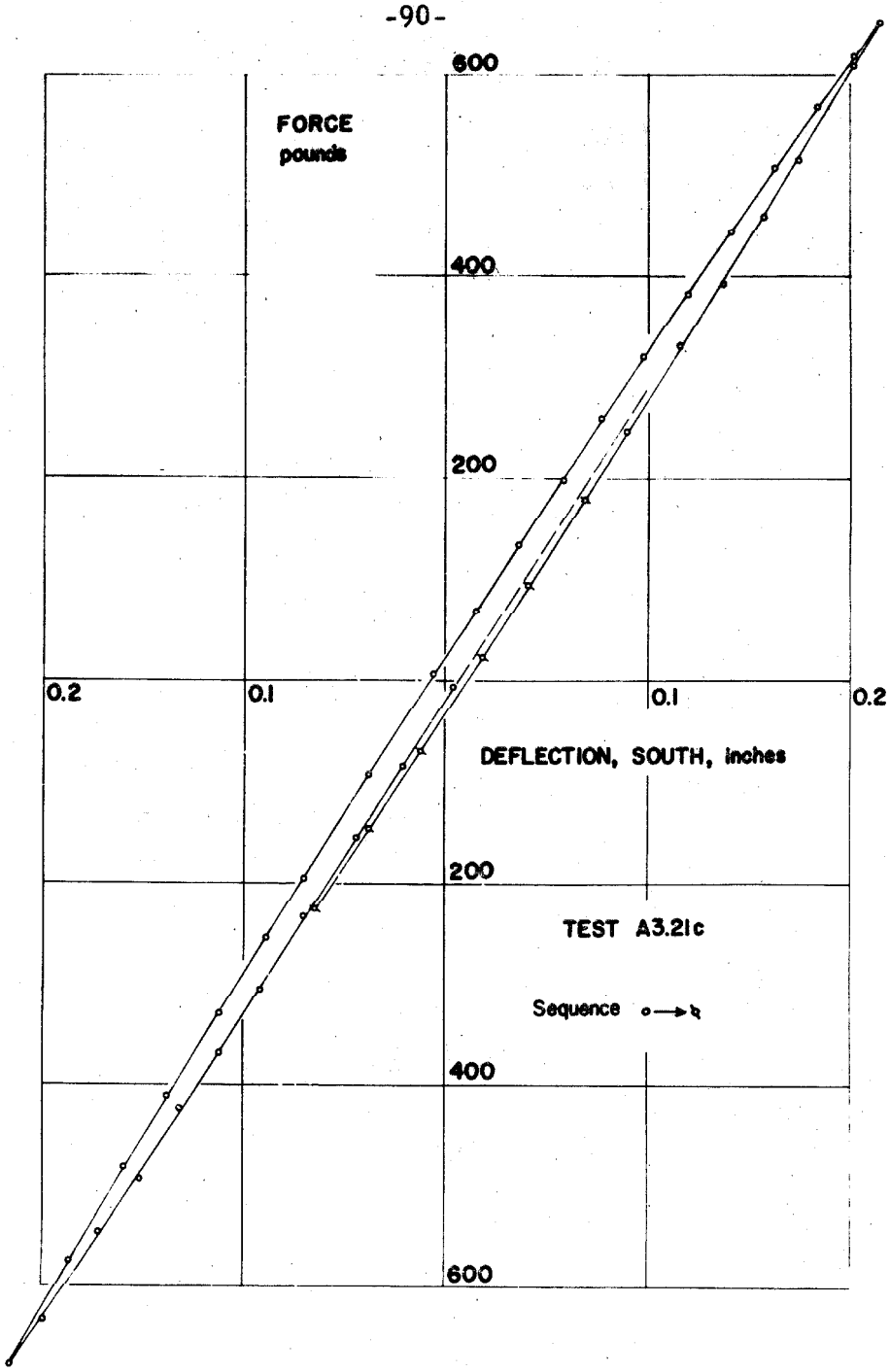

FIG. 4. 24 STATIC FORCE-DEFLECTION, LI (N-S)

cycles and figure 4. 23 continues where figure 4. 22 ends for an additional one and one quarter cycle. Figure 4. 24 repeats about one half of the last quarter cycle given in figure 4. 23 and then continues for slightly more than one cycle. The dashed line indicates the repeated section of data. The structure was deflected to the next data point beyond the last plotted point when a fuse in the recorder blew out. At this point the experiment was discontinued until two days later when test A3. 22 data were taken. Again the data from one test, A3. 22, are plotted progressively in two figures, figures 4. 25 and 4. 26. The final static experiment of column LI, A3. 31, was preceded by two cycles of 0. 320 inch static deflections and one cycle of 0. 400 inch static deflection before beginning to take data at 0. 320 inch. The data taken for this test are plotted in figure 4. 27. The column set LI failed during the dynamic response test A3. 32, reaching a maximum dynamic deflection amplitude of about 0. 383 inch.

2b. Column SI. The first static experiment on column set SI, A3. 35, was an attempt to obtain the virgin force-deflection curve for the structure. Difficulties developed during the testing primarily because the required forces were substantially in excess of the forces previously used. The larger forces caused a failure of the existing three inch concrete floor slab-on-grade near the slab to foundation isolation joint. Temporary repair of the static loading frame permitted taking data in two subsequent tests but not at full load. The three static experiments of SI are plotted in figure 4. 28.

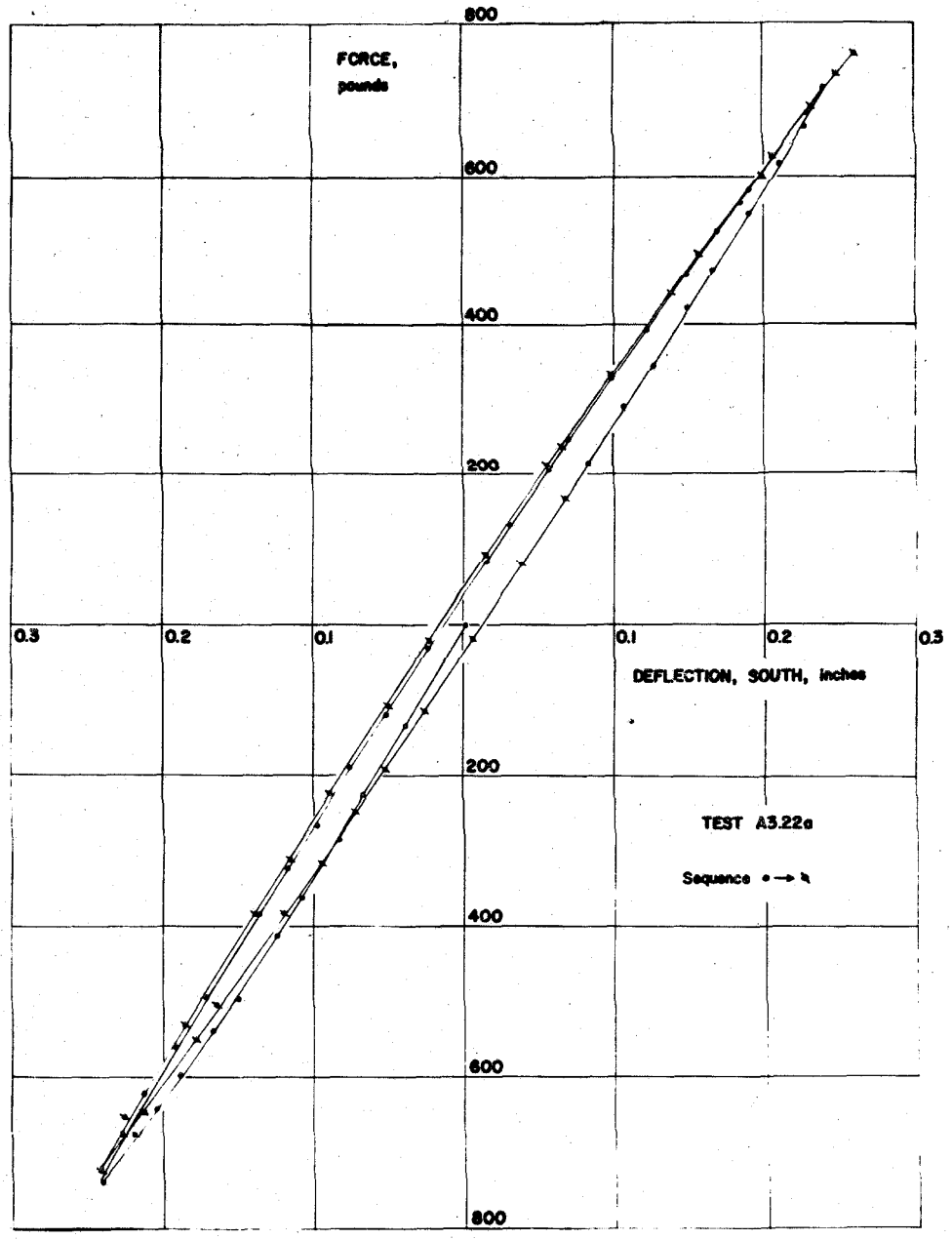

FIG. 4.25 STATIC FORCE-DEFLECTION, LI (N-S)

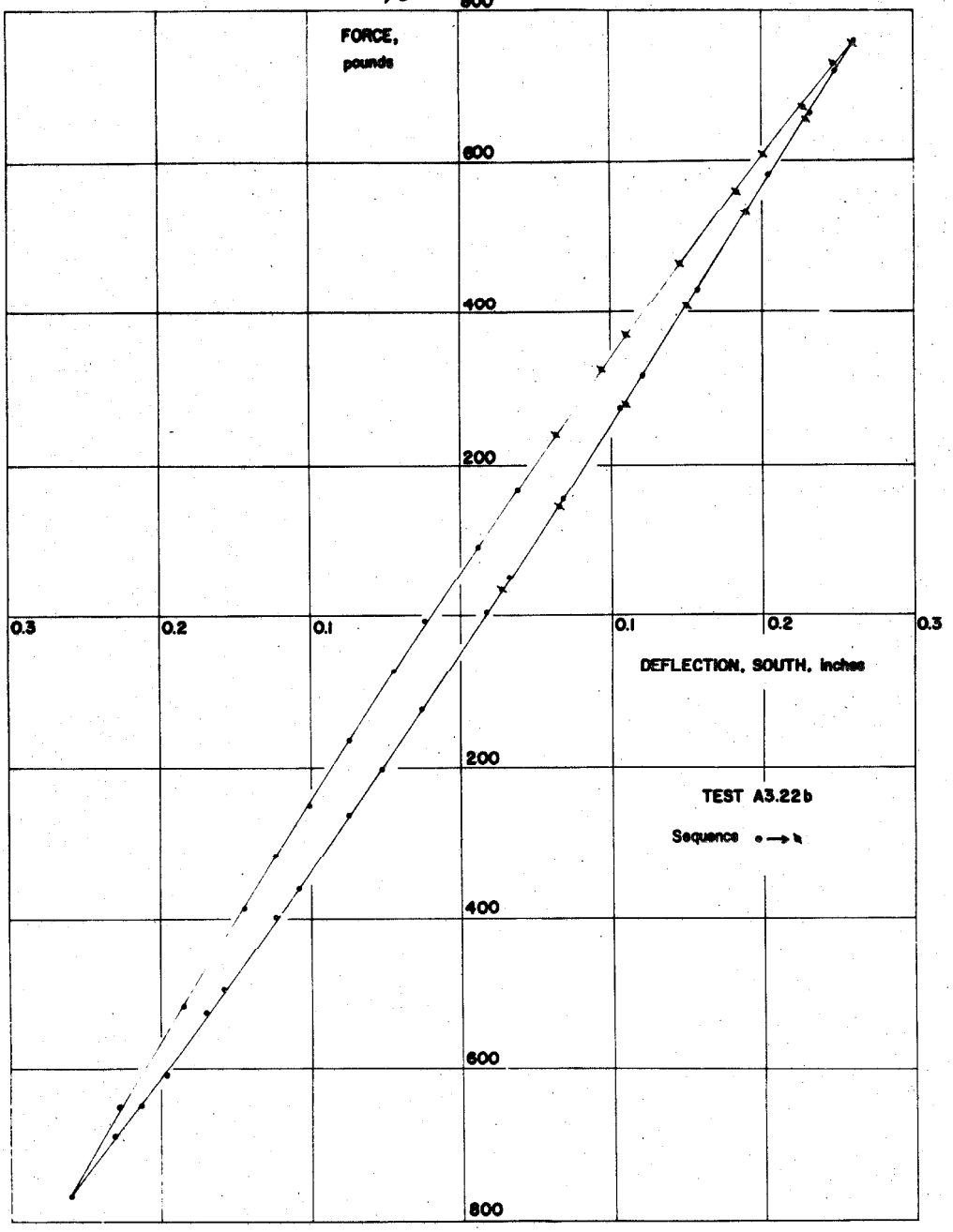

FIG. 4.26 STATIC FORCE-DEFLECTION, LI (N-S)

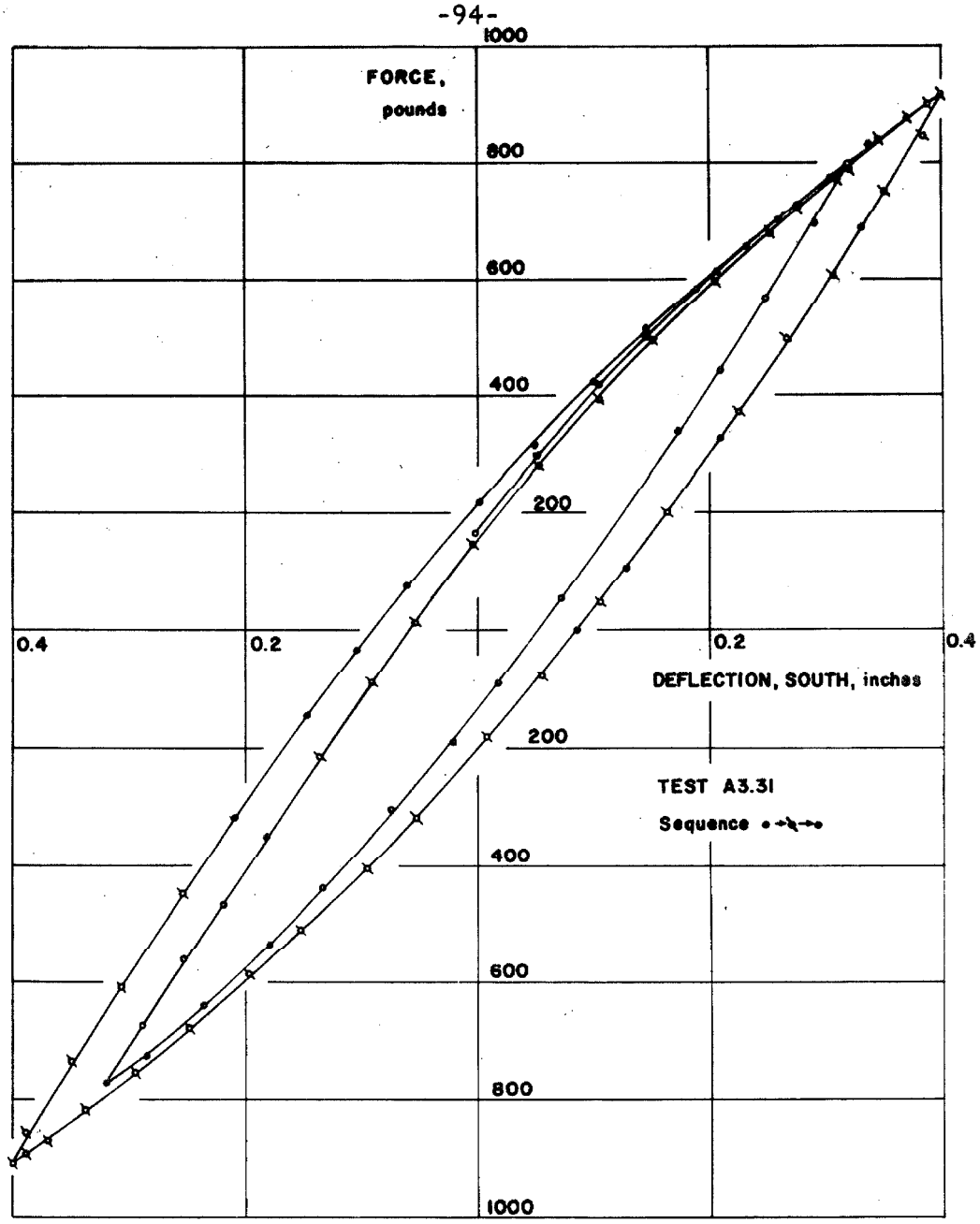

FIG. 4.27 STATIC FORCE-DEFLECTION OF LI (N-S)

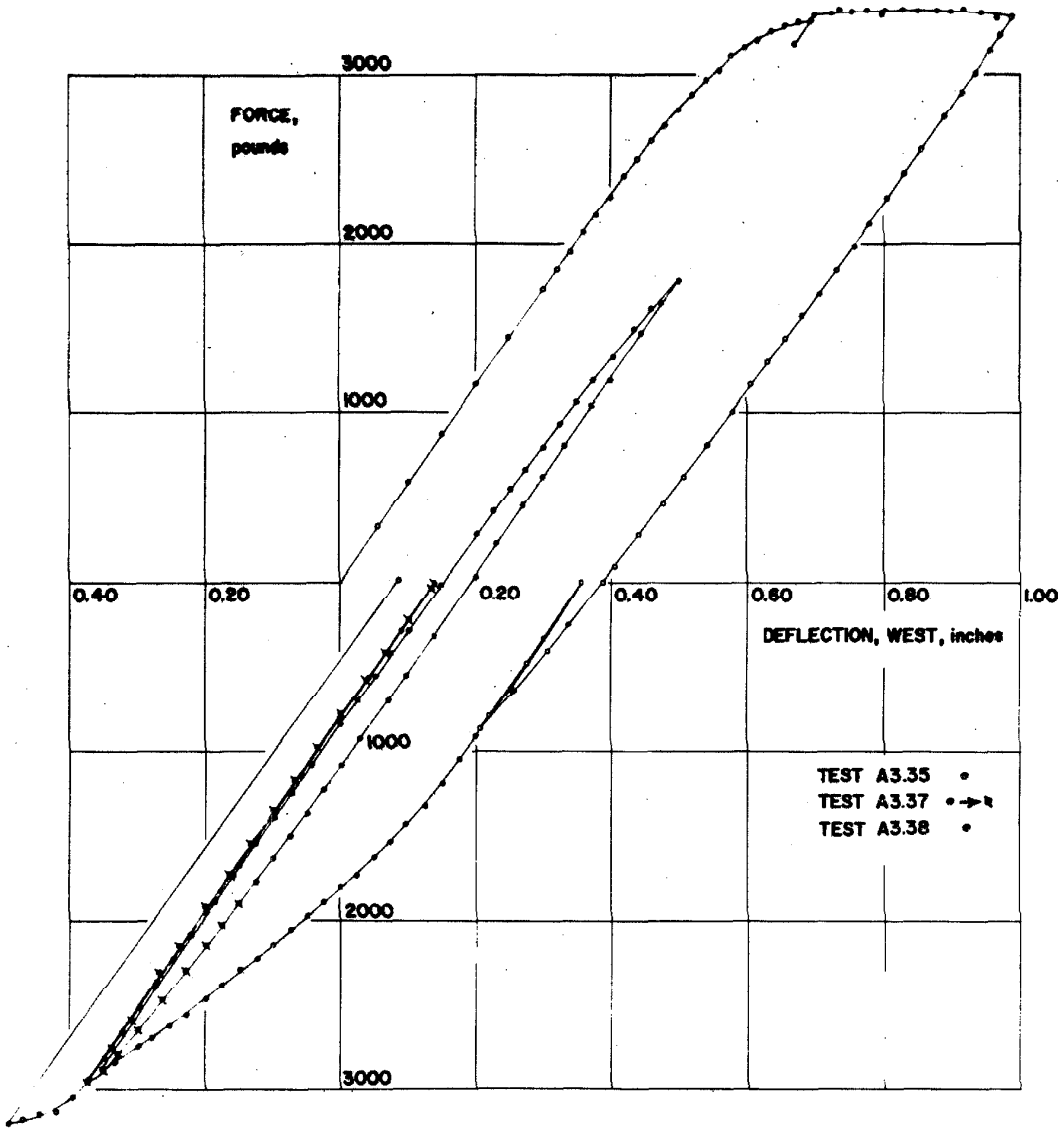

FIG. 4.28 STATIC FORCE-DEFLECTION, SI (E-W)
(VIRGIN STRUCTURE)

2c. Column SIII. The static loading system was permanently repaired by bolting the frame to the foundation of the structure rather than to the existing laboratory floor. With this new arrangement all the static experiments of column SIII were run without the difficulty of the moving forcing frame. Test A3. 56 of the virgin SIII columns is given in figure 4. 29 and test A3. 58 is plotted progressively in figures 4. 30 and 4. 31. Because the static tests were usually alternated with dynamic tests, it was assumed that each static test of column set SIII began with the structure in its original equilibrium position. This was found to be approximately true regardless of the magnitude of the residual static deflection, see section li of this chapter. Test A3. 60 is also separated into two figures, figures 4. 32 and 4. 33, for clarity of the results. Test A3. 66 consists of a decreasing size of cyclic deflection, whereas, the previous experiments have all had increasing cyclic deflections. This test is divided into the three figures 4. 34, 4. 35 and 4. 36. The dashed lines in figure 4. 34 have a meaning opposite to that used in all other figures, i. e., the dashed lines in figure 4. 34 show the results of subsequent data of the same test. Test A3. 68 is plotted in figure 4. 37.

A few general comments will be made before regrouping some of this data. Structural deterioration with successive loading cycles is especially obvious in figure 4. 37. The relationship of this characteristic of deterioration to the characteristic shown in the dynamic frequency-response studies, figures 4. 2 and 4. 3, will be investigated in the next chapter.

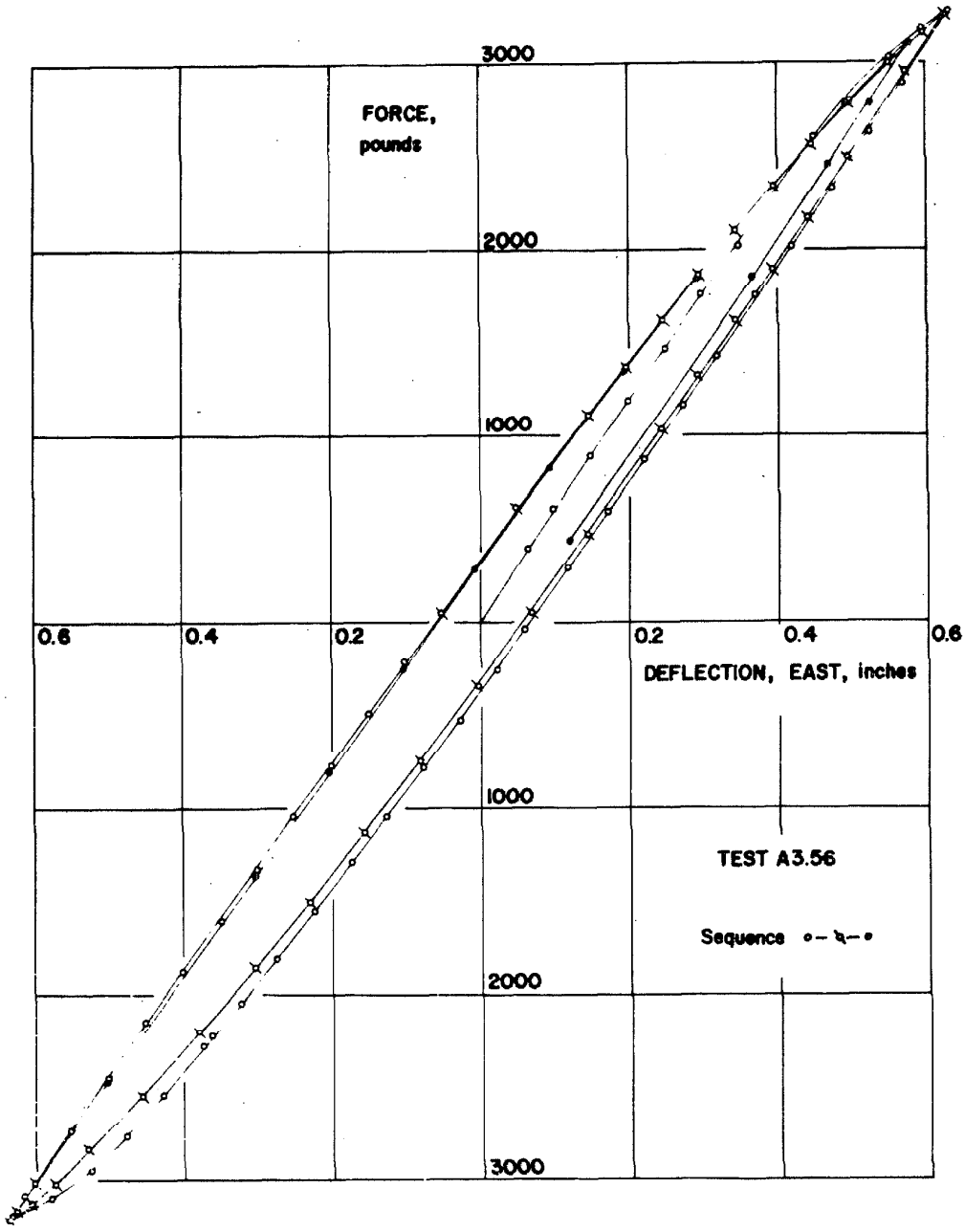

FIG. 4.29 STATIC FORCE-DEFLECTION, SIII (E-W)
(VIRGIN STRUCTURE)

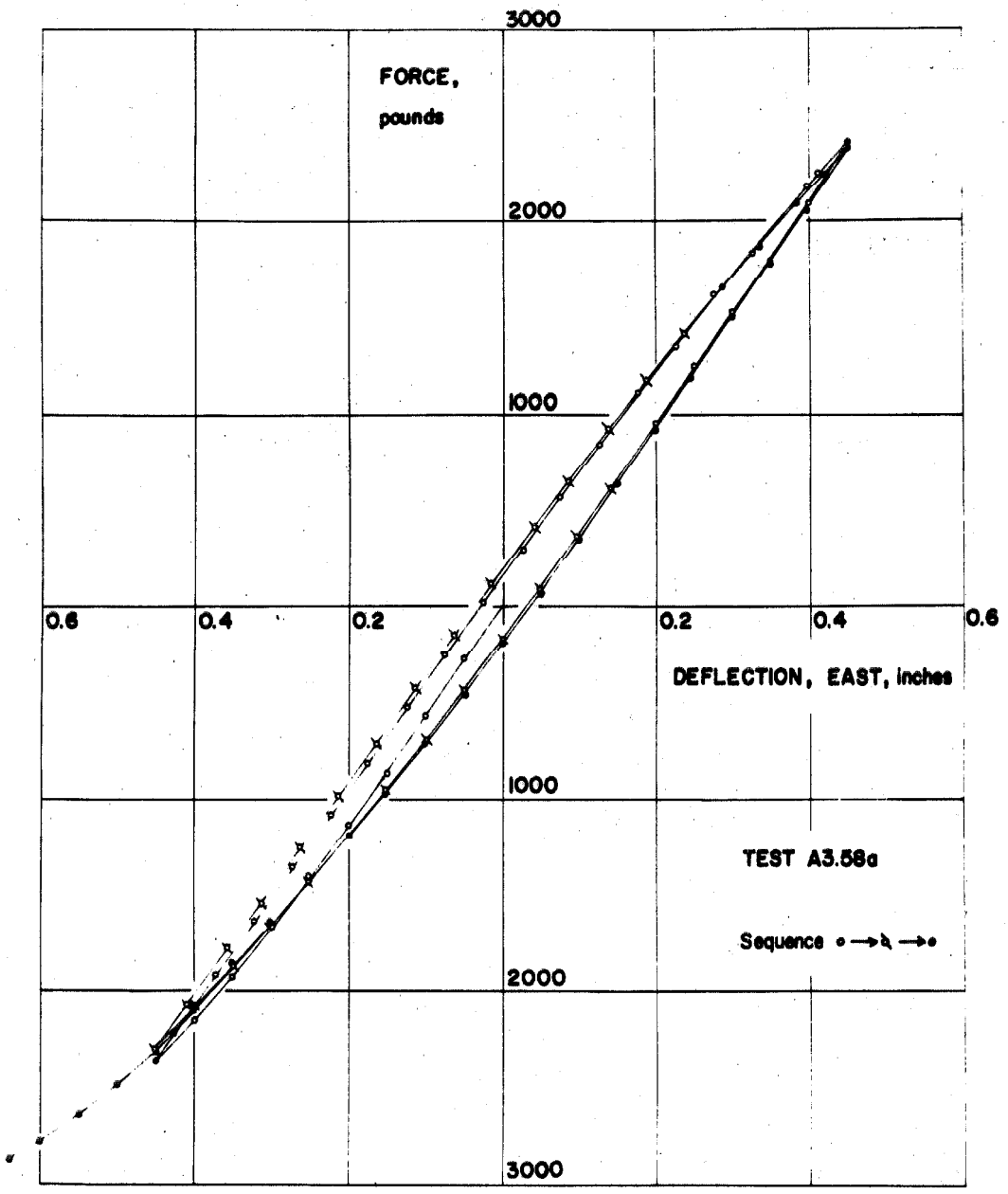

FIG. 4.30 STATIC FORCE-DEFLECTION, SIII (E-W)

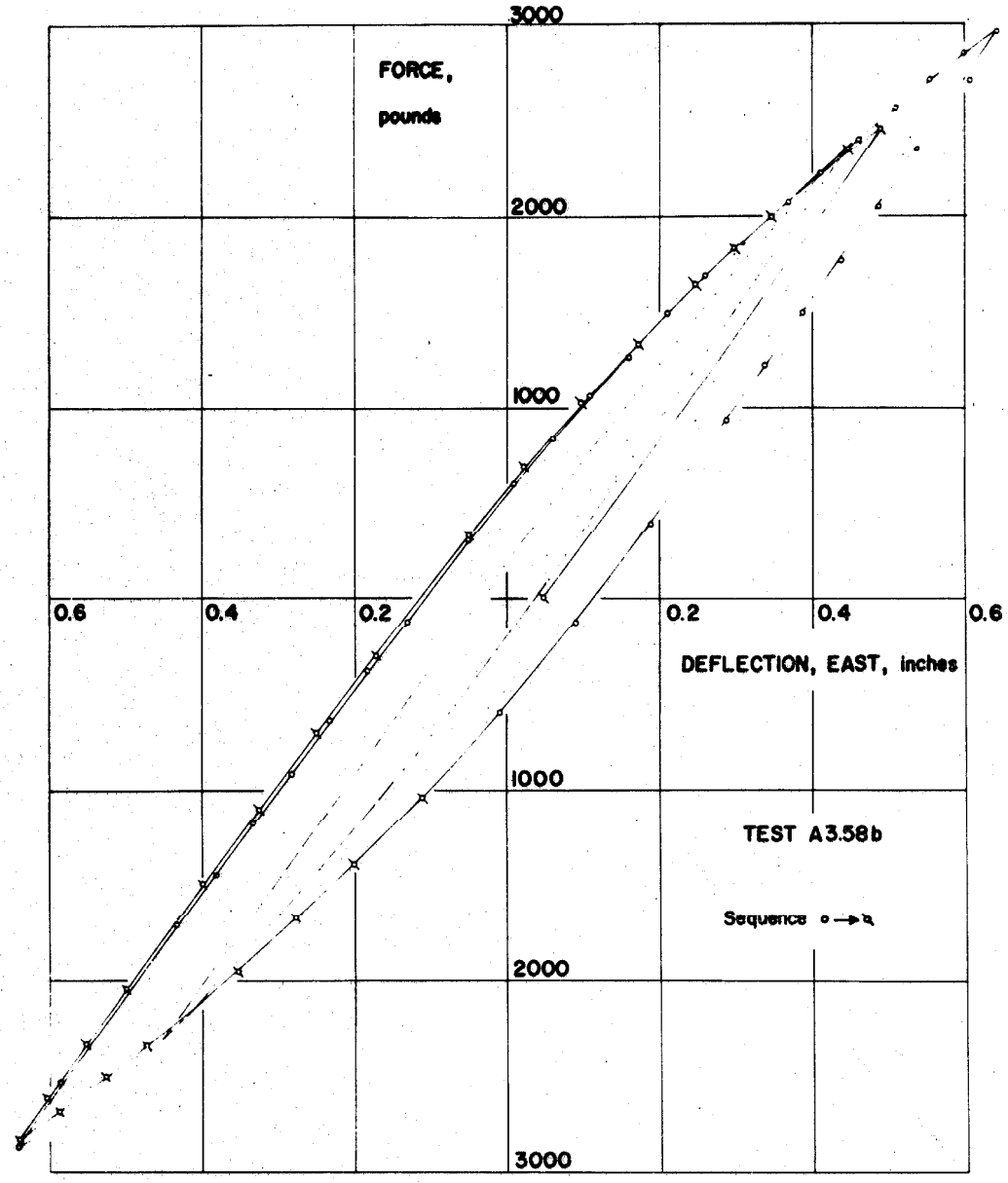

FIG. 4.31 STATIC FORCE-DEFLECTION, SIII (E-W)

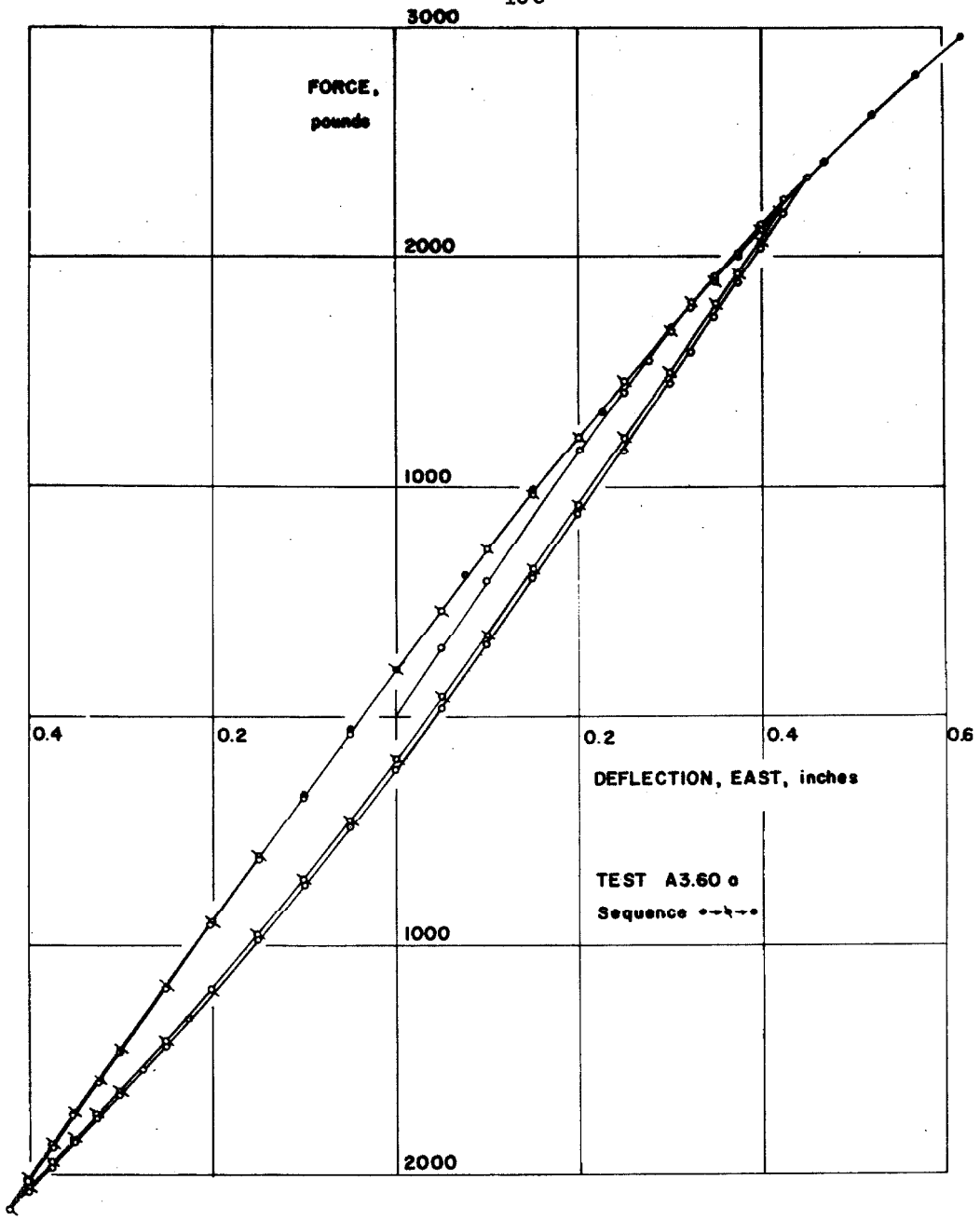

FIG. 4.32 STATIC FORCE-DEFLECTION OF SIII (E-W)

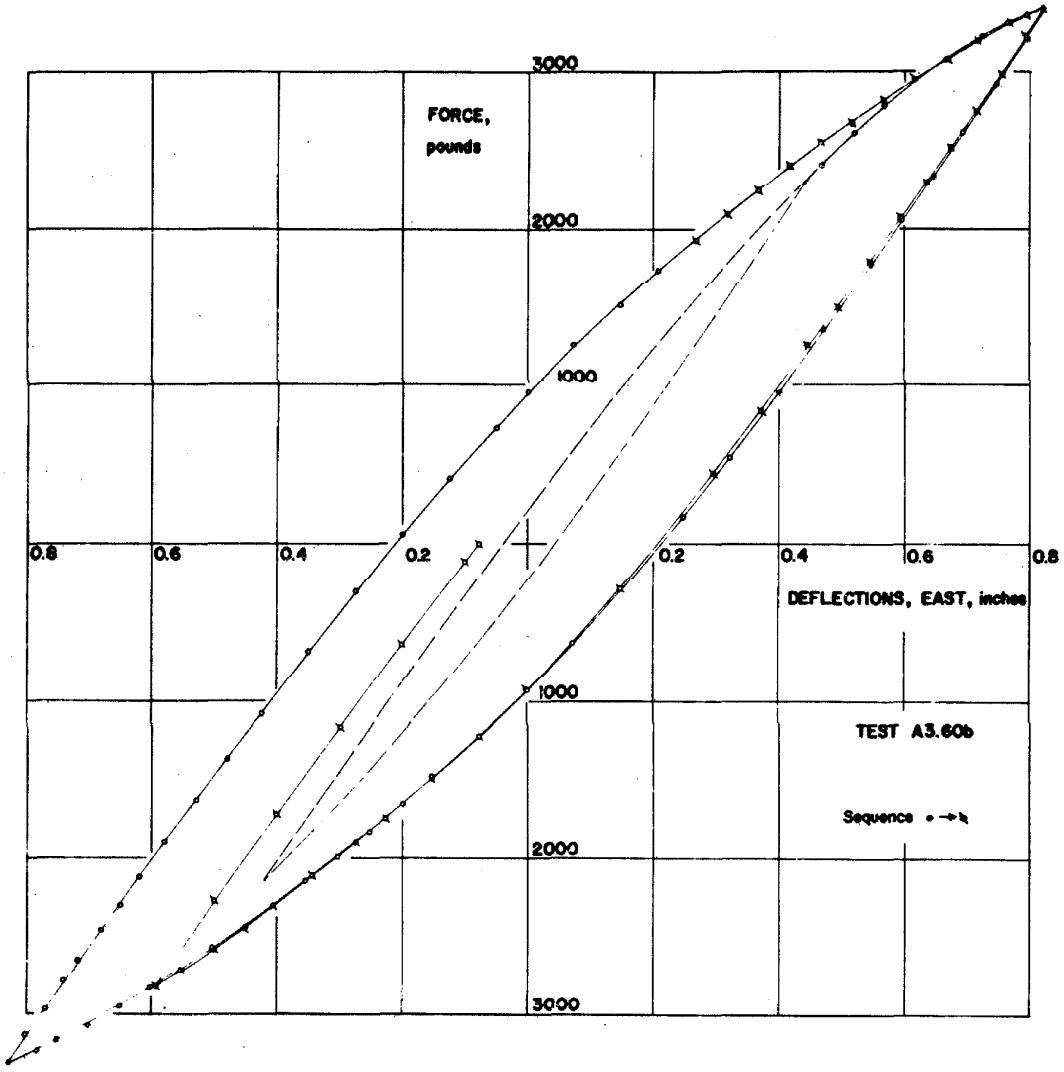

FIG. 4.33 STATIC FORCE-DEFLECTION, SIII (E-W)

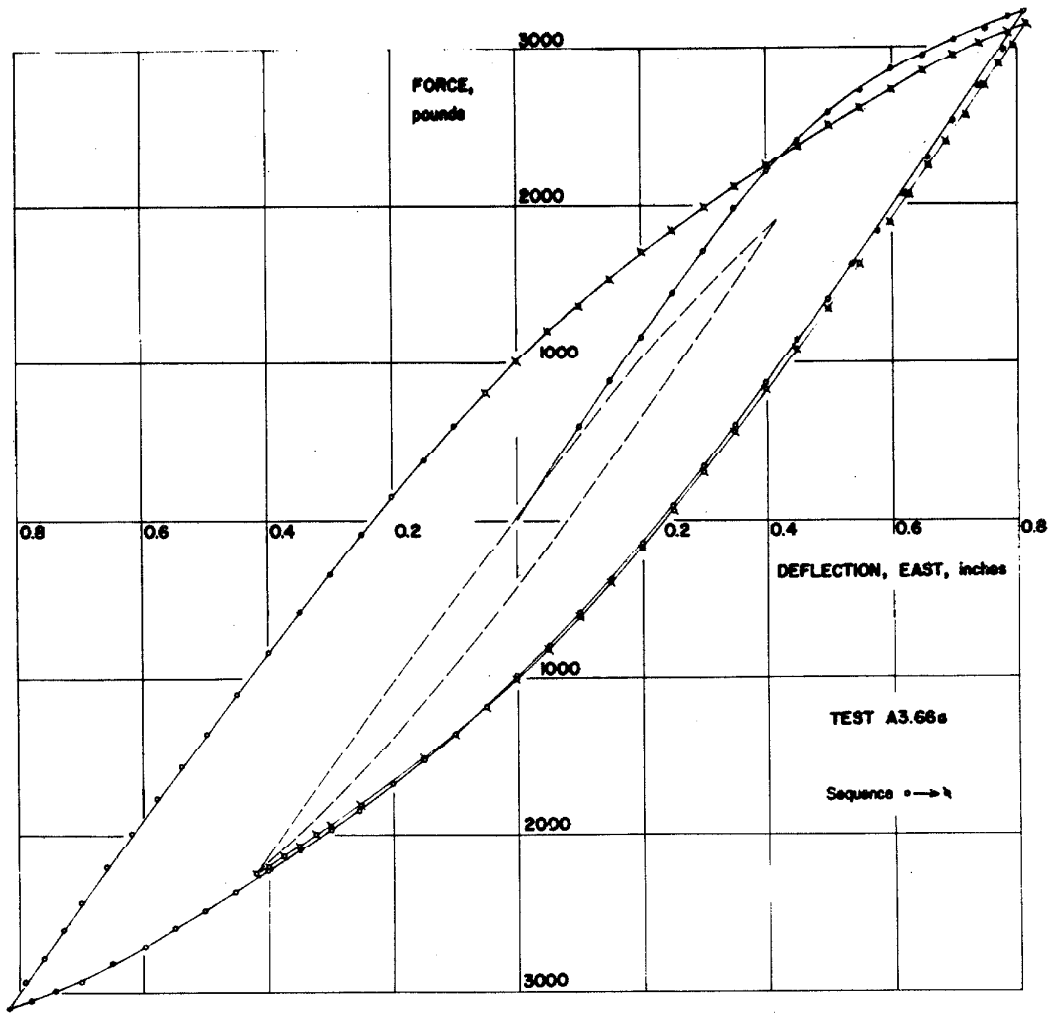

FIG. 4. 34 STATIC FORCE-DEFLECTION, SIII (E-W)

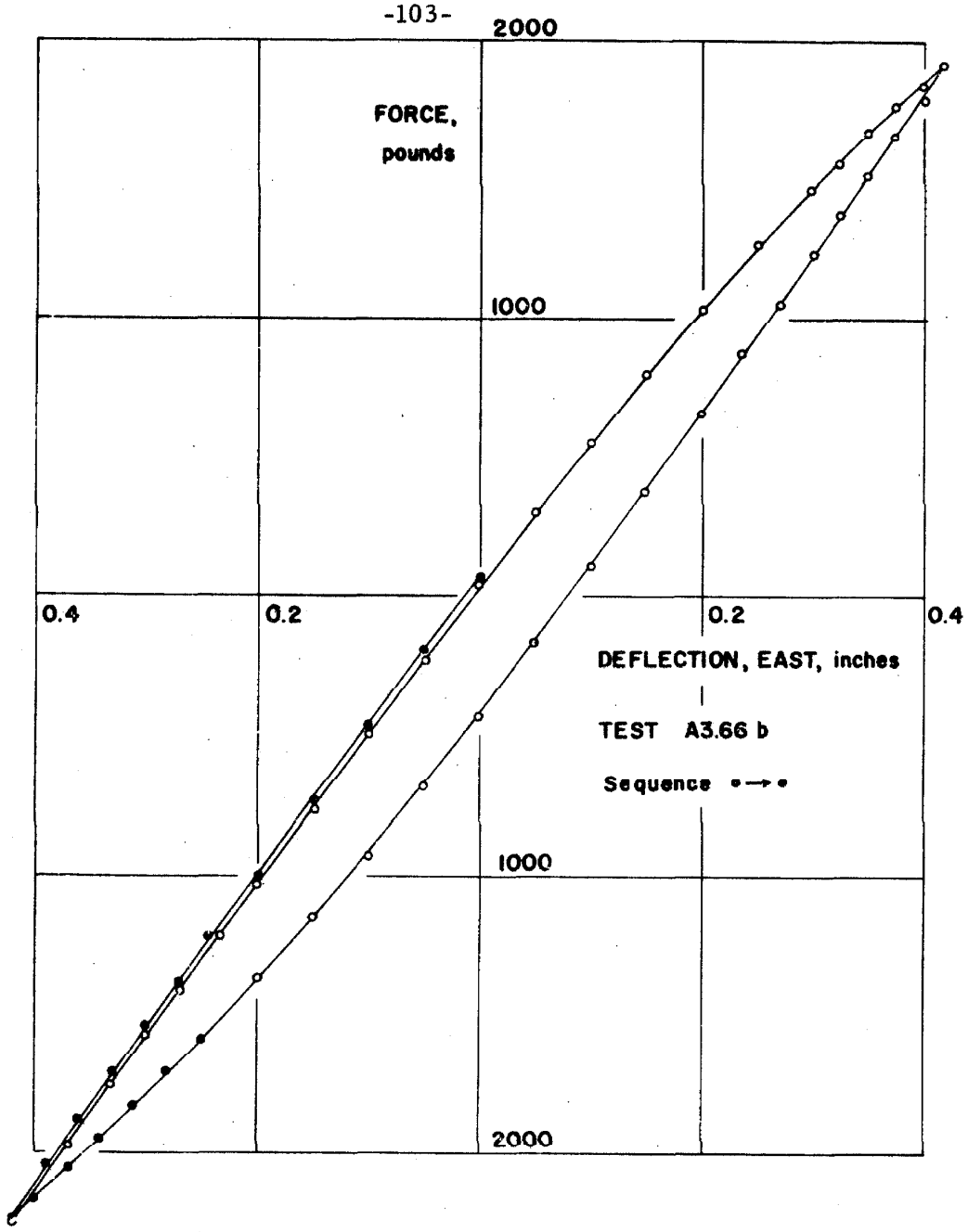

FIG. 4. 35 STATIC FORCE-DEFLECTION OF SIII (E-W)

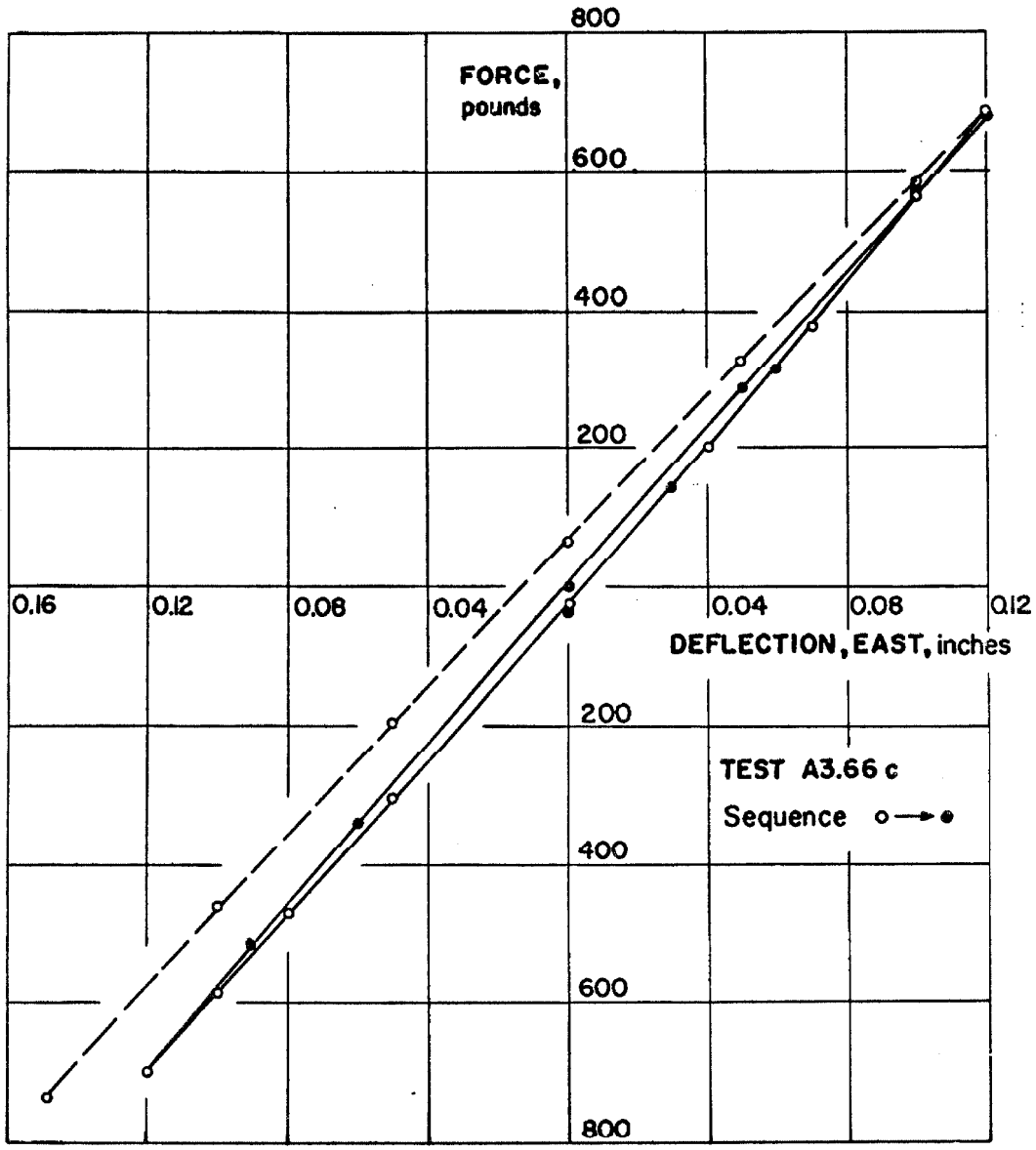

FIG. 4.36 STATIC FORCE-DEFLECTION OF SIII (E-W)

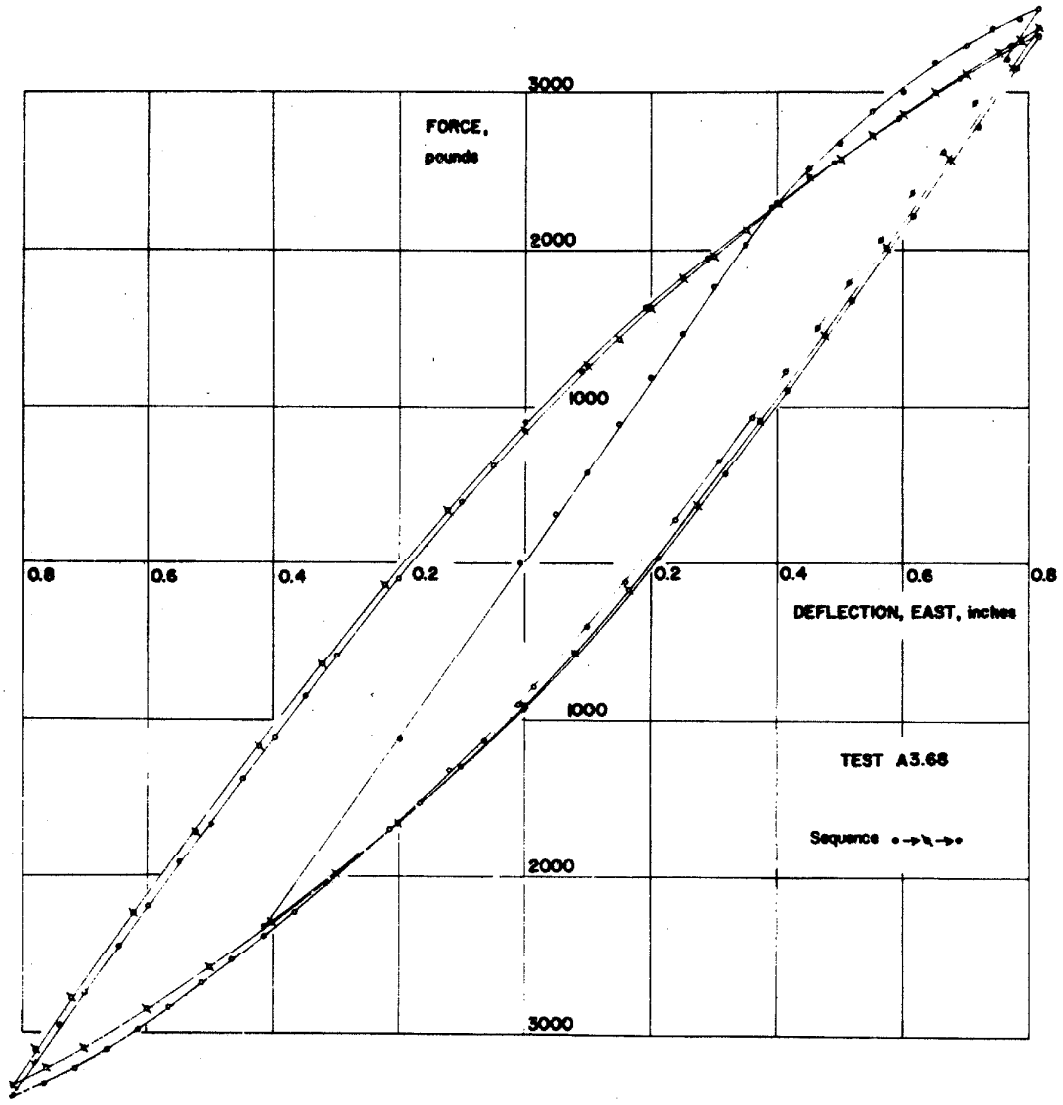

FIG. 4.37 STATIC FORCE-DEFLECTION, SIII (E-W)

Figure 4. 38 shows specific data cycles taken from figures 4. 33, 4. 34 and 4. 37. As can be seen from Appendix III, test A3. 60 curve was obtained on June 30 as the final static loop of that experiment. Neglecting the effect of small free vibration tests, only three vibration tests were made before test A3. 66 curve was obtained. The first two forced vibration tests had a maximum response amplitude of 0. 120 inch and 0. 592 inch respectively. The final forced vibration test was made July 7 and had a maximum response amplitude of 0. 816 inch. On July 8 the test A3. 66 curve was obtained as the first cycles of the test. Thus, the difference between test A3. 60 curve and test A3. 66 curve of figure 4. 38 is attributed to the dynamic tests and the rest periods which occurred between them. The structure was not tested further until August 17 when test A3. 68 curve was obtained. Thus the difference between test A3. 66 curve and test A3. 68 curve must have been caused by the rest period of 42 days between the successive static tests. The only test between these two was the free vibration test preceding the static test on August 17 which should not have altered the structure. In summary, the effect of dynamic tests of an amplitude up to 0. 816 inch was to modify the static structural response from curve A3. 60 to curve A3. 66 and after 42 days of rest the structure recovered to curve A3. 68 as shown in figure 4. 38. This same action is believed to exist in a lesser degree at smaller amplitudes also.

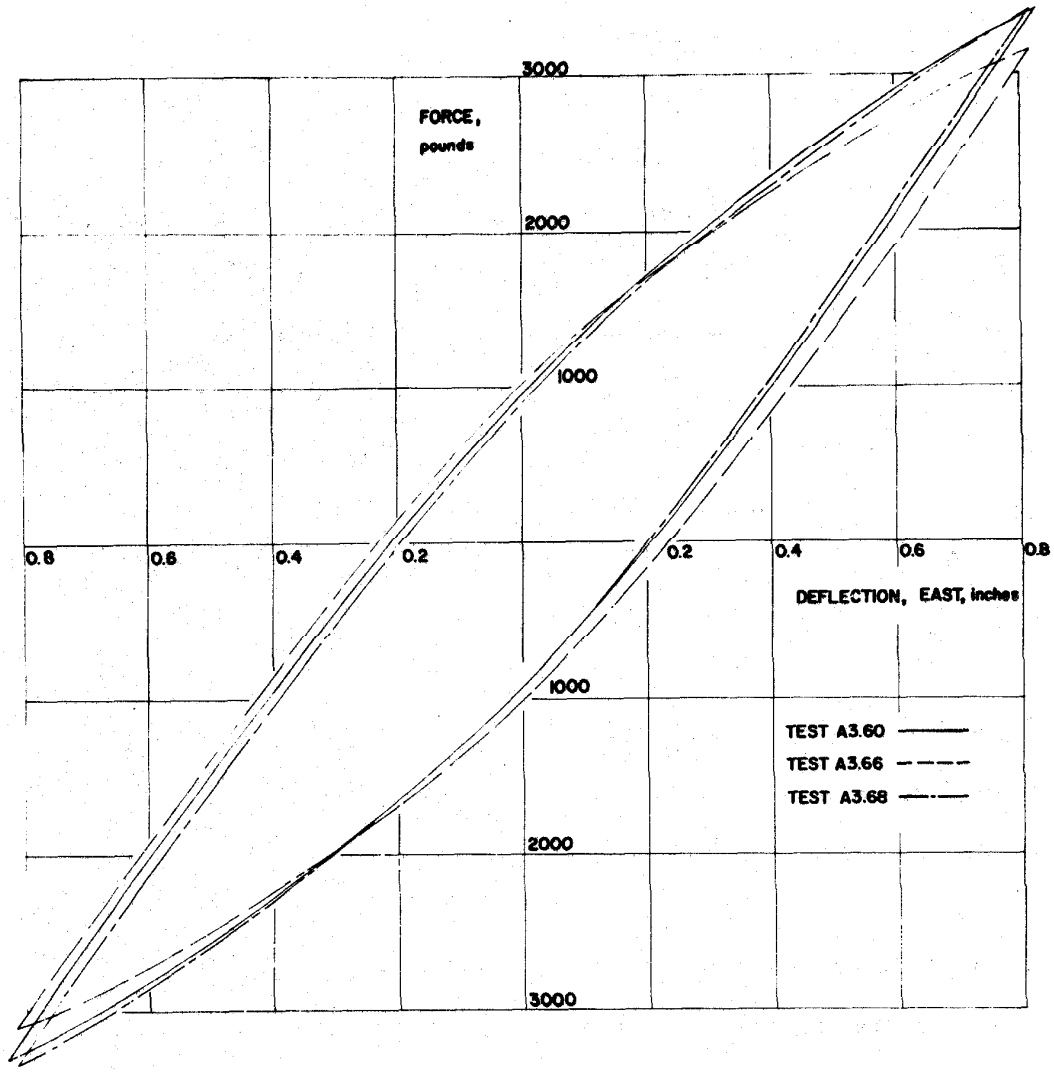

FIG. 4.38 COMPARISON OF STATIC FORCE-DEFLECTION CURVES

3. Dynamic Hysteresis Loops

Since static test results have often been assumed to give conservative results when used to predict dynamic response, an actual comparison of the dynamic and static response of the structure will be made in this section. This comparison will, of course, only be valid for the dynamic strain rates occurring in the experiments. The range of validity of the comparison could possibly be extended by using test results at various strain rates obtained by other investigators, as will be indicated in Chapter V.

3a. Introduction. The differential equation of motion for the structure is

$$m\ddot{x} + R(x) = F \tag{4.15}$$

where R(x) may be a function of the deflection and velocity as illustrated by the linear viscously damped case, e. g. , equation 2. 30. Rearranging equation 4. 15 gives

$$R(x) = F - m\ddot{x} \tag{4.16}$$

and the resulting force-deflection curve was obtained by plotting R(x) and x at corresponding successive instants in time. A linear, viscously damped single-degree-of-freedom system excited by a sinusoidal force produces a restoring force R(x) whose component amplitudes at resonance can be shown to be in the ratio

$$\frac{|F|}{|m\ddot{x}|} = 2n \tag{4.17}$$

where n is the fraction of critical damping. Thus, for a system with 0. 10 fraction of critical damping, the amplitude of the acceleration term will be five times the amplitude of the force term. Since

$|m\ddot{x}|$ is considerably larger than $|F|$, the value of R(x) was expected to be more sensitive to errors in the acceleration than errors in the force. The force was assumed to be sinusoidal. This is a reasonable assumption because any change from the average circular frequency must have had its positive and negative variations during a half cycle of motion. If there was any variation of the excitation frequency from the average, it must have been small and in the following it is neglected.

In order to obtain the data to plot the dynamic force-deflection curves the simplest approach appeared to be to record the acceleration, deflection and force phase simultaneously on one record. Since each amplifier, transducer and recording system has its individual phase lag which can be determined within a certain range of accuracy, say ± 1 degree, the possible phase error between the acceleration and deflection could be two degrees. A linear viscously damped system will be used to estimate the expected error in R(x) that would be introduced by this phase shift error between acceleration and deflection. Let

$$\begin{aligned} F &= F_o \sin(\omega t + \phi) \\ \ddot{x} &= -\omega^2 x_o \sin(\omega t + \psi) \\ x &= x_o \sin \omega t \end{aligned} \tag{4.18}$$

where ϕ is the phase angle by which the force leads the deflection and ψ is the measuring phase error between acceleration and deflection. The energy dissipated per cycle is equal to the area of the hysteresis loop, i.e.,

$$\text{Energy Dissipated} = \oint R(x)\, dx \qquad (4.19)$$

This integral evaluated over one cycle using equations 4.16 and 4.18 yields

$$\text{Energy Dissipated} = \pi x_o F_o \sin\phi + \pi m x_o^2 \omega^2 \sin\psi \qquad (4.20)$$

Using equation 4.17, the ratio of equation 4.20 evaluated at $\psi = 2^o$ to that evaluated at $\psi = 0^o$ is plotted in figure 4.39 for various values of ϕ and n. It can be seen from figure 4.39 that the error in the dynamic force-deflection curve is sensitive to the fraction of critical damping and that the minimum expected error should be about 17 percent. This error was too large to be tolerated so an alternate approach to the determination of the deflection was made by integrating the measured acceleration data. This method eliminated the phase error between deflection and acceleration so that the only available phase error was relative to the exciting force. As was mentioned above, the exciting force term is the least significant term of the restoring force, R(x). The amount of error in R(x) caused by an error in the exciting phase is dependent on sin ϕ .

3b. Integration procedure. The acceleration data were taken at equal time intervals either at every time line on the oscillograph record or at both the time and the mid-time line positions. Figure 4.40 exemplifies the dynamic data record used for the integration and is approximately 0.8 of the original record size. The force pulses, (a) and (f), of force generators No. 1 and No. 4 respectively together with the three accelerations, (b), (c) and (d), and the strain,

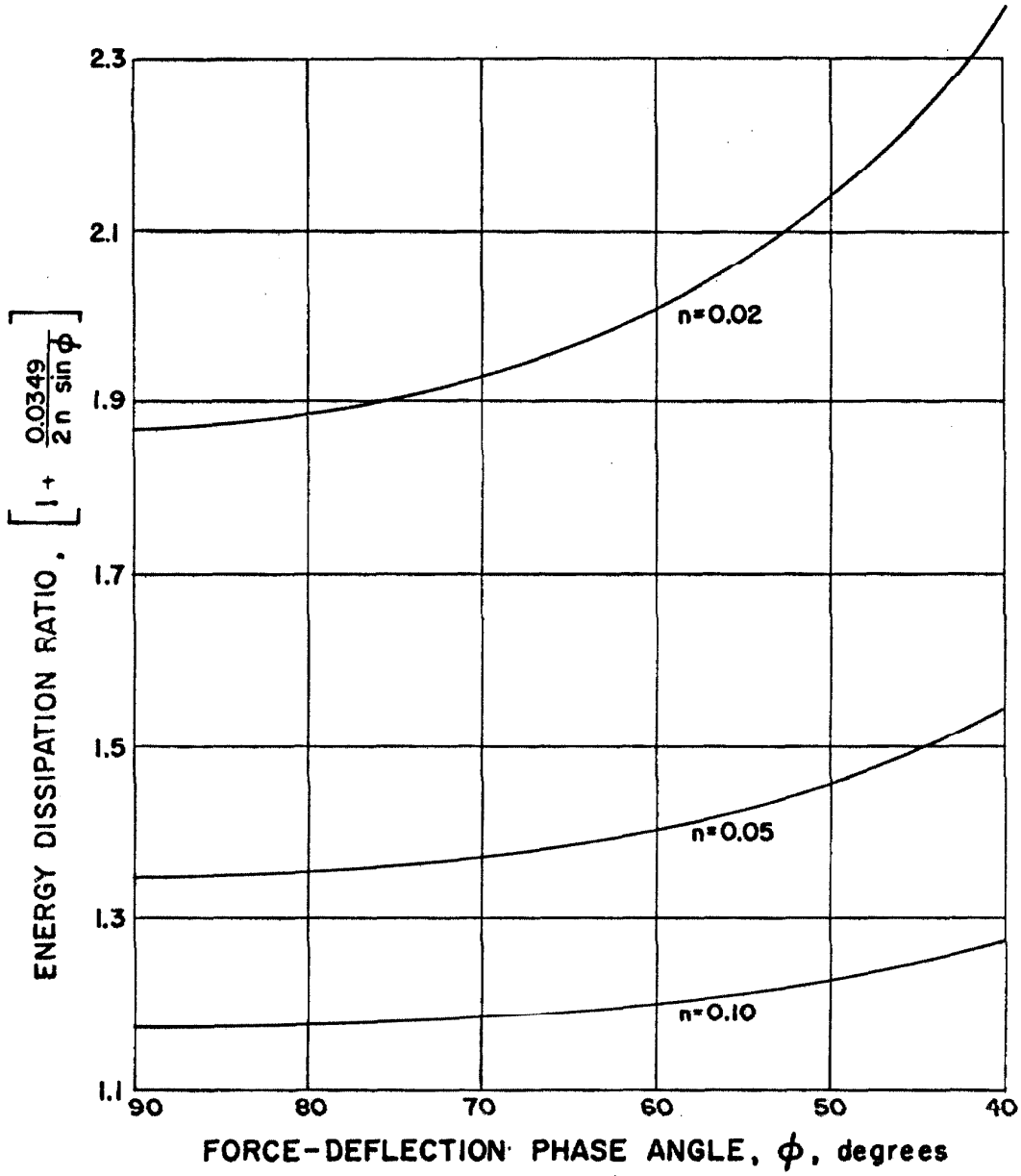

FIG. 4.39 ENERGY DISSIPATION RATIO FOR TWO DEGREE PHASE ERROR BETWEEN x AND $\ddot{x}$

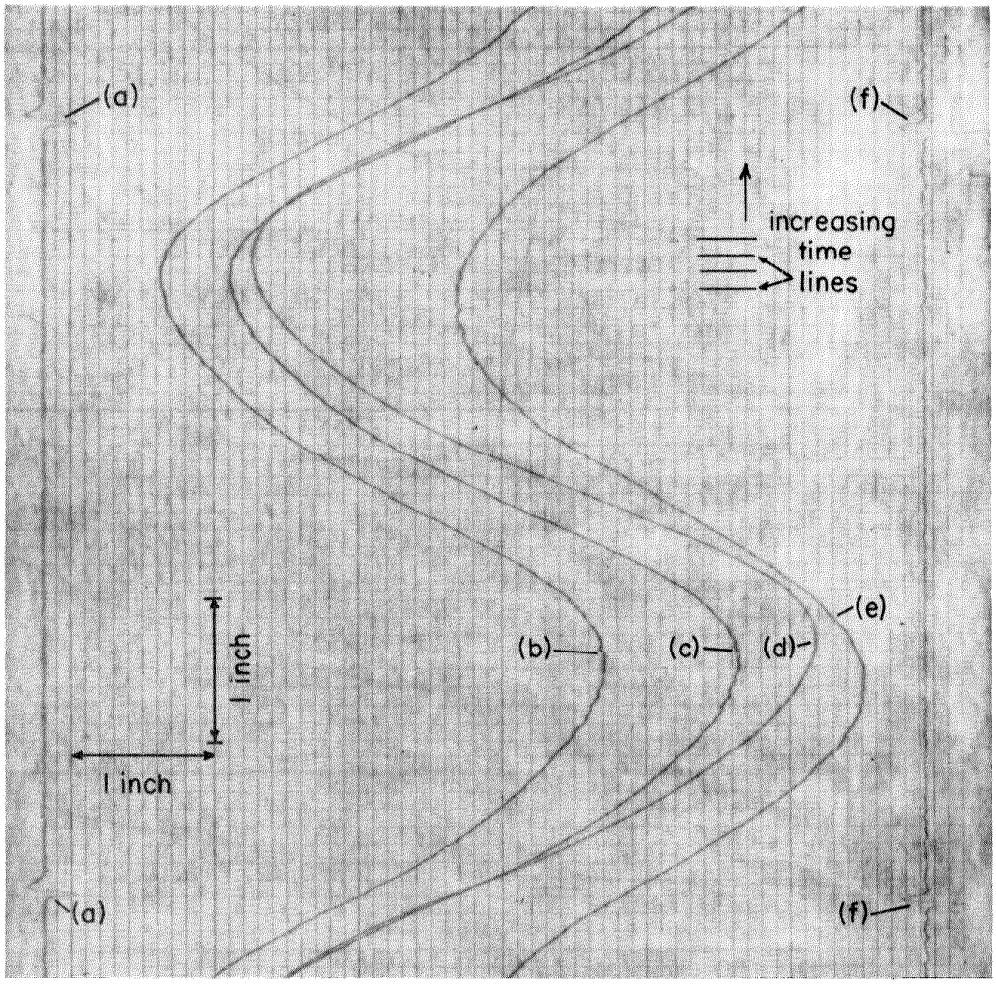

FIG. 4.40 PHOTOGRAPH OF A3.69 DATA RECORD

(e), are marked in figure 4.40. Acceleration records (b) and (c) and the strain (e) were recorded with 100 cps galvanometers and acceleration (d) was recorded with a 20 cps galvanometer. The difference in recording phase shift is obvious in this figure.

Numerical integration of the acceleration data and additional numerical calculations were made on the Burroughs 220 Datatron digital computer owned by the California Institute of Technology. The integration formula

$$\int_{t_1}^{t_1+\Delta t} \ddot{x}(\tau)\,d\tau = \frac{\Delta t}{24}\left[9\,\ddot{x}(t_1) + 19\,\ddot{x}(t_1+\Delta t) - 5\,\ddot{x}(t_1+2\Delta t) + \ddot{x}(t_1+3\Delta t)\right] \tag{4.21}$$

was used successively along the entire length of the record. This is a starting type of numerical integration procedure since it uses future data points to evaluate the integral through the first step. The principal correction term for this formula[38] is -19/720 times the fourth difference of the integrand. Since the fourth differences of a sine are small, the numerical error accumulating from this calculation was expected to be small. The typical record consisted of from 3-1/4 cycles to 6-1/4 cycles of data which contained 80 or 40 data points per cycle depending upon whether data were reduced at the 1/2 time line positions or not.

Since steady-state motion was assumed when the data record was taken, a logical condition on the integration procedure was to require that the initial velocity and final velocity an integral number of cycles later must be the same. A linear correction to the velocity

was made and the corresponding parallel shift of the acceleration axis was also made. This procedure was repeated to determine and correct the deflection. The zero axis of the deflection was obtained by applying the above condition to the integral of the deflection. This integration procedure was tested for accuracy with six cycles of tabulated sine data rounded off to three figures. Forty data points per cycle were used which corresponds to the largest steps taken with actual data. The resulting deflection appeared to be sinusoidal with a positive amplitude of 1.13633 inch and a negative amplitude of 1.13652 inch when the correct amplitude should have been 1.13633 inch. This corresponds to less than 0.02 percent error in the deflection.

The restoring force R(x) was calculated according to equation 4.16 with the initial phase angle of the assumed sinusoidal force determined from the acceleration record. The energy dissipated per cycle was determined by evaluating equation 4.19 assuming the curve linear between points. A check on this integration procedure was made by evaluating the amount of energy input per cycle to the system in linear steps, i.e.,

$$\text{Energy Input} = \oint F\,\dot{x}\,dt \tag{4.22}$$

This can be shown to be only an integration check by considering equation 4.15. Multiplying equation 4.15 by $\dot{x}$ and integrating over one cycle gives

$$\begin{aligned}\oint F\,\dot{x}\,dt &= \oint R(x)\,dx\,dt/dt + \oint m\ddot{x}\,\dot{x}\,dt \\ &= \oint R(x)\,dx + m\,\dot{x}^2/2\,\Big|_0^T\end{aligned} \tag{4.23}$$

Since the velocity should be equal at points one cycle apart, the second term of equation 4. 23 is zero. For the program check data described above and a force-deflection phase angle of 88. 5 degrees, the program result of equation 4. 19 was 2825. 6 inch-pounds and of equation 4. 22 was 2837. 3 inch-pounds. The correct value was 2829. 7 inch-pounds which results in errors of about -0. 15 and +0. 27 percent respectively.

Since the errors associated with the numerical calculation are sufficiently small, 6-1/4 cycles of dynamic test data with about 41 data points per cycle were calculated by the above program. The resulting deflection when plotted had the general appearance shown in figure 4. 41. By checking back to the strain record taken simultaneously with the acceleration record it was determined that the structure did not shift its center of vibration a measurable amount over the given six cycles. In an attempt to evaluate the effect of a possible data reduction error, the previous program test data ordinates were given a randomly distributed error of ± 2%, ± 1% or 0% of the maximum amplitude. This maximum magnitude of error overestimates peak data errors and underestimates mid-amplitude data errors. The resulting peak deflections for 12 individual integrations are given in Table IV-2 and integration 10 is plotted in figure 4. 41. The similarity between figure 4. 41 and the deflection calculated from data showed that random reading errors could be responsible for the curvature of the deflection envelope.

By imposing the steady-state condition at the end of each cycle

FIG. 4.41 DEFLECTION BY DOUBLE INTEGRATION,
2% RANDOM ERROR
(INTEGRATION 10, TABLE IV-2)

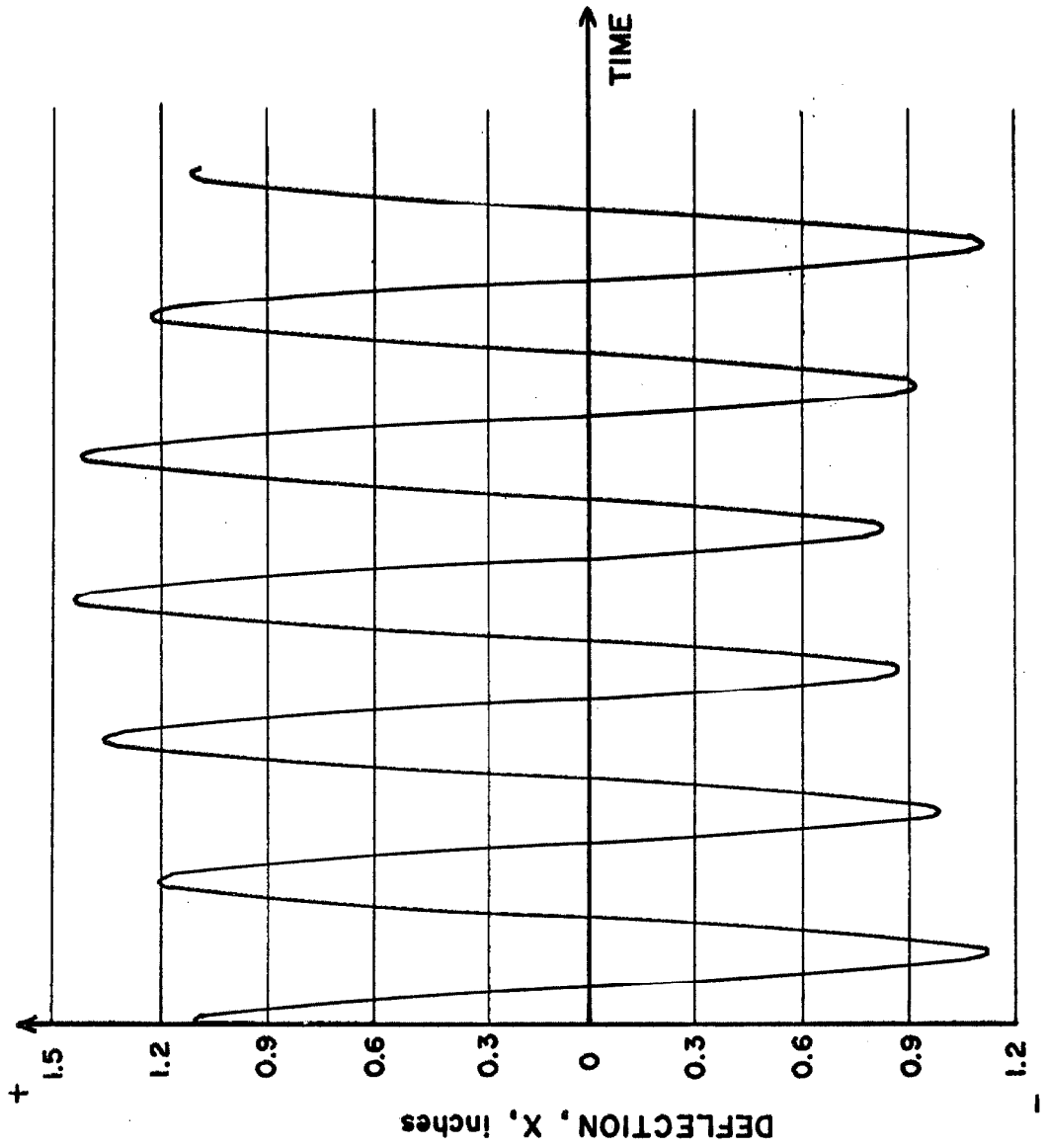

TABLE IV-2

± 2% Random Perturbation of Cosine Test Acceleration

Peak Deflections, inches	Integration 1	2	3	4	5	6	7	8	9	10	11	12
	1.125	1.113	1.137	1.125	1.147	1.114	1.137	1.126	1.148	1.124	1.126	1.148
	-1.152	-1.147	-1.149	-1.146	-1.112	-1.195	-1.138	-1.121	-1.172	-1.122	-1.148	-1.114
	1.116	1.131	1.122	1.104	1.188	1.043	1.097	1.131	1.075	1.215	1.148	1.179
	-1.150	-1.136	-1.128	-1.189	-1.077	-1.305	-1.204	-1.233	-1.208	-0.986	-1.132	-1.093
	1.135	1.196	1.149	1.042	1.203	0.943	1.088	0.962	1.061	1.363	1.095	1.150
	-1.142	-1.043	-1.121	-1.263	-1.032	-1.313	-1.150	-1.336	-1.204	-0.872	-1.259	-1.182
	1.167	1.236	1.089	1.029	1.268	1.004	1.103	0.923	1.076	1.437	0.956	1.045
	-1.066	-1.068	-1.148	-1.184	-1.015	-1.184	-1.195	-1.371	-1.154	-0.826	-1.332	-1.248
	1.235	1.193	1.068	1.114	1.247	1.138	1.067	0.921	1.147	1.421	0.916	1.055
	-1.061	-1.098	-1.203	-1.164	-1.068	-1.094	-1.202	-1.311	-1.084	-0.921	-1.324	-1.184
	1.177	1.156	1.092	1.096	1.169	1.178	1.098	1.007	1.223	1.237	1.035	1.161
	-1.116	-1.146	-1.147	-1.172	-1.116	-1.110	-1.150	-1.210	-1.067	-1.107	-1.176	-1.104
	1.125	1.113	1.137	1.125	1.147	1.114	1.137	1.126	1.148	1.124	1.126	1.148

and limiting the number of data cycles to 3-1/4, the problem of the drifting center of deflection was eliminated. The final integration procedure consisted of integrating the acceleration data according to equation 4. 21 and correcting the resulting velocity by linear corrections to each of the three cycles separately and using the average slope of these three corrections to adjust the base line of the acceleration. This procedure was continued as before until the base line of the deflection had been adjusted. The other sections of the program were not changed. Checking the new program with the program test data, answers identical to those given above were obtained. Dynamic test data were used and seemed to give physically significant results. The remainder of this section will give the results of applying the above numerical calculations to specific dynamic tests.

3c. Results. Since data recording galvanometers of both 100 cps and 20 cps natural frequencies had been used in the testing program, it was of interest to determine the effect of the recording galvanometer frequency upon the dynamic results. This has been done in test A3. 69 where data were taken simultaneously with 100 cps and 20 cps galvanometers connected to accelerometers located next to each other. The data were reduced at the same time and mid-time marks of the record. The relationship of the force position as indicated by the force pulses and the starting time line of the data had to be determined individually since the phase lag of the 20 cps and 100 cps galvanometer recording systems were significantly different (see the

discussion in Appendix I and figure 4.40). The resulting dynamic hysteresis loop as calculated from the 20 cps record, record (d) in figure 4.40, is plotted in figure 4.42. The 100 cps record, record (c) in figure 4.40, produces the points plotted in figure 4.43 and the line indicates the 20 cps record curve traced from figure 4.42. As can be seen from figure 4.43, no significant difference between the results was obtained by using the 100 cps or the 20 cps recording galvanometers. On this basis, reference to the particular galvanometer used to obtain specific data will not be included.

Test A3.57 is plotted in figure 4.44 and test A3.63 in figure 4.45. These figures give the dynamic force-deflection curves for different deflections and will be utilized later in comparisons with static force-deflection curves. Test A3.64, figure 4.46, has approximately the same maximum deflection as test A3.69. The comparison of figures 4.42 and 4.46 given in figure 4.47 shows that structural deterioration has taken place which overcomes the strength recovered during the 42 days of rest. This will be discussed in more detail in the next chapter.

Another check of the integration procedure was made by satisfying the steady-state condition at the end of one and two cycles simultaneously by means of a parabolic correction of the integrated data. The proper linear corrections and constant corrections were made to the acceleration and velocity data. This procedure did not seem to be as accurate in placing the origin of the deflection as the previous integration procedure. The data of test A3.64 was used in

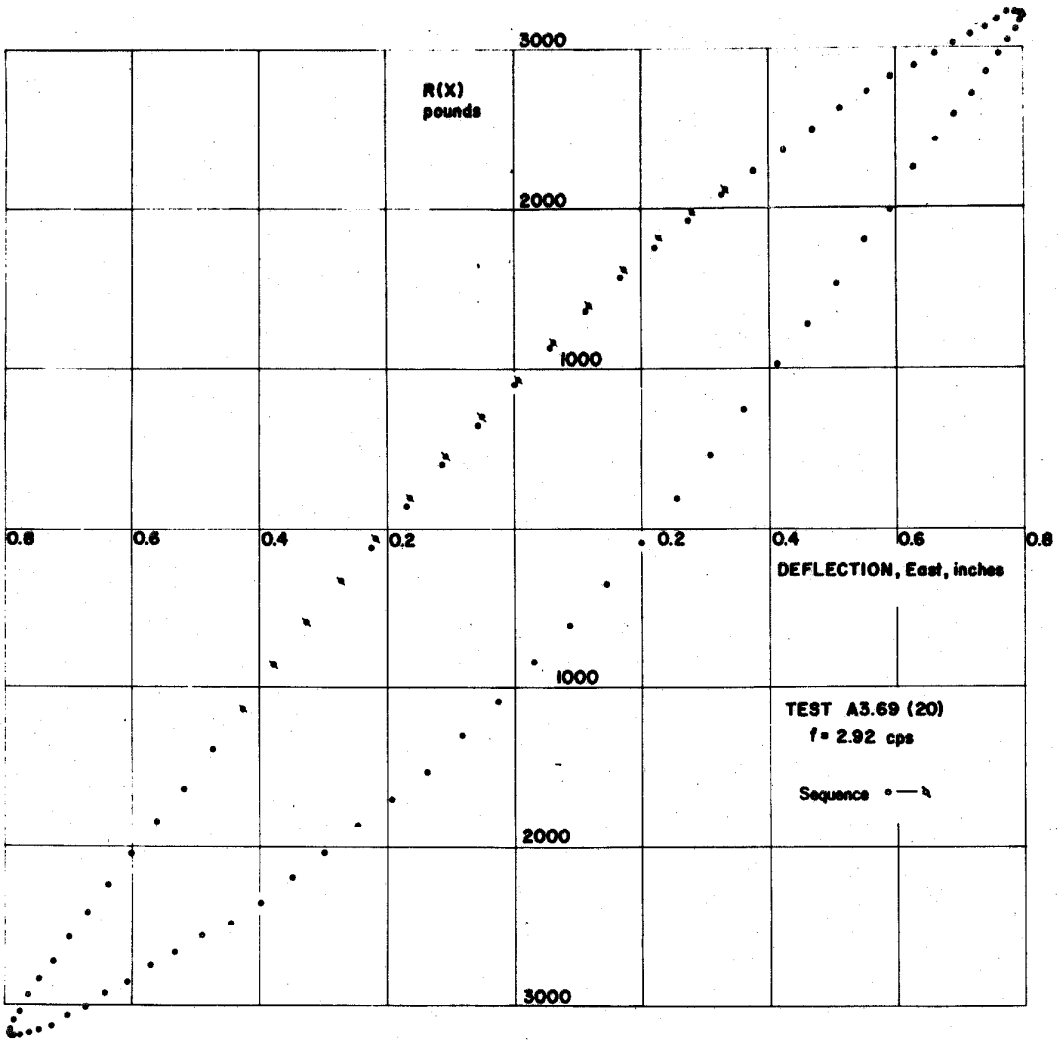

FIG. 4.42 DYNAMIC FORCE-DEFLECTION, SIII (E-W)

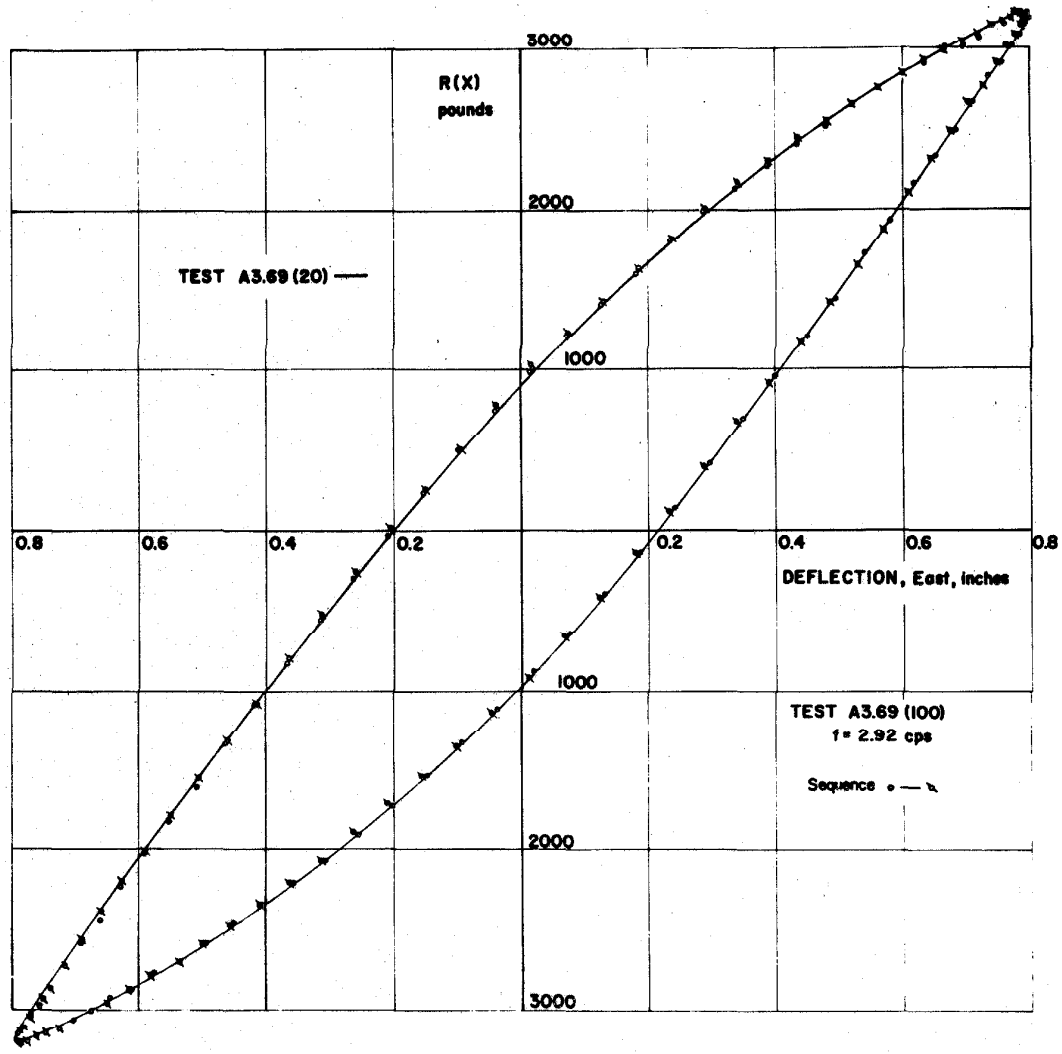

FIG. 4.43 DYNAMIC FORCE-DEFLECTION, SIII (E-W)

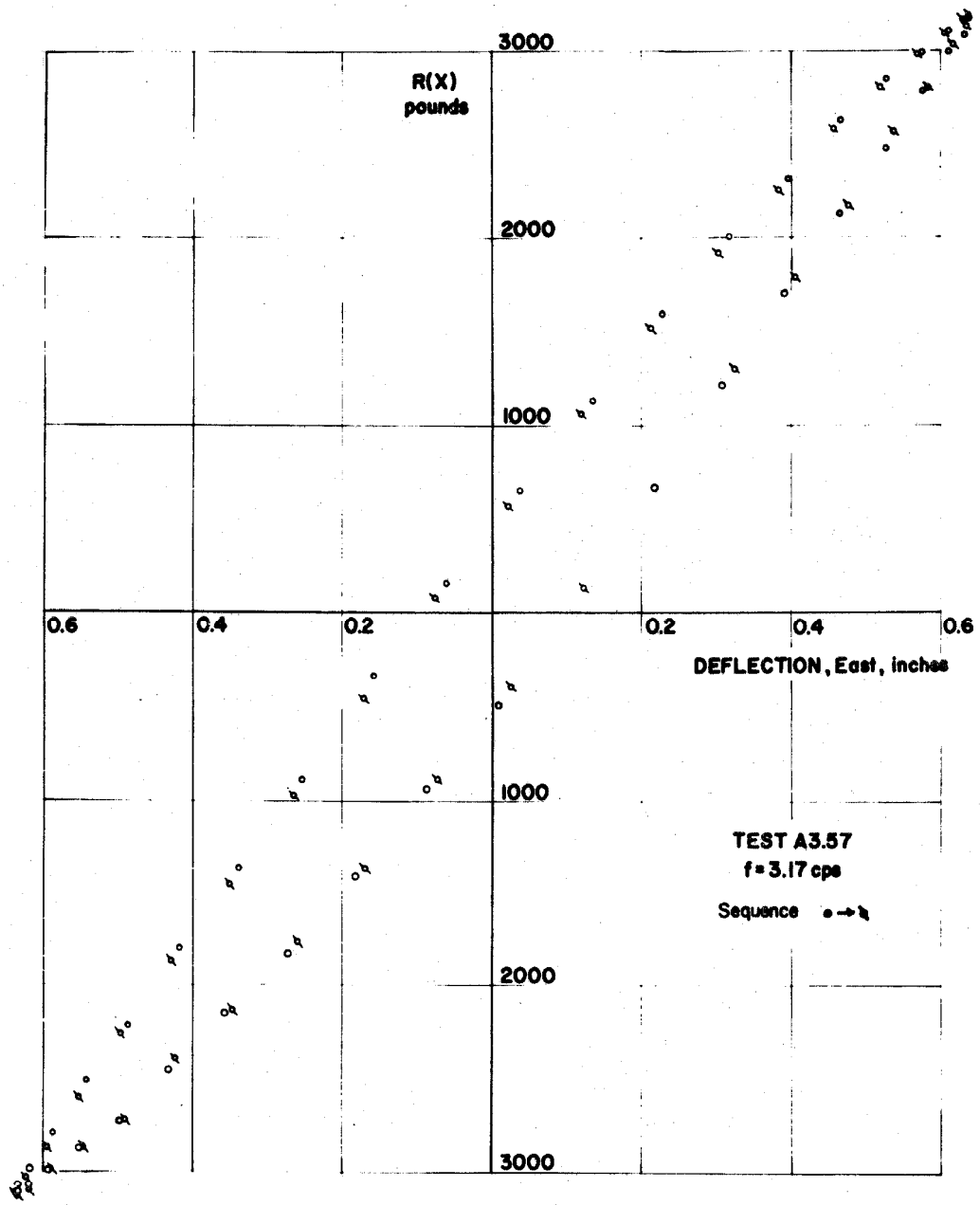

FIG. 4.44 DYNAMIC FORCE-DEFLECTION, SIII (E-W)

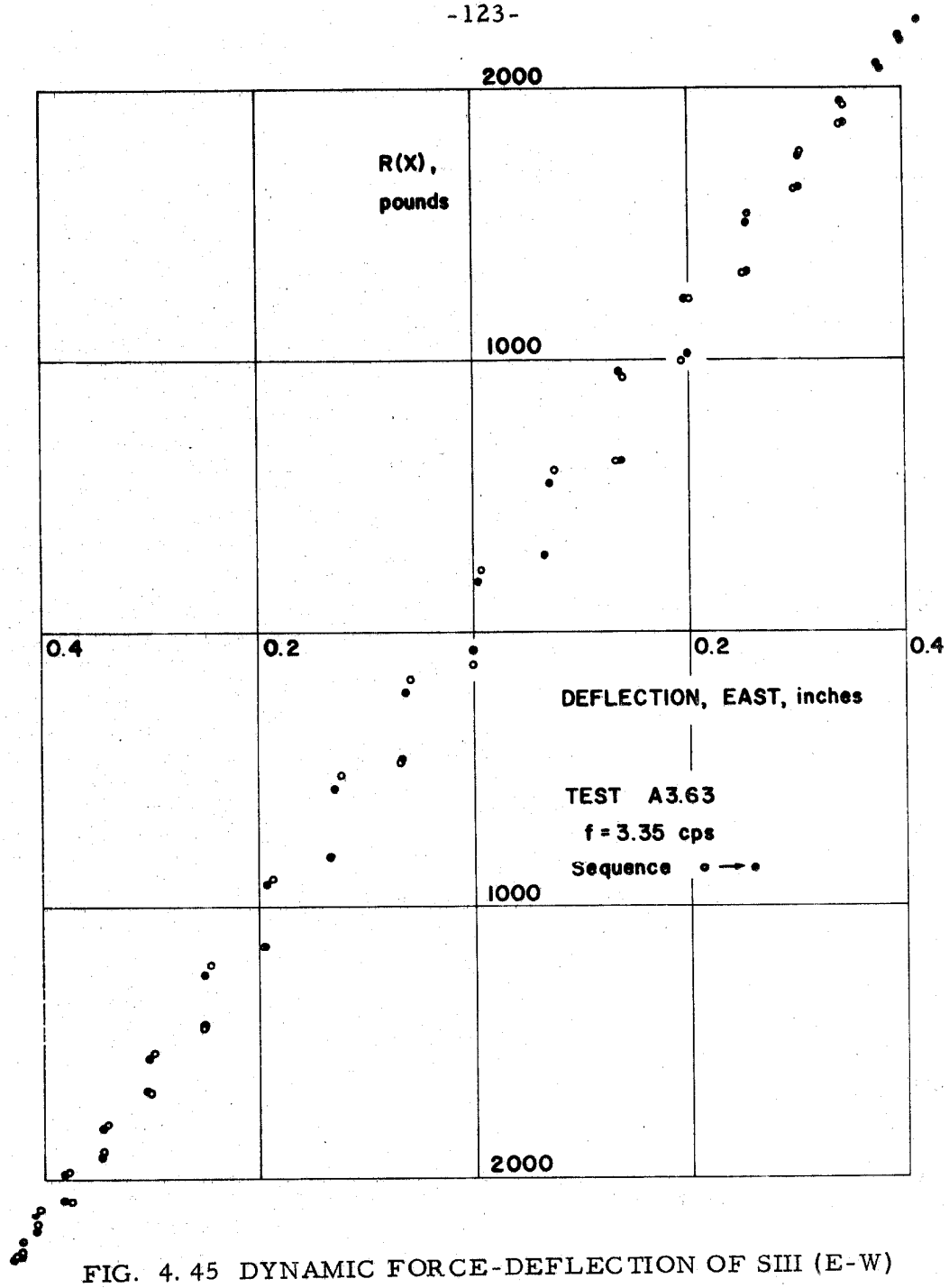

FIG. 4.45 DYNAMIC FORCE-DEFLECTION OF SIII (E-W)

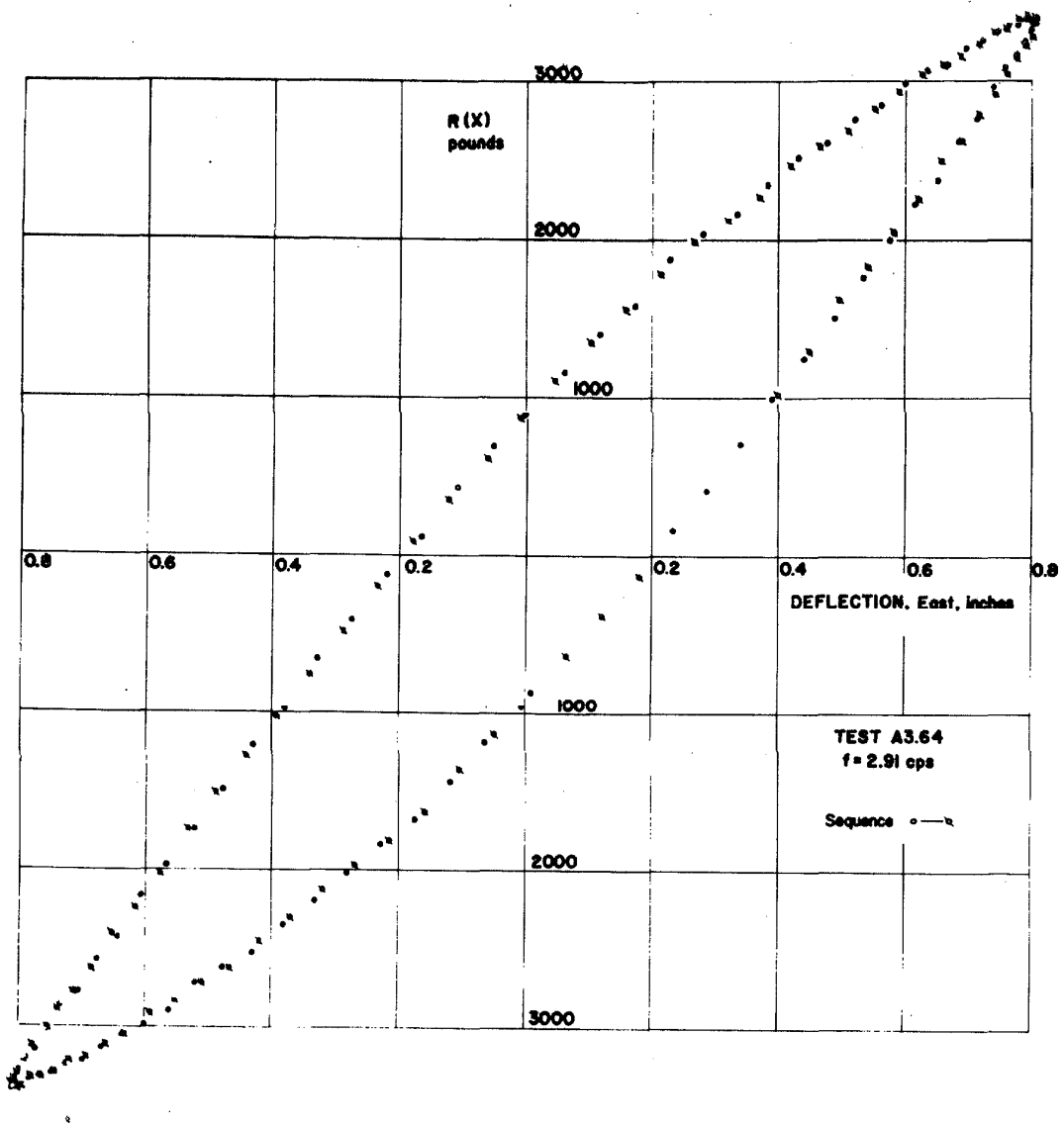

FIG. 4.46 DYNAMIC FORCE-DEFLECTION, SIII (E-W)

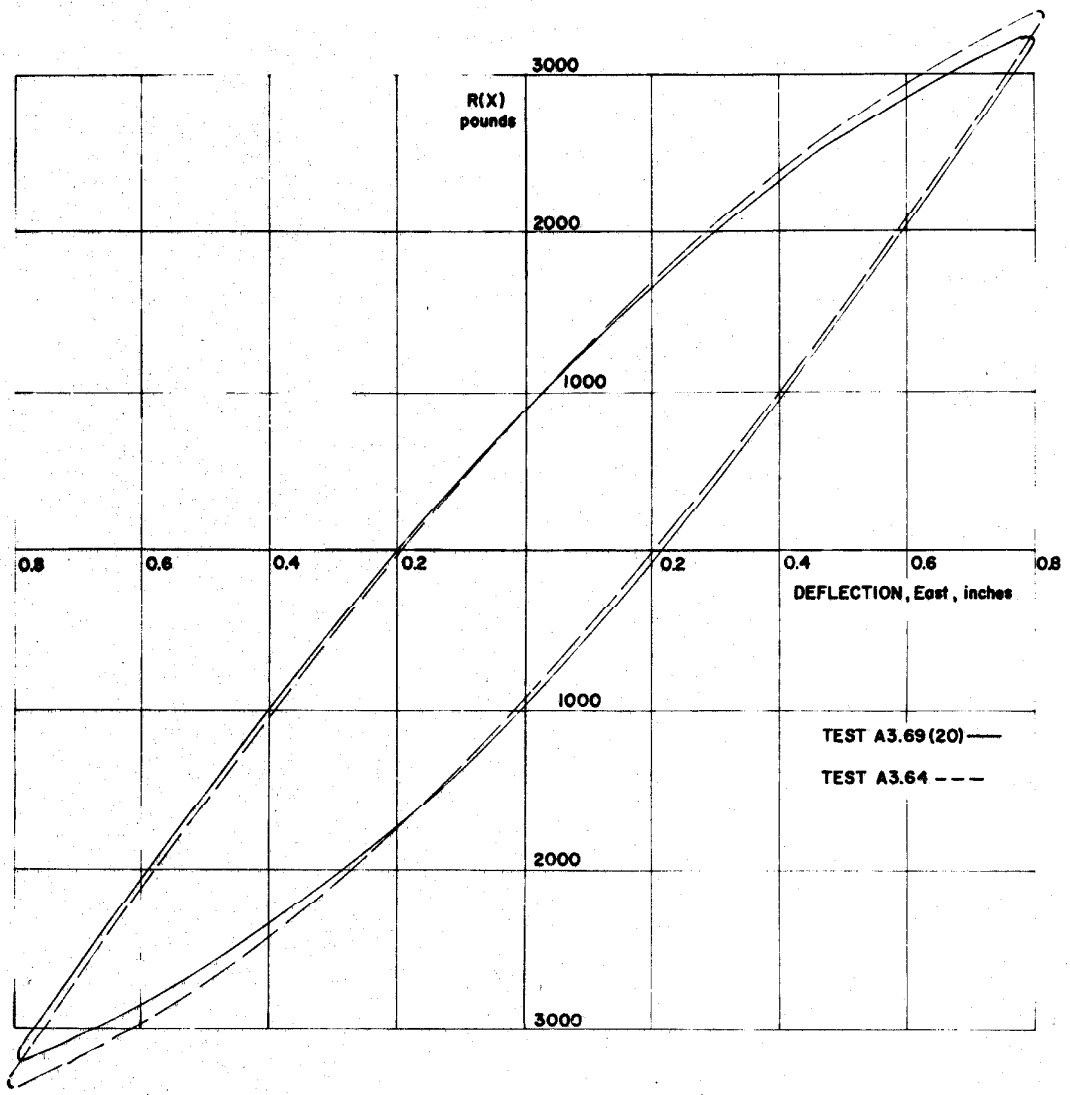

FIG. 4.47 DYNAMIC FORCE-DEFLECTION, SIII (E-W)

this program and the result is plotted in figure 4. 48. Since the mean deflection of the new integrated deflection was not zero, the original test A3. 64 dynamic curve, figure 4. 46, had to be shifted by 0. 018 inch before tracing on figure 4. 48 as the line. It can be seen by figure 4. 48 that the type and solution of the integration procedure does not seem to alter the character of the dynamic force-deflection relationship. The area of the dynamic force-deflection curves together with some other properties are summarized in Table IV-3.

3d. Comparison of dynamic and static hysteresis curves. All of the comparisons made in this section are for column set SIII, thereby eliminating any differences between the column sets. The areas enclosed by the hysteresis loops are summarized in Table IV-4 together with the average maximum deflections.

Figure 4. 49 combines the results of test A3. 56 (figure 4. 29), test A3. 57 (figure 4. 44) and test A3. 58 (figure 4. 31). Because of the large change in response caused by progressive experimentation, no specific comparison of static and dynamic response can be made. It should be mentioned that the structure had not been tested at deflections larger than those in figure 4. 49 when those tests were made.

The portion of test A3. 60 (figure 4. 32) given in figure 4. 50 preceded a deflection of the structure to -0. 825 inch while test A3. 66 (figure 4. 35) followed a dynamic study at 0. 810 inch amplitude and was a portion of the descending amplitude static experiment from 0. 815 inch. A shift in the force axis of 170 pounds was made when replotting test A3. 66. The dynamic test A3. 63 is taken from figure 4. 45. In

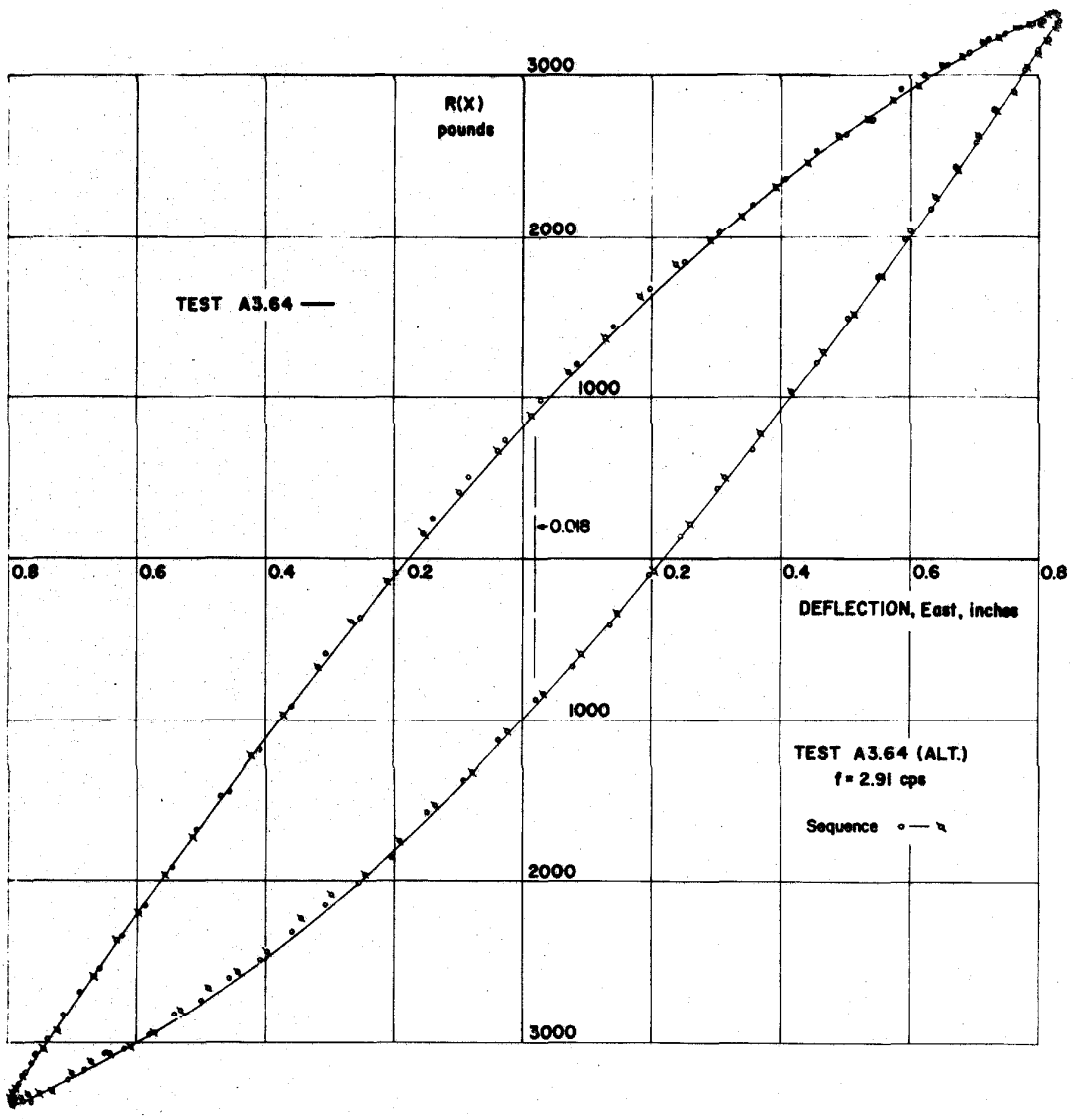

FIG. 4.48 DYNAMIC FORCE-DEFLECTION, SIII (E-W)

TABLE IV-3

Dynamic Force-Deflection Results

Test	Deflection x, inch	Degrees	$\oint R(x)dx$ inch-lbs.	$\oint F\dot{x}dt$ inch-lbs.	Change in $\oint R(x)dx$ for $\pm 2^{\circ}$ phase inch-lbs.	Reference figure	Test frequency radians/sec
A3.57	-.637	84	850	854	+3	4.44	19.90
	+.632		849	852	-4		
A3.62	-.121	178	.26	.26	-.23	--	22.16
	+.122		.48	.49	+.23		
A3.63	-.414	81	159	159	+1	4.45	21.03
	+.427		157	157	-1		
A3.64	-.810	81	1981	1983	+5	4.46	18.28
	+.809		1985	1987	-7		
A3.64 (Alt.)	-.797	85	1995	1982	+6	4.48	18.28
	+.833		1996	1985	-8		
A3.69 (20)	+.795	94	1964	1966	-9	4.42	18.37
	-.793		1965	1967	+7		
A3.69 (100)	+.790	93	1955	1957	-7	4.43	18.37
	-.790		1955	1957	+5		

TABLE IV-4

Summary of Energy Dissipation per Cycle at Maximum Deflection

Test	Type	in-pounds E. D. per cycle	inch Max. X	Ref. figure
A3. 56	static	598	0. 635	
A3. 57	dynamic	850	0. 635	4. 49
A3. 58	static	934	0. 640	
Theoretical		859	0. 635	5. 17
A3. 60	static	230	0. 420	
A3. 63	dynamic	158	0. 420	4. 50
A3. 66	static	262	0. 420	
Theoretical		0^{+}	0. 420	5. 17
A3. 60	static	1951	0. 825	
A3. 64	dynamic	1983	0. 810	4. 38
A3. 66	static	2026	0. 815	4. 47
A. 368	static	1860	0. 815	4. 51
A3. 69	dynamic	1960	0. 792	
Theoretical		2756	0. 810	5. 17

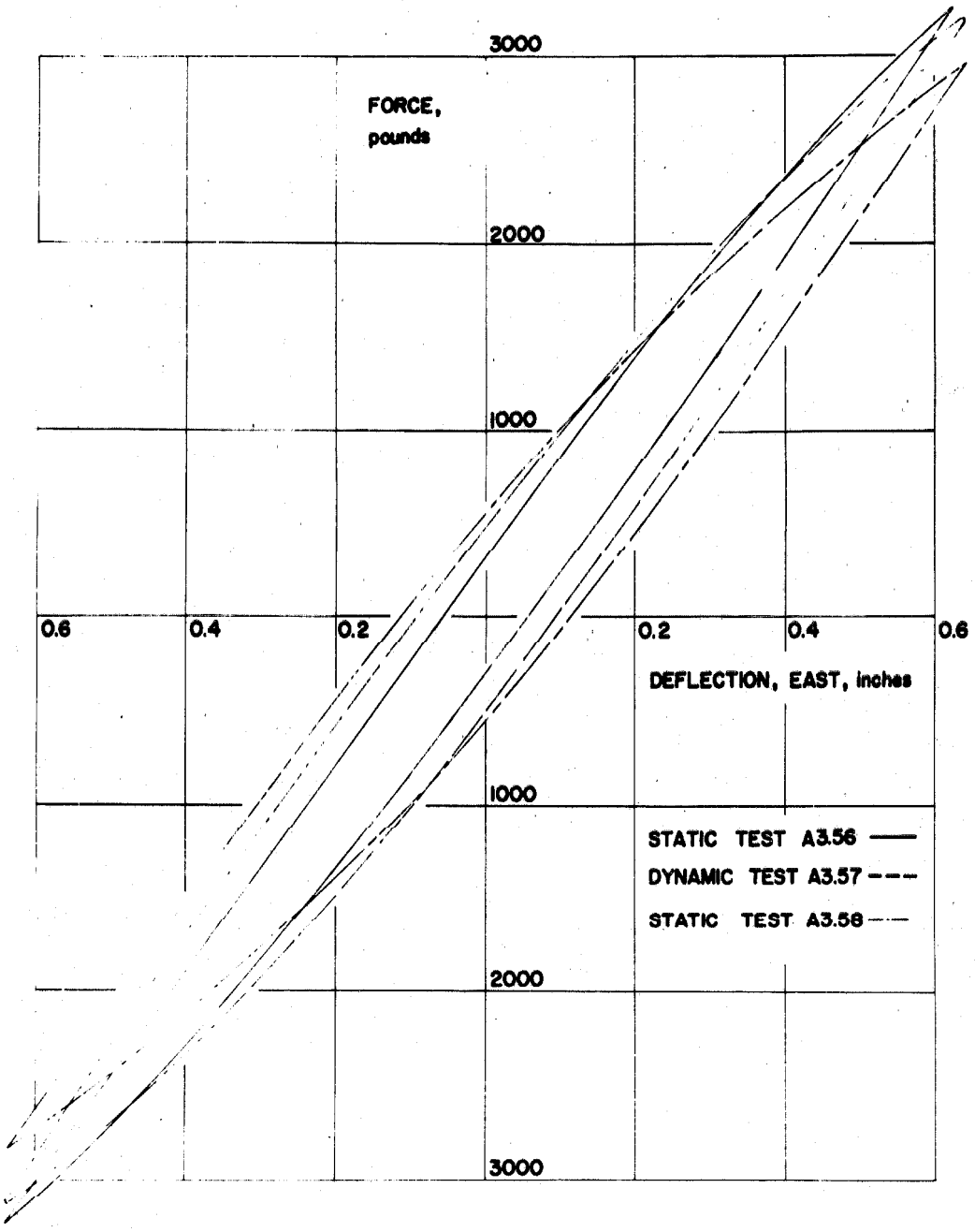

FIG. 4.49 DYNAMIC-STATIC COMPARISON OF FORCE-DEFLECTION CURVES

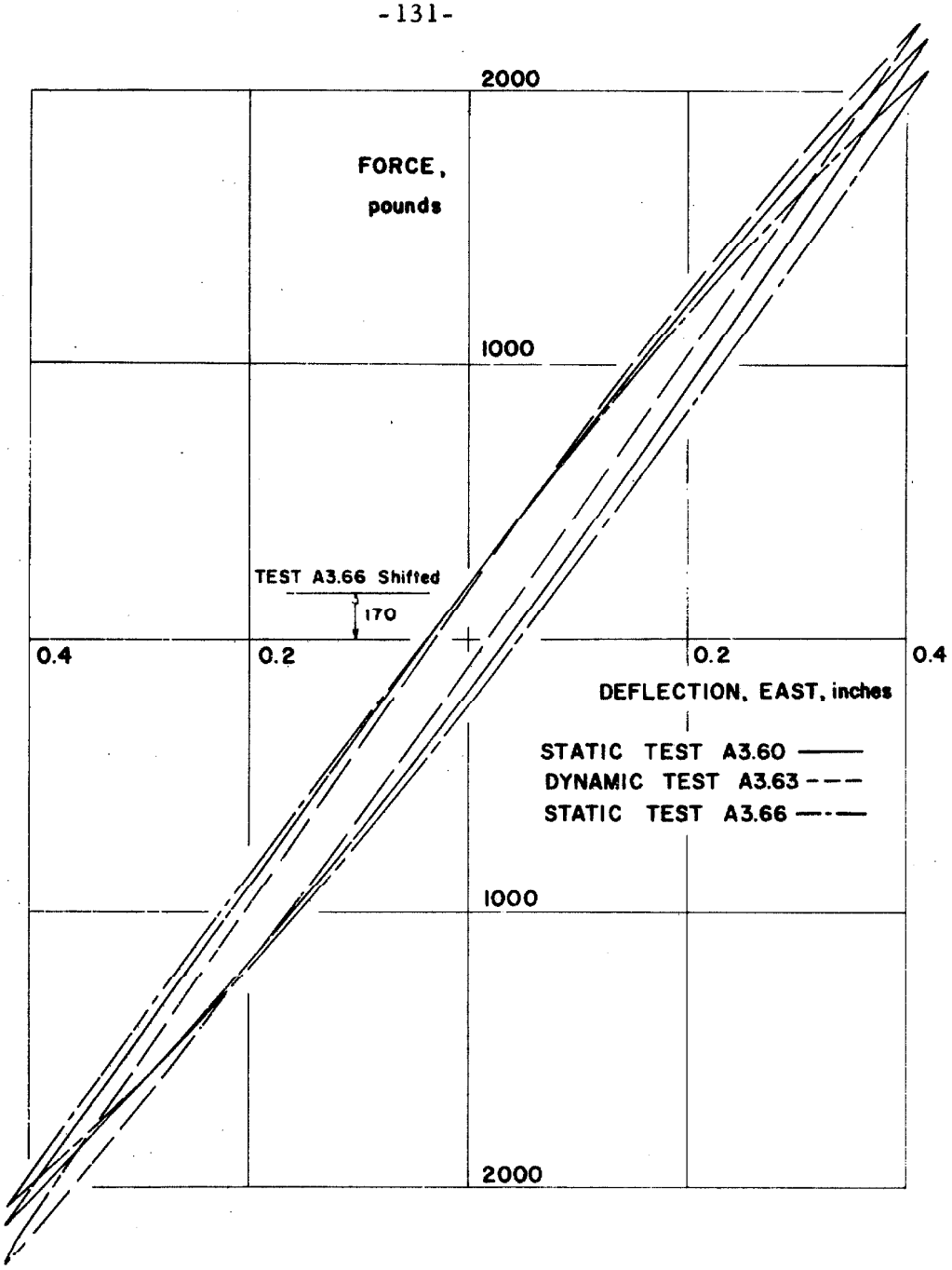

FIG. 4.50 DYNAMIC-STATIC COMPARISON OF FORCE-DEFLECTION CURVES

this case, the dynamic response indicates a larger restoring force and a smaller amount of energy dissipated per cycle.

Static tests A3. 60 (figure 4. 33) and A3. 66 (figure 4. 34) are compared with the dynamic test A3. 64 (figure 4. 46) in figure 4. 51. The static comparison made in figure 4. 38 and the dynamic comparison made in figure 4. 47 shall be used in conjunction with figure 4. 51 in the following discussion. Figure 4. 51 does not yield a valid basis of comparing static and dynamic force-deflection curves, again because of the large changes in the curves based on experimental history. This column had not been studied at deflections greater than ± 0. 825 inch at that time.

An estimate of the strain rate of loading for the various dynamic curves will be given in the next chapter, where the properties of the deflection-maximum strain relationship are discussed. An interpretation of the test results presented and compared here will also be made in the following chapter.

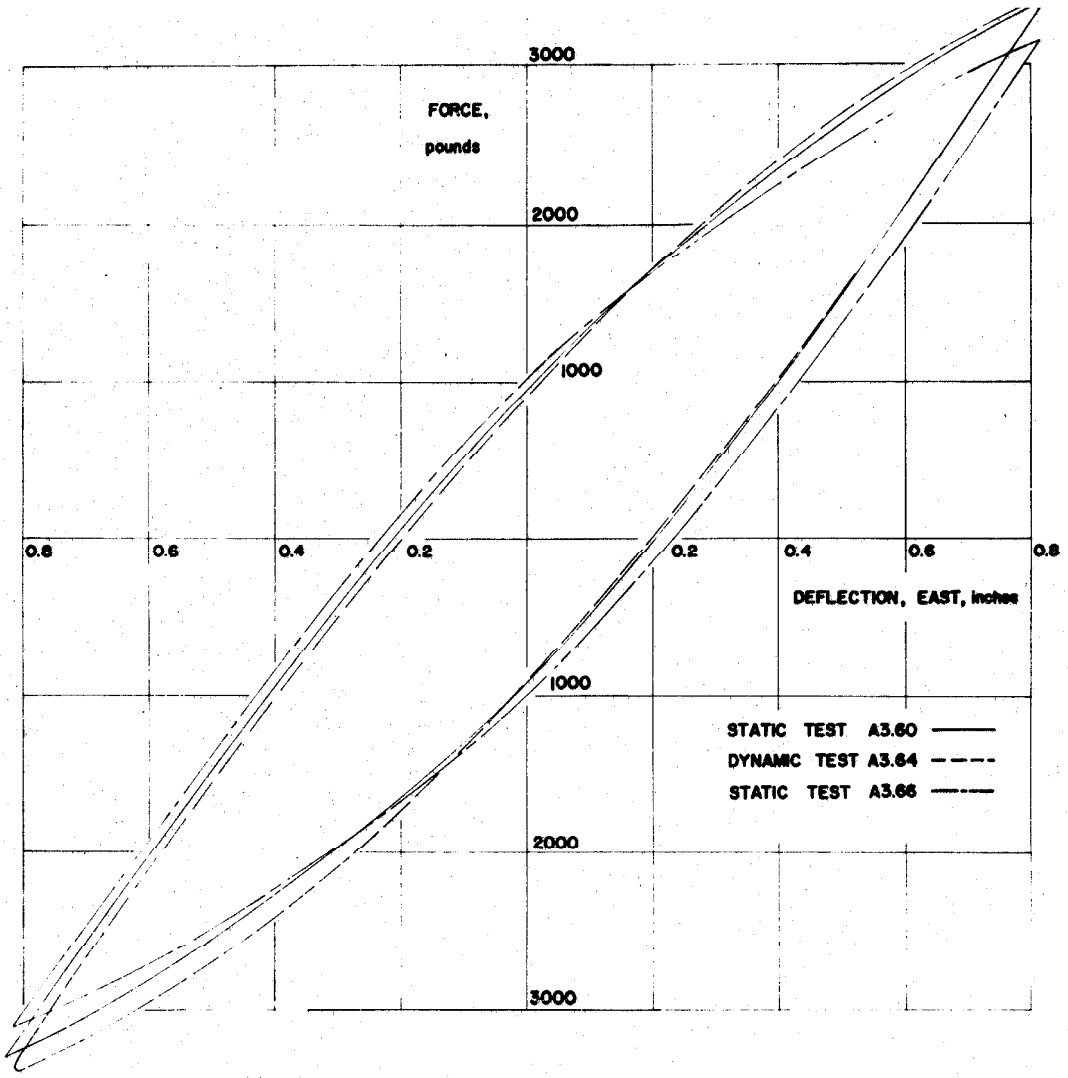

FIG. 4.51 DYNAMIC-STATIC COMPARISON OF FORCE-DEFLECTION CURVES

V. ANALYSIS AND INTERPRETATION OF THE EXPERIMENTAL RESULTS

The comparison of theoretical and experimental results is always useful because it permits an evaluation of the theoretical approach and may suggest modifications which will improve the theoretical analysis. The theoretical analysis may also be used as an aid in understanding the experimental results. This is true both for static and dynamic conditions.

In this chapter a simplified theoretical analysis will be made of the structure described in Chapter III for comparison with the experimental results reported in Chapter IV. Additional theoretical analyses for use in interpreting the results will also be given in this chapter.

A. Theoretical Analyses

1. Plastic Hinge

A post-elastic analysis of a rectangular section and of the 5 I 14.75 end sections will now be made for use in determining the force-deflection relationship for the structure. A number of simplifying assumptions are necessary for this analysis. It will be assumed that the stress-strain relationship for flexure is the same as that established in the tension tests reported in Appendix II. Second, it will be assumed that during flexure plane sections remain plane even for large plastic deformations.* For a rectangular cross

* For example: Freudenthal.(39)

section, see figure 5.1, the static moment of the stresses with respect to the neutral axis is given by

$$M_s = \int_{-c}^{c} \sigma\, y\, b\, dy \tag{5.1}$$

where M_s is the moment at the section, σ is the normal stress, b is the width of the rectangular section, and y is the distance from the neutral axis. The effect of the shearing stress

$$\tau_{zy} = \frac{1}{2}\,\frac{P}{I}\,(c^2 - y^2) \tag{5.2}$$

is assumed to be small and will be neglected in the following development. P is the force acting in the y direction and I is the moment of inertia of the cross section.

For the linear elastic condition, the change in slope per unit length (curvature) is equal to

$$\theta = M_s / EI \tag{5.3}$$

and the maximum fiber strain is equal to

$$\epsilon_c = \frac{M_s c}{EI} \tag{5.4}$$

where ϵ is the strain. Therefore, the curvature can be defined as

$$\theta = \frac{\epsilon_c}{c} \tag{5.5}$$

The assumption that plane sections remain plane implies that equation 5.5 is valid for all strain values, even when equations 5.3 and 5.4 are no longer valid. Using equations 5.1 and 5.5 and the material stress-strain properties given in Appendix II, the moment-

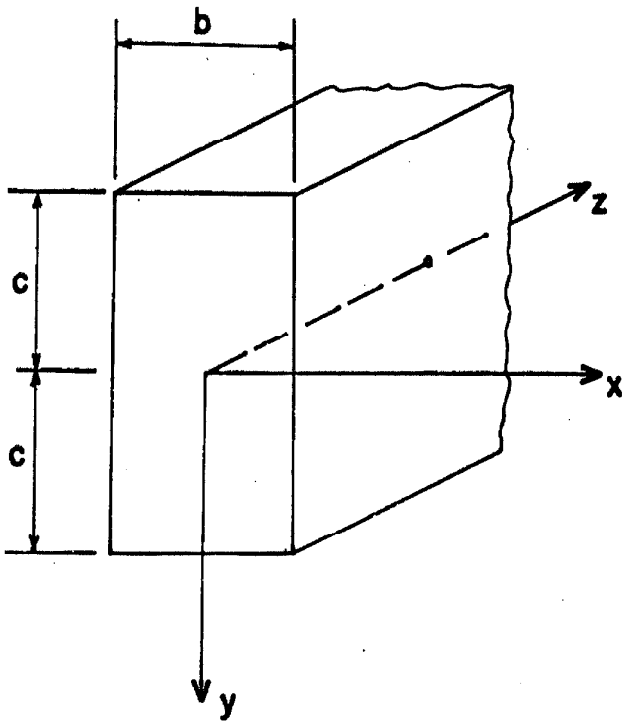

FIG. 5.1 RECTANGULAR SECTION

curvature relationship can be established for all θ. Dividing the stress-strain relationship into the three parts indicated in figure 5. 2, the moment at the section can be evaluated according to equation 5. 1.

For case I: Elastic

$$\sigma = yE\theta \qquad \text{with} \qquad \epsilon_c \leq \epsilon_{e\ell} \tag{5. 6}$$

where $\epsilon_{e\ell}$ is the initial yield strain occurring at $y=y_{e\ell}$, see figures 5. 1 and 5. 2.

$$M_s = bE\theta \int_{-c}^{c} y^2 dy = \theta EI \tag{5. 7}$$

For case II: Elastic-Plastic

$$\begin{aligned} \sigma &= yE\theta \qquad \text{for} \qquad y \leq y_{e\ell} \\ \sigma &= \sigma_{e\ell} \qquad \text{for} \qquad y_{e\ell} \leq y \leq Ay_{e\ell} \end{aligned} \tag{5. 8}$$

$$\begin{aligned} M_s &= 2\int_0^{y_{e\ell}} yE\theta\, ybdy + 2\int_{y_{e\ell}}^{c} y_{e\ell} E\theta\, yb\, dy \\ &= y_{e\ell} E\theta b\left[c^2 - \frac{1}{3} y_{e\ell}^2\right] \\ &= \frac{3}{2} E\theta \left(\frac{y_{e\ell}}{c}\right) \frac{2}{3} bc^3 - \frac{1}{2} E\theta \frac{2}{3} b\, y_{e\ell}^3 \\ &= \frac{3}{2} E\theta I \left(\frac{y_{e\ell}}{c}\right) - \frac{1}{2} E\theta I \left(\frac{y_{e\ell}}{c}\right)^3 \end{aligned} \tag{5. 9}$$

Since

$$M_{e\ell} = EI\theta_{e\ell},\ I = bc^3 \frac{2}{3} \text{ and } \left(\frac{\theta}{\theta_{e\ell}}\right) = \left(\frac{\epsilon}{\epsilon_{e\ell}}\right) = \left(\frac{c}{y_{e\ell}}\right) \tag{5. 10}$$

equation 5. 9 can be rearranged to give

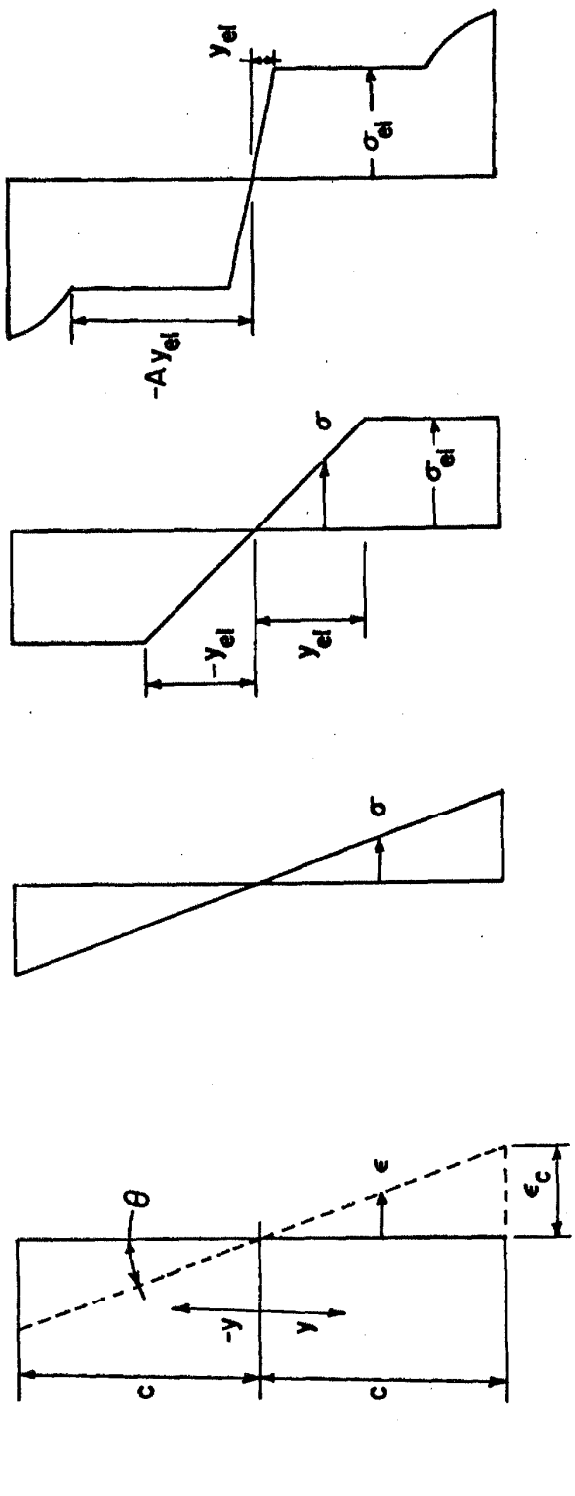

FIG. 5.2 ASSUMED STRESS CONDITIONS

$$\frac{\theta}{\theta_{e\ell}} = \sqrt{\frac{1}{3 - \frac{2M_s}{M_{e\ell}}}} \tag{5.11}$$

For case III: Area of Strain Hardening

The strain hardening case will be determined by including the additional terms resulting from the strain hardening to the extended results of Case II. The actual stress-strain relationship given in Appendix II will be approximated by the segmentally linear relationship given in figure 5.3.

For the region $Ay_{e\ell} \leq y \leq By_{e\ell}$

$$\sigma_{sHA} = G\theta E(y - Ay_{e\ell}) \tag{5.12}$$

and

$$M_s = M_{sII} + M_{sHA} \tag{5.13}$$

where $\sigma_{sHA} = (\sigma - \sigma_{e\ell})$ and M_{sII} is the solution for case II from equation 5.9 or 5.11 without the upper limit on y. From equations 5.12 and 5.1,

$$\begin{aligned} M_{sHA} &= \int_{Ay_{e\ell}}^{c} G\theta E(y - Ay_{e\ell}) y \, dy + 0 \\ &= GE\theta b \left[\frac{c^3}{3} - \frac{1}{2} c^2 Ay_{e\ell} + \frac{1}{6} A^3 y_{e\ell}^3\right] \end{aligned} \tag{5.14}$$

With the aid of equation 5.10, this equation reduces to

$$M_{sHA} = G\left(\frac{\theta}{\theta_{e\ell}}\right) M_{e\ell}\left[\frac{1}{2} - \frac{3}{4} A\left(\frac{\theta_{e\ell}}{\theta}\right) + \frac{1}{4} A^3 \left(\frac{\theta_{e\ell}}{\theta}\right)^3\right] \tag{5.15}$$

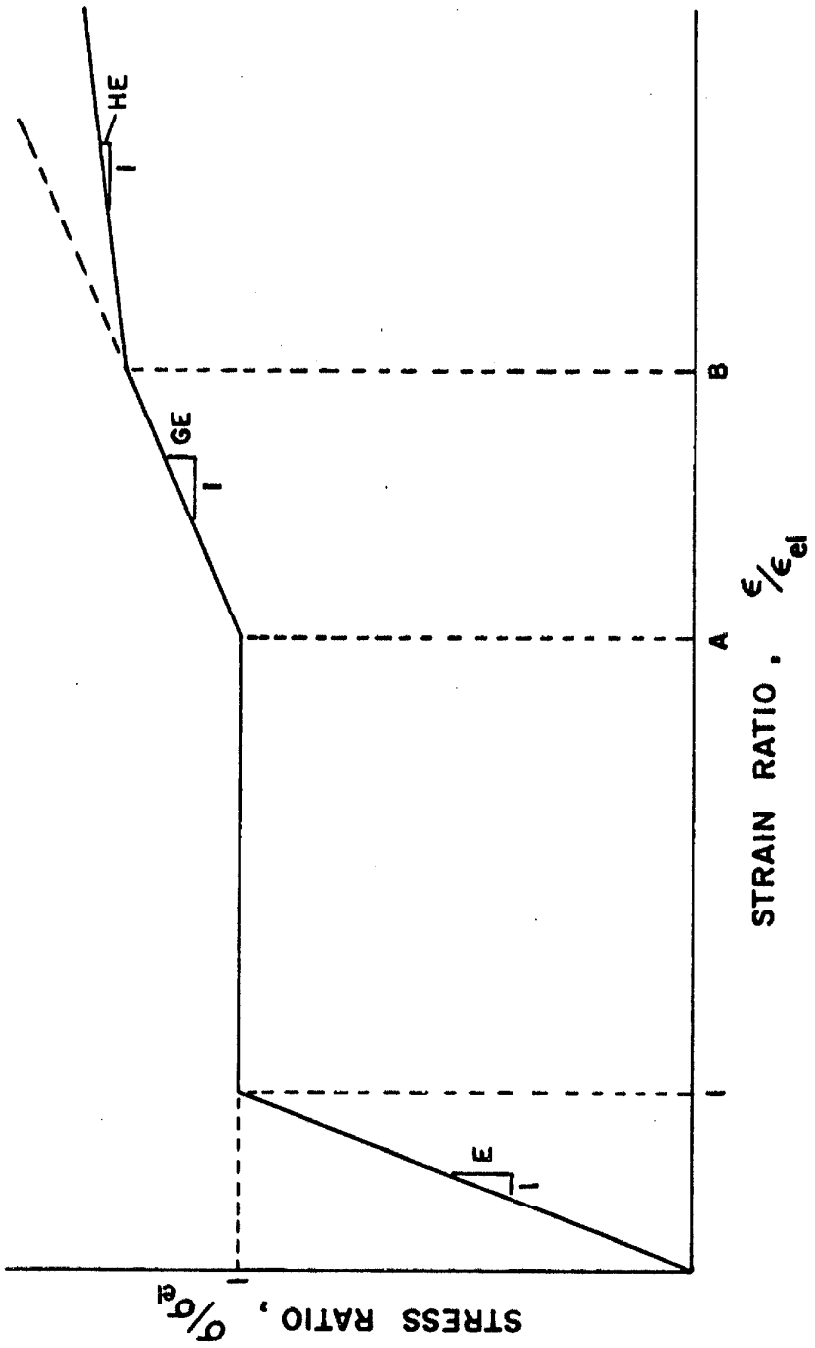

FIG. 5.3 ASSUMED STRESS-STRAIN RELATIONSHIP

For the region $y \geq By_{e\ell}$

$$\sigma_{sHB} = (G-H)\theta E(y-By_{e\ell}) \tag{5.16}$$

and

$$M_s = M_{sII} + M_{sHA} - M_{sHB} \tag{5.17}$$

where

$$M_{sHB} = (G-H)\left|\frac{\theta}{\theta_{e\ell}}\right| \frac{M_{e\ell}}{2}\left[1 - \frac{3}{2}B\left|\frac{\theta_{e\ell}}{\theta}\right| + \frac{1}{2}B^3\left|\frac{\theta_{e\ell}}{\theta}\right|^3\right] \tag{5.18}$$

The resulting moment-curvature or moment-maximum strain ratio is given in figure 5.4. The strain hardening region has been approximated using G = 0.014, A = 10, B = 34, and H = 0.0024 (see Appendix II, figure A2.2).

The significance of the curvature or maximum strain ratio in terms of yielding material can be investigated by considering the maximum strain ratio, e.g., 20. From equation 5.10,

$$y_{e\ell} = c/20 \tag{5.19}$$

This means that only 5 percent of the material at that section is acting elastically for a curvature 20 times the elastic curvature. The thickness or core of elastic material surrounding the neutral axis of the section is a function of the bending moment at that section. For a linear change in moment increasing from $M_{e\ell}$ and neglecting strain hardening effects, the equation for $y_{e\ell}$ can be determined from equations 5.10 and 5.11 to be

$$y_{e\ell} = \pm c\sqrt{3-2v} \tag{5.20}$$

where $M_s = vM_{e\ell}$ and v varies linearly from 1.0 to 1.5. The result

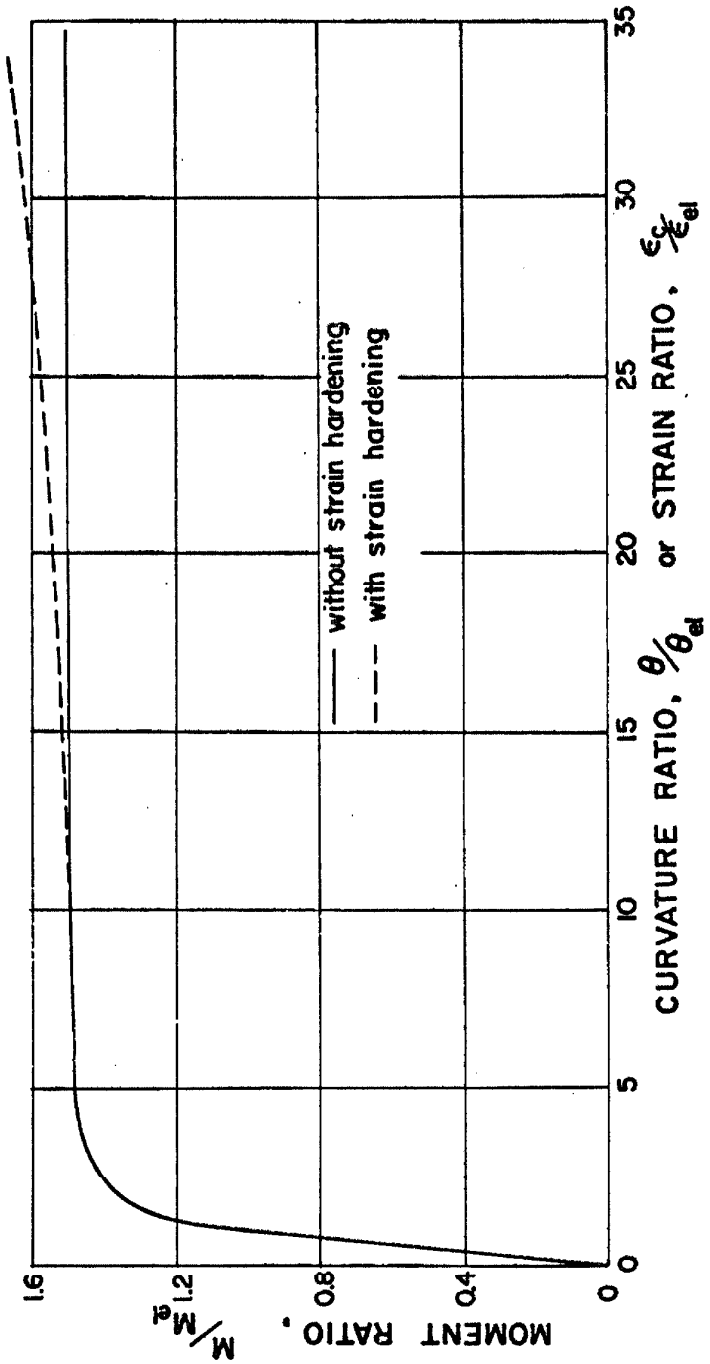

FIG. 5.4 MOMENT-CURVATURE RELATIONSHIP
(RECTANGULAR SECTION)

of equation 5. 20 and the moment are plotted in figure 5. 5.

To illustrate the yielding areas of the 5 I 14. 75 column and sections, it will be assumed that the only effect of the flange fillets is to increase the depth of the section. In other words, the stress and strain modifications caused by the curved surface will be assumed to be second order effects and will be neglected. As will be shown in the following sections, a satisfactory approximation to the actual column bending diagram is to have equal and opposite maximum moments at the column ends with a linear distribution between them, see figure 5. 9(c). Specifically taking column SII NE which has an overall length of 24. 94 inches and with maximum end moments of 1. 58 $M_{e\ell}$, where $M_{e\ell}$ is the calculated maximum elastic moment in the web of the 5 I 14. 75 section, the material yield distribution similar to figure 5. 5(b) will be determined. Selecting the origin of the z axis at one column end, the moment at any section is

$$M_s = 1.58\, M_{e\ell}(1-z/12.47) \tag{5.21}$$

For sections with a depth greater than the web thickness, the corrected maximum elastic moment is

$$M^*_{e\ell} = (c^*/c)^3 M_{e\ell} \tag{5.22}$$

The critical z which terminates the possible yielding sections is determined from equation 5. 21 to be z = 4. 59 and 20. 35 inches. The theoretical material yield distribution for the 5 I 14. 75 end section is drawn at full scale in figure 5. 6. The section of the 5 I 14. 75 enclosed in the dashed lines was cut from the top section of column

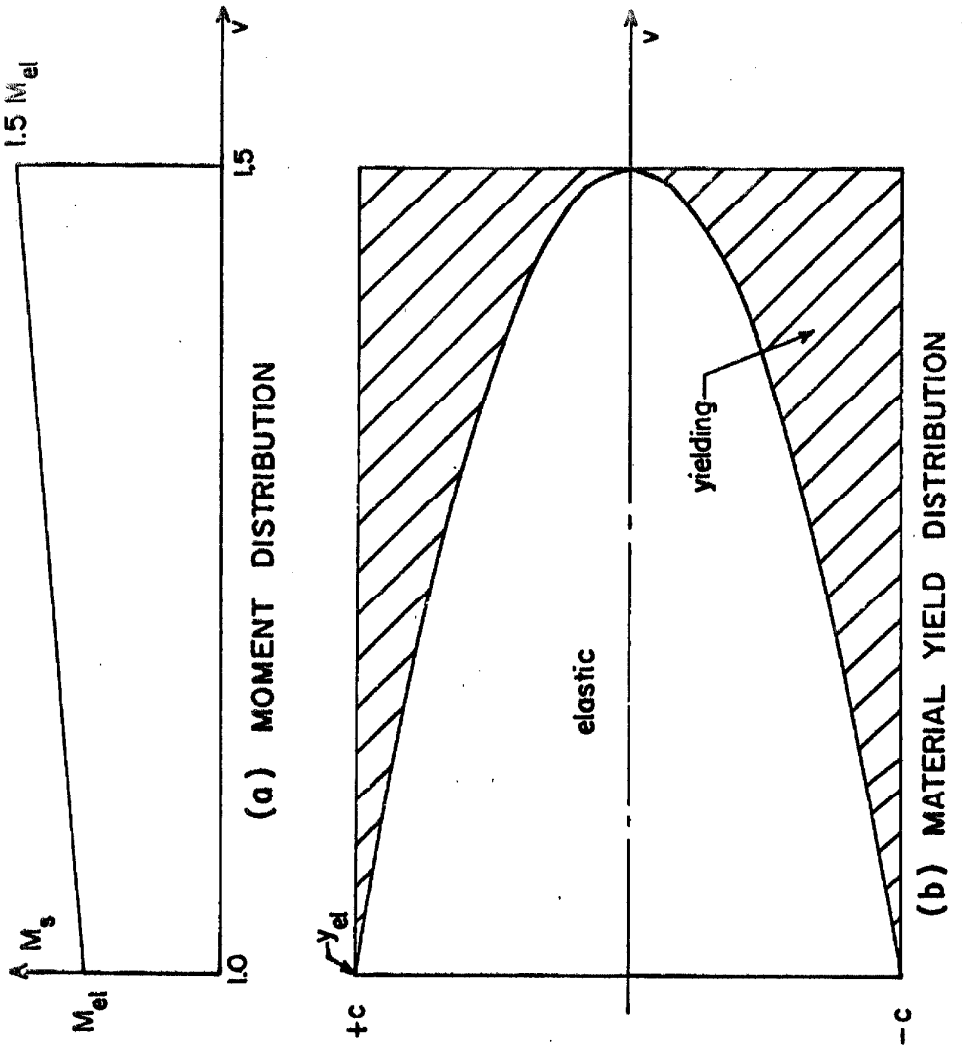

FIG. 5.5 RECTANGULAR SECTION

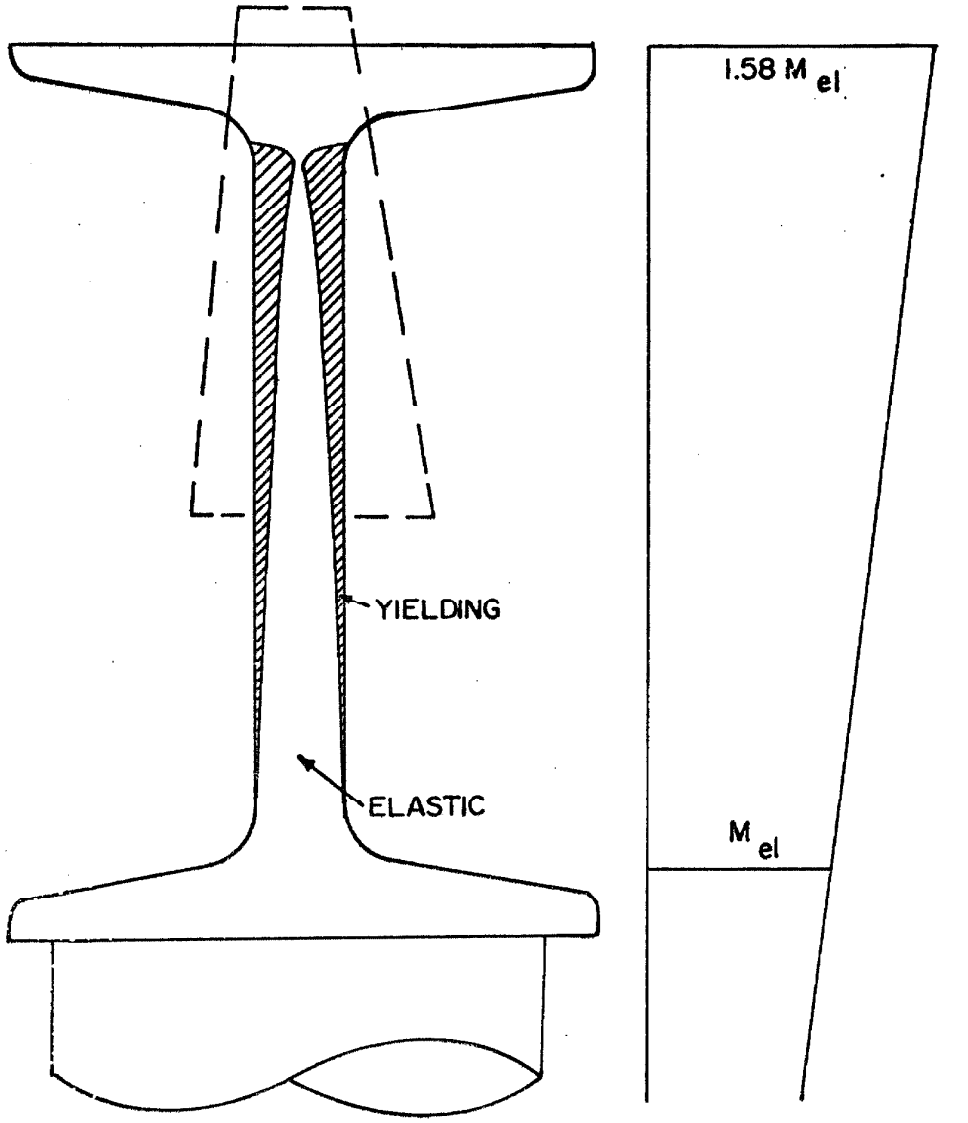

FIG. 5.6 MATERIAL YIELD DISTRIBUTION FOR
5 I 14.75 COLUMN ENDS

SII NE, and was treated and etched to show the areas of metal yield.* This operation was performed after the SII column set had failed with the top section of two other columns in the set cracked completely across the section and the third easily broken by hand. A photograph of the processed and etched section is given as figure 5.7 where the darker areas indicate yielding of the metal. The process was not a complete success in that only the areas of massive yielding appear dark. This can be seen by noting that the hardness test marks at the top and bottom ends of the specimen do not indicate the small yielding known to exist. The extremely dark portion near the fillet was caused by the etching acid in the crack and is not evidence of extreme yielding. A second photograph, figure 5.8, of the same specimen is given to show the fracture. Because of the lighting of the specimen, the yielding areas of figure 5.8 appear to be lighter than the elastic areas. Comparison of figures 5.7 and 5.8 with figure 5.6 indicates that the actual moments existing at the column ends must have been larger than the moments assumed for figure 5.6.

2. Force-Deflection Relationship for the Structures

The column dimensions and details were given in figure 3.5 and in Table III-1. As was shown in the preceding analysis, all of the material yielding occurred in the end 5 I 14.75 sections with the majority of the yielding restricted to the rectangular sections of these column ends. Because the yielding in the columns occurred at

*The writer wishes to acknowledge the time and effort expended by Mr. Dan Krause in performing this operation.

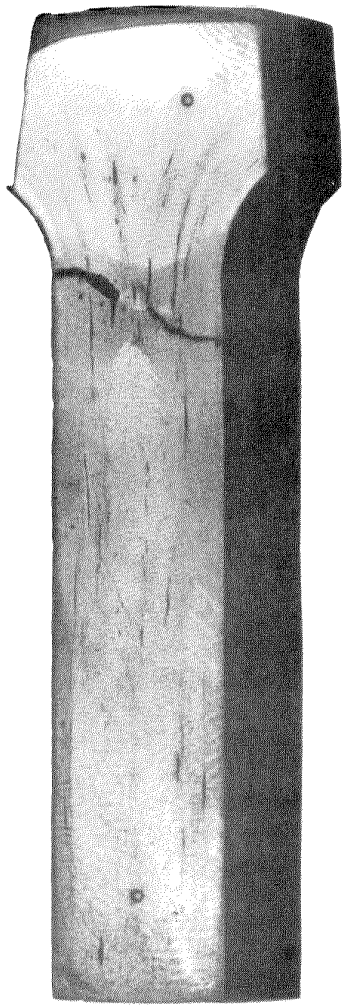

FIG. 5.7 ETCHED END SECTION SHOWING AREAS OF MASSIVE YIELDING

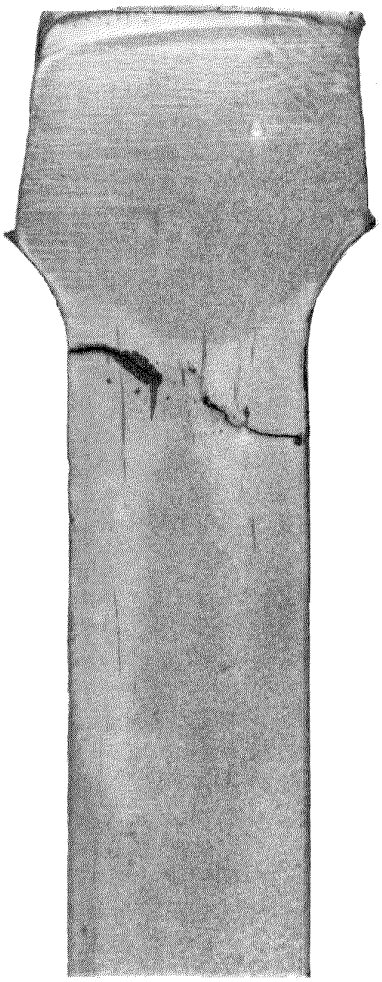

FIG. 5.8 ETCHED END SECTION SHOWING FATIGUE FRACTURE

rectangular sections, the theoretical calculations were simplified. First, the elastic properties of the columns were evaluated so that the stiffness and natural frequencies of the structure could be calculated. Then using the material properties as approximated in the preceding section, the theoretical force-deflection skeleton curve and the theoretical maximum strain-deflection relationship for the structure were calculated.

For the preliminary theoretical analysis of the column stiffnesses, several simplifying assumptions were made. First, it was assumed that the ends of the columns were rigidly fixed 3/8 inch below the floor frame and 3/8 inch above the base plate, see figure 5.6. The moment-area theorem of structural analysis states that the deflection of any point on the axis of a beam from a tangent through any other point equals the moment about the first point of the M/EI diagram between the two points. This can be used to determine the deflection of the floor frame relative to the base plates because the column axis tangent at the base plate is always vertical. It should be mentioned here that M is the bending moment, E is Young's Modulus of Elasticity and I is the static moment of inertia of the section. Since the columns are symmetrical with respect to mid-length, the moments at the top and bottom ends are equal. If the axial loads in the columns due to the weight of the supported structure and due to the horizontal load are neglected in calculating the bending moment, a simple calculation determines the stiffness of the column. This approximation gives easily corrected results, as

will be shown later. The relationship between the end moments M_1 and the horizontal load P of each column is

$$M_1 = PL/2 \tag{5.23}$$

For the cases to be considered here, L equals the column height minus 3/4 inch. Figure 5.9 gives the idealized column section and moment diagram together with the notation used in the following development.

Elastic

The deflection of point B relative to the tangent at point A is equal to

$$X = \int_A^B \frac{M}{EI} \, z dz \tag{5.24}$$

Using the idealized column section and moment diagram, figure 5.9, equation 5.24 can be evaluated to be

$$X = \frac{M_1}{EI_1}\left(\frac{\ell_1}{\ell_1+\ell_2}\right)\left[2\ell_2\ell_1 + \frac{2}{3}\ell_1^2 + 2\ell_2^2\right] + \frac{M_1}{EI_2}\left(\frac{\ell_2}{\ell_1+\ell_2}\right)\left[\frac{2}{3}\ell_2^2\right] \tag{5.25}$$

With

$$L/2 = \ell_1+\ell_2 \qquad \text{and} \qquad \frac{2M_1}{L} = P = \frac{M_1}{\ell_1+\ell_2} \tag{5.26}$$

equation 5.25 becomes

$$X = \frac{P}{EI_1}\,\ell_1\left[\frac{2}{3}\ell_1^2 + 2\ell_1\ell_2 + 2\ell_2^2\right] + \frac{P}{EI_2}\left[\frac{2}{3}\ell_2^3\right] \tag{5.27}$$

Equation 5.27 can be used to calculate the stiffness when the stiffness is defined as

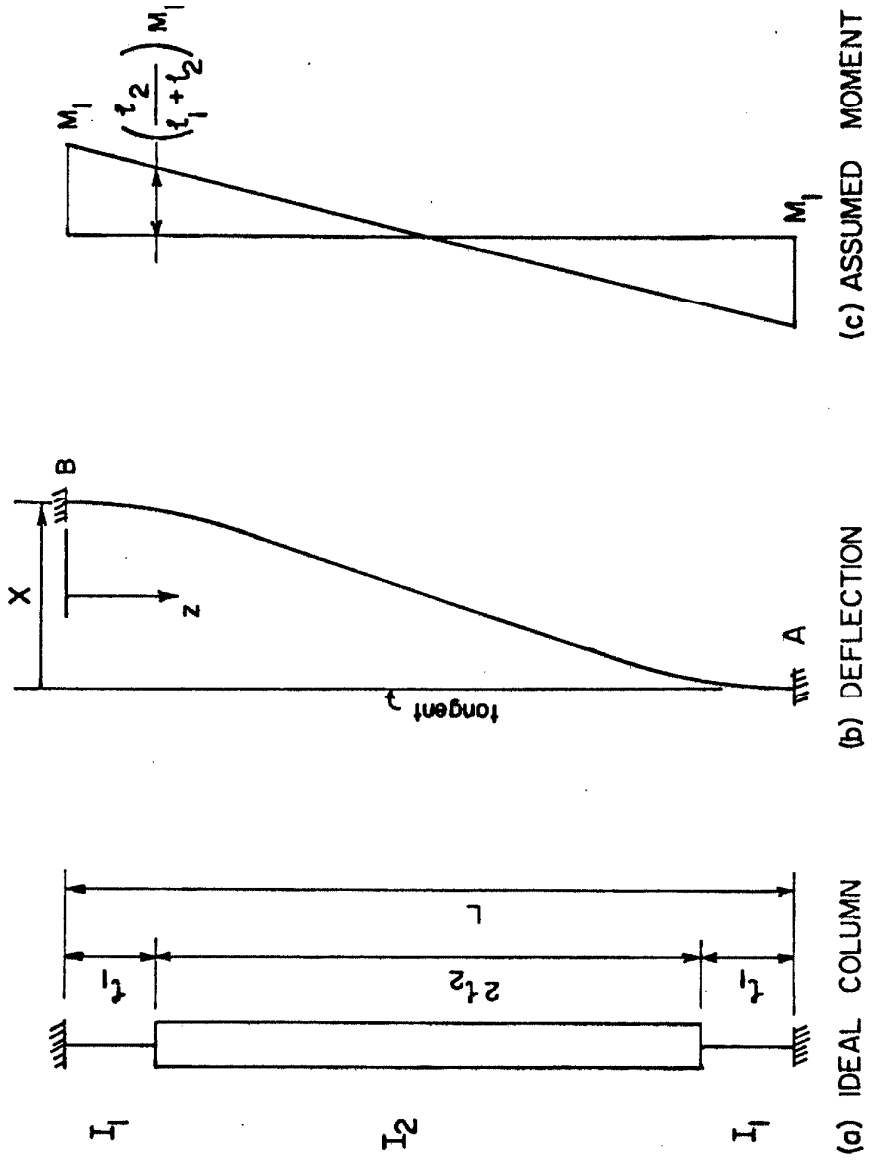

FIG. 5.9 COLUMN NOTATION

$$K = \frac{P}{X} \tag{5.28}$$

For a numerical example, the values for the short columns (E-W) will be used. The column height is approximately 24.91 inches therefore, L = 24.16 inches with ℓ_1 = 4.25 and ℓ_2 = 7.83 inches. The moments of inertia are I_1 = 0.0463 in.^{4} and I_2 = 1.530 in.^{4} with $E = 29.1 \times 10^6$ psi from the results of the tensile tests reported in Appendix II. Thus, the stiffness of one column can be evaluated to be

$$K_1 = \frac{29.1 \times 10^6}{18.64 \times 10^3} = 1561 \text{ pounds/in.} \tag{5.29}$$

or for all four columns

$$K = 6244 \text{ lbs./in.} \tag{5.30}$$

Assuming a yielding stress of 40,000 psi as determined in the tensile tests, the deflection of the structure at initial yielding of the column section can be determined. Using

$$M_{e\ell} = \sigma_{e\ell} \frac{I}{c} = 7450 \text{ in.-lbs.}$$

with equation 2.53,

$$P_{e\ell} = 616 \text{ lbs. per column} \tag{5.31}$$

$$X_{e\ell} = 0.394 \text{ inch}$$

for initial yield. The undamped natural frequency can be calculated assuming the structure acts as a single-degree-of-freedom oscillator to be

$$f_n = \frac{\omega_n}{2\pi} = \frac{1}{2\pi}\sqrt{\frac{Kg}{W}} \tag{5.32}$$

where f_n is the undamped natural frequency in cps, ω_n is the

circular frequency in radians per second, K is the stiffness of the structure in lbs./in., and W is the entire effective weight supported by the columns.

Post Elastic

In calculating the deflection of the structure in the non-elastic range, two distinct column regions were considered. They were the region which was always elastic, I_2, and the region which could yield, I_1. The column regions were assumed symmetrical. Using the notation as defined in figure 5.10, it can be seen that the deflection of the structure is equal to

$$X = 2\left[\ell_2 \sin(\theta_1 + \theta_2) - Y_2 \cos(\theta_1 + \theta_2) + Y_1 \right] \tag{5.33}$$

θ_1 and Y_1 were the only terms which were affected by yielding. Assuming the bending moment distribution as shown in figure 5.9(c), Y_2 and θ_2 can be calculated

by $$\theta_2 = \int_A^B \frac{M}{EI}\, dz \tag{5.34}$$

and $$Y_2 = \int_A^B \frac{M}{EI}\, z\, dz \tag{5.35}$$

where z is measured from A in figure 5.10. θ_1 is equal to the sum of all elemental curvatures occurring from B to C or

$$\theta_1 = \int_B^C \theta(z)\, dz \tag{5.36}$$

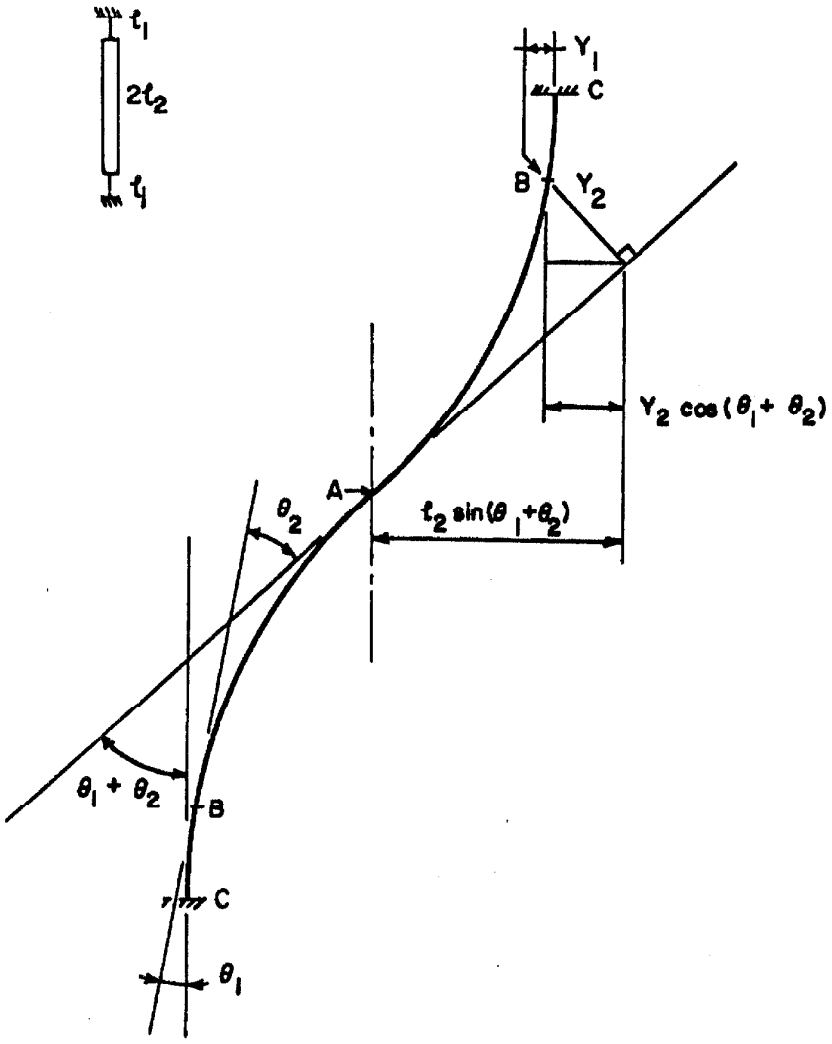

FIG. 5.10 COLUMN DEFLECTION

and again similar to equation 5. 35

$$Y_1 = \int_B^C \theta(z)\, z\, dz \tag{5. 37}$$

where z is measured from B in figure 5. 10. Applying these results to Case I was trivial and gave results identical to those previously obtained for the elastic deflection.

For Case II:

$$\theta_2 = \frac{1}{2} \frac{M_1 \ell_2^2}{(\ell_1 + \ell_2) EI_2} \tag{5. 38}$$

$$Y_2 = \frac{1}{3} \frac{M_1}{\ell_1 + \ell_2} \frac{\ell_2^3}{EI_2} \tag{5. 39}$$

$$\theta_1 = \int_0^{z_{e\ell}} \left(\frac{M_1}{\ell_1+\ell_2}\right)\left(\frac{\ell_2+z}{EI_1}\right) dz + \int_{z_{e\ell}}^{\ell_1} \theta_{e\ell} \sqrt{\frac{1}{3-2\left(\frac{\ell_2+z}{\ell_1+\ell_2}\right)\frac{M_1}{M_{e\ell}}}}\, dz \tag{5. 40}$$

and

$$Y_1 = \int_0^{z_{e\ell}} \left(\frac{M_1}{\ell_1+\ell_2}\right)\left(\frac{\ell_2+z}{EI_1}\right) z\, dz + \int_{z_{e\ell}}^{\ell_1} \theta_{e\ell} \sqrt{\frac{1}{3-2\left(\frac{\ell_2+z}{\ell_1+\ell_2}\right)\frac{M_1}{M_{e\ell}}}}\, z\, dz \tag{5. 41}$$

In addition to illustrating the application of the preceding formulae, a numerical example will give the theoretical deflection skeleton curve to compare with an experimental skeleton curve. Column set SI (E-W) will be used again, with the additional numerical values of $\epsilon_{e\ell} = 0.0014$, $\sigma_{e\ell} = 40,000$ psi, $M_{e\ell} = 7450$ in. -lbs. and $X_{e\ell} = 0.394$ inch. First, consider the limiting ranges of Case II: Lower limit, i.e.,

the elastic case. $z_{e\ell} = \ell_1$, $M_1 = M_{e\ell}$, $(\ell_1 + \ell_2) - 12.08$, $\ell_1 = 4.25$, $\ell_2 = 7.83$, $I_2 = 1.530$, $I_1 = 0.0463$. From equations 5.38 through 5.41,

$$\begin{aligned} \theta_2 &= 0.00042, \quad Y_2 = 0.00221 \text{ inch} \\ \theta_1 &= 0.01934, \quad Y_1 = 0.04401 \text{ inch} \end{aligned} \tag{5.42}$$

Substitution into equation 5.33 yields

$$X = X_{e\ell} = 0.394 \text{ inch} \tag{5.43}$$

The material is not perfectly elastic up to yield. Therefore, an average value of the yield strain will be used to determine a new E for section ℓ_1. On this basis

$$\begin{aligned} \epsilon_{e\ell} &= 0.00142 \\ E_1 &= 28.6 \times 10^6 \text{ psi} \end{aligned} \tag{5.44}$$

and

$$E_2 = 29.1 \times 10^6 \text{ psi} \tag{5.45}$$

This gives a new deflection at yield equal to

$$X = X_{e\ell} = 0.406 \text{ inch} \tag{5.46}$$

which should be more realistic.

The other limiting condition for case II is $\epsilon_c = 10\ \epsilon_{e\ell}$ and $y_{e\ell} = c/10$. This gives

$$\begin{aligned} M_1 &= 1.495\ M_{e\ell} \\ z_{e\ell} &= 0.25 \text{ inch} \end{aligned} \tag{5.47}$$

From equations 5.38 through 5.41,

$$\begin{aligned} \theta_1 &= 0.04291 \qquad Y_1 = 0.11606 \\ \theta_2 &= 0.00064 \qquad Y_2 = 0.00333 \end{aligned} \tag{5.48}$$

Substitution of equation 5. 48 into equation 5. 33 yields

$$X = 0.906 \text{ inch} \tag{5.49}$$

The horizontal force P required on the structure is four times that required for one column. Thus, from equation 5. 23, the horizontal load P of the structure is

$$P = 8 M_1/L \tag{5.50}$$

For a deflection of 0. 906 inch, P = 3690 pounds. Other values of X and P are calculated in a similar way. The skeleton curve will be plotted later.

From the calculations made above, a plot of the structural deflection versus the ratio of the maximum strain to yield strain can be made. This plot is given in figure 5. 11 for the short columns (E-W) and the long columns (N-S) both with and without including the effect of strain hardening. It can be seen from figure 5. 11 that the effect of the strain hardening is to decrease the maximum strain associated with a given deflection below the maximum strain which would exist without strain hardening. This effect is caused by a shift of the yielding rotation section from the ends toward the center of the column. In other words, the effect of the strain hardening is to produce more yielding material without significant increases in the applied force. The decrease in the maximum strain, for a given deflection, is an important factor when considering the fatigue life of the member.

No apparent differences in the theoretical force-deflection curves of the structure with and without strain hardening can be

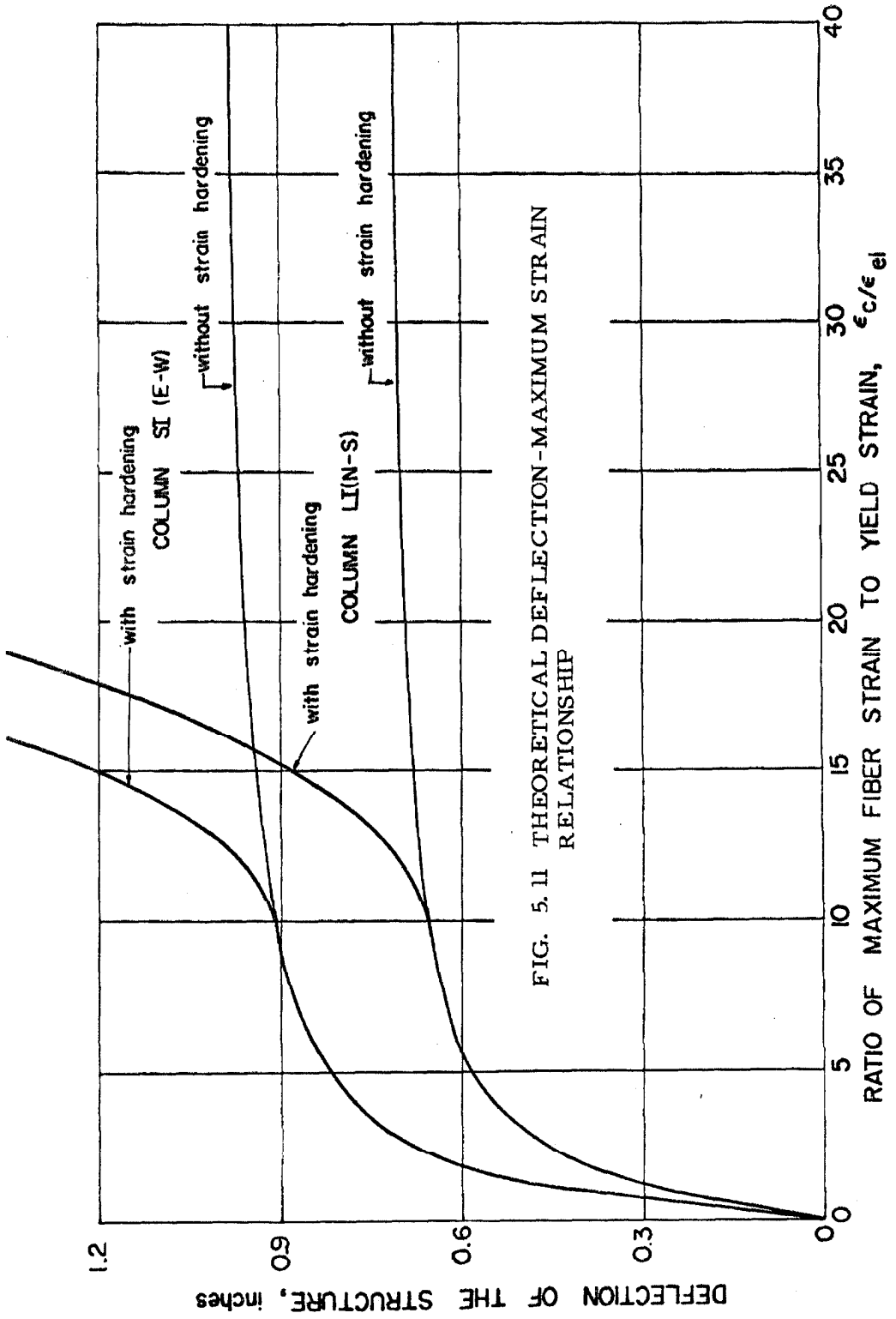

FIG. 5.11 THEORETICAL DEFLECTION-MAXIMUM STRAIN RELATIONSHIP

noted at the deflections used.

Checking the Assumptions

The major assumptions used in the simplified theory should be checked with the actual conditions in order to estimate the accuracy of the calculated numerical values. Consider the conditions indicated by figure 5.12(a) where *all four columns are identical and symmetrical* about the center line of their height, L. Due to this symmetry, the moments at the top and bottom must be equal in magnitude. Using the free body diagrams shown in figures 5.12(b) and 5.12(c),

$$P(a + L) - 4M_1 - 2VS + WX = 0 \qquad (5.51)$$

$$P\,a + 4M_1 - 2VS = 0 \qquad (5.52)$$

Subtracting equation 5.52 from 5.51 results in

$$8M_1 = PL + WX \qquad (5.53)$$

which is the moment at each column end, and for small deflections, it is the same as equation 5.50. By adding equations 5.51 and 5.52

$$4VS = P(2a + L) + WX \qquad (5.54)$$

in which V is the vertical column load due to the deflection and the horizontal force P. Measuring the column horizontal displacement, x, from the fixed column position at the base plate, the general moment in the column is found to be

$$M = M_1 - Pz/4 \pm P(2a + L)\,x/4S - Wx/4 \qquad (5.55)$$

The above expression is valid for any one column. However, since all four columns must have the same deflection X and this deflection specifies the value of M_1, the effect of the ± term in the expression

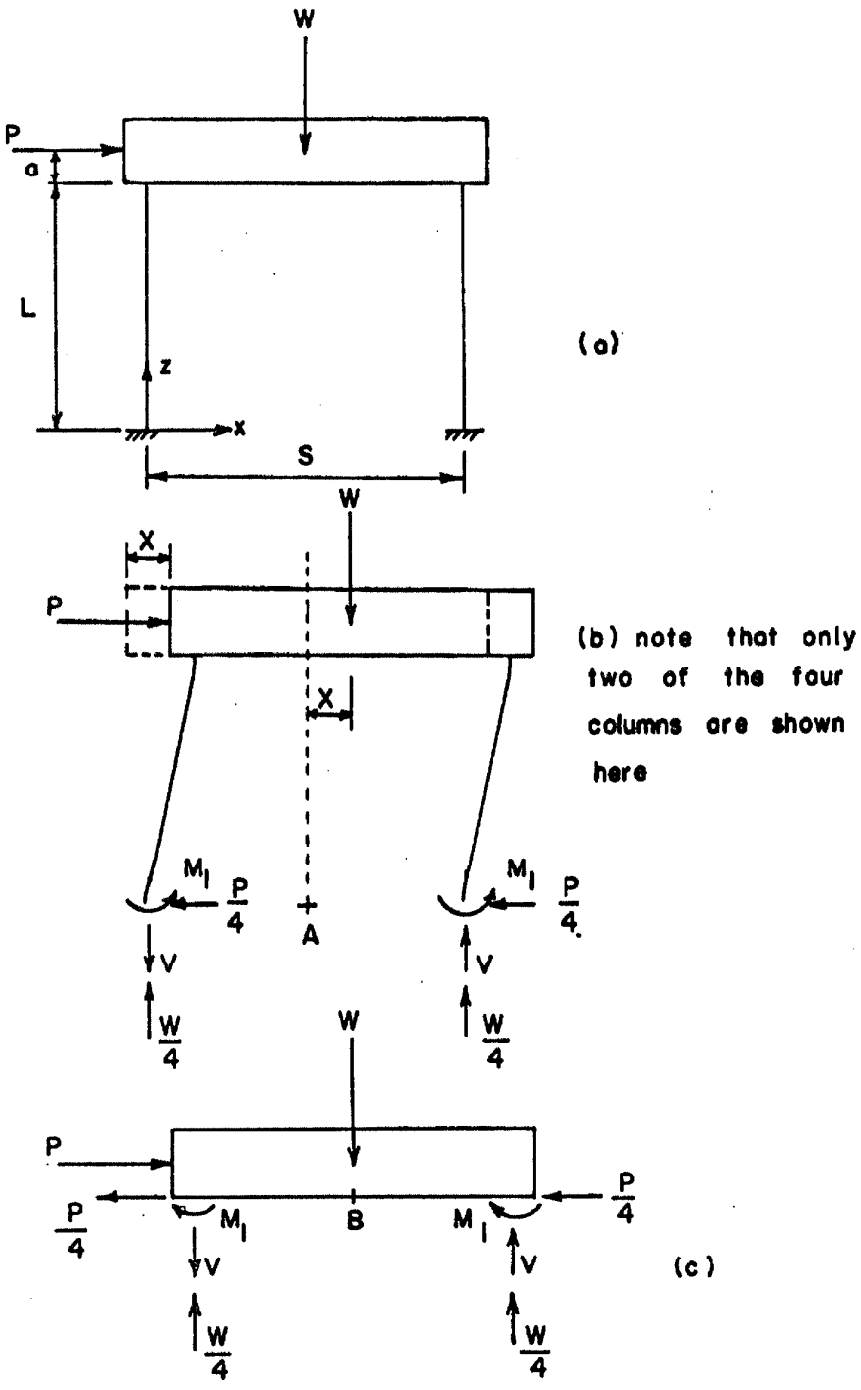

FIG. 5.12 FREE BODY DIAGRAMS

for M is to distribute the horizontal force P in unequal proportions to the columns. This can be stated mathematically as

$$P^*L/8 \pm P^*X(2a + L)/8S = PL/8 \qquad (5.56)$$

where P^* is a portion of the total horizontal force P which goes to that particular column. Using equations 5.56 and 5.53 to determine P^* and M_1, equation 5.55 can be used for the general moment when P^* replaces P.

The displacement of the column is not linear with height, but rather has a characteristic as indicated in figure 5.13(a). For this reason the correction terms of the general moment are not linear with height. However, since the correction terms are second order effects, they will be approximated by a linear function such that

$$x = X\,z/L \qquad (5.57)$$

With this linear approximation of the correction terms, the only moments needed to be calculated are the end moments given by equation 5.53.

The total horizontal force determined by this linearized correction is

$$P' = (8M_1 - WX)/L \qquad (5.58)$$

In terms of the previously determined value P,

$$P' = P - WX/L \qquad (5.59)$$

The column stiffness must also be corrected to be

$$K' = P/X - W/L = K - W/L \qquad (5.60)$$

It was also assumed that the stress-strain relationship derived from the tension tests could be applied directly to the

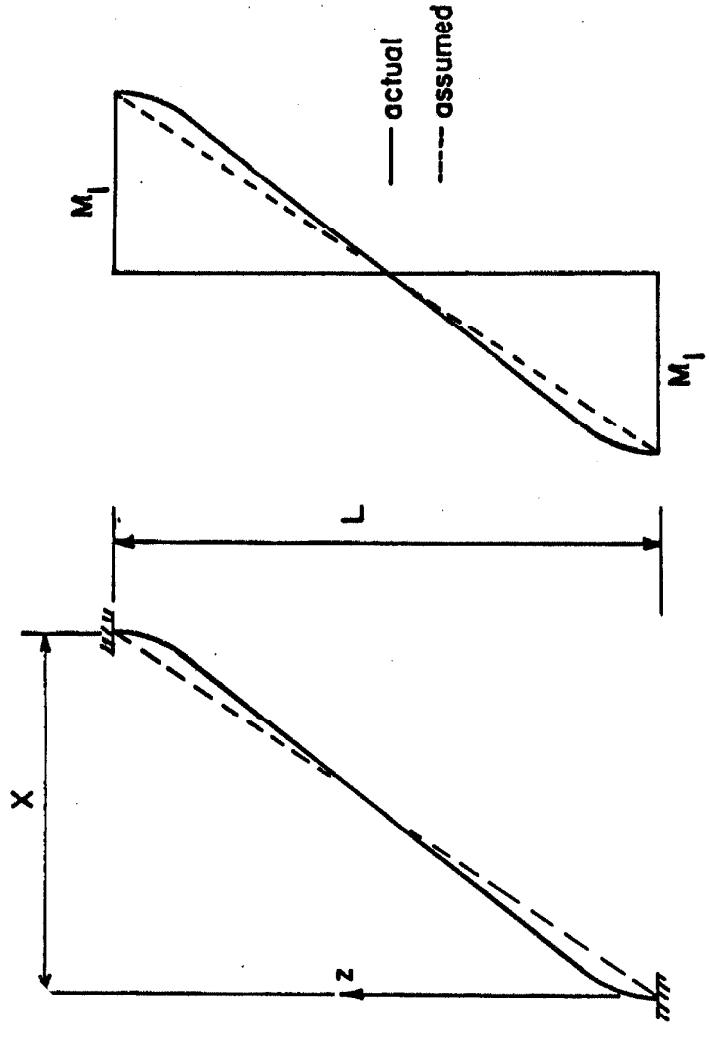

FIG. 5.13 EFFECT OF COLUMN DEFLECTION

conditions of this test. Since normal and shear stresses are acting at the column section in addition to the flexural stresses, it is important to check the magnitudes of these stresses and to determine their effect upon the previous calculations. Among the factors Neal[40] discusses which affect the full plastic moment, neglecting strain hardening, are the normal stress and the shear stress. Using the formulae presented there for normal stress, the ratio of the corrected plastic moment to the original plastic moment is

$$M_N/M_p = 1-(N/N_p)^2 \tag{5.61}$$

for a rectangular section, where N is the normal force and N_p is the area of the section times the yield stress. Similarly for the shear stress factor for a rectangular section,

$$M_F/M_p = 1-0.44\,(F/F_p)^2 \tag{5.62}$$

for $F/F_p \leq 0.79$, where F_p is the one half the area of the section times the yield stress and F is the shear force. Using the same numerical constants for the short columns as previously determined,

$$\begin{aligned} N_p &= 89,700 \text{ lbs.} \\ F_p &= 44,850 \text{ lbs.} \\ N &= W/4 \approx 1200 \text{ lbs.} \end{aligned} \tag{5.63}$$

and

$$F = P/4 \approx 940 \text{ lbs.}$$

This gives

$$\begin{aligned} N/N_p &= 0.0134 \\ (N/N_p)^2 &= 0.00018 \end{aligned} \tag{5.64}$$

which corresponds to a change in the plastic moment of less than 0.02 percent due to normal stresses. For the shear stresses,

$$F/F_p = 0.021$$
$$(F/F_p)^2 = 0.000194 \qquad (5.65)$$

which also corresponds to a change of less than 0.02 percent. Therefore, the assumption to neglect the effects of the normal and shear stresses upon the plastification of the column section is valid.

An alternate method of determining the combined effect of the normal and shear stresses upon the yield stress of the column section is as follows: The second stress invariant expressed in terms of the distortional stresses only is

$$I_2' = \frac{1}{3}(\sigma_x - \sigma_y)^2 + \frac{1}{3}(\sigma_y - \sigma_z)^2 + \frac{1}{3}(\sigma_z - \sigma_x)^2 + \frac{1}{3}\tau_{xy}^2 + \frac{1}{3}\tau_{yz}^2 + \frac{1}{3}\tau_{zx}^2 \qquad (5.66)$$

where σ_x, σ_y, σ_z are normal stresses in the x, y, z directions and τ_{xy}, τ_{yz}, τ_{zx} are shearing stresses. The Hencky-Mises yield condition equates this second stress invariant to a constant which can be evaluated from the tension tests. The resulting flexural stress for the yield condition will be determined.

For axial tension tests, $\sigma_x = \sigma_{e\ell}$ at yield and $\sigma_y = \sigma_z = \tau_{xy} = \tau_{yz} = \tau_{zx} = 0$. The stress invariant constant for the yield condition can be evaluated from equation 5.66 to be

$$I_2' = \text{constant} = \frac{2}{3}\sigma_{e\ell}^2 \qquad (5.67)$$

Using the directions indicated in figure 5.1 where the moment acts about the x axis and the shear load acts in the y direction, the resulting stresses can be determined[41] when b is large compared

with c to be

$$\sigma_x = \sigma_y = \tau_{xy} = 0$$

$$\sigma_z = Py(L-z)/I + N/A_s$$

$$\tau_{yz} = P(c^2-y^2)/2I\,(1+\upsilon) \qquad (5.68)$$

$$\tau_{zx} = Pxy\,\upsilon\,/I\,(1+\upsilon)$$

where P is the shear force, N is the axial force, A_s is the cross sectional area, and υ is Poisson's ratio. Let

$$\sigma = Py(L-z)/I \qquad (5.69)$$

The maximum shear stress from elementary theory is $3P/2A_s$. Timoshenko and Goodier[41] have developed appropriate magnification factors to use for various values of b/c. First, consider column LI at initial yield

$$\text{compression } \frac{N}{A_s} = 2400 \text{ psi}, \quad \frac{3}{2}\frac{P}{A_s} = 1500 \text{ psi}$$

and

$$b/c = \frac{1}{2} \qquad (5.70)$$

The magnification factors result in

$$\tau_{yz} = 1.1\ \frac{3}{2}\frac{P}{A_s} \quad \text{and} \quad \tau_{xz} = 0.10\ \frac{3}{2}\frac{P}{A_s} \qquad (5.71)$$

Substituting these results into equations 5.66 and 5.67 yields

$$\frac{2}{3}(\sigma + 2400)^2 + \frac{1}{3}(1650)^2 + \frac{1}{3}(150)^2 = \frac{2}{3}\sigma_{e\ell}^2$$

or

$$\left(\frac{\sigma}{\sigma_{e\ell}} + \frac{2400}{\sigma_{e\ell}}\right)^2 + \frac{1}{2}\left(\frac{1650}{\sigma_{e\ell}}\right)^2 + \frac{1}{2}\left(\frac{150}{\sigma_{e\ell}}\right)^2 = 1 \qquad (5.72)$$

Since $\sigma_{e\ell} = 40,000$ psi

$$\frac{1}{2}\left(\frac{1650}{\sigma_{e\ell}}\right)^2 \approx 0.00085 \qquad (5.73a)$$

$$\frac{1}{2}\left(\frac{150}{\sigma_{e\ell}}\right)^2 \approx 7 \times 10^{-6} \qquad (5.73b)$$

and

$$\left(\frac{2400}{\sigma_{e\ell}}\right) \approx 0.060 \qquad (5.73c)$$

The values of 5.73(a) and 5.73(b) can be neglected which means that the effect of the shear stress on yielding is negligible. The flexural stress required to initiate yielding in compression can be seen from 5.73(c) and 5.72 to be about 6 percent below the tensile yield value. The effect on the full plastic moment for a rectangular section assuming an elasto-plastic stress-strain relationship can be shown to be the same as equation 5.65.

The corresponding values of equation 5.70 for SI are

$$\text{compression } \frac{N}{A_s} = 535 \text{ psi}, \quad \frac{3}{2}\frac{P}{A_s} = 430 \text{ psi}$$

and

$$b/c = 18 \qquad (5.74)$$

The magnification factors result in

$$\tau_{yz} = 3.7\ \frac{3}{2}\frac{P}{A_s} \quad \text{and} \quad \tau_{xz} = 3.2\ \frac{3}{2}\frac{P}{A_s} \qquad (5.75)$$

Substituting these results into equations 5.66 and 5.67 yields

$$\frac{2}{3}(\sigma + 535)^2 + \frac{1}{3}(1600)^2 + \frac{1}{3}(1380)^2 = \frac{2}{3}\sigma_{e\ell}^2 \qquad (5.76)$$

Results similar to those for LI are obtained with the exception that the initial yielding stress in compression will be about 1.3 percent

below the tensile yield value.

The last assumption to be checked is that the column ends are rigidly fixed 3/8 inch from the ends of the column, see figure 5.14(a). Since the ASTM 325 proof load is developed with a suggested torque of 100 foot-pounds and the bolts for the structure had torques of 65 and 50 foot-pounds applied to the column top and bottom bolts respectively, it will be assumed that the 1/2 inch diameter bolts are initially tensioned to one-half their proof load of 12,050 lbs. This results in an initial load at the column ends of 24,100 lbs., and which corresponds to a uniformly distributed load across the ends, neglecting the bolt holes, of

$$\text{End stress} = \frac{24,100}{4.5(3.25)} = 1650 \text{ psi} \tag{5.77}$$

If the end sections remained plane, the maximum moment capacity of this end plane without reaching zero stress is

$$M = 13,100 \text{ inch pounds} \tag{5.78}$$

The maximum moment to be expected at this section, considering strain hardening, was for column SI

$$M = \left[\frac{L}{L-\frac{3}{4}}\right] 11,203 = 11,570 \text{ inch-pounds} \tag{5.79}$$

Therefore, the column ends have zero rotation. Figures 5.14(b) and (c) show the actual moments and M/EI diagrams for the end section. Using the idealized M/EI as shown in figure 5.14(d) with a moment equal to 12,000 in.-lbs., the rotation of the tangent at B relative to the tangent at A is

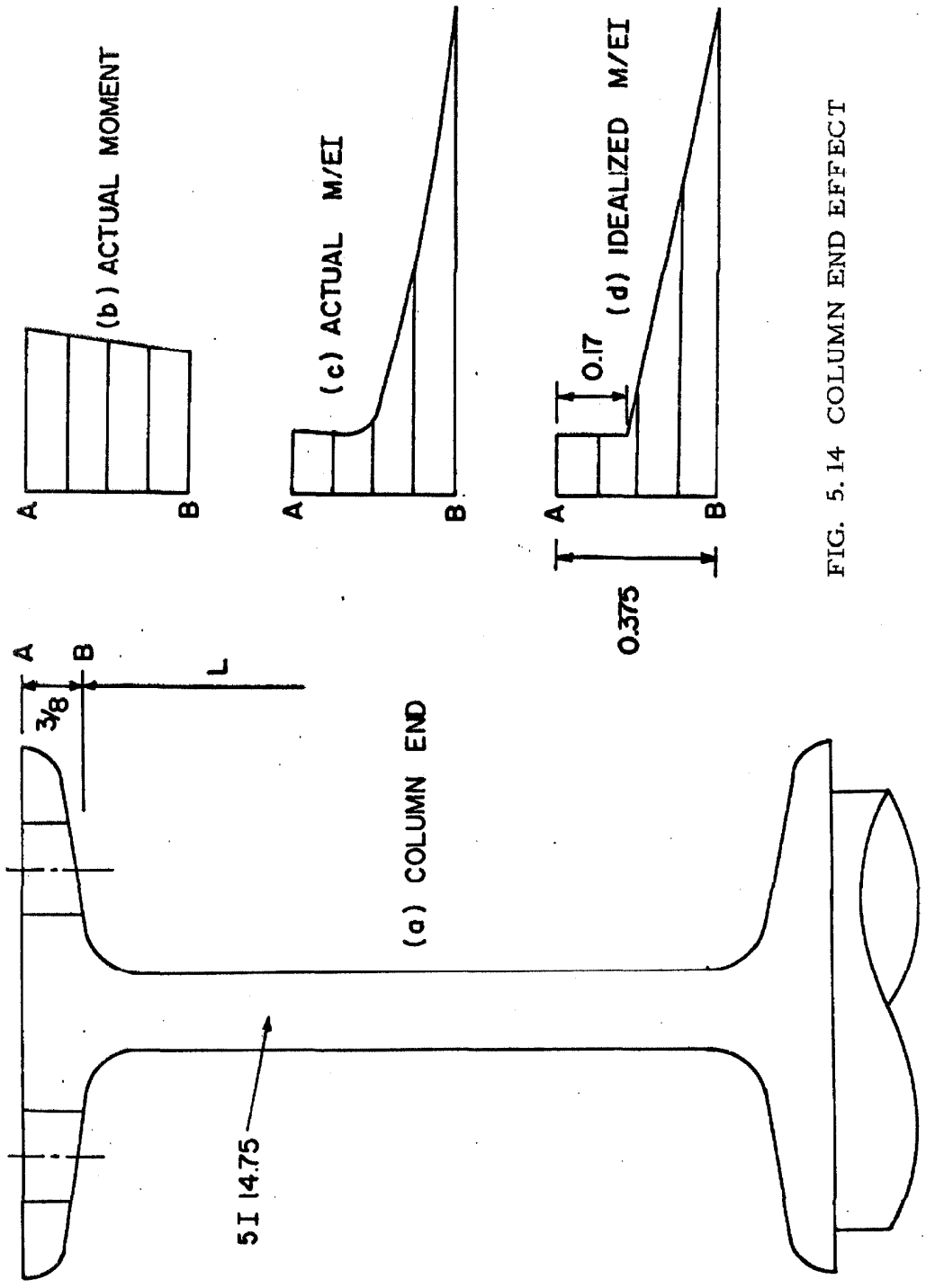

FIG. 5.14 COLUMN END EFFECT

$$\theta_3 = \frac{1}{E}\left[930(.375) + 42,870\left(\frac{.205}{2}\right)\right] = 0.000163 \text{ radians} \quad (5.80)$$

where E equals 29.1×10^6 psi. This corresponds to an additional deflection of

$$(L - \tfrac{3}{4})\,\theta_3 = 0.004 \text{ inch} \quad (5.81)$$

which compared to the previously calculated deflection of about 1.000 inch is less than 1/2%.

Therefore, the assumptions made for this theoretical analysis appear to be justified because of the relatively small errors introduced when the weight of the structure is not neglected. The virgin force-deflection curve of column SI is plotted in figure 5.16 both with and without considering the effect of strain hardening by using equations 5.25, 5.33, 5.38 to 5.41, 5.58, 5.13 and 5.14. The values obtained for a sample calculation are included here for illustration while the actual numerical calculations were made with the Burroughs 220 Datatron digital computer.

The constants required for column SI calculations are

$W = 4038$ pounds	$I_1 = 0.0463 \text{ inch}^4$	
$L = 24.16$ inches	$I_2 = 1.530 \text{ inch}^4$	
$\ell_1 = 4.25$ inches	$EI_1 = 1.3057 \times 10^6$ lbs-inch^2	
$\ell_2 = 7.83$ inches	$EI_2 = 44.37 \times 10^6$ lbs-inch^2	(5.82)
$\epsilon_{e\ell} = 0.00142$	$\sigma_{e\ell} = 40,000$ psi	
$M_{e\ell} = 7450$ inch-lbs.	$\theta_{e\ell} = 0.00570$ 1/inch	

By letting the point to be calculated be associated with $\epsilon / \epsilon_{e\ell} = 13$ with strain hardening

$M_1 = 1.505\, M_{el}$ $\qquad$ $z_{el} = 0.197$

$\theta_2 = 0.0006407$ (5.38) $\qquad$ $Y_2 = 0.003345$ (5.39)

$\theta_1 = 0.04791$ (5.40) $\qquad$ $Y_1 = 0.13660$ (5.41)

$X = 1.0266$ (5.33) $\qquad$ $P' = 3538$ (5.58)

Using equation 5.60 to calculate the column stiffness, equation 5.32 gives the theoretical free vibration natural frequencies listed in Table IV-1.

3. Theoretical Hysteresis Relationship

It will be shown here that the theoretical cyclic hysteresis curves based on column moments can be described by a function equal to two times the virgin force-deflection function with only a shift of the origin and possible change in sign. It is assumed that when the direction of the loading increment is changed, the original stress-strain relationship is valid. This assumption is illustrated in figure 5.15 where the stress and strain conditions at the final virgin curve point are given in figure 5.15(a). If in addition to the conditions given in figure 5.15(a) a new moment M_2 in the opposite direction is applied, figure 5.15(b), then the resulting stress and strain condition is given in figure 5.15(c). From this it can be seen that the stresses and strains are directly additive algebraically. Since the stress associated with M_2 is to be added algebraically to the stress associated with M_{max}, it can be seen from figure 5.15 that the M_2 stress limit has to be twice the yield stress in order to produce a resulting reversed limit stress equal to the yield stress.

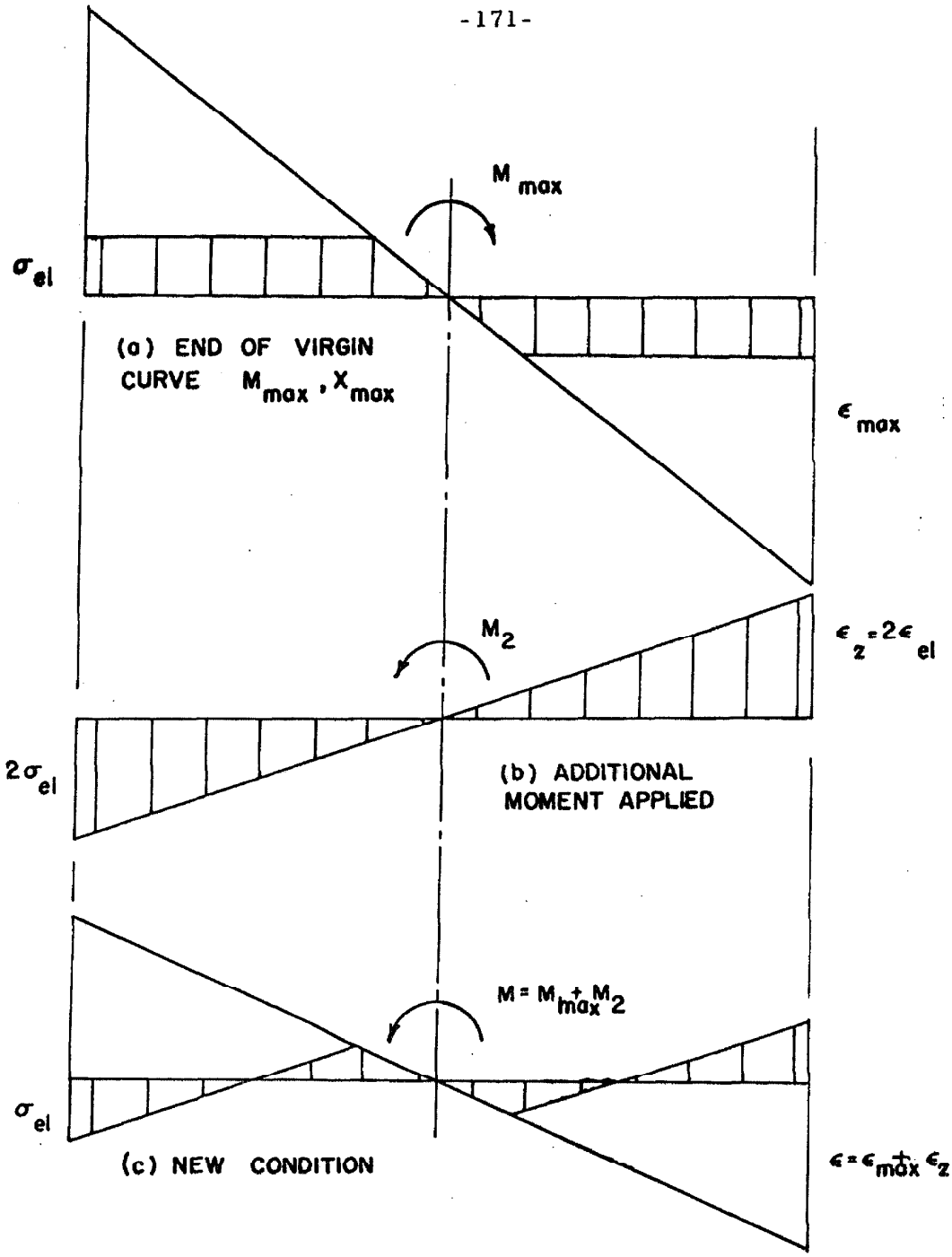

FIG. 5.15 HYSTERESIS CONDITION

The limit of the cyclic hysteresis curve is associated with $-M_{max}$ or in other words, $M_2 = -2M_{max}$. This condition can only be achieved when $\epsilon = \epsilon_{max} - \epsilon_2 = -\epsilon_{max}$. This means that the elastic portions of the structure at M_{max} continue to be elastic throughout the entire cycle. Selecting the new moment and deflection origin at M_{max}, X_{max} with axes M_2 and X_2, the problem reduces to the determination of X_2.

Since the elastic portions of X_2 are equal to M_2/M_{max} times the corresponding elastic value of X_{max}, only the nonlinear portions of the deflection have to be considered in detail. From figure 5.15(a)

$$M_{max} = \frac{3}{2} M_{e\ell} \left[1 - \frac{1}{3} \left(\frac{\epsilon_{e\ell}}{\epsilon_{max}} \right)^2 \right] \tag{5.83}$$

As was mentioned above, the new stress limit for yielding is $2\sigma_{e\ell}$ and similarly the new strain is $2\epsilon_{e\ell}$ when considering M_2. Therefore,

$$M_2 = 3M_{e\ell} \left[1 - \frac{4}{3} \left(\frac{\epsilon_{e\ell}}{\epsilon_2} \right)^2 \right] \tag{5.84}$$

or in general $M_2(z) = M_2 (\ell_2 + z/\ell_1 + \ell_2)$ for the column and

$$\frac{\epsilon}{\epsilon_{e\ell}} = \frac{2}{\sqrt{3 - \frac{M_2}{M_{e\ell}} \left(\frac{\ell_2 + z}{\ell_1 + \ell_2} \right)}} \tag{5.85}$$

With equations 5.10 and the second terms of equations 5.36 and 5.37, there results

$$ {}^{2}\theta_1 \text{ (for } M_2(z)) = \int_{z_{e\ell}}^{\ell_1} \theta_{e\ell} \frac{2}{\sqrt{3-2\frac{M_2}{M_{e\ell}}\left(\frac{\ell_2+z}{\ell_1+\ell_2}\right)}}\, dz \qquad (5.86) $$

and

$$ {}^{2}Y_1 \text{ (for } M_2(z)) = \int_{z_{e\ell}}^{\ell_1} \theta_{e\ell} \frac{2z\,dz}{\sqrt{3-2\frac{M_2}{M_{e\ell}}\left(\frac{\ell_2+z}{\ell_1+\ell_2}\right)}} \qquad (5.87) $$

which can be compared with the second terms of equations 5. 40 and 5. 41. If $M_2 = {}^{2}M_{max}$ is substituted into equations 5. 86 and 5. 87 and into the elastic terms, then it is found that

$$ X_2 = 2X_{max} \qquad (5.88) $$

Thus, it has been shown that the hysteresis curve is just twice as large as the virgin curve based on column moments.

Since equation 5. 58 contains the term X which is not independent of the selected origin, the above discussion is not valid for the force-deflection curves. However, the correction associated with the weight term is easily determined and has been made for all plotted theoretical force-deflection curves.

In addition to the theoretical virgin force-deflection curve and a section of the hysteresis curve, figure 5. 16 also includes the experimental virgin curve for column SI taken from figure 4. 28. Strain hardening theoretical data were used. However, it should be mentioned again that at this deflection no visible differences between the theoretical force-deflection curves with and without strain

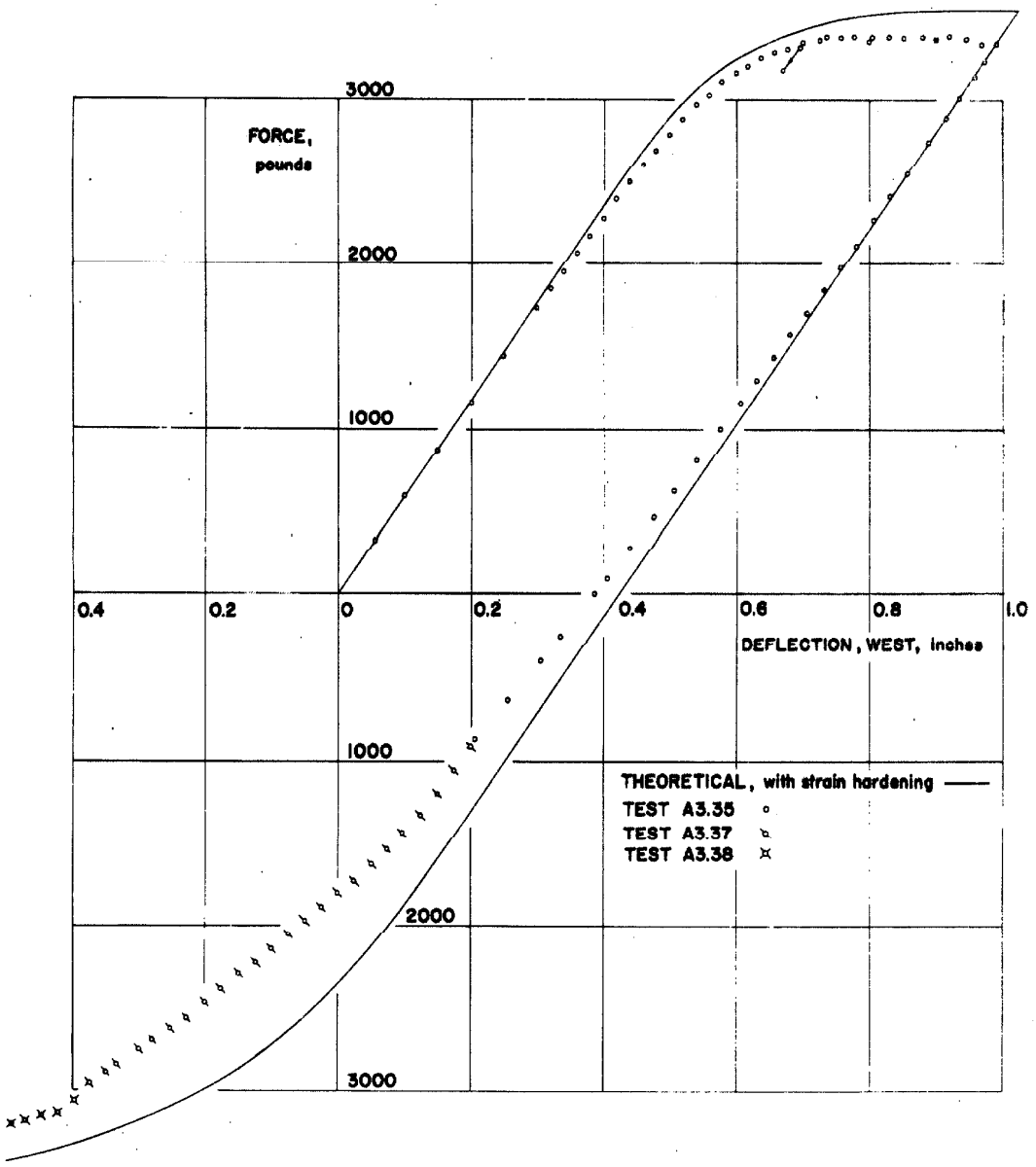

FIG. 5.16 VIRGIN FORCE-DEFLECTION CURVE

hardening occurred. The theoretical and experimental curves have the same general appearance but the theoretical curve overestimates the horizontal force.

Assuming the above column properties are equally valid for column set SIII, the theoretical force-deflection hysteresis curves were calculated for the maximum deflections of 0.420, 0.635 and 0.810 inch with the effective weight of the structure for these calculations taken as 4731 pounds. These curves are plotted in figure 5.17 together with the results of the dynamic tests A3.57, A3.63 and A3.64. The areas of the theoretical curves are given in Table IV-4 with the areas of the static and dynamic experimental curves. Figures 4.49, 4.50 and 4.51 can be used in conjunction with figure 5.17 to compare other experimental static or dynamic curves with the theoretical curves.

The two major discrepancies in the theoretical force-deflection relationship are the overestimation of the force required for a specific deflection and the corresponding errors in the theoretical area of the hysteresis curve. The reasons for these deficiencies will be explored in Part B of this chapter.

4. Theoretical Dynamic Response According to Jennings [28]

4a. Introduction. The analysis of the theoretical dynamic response of a yielding structure must be based upon a specification of the force-deflection relations for an arbitrary sequence of imposed deflections. A general formula is presented for virgin force-

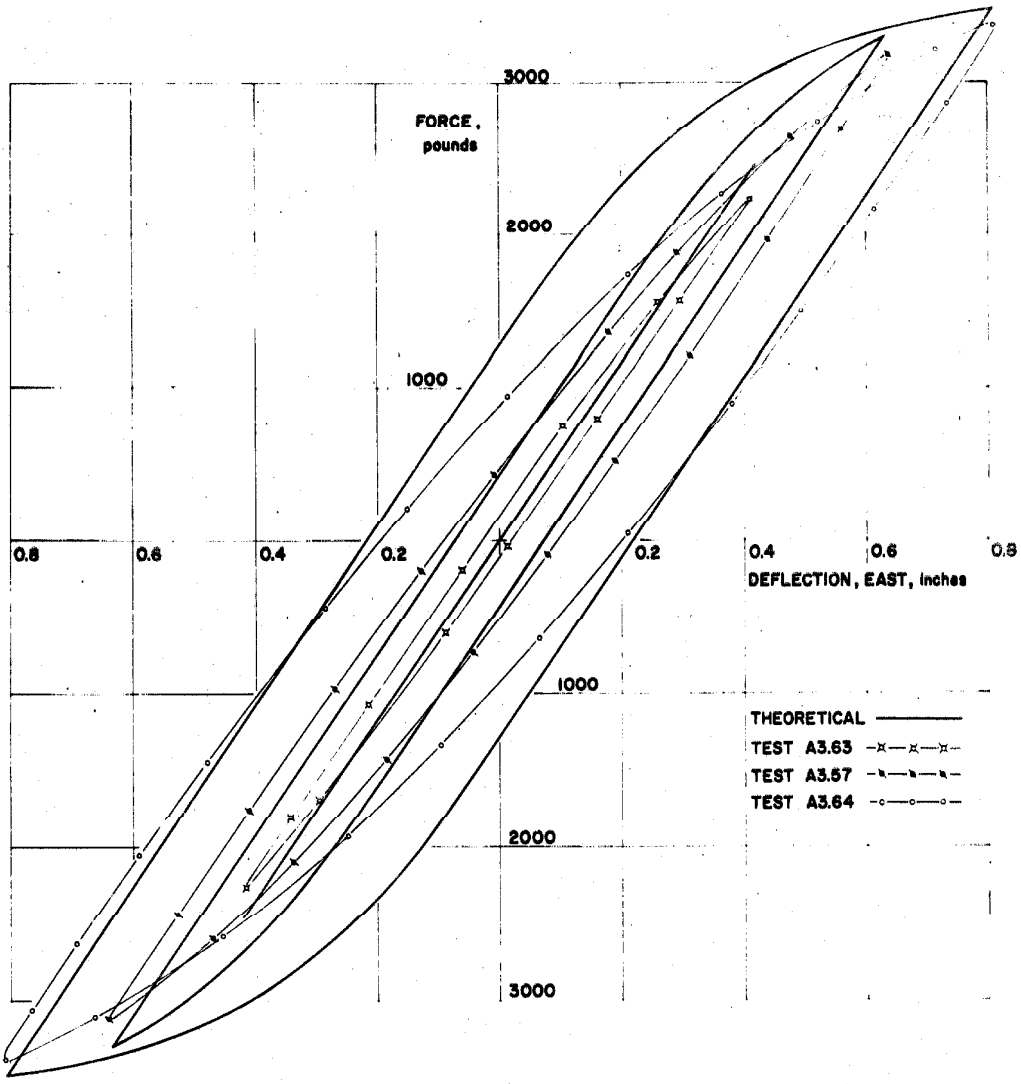

FIG. 5.17 COMPARISON OF THEORETICAL AND DYNAMIC HYSTERETIC FORCE-DEFLECTION CURVES

deflection (skeleton) curves of the softening type which are symmetric about the origin, and which can be considered linear for small deflections. The skeleton curves of the general force deflection relationship presented here are described by the equation

$$\frac{x}{x_y} = \frac{p}{p_y} + \alpha\left(\frac{p}{p_y}\right)^r \qquad (5.89)$$

where x is the displacement of the structure, x_y is a characteristic displacement, p is the restoring force, p_y is a characteristic force, α is a positive constant, and r is a positive odd integer greater than one. If only real numbers are considered, there is always a one-to-one correspondence between force and displacement in equation 5.89.

Some of the curves described by equation 5.89 are shown in figure 5.18; in view of the symmetry about the origin only the positive portions of the curves are given. From the figure and from equation 5.89 it is seen that a wide range of softening systems can be represented by this relationship. In particular, a linear characteristic is described by $\alpha=0$ and an elastic-plastic characteristic is approached as r tends to ∞. Examination of equation 5.89 shows that this tendency to an elastic-plastic characteristic for large r occurs for all values of α greater than zero.

To find the values of r and α that give the best fit between equation 5.89 and experimental data, a logarithmic plot may be made of the departure from linearity of the deflection versus the applied force. From equation 5.89 it is seen that the logarithm of the departure from linearity is $\log\alpha + r \log(p/p_y)$. Thus, α and r are

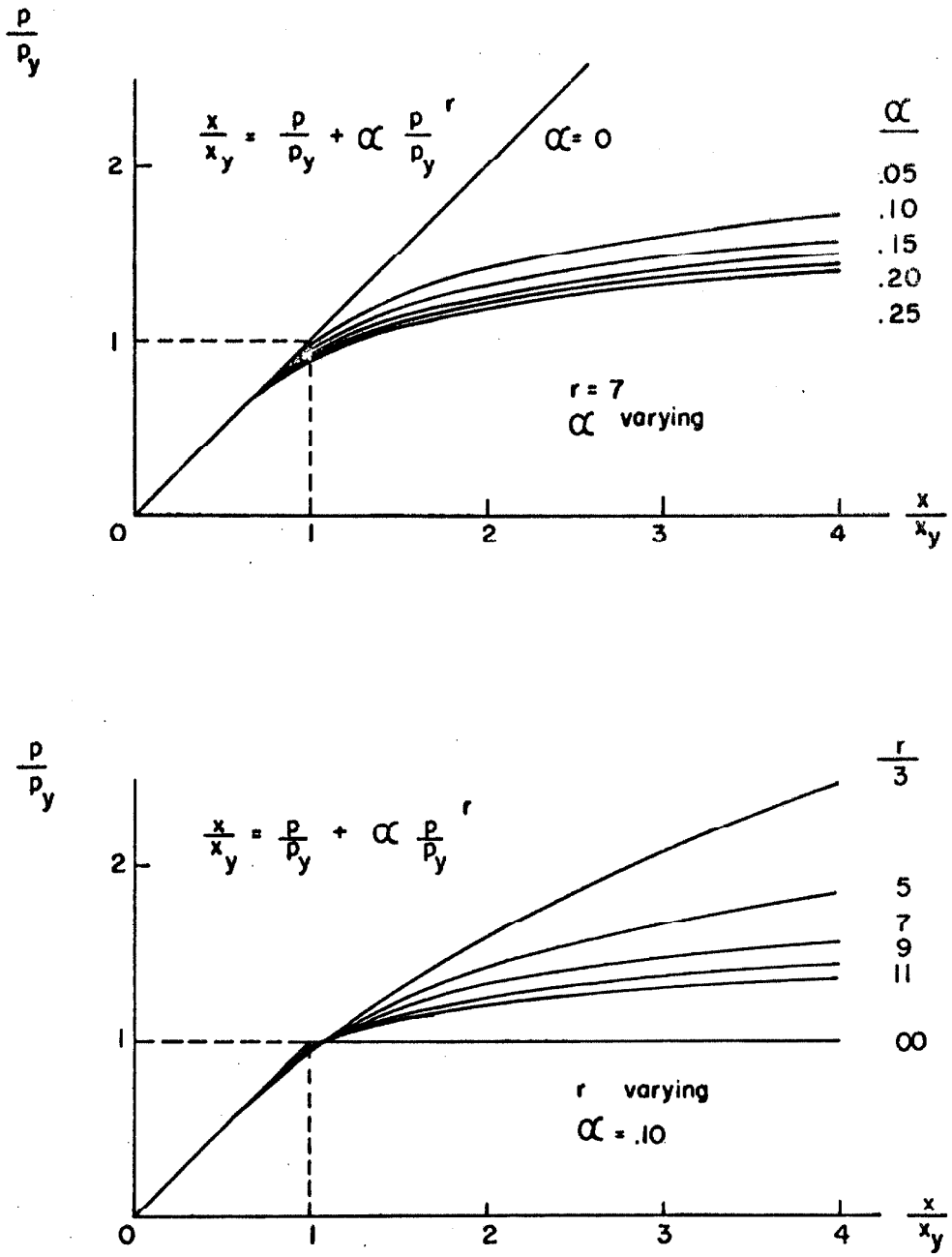

FIG. 5.18 EXAMPLES OF SKELETON CURVES DESCRIBED BY EQUATION 5.89

the intercept and the slope of the straight line which fits best the data of this logarithmic plot.

The hysteretic behavior of the structure with a skeleton curve given by equation 5. 89 is described by

$$\frac{x-x_i}{2x_y} = \frac{p-p_i}{2p_y} + a\left(\frac{p-p_i}{2p_y}\right)^r \tag{5.90}$$

where the point $(x_i/x_y,\ p_i/p_y)$ is the most recent point at which the direction of the loading has been reversed. Applying this equation to a hysteresis loop describing cyclic loading between $(x_o/x_y,\ p_o/p_y)$ and $(-x_o/x_y,\ -p_o/p_y)$ gives for the ascending branch of the loop

$$\frac{x+x_o}{2x_y} = \frac{p+p_o}{2p_y} + a\left(\frac{p+p_o}{2p_y}\right)^r \tag{5.91}$$

where, in the region where equation 5. 91 applies, $x + x_o$ and $p + p_o$ are never negative. The descending branch of the hysteresis loop is given by

$$\frac{x-x_o}{2x_y} = \frac{p-p_o}{2p_y} + a\left(\frac{p-p_o}{2p_y}\right)^r \tag{5.92}$$

and in the region of application $x-x_o$ and $p-p_o$ are never positive. The general hysteresis loop described by equations 5. 91 and 5. 92 and the skeleton curve of equation 5. 89 are shown in figure 5. 19.

4b. Amplitude of Steady-State Response. When steady-state response is achieved, the energy dissipated per cycle must equal the amount of energy input per cycle and it follows that[28]

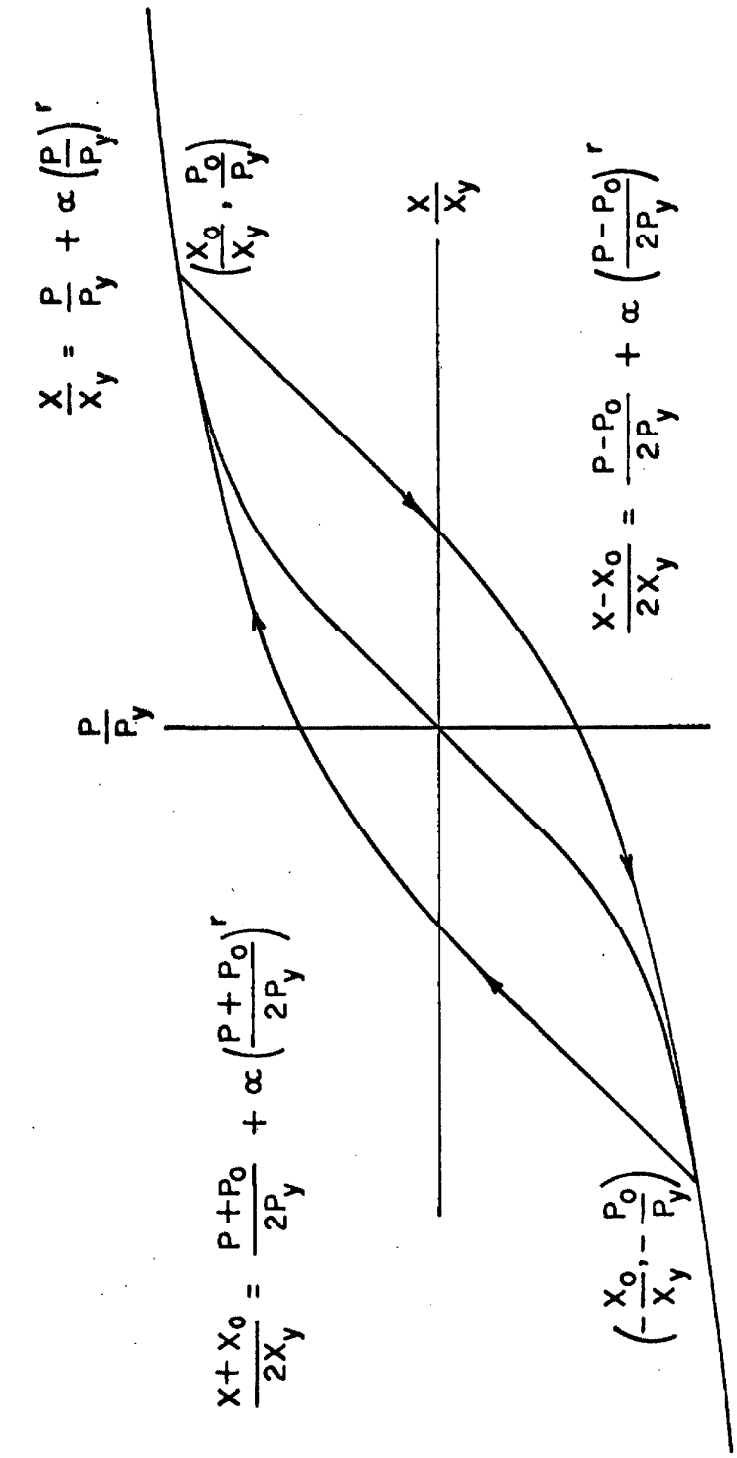

FIG. 5.19 GENERAL HYSTERESIS LOOP

JENNINGS

$$\frac{x_o}{x_y} = \frac{4\alpha \frac{r-1}{r+1} \left(\frac{P_o}{P_y}\right)^{r+1}}{\pi q \sin \phi_1 \left(\frac{F_o}{P_y}\right)} \tag{5.93}$$

By use of equation 5.89 this result can be expressed in terms of the restoring force amplitude:

$$\frac{F_o}{P_y} = \frac{4\alpha \frac{r-1}{r+1} \left(\frac{P_o}{P_y}\right)^{r}}{\pi q \sin \phi_1 \left[1+\alpha \left(\frac{P_o}{P_y}\right)^{r-1}\right]} \tag{5.94}$$

where F_o is the sinusoidal force amplitude, q is the ratio of the first coefficient of the Fourier series expansion of the displacement to x_o, and ϕ_1 is the phase angle in the Fourier series associated with the preceding coefficient.

Equation 5.94 relates the force level of the excitation to the amplitude of steady state vibrations of the structure. If the phase angle between the excitation and the response could be determined, this equation would define response curves for the family of nonlinear structures.

4c. Equations of the Response Curves. The equation of motion of the general structure in response to sinusoidal excitation is

$$m\ddot{x} + p(x) = F_o \cos \omega t \tag{5.95}$$

Introducing the following dimensionless parameters:

$$\omega_n^2 = \frac{p_y}{x_y m}$$

$$\eta = \omega / \omega_n \tag{5.96}$$

where ω_n is the natural frequency of small vibrations. Then the equation for the response curve is found to be[28]

$$\left(\frac{\omega}{\omega_n}\right)^2 = C(x_o) \pm \sqrt{\left(\frac{F_o}{p_y}\right)^2 \left(\frac{x_y}{x_o}\right)^2 - S^2(x_o)} \tag{5.97}$$

The response curves can be constructed from equation 5.97 as shown in figure 5.20 where it is seen that $C(x_o)$ describes the resonant frequency as a function of amplitude. This is equal to C(A) of equation 4.10.

It follows that

$$\tan\phi = \frac{S(x_o)}{C(x_o) - \eta^2} \tag{5.98}$$

The maximum amplitude of the response curves given by equation 5.97 occurs when the radical is zero; at this point $\eta^2 = C(x_o)$. It can be shown that $S(x_o)$ is negative so it follows that resonance occurs when

$$\tan\phi = -\infty, \quad \phi = -\pi/2 \tag{5.99}$$

From equation 5.97 and figure 5.20, it is seen that the maximum amplitude is determined from

$$\left(\frac{F_o}{p_y}\right)^2 = \left(\frac{x_o}{x_y}\right)^2 S^2(x_o) \tag{5.100}$$

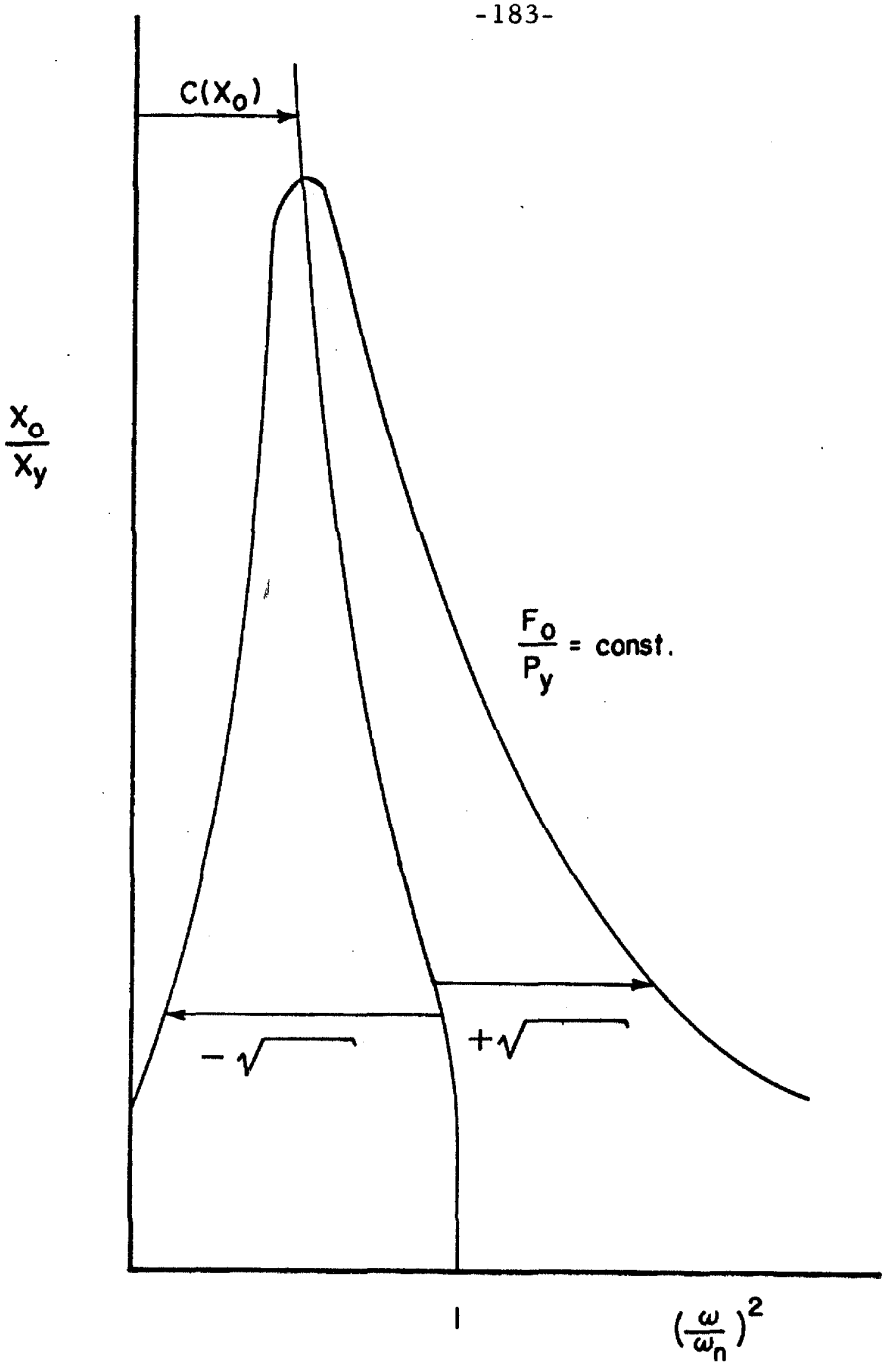

FIG. 5.20 CONSTRUCTION OF RESPONSE CURVES FROM EQUATION 5.97

Since

$$C(x_o) = \left(\frac{\omega_p}{\omega_n}\right)^2 = \frac{2x_y}{\pi x_o} \int_0^{\pi} \frac{p}{p_y}\left(\frac{x_o}{x_y}\cos\theta\right)\cos\theta\, d\theta$$

and (5.101)

$$S(x_o) = \frac{2x_y}{\pi x_o} \int_0^{\pi} \frac{p}{p_y}\left(\frac{x_o}{x_y}\cos\theta\right)\sin\theta\, d\theta$$

there results

$$C(x_o) = \frac{8}{\pi}\left(\frac{x_y}{x_o}\right)^2 \int_0^{p_o/p_y} \sqrt{(y+ay^r)\left[\frac{x_o}{x_y} - (y+dy^r)\right]}\, dy \qquad (5.102)$$

and

$$S(x_o) = \frac{\frac{-4a}{\pi}\,\frac{r-1}{r+1}\left(\frac{p_o}{p_y}\right)^{r+1}}{\left(\frac{x_o}{x_y}\right)^2} \qquad (5.103)$$

The integral for $C(x_o)$ was evaluated on the digital computer for $r = 3, 5, 7, 9$ and 11 and for $a = 0.05,\ 0.10,\ 0.15,\ 0.20$ and 0.25 by Jennings. Figure 5.21 gives an example of the frequency response curves obtained.

4d. Equivalent Viscous Damping. An equivalent viscous damping coefficient for the general structure can be found by making an energy balance. For a linear, viscously damped structure at resonance under sinusoidal excitation the energy dissipated per cycle is obtained as

$$\frac{E_d}{\frac{1}{2}x_y p_y} = 4n\pi\left(\frac{x_o}{x_y}\right)^2 \qquad (5.104)$$

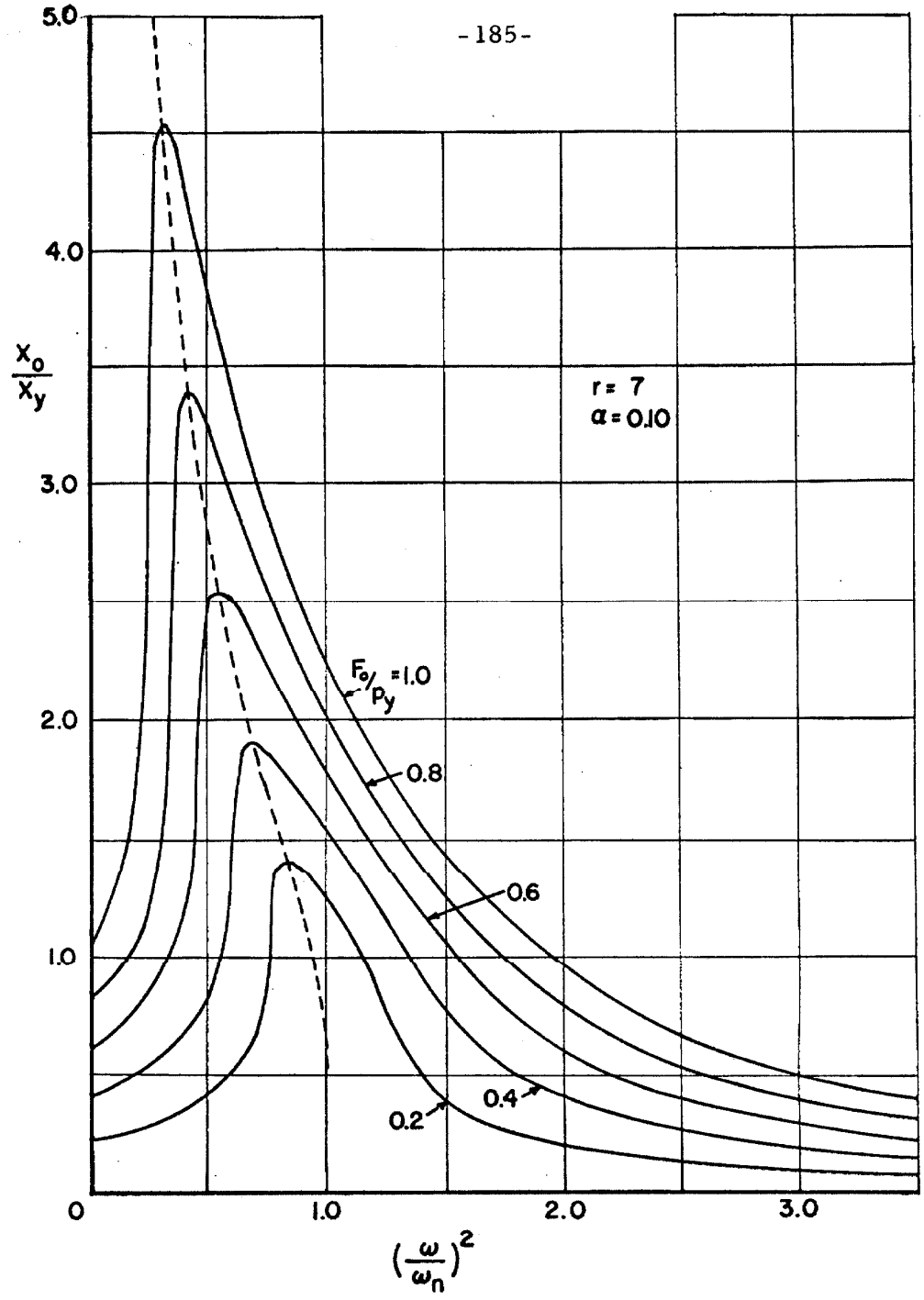

FIG. 5.21 EXAMPLE OF RESPONSE CURVES

where n is the fraction of critical damping. If the energy dissipated by a linear structure, as given by this equation, is equated to that of the general structure, an equivalent viscous damping coefficient can be determined with the help of equation 5. 89:

$$n_{eq} = \frac{\frac{2a}{\pi} \frac{r-1}{r+1} \left(\frac{p_o}{p_y}\right)^{r-1}}{\left[1+a\left(\frac{p_o}{p_y}\right)^{r-1}\right]^2} \qquad (5.105)$$

where n_{eq} is the fraction of critical damping of the linear structure which at resonance will dissipate the same energy as a function of amplitude as the general structure. At resonance of the nonlinear structure, $(\omega_p / \omega_n)^2 = C(x_o)$ as given by equation 5. 101. The foregoing analysis is substantially that developed by Jennings, and its suitability for estimating the dynamic characteristics of a structure from static test data will now be examined.

4e. Evaluation of the constants. The theory developed above requires the evaluation of the four constants x_y, p_y, a and r. Once the values of x_y and p_y are obtained the method of making a logarithmic plot of the departure from linearity of the deflection versus the applied force may be used. The only condition on the constants x_y and p_y is that $p_y/x_y = K$, a constant equal to the initial stiffness of the structure. The absolute values of p_y and x_y are not restricted. Since x_y and p_y were introduced into the theoretical analysis only as a mathematical convenience and do not necessarily have physical significance in the general case, the resulting formulae of interest

here will be reformulated.

The data from the static hysteresis loop of test A3. 22 has been used as an example of the type of results obtained by using arbitrarily selected x_y and p_y values. The values of X and P for test A3. 22 are listed in Table V-1. By selecting the initial values of $x_y = X_{e\ell} = 0.259$ inch and $p_y = p_{e\ell} = 870$ pounds, the curve (a) in figures 5. 22 and 5. 23 was obtained. The resulting constants are

$$\begin{aligned} \alpha &= 0.20 \\ r &= 3 \end{aligned} \tag{5.106}$$

TABLE V-1

Test A3. 22 Reduced Hysteretic Data	
x_i	P_i
0	0
0. 0375	125
0. 0578	190. 5
0. 0680	225
0. 0795	258. 5
0. 0928	301. 5
0. 1075	346. 5
0. 1180	380
0. 1358	429
0. 1490	466
0. 1618	504
0. 1770	546. 5
0. 1850	568. 5
0. 2028	615. 5
0. 2215	663
0. 2302	687. 5
0. 2438	719
0. 2535	748
0. 2600	761

The equivalent fraction of critical damping shown by curve (a) of figure 5. 24 results from substituting equation 5. 106 into equation 5. 105. Similarly, using $x_y = 0.194$ inch and $p_y = 652$ pounds, curve (b) of figures 5. 22, 5. 23 and 5. 24 results with

$$\begin{aligned} \alpha &= 0.12 \\ r &= 3 \end{aligned} \tag{5.107}$$

The ratio of p_y to x_y is the same constant for both curves (a) and (b) and is equal to the initial stiffness of the structure. Although the choice of p_y and x_y did not significantly affect the theoretical force-deflection curve, figure 5. 23, it did give substantially different values of the predicted equivalent viscous

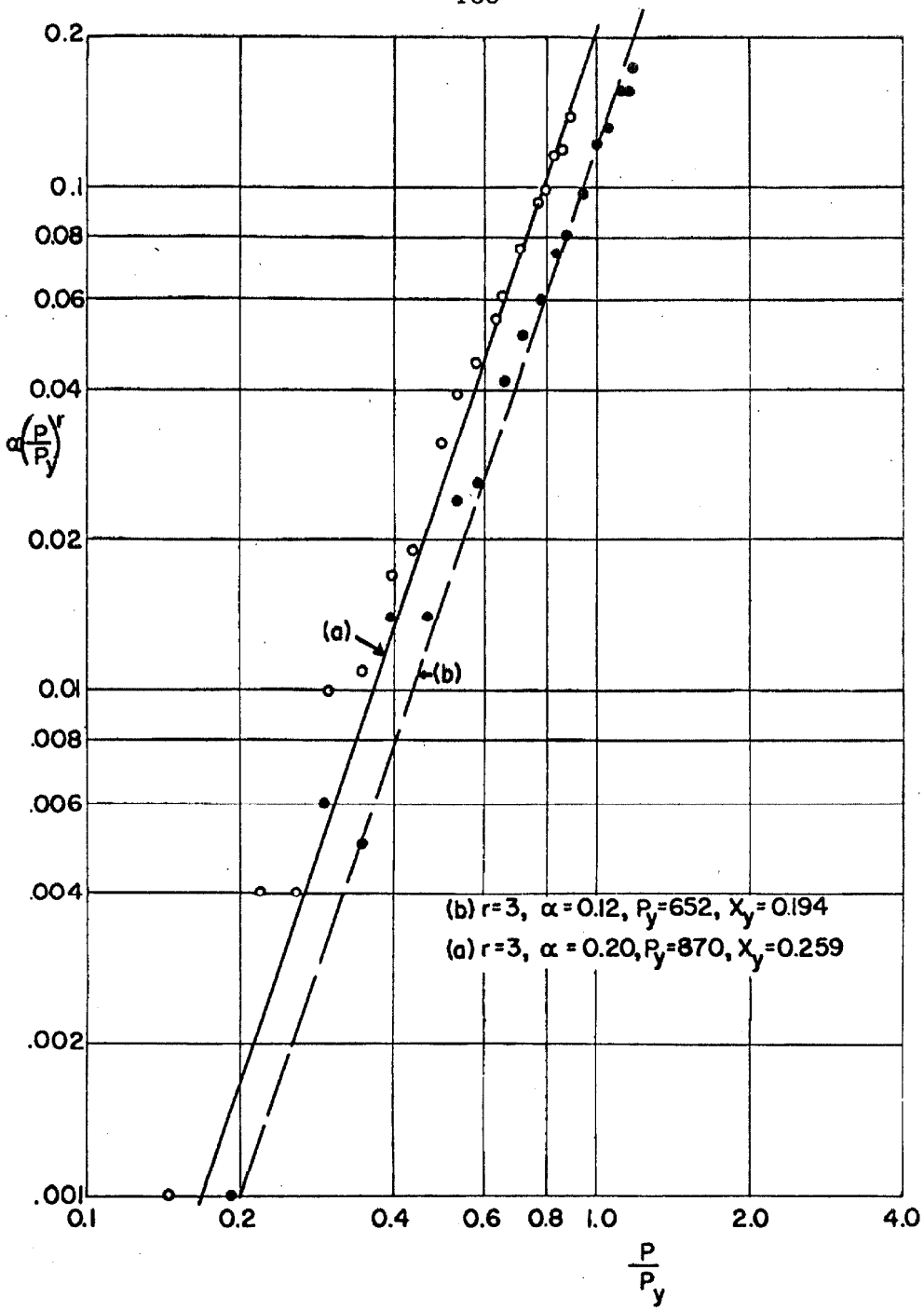

FIG. 5.22 DETERMINATION OF α AND r

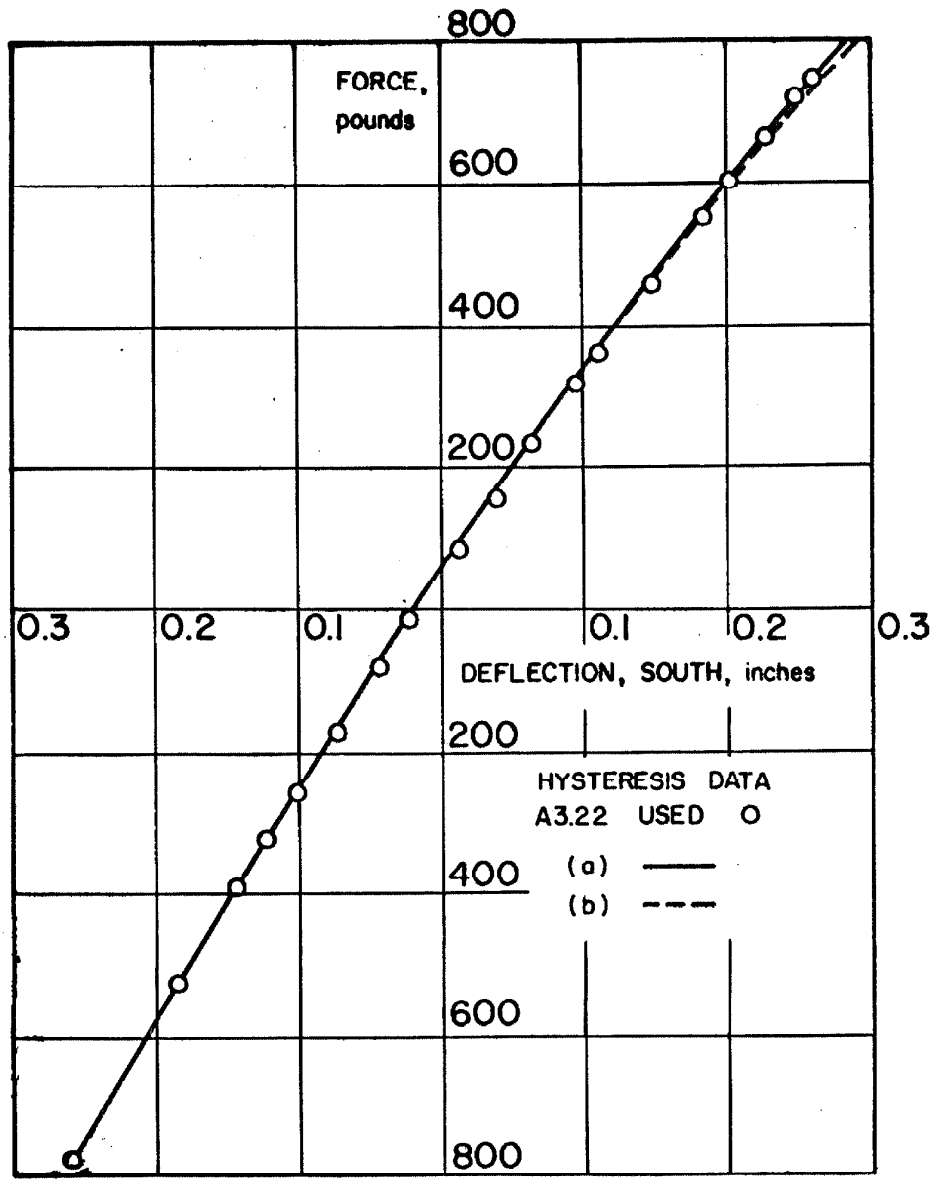

FIG. 5.23 COMPARISON OF POLYNOMIAL CURVE WITH DATA USED (LI (N-S))

damping, figure 5.24. Comparison of the theoretical force-deflection curves to the experimental data, figure 5.23, did not permit selecting curve (a) or curve (b) as being the most appropriate approximation. Therefore, the ambiguity of selecting p_y and x_y must be eliminated before using this theory.

A reformulation of the equations of interest will now be made to eliminate the necessity of selecting x_y and p_y. Equation 5.89 when multiplied by x_y becomes

$$x = \left(\frac{x_y}{p_y}\right) P + \left(\frac{x_y a}{p_y{}^r}\right) P^r \tag{5.108}$$

By letting

$$d = \frac{x_y}{p_y}$$

and

$$e = \frac{x_y a}{p_y{}^r} \tag{5.109}$$

equation 5.108 becomes

$$x = dP + eP^r \tag{5.110}$$

Now three constants d, e and r must be determined. As before, d is just the reciprocal of the initial stiffness of the skeleton curve.

The best method for determining e and r would be to make a least squares fit of the data, but this is impractical for the polynomial as given in equation 5.110. Since the values of r are limited to odd integers by the theory outlined above and since the value of r is not sensitive to x_y and p_y, as can be seen from figure 5.22, the value of r can be determined by the method used in figure 5.22.

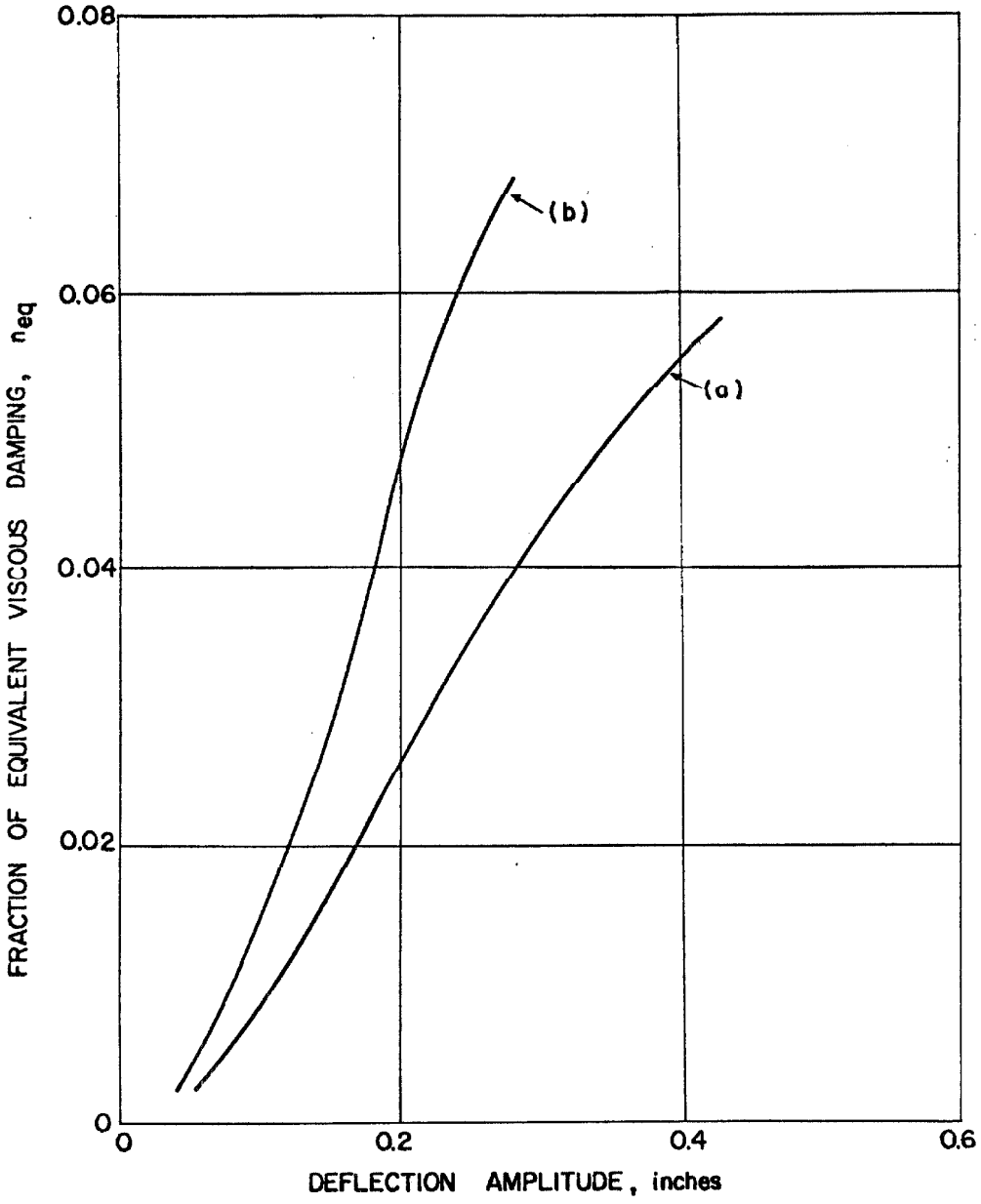

FIG. 5.24 EQUIVALENT VISCOUS DAMPING

Using the determined values of d and r, the least squares method will evaluate the remaining constant e.

The least squares formulation will now be made. Since x is a given function of P, equation 5.110, the differences between the theoretical curve and data will be made in terms of the deflections. Letting x_i and P_i be the corresponding i^{th} data terms, the general least squares expression is

$$\frac{\partial}{\partial e}\left[\sum_i \left| x(P_i, e) - x_i \right|^2\right] = 0 \qquad (5.111)$$

With the use of equation 5.110, equation 5.111 reduces to

$$\sum_i \left| dP_i + eP_i^{\,r} - x_i \right| P_i^{\,r} = 0 \qquad (5.112)$$

or

$$e = \frac{\sum_i (x_i - dP_i)P_i^{\,r}}{\sum_i P_i^{\,2r}}$$

Therefore, given d and r, the value of e can be determined from equation 5.112 for any set of data x_i and P_i. This calculation has been programmed for the Burroughs 220 Datatron digital computer.

Applying the constants defined in equations 5.109 and 5.110 to equation 5.94, the steady-state excitation force becomes

$$F_o = \frac{4\,\frac{r-1}{r+1}}{\pi q \sin\phi_1}\, e\,\frac{P_o^{\,r+1}}{x_o} = \frac{4\,\frac{r-1}{r+1}}{\pi q \sin\phi_1}\, P_o\left|1 - d\frac{P_o}{x_o}\right| \qquad (5.113)$$

At resonance ϕ_1 is assumed to equal $\pi/2$ and $q \approx 1$. The equivalent fraction of critical damping near resonance, equation 5.105 becomes

$$n_{eq} = \frac{2}{\pi} \frac{r-1}{r+1} \frac{P_o^{r+1}}{x_o^2} de = \frac{2}{\pi} \frac{r-1}{r+1} d \frac{P_o}{x_o} \left(1-d \frac{P_o}{x_o}\right) \qquad (5.114)$$

Comparing equations 5.113 and 5.114 near resonance shows that

$$F_o = \frac{2x_o}{d} n_{eq} \qquad (5.115)$$

is valid.

The resonant excitation frequency as defined by $C(x_o)$, see figure 5.20 and equation 5.102, cannot be expressed in the terms of equation 5.110. Therefore, equation 5.109 will be used to determine a for an appropriate choice of x_y or p_y with the established constants d, e, and r. With this a and r, the theoretical values of $C(x_o)$ may be interpolated from the numerical values determined by Jennings.[42] Sensitivity of $C(x_o)$ with variation of the selected x_y or p_y was found to be negligible for reasonable values of x_y or p_y.

4f. Comparing the predicted and the experimental response.

Three alternate static structural responses can be used as bases for determining an approximate polynomial force-deflection relationship. These are the experimental static virgin force-deflection curve, the experimental static hysteretic force-deflection curve, and the theoretically predicted static virgin force-deflection curve. Using the results developed above, the predicted dynamic response characteristics, such as, excitation force-resonant amplitude, shift in resonant frequency with amplitude, fraction of critical viscous damping as a function of amplitude, and the energy absorption per cycle as a function of amplitude, will be compared with experimental

dynamic results.

Since an experimental virgin force-deflection curve for column LI (N-S) was not obtained, a prediction of its dynamic response will be made by using two of its static hysteresis curves, A3. 22 and A3. 31. The polynomial expression of equation 5. 110, determined by the least squares method outlined above, is plotted with the A3. 31 data used in figure 5. 25. Using the calculated constants d, e, and r, equations 5. 113 and 5. 114 give the predicted force amplitude and fraction of equivalent viscous damping as functions of the resonant amplitude. These results are plotted in figures 5. 26 and 5. 27 together with the experimental dynamic results taken from figures 4. 6, 4. 9 and 4. 15. The excitation frequency at resonance divided by the small, free vibration natural frequency, is predicted by the square root of $C(x_o)$, figure 5. 20. Using the method outlined above, the predicted frequency shift is given in figure 5. 28 together with the experimental dynamic frequency response peaks of figure 4. 9. It can be seen from figures 5. 25 through 5. 28 that even though the static hysteretic curve is well matched with the polynomial, the predicted dynamic response is only a rough approximation of the experimental dynamic response.

In an attempt to obtain better predicted dynamic response results for LI (N-S), the theoretical static skeleton curve was used as an alternate basis for determining the appropriate polynomial. The polynomial was calculated by the least squares method for values r = 3, 5, 7, 9 and 11. The data used and the resulting poly-

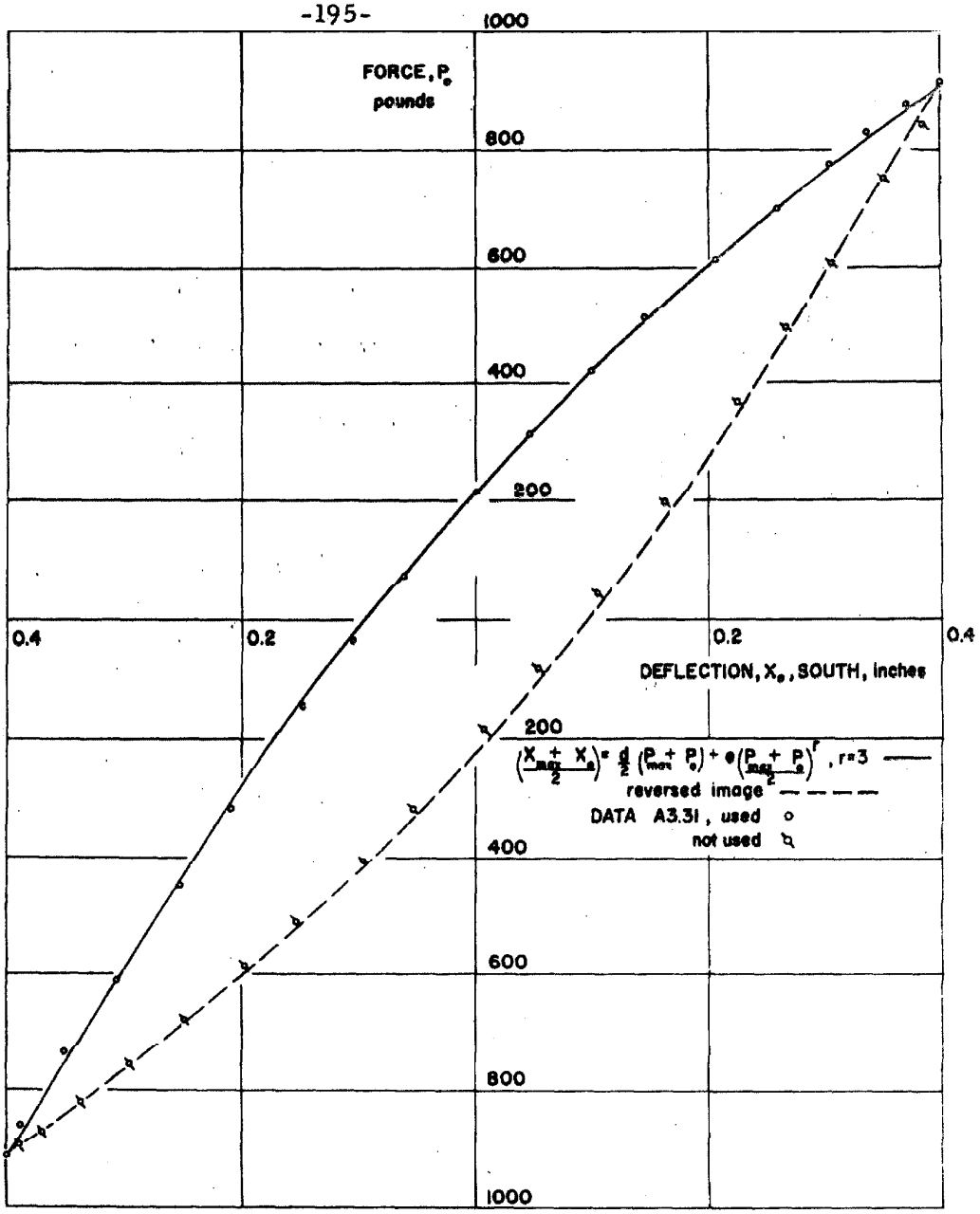

FIG. 5.25 COMPARISON OF LEAST SQUARES APPROXIMATED CURVE WITH DATA USED (LI (N-S))

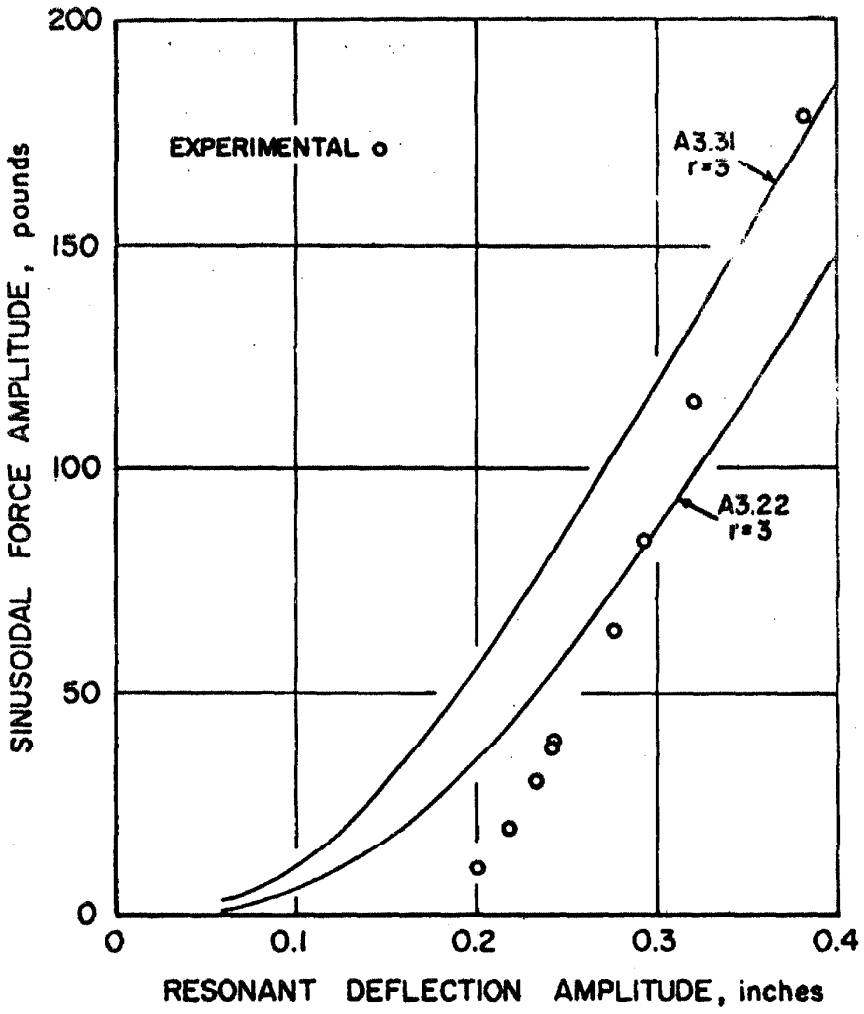

FIG. 5.26 COMPARISON OF EXPERIMENTAL AND PREDICTED RESONANT RESPONSE FOR LI (N-S)

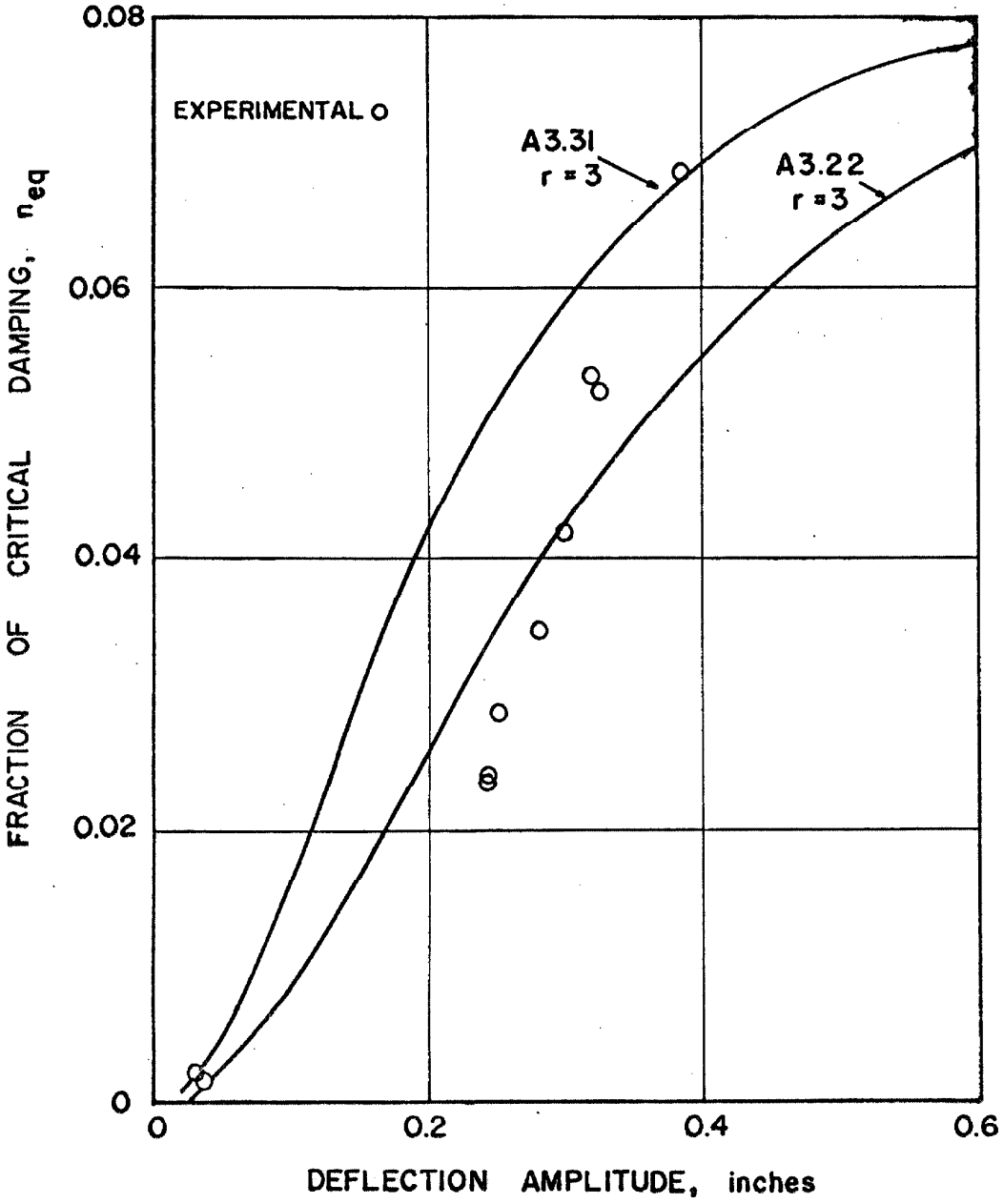

FIG. 5.27 COMPARISON OF EXPERIMENTAL AND PREDICTED EQUIVALENT VISCOUS DAMPING FOR LI (N-S)

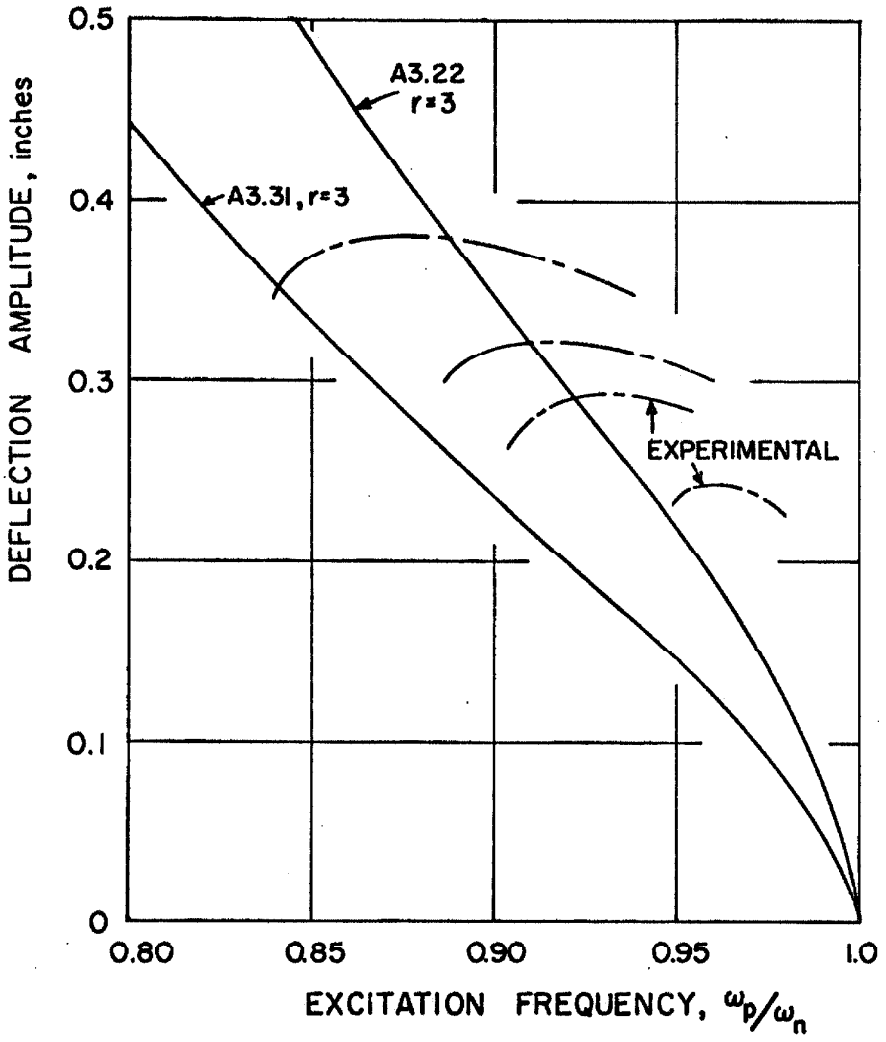

FIG. 5.28 COMPARISON OF EXPERIMENTAL AND PREDICTED RESONANT FREQUENCY FOR LI (N-S)

nomials for r = 3, 7, and 11 are plotted in figure 5. 29. The predicted and experimental dynamic steady-state force amplitude and resonant frequency shift, as functions of the deflection amplitude, are given in figure 5. 30 and 5. 31 respectively. These results will be discussed after considering other results based on experimental static skeleton curves.

Test A3. 35 (SI) gave the virgin force-deflection curve for the short columns. For test A3. 35, the logarithmic plot of the departure from linearity of the deflection versus the applied force is made in figure 5. 32 for arbitrarily selected values x_y = 0. 406 inch and p_y = 2399 pounds. In this case, a large number of selected r values seem equally appropriate. Therefore, the least squares determination of e for given r and d values of test A3. 35 was made with r=11, 9, 7 and 5. The resulting polynomial force-deflection curves are plotted in figure 5. 33, together with the test A3. 35 data. Again, the best theoretical curve to select is not obvious since it will depend upon the range of deflections of interest, but r=11 has smaller differences over the entire range than the other r values plotted. From figure 5. 33 it would be expected that larger r values would produce a better fit to the virgin static curve. The predicted sinusoidal force amplitude, as a function of the resonant amplitude, is plotted in figure 5. 34 together with the experimental results from figure 4. 10. It can be seen that r=7 predicts the resonant response amplitude better than the other two values for deflection, up to 0. 6 inches. At the largest experimental deflection point, the r=11 curve underestimates the

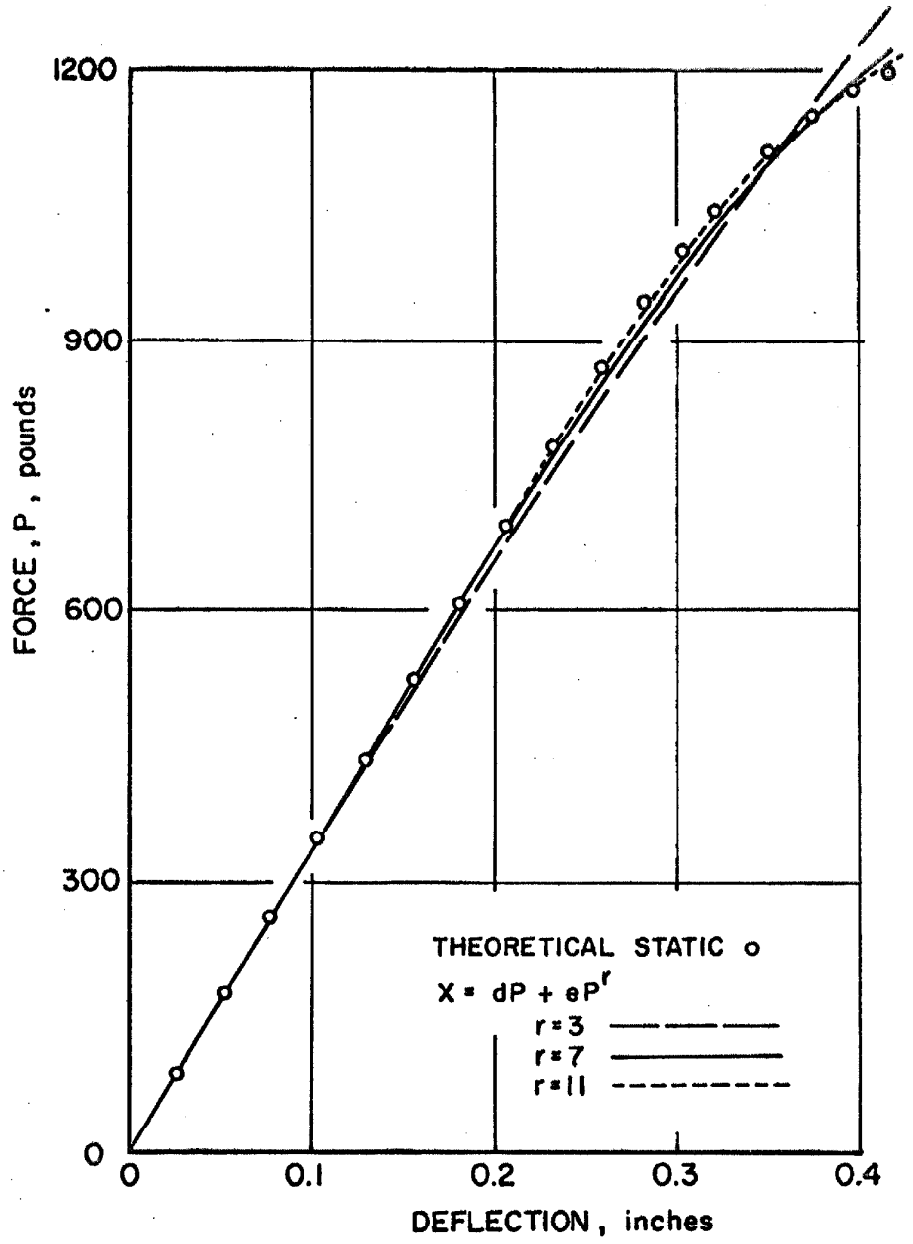

FIG. 5.29 COMPARISON OF LEAST SQUARES APPROXIMATED CURVE WITH DATA USED (LI (N-S))

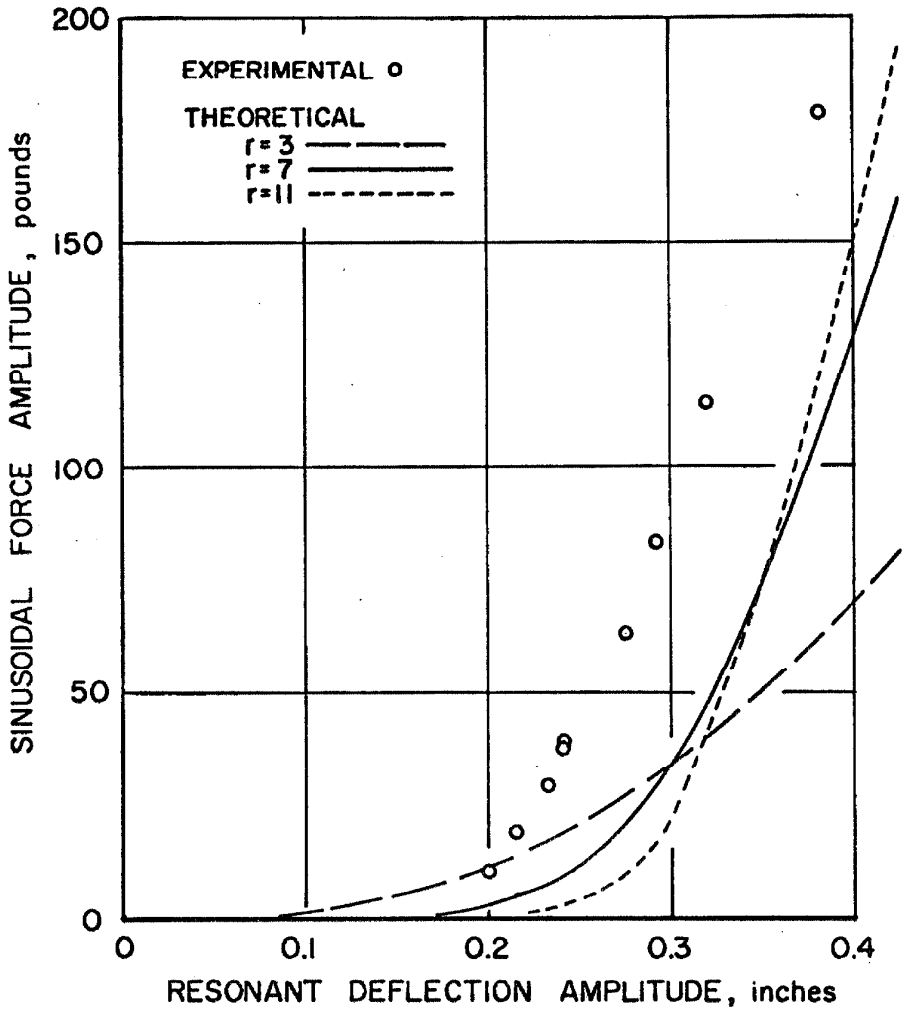

FIG. 5.30 COMPARISON OF EXPERIMENTAL AND PREDICTED RESONANT RESPONSE FOR LI (N-S)

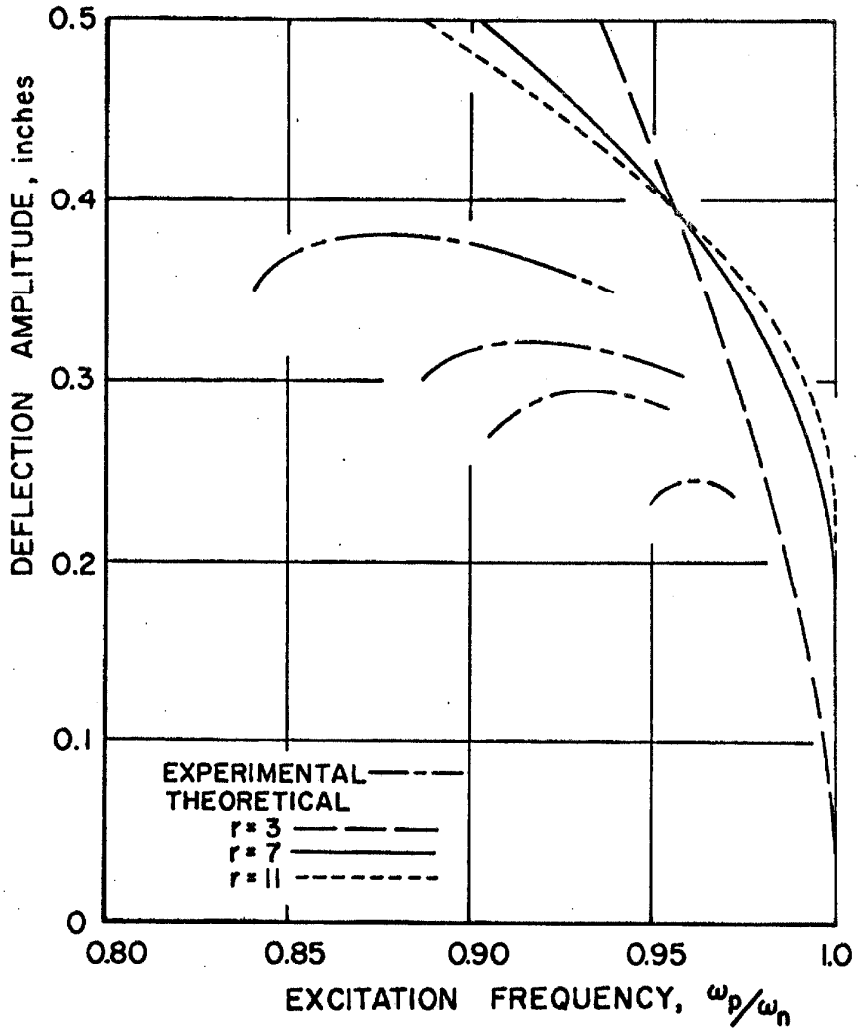

FIG. 5.31 COMPARISON OF EXPERIMENTAL AND PREDICTED RESONANT FREQUENCY FOR LI(N-S)

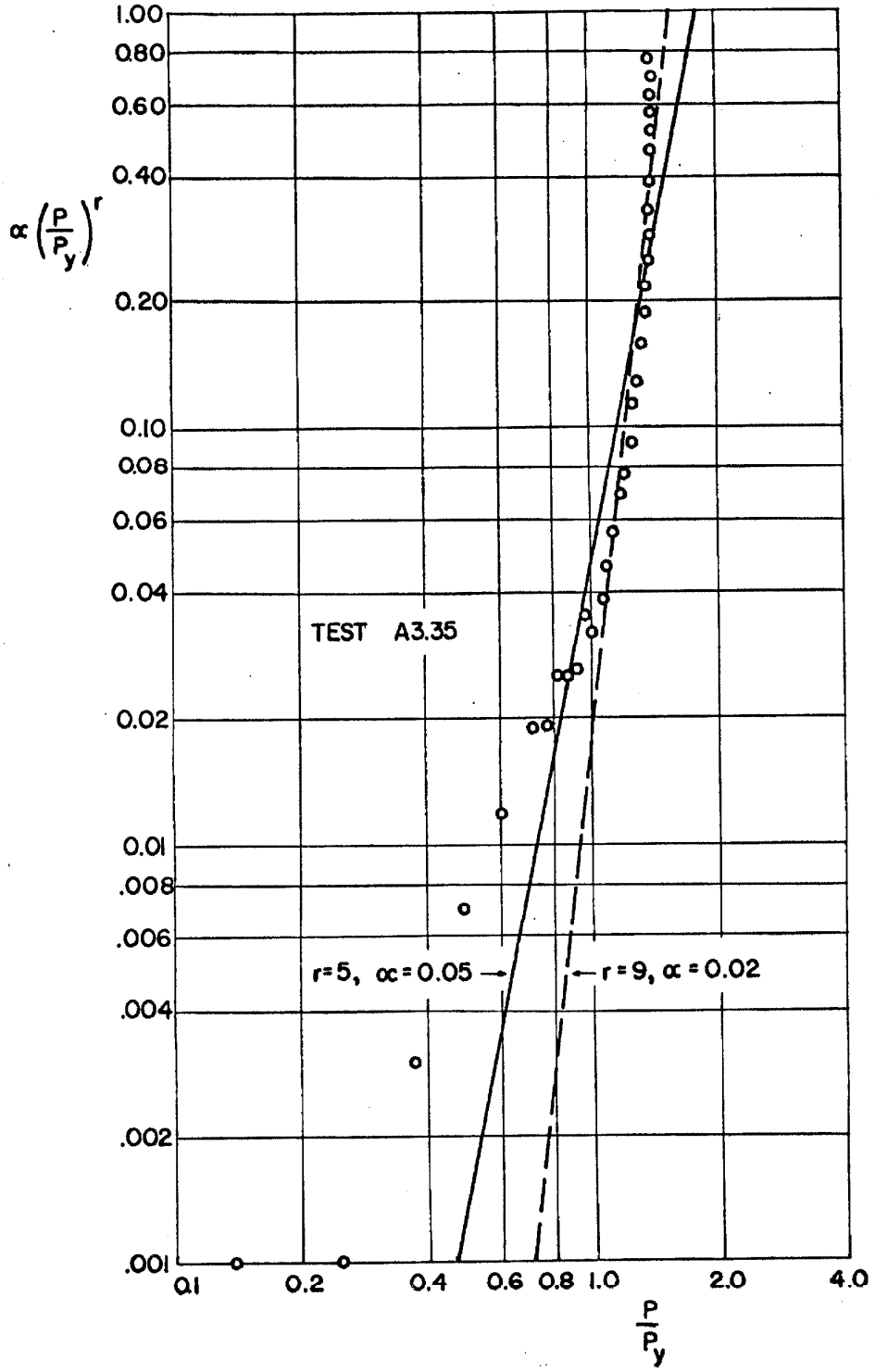

FIG. 5.32 DETERMINATION OF α AND r

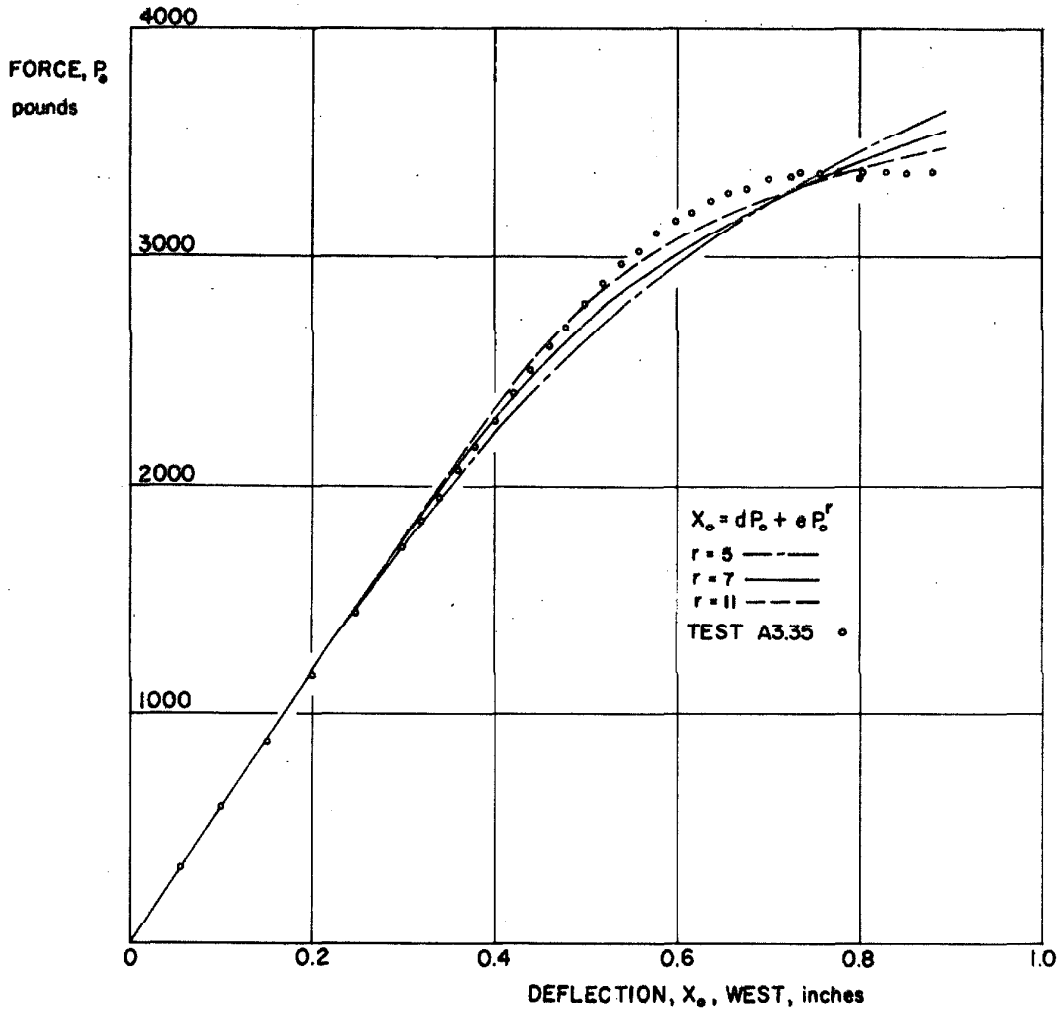

FIG. 5.33 COMPARISON OF LEAST SQUARES APPROXIMATED CURVE WITH DATA USED (SI)

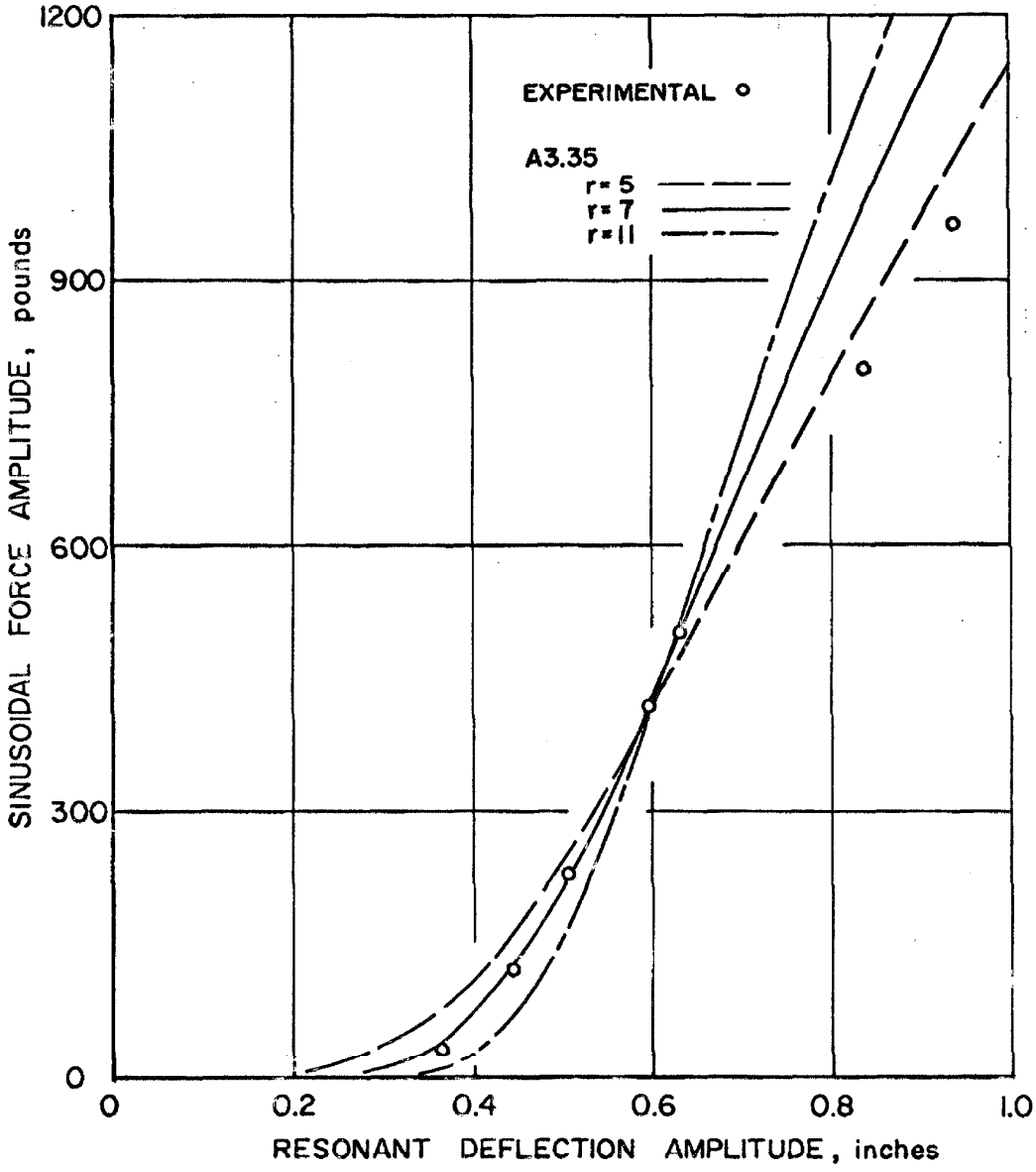

FIG. 5.34 COMPARISON OF EXPERIMENTAL AND PREDICTED RESONANT RESPONSE OF SI AND SII

actual deflection by 20 per cent. The predicted shift in the excitation frequency at resonance, together with the experimental frequency response peaks from figure 4. 10, are given in figure 5. 35. Again, r=7 seems to be the most appropriate, although, any r value seems to give a reasonable prediction of the shift. The predicted fraction of critical damping, together with the experimental results of figure 4. 16, are given in figure 5. 36. The energy dissipated per cycle, i. e., the area of the hysteresis loop, is included as an additional method of comparing the experimental and predicted results, figure 5. 37.

The predicted dynamic response based on a polynomial approximation of the experimental virgin force-deflection curve, will be discussed first. The shift of resonant frequency with increasing amplitude can be predicted with acceptable accuracy without having the polynomial match the experimental curve exactly. The resonant deflection, as a function of the selected force, can be predicted within approximately 20% with the experimental deflection exceeding the predicted. This accuracy is not too bad when it is remembered that the resonant deflection decreases with additional testing. Figure 4. 4 illustrates a case where the resonant deflection has been decreased by about 20% due to the experimentation occurring between the two plotted results.

The attempts at predicting dynamic response, based on an experimental static hysteresis loop and a theoretical static skeleton curve were disappointing. It should be noted that the resonant deflection for a given force based on the static hysteresis loops, are

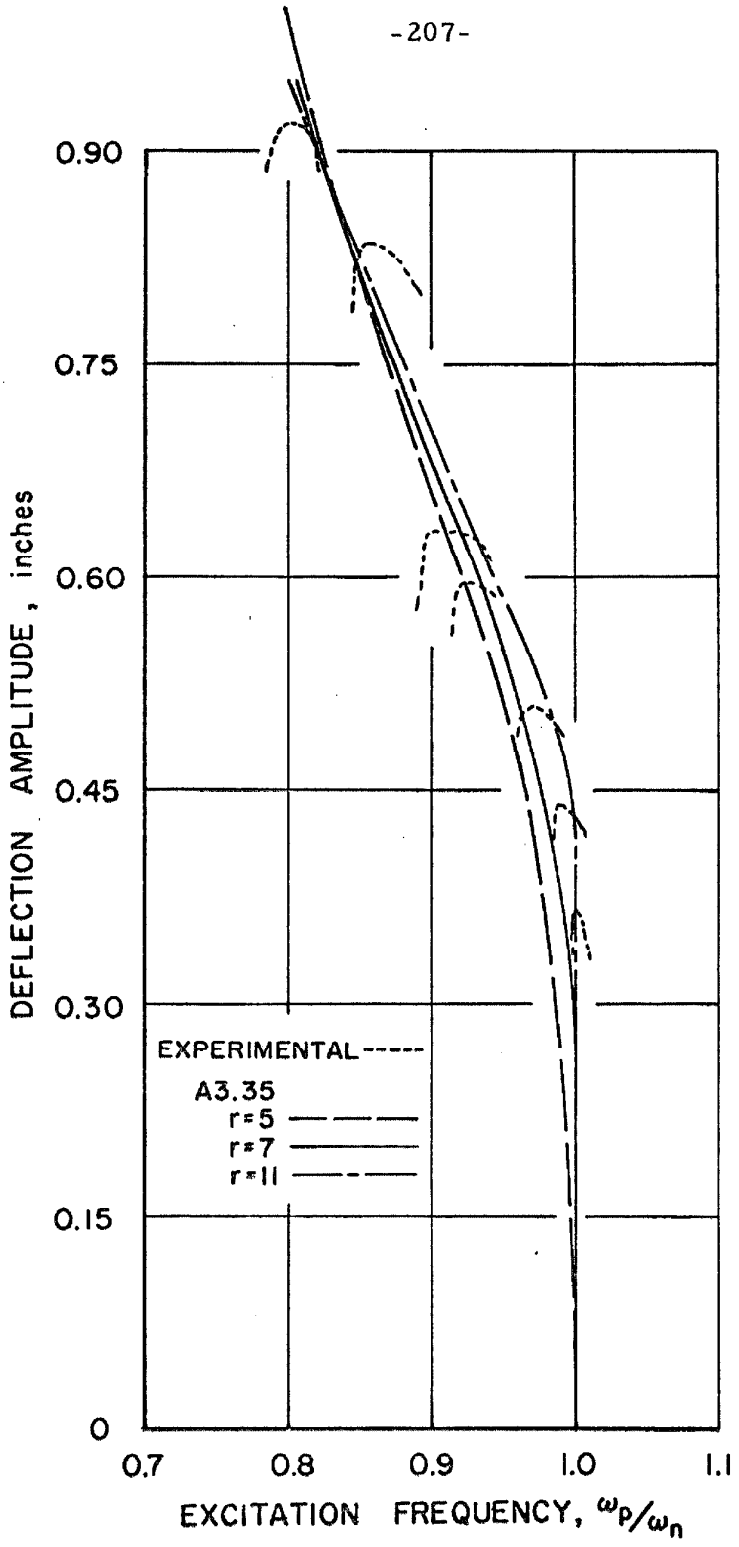

FIG. 5.35 COMPARISON OF EXPERIMENTAL AND PREDICTED RESONANT FREQUENCY OF SI AND SII

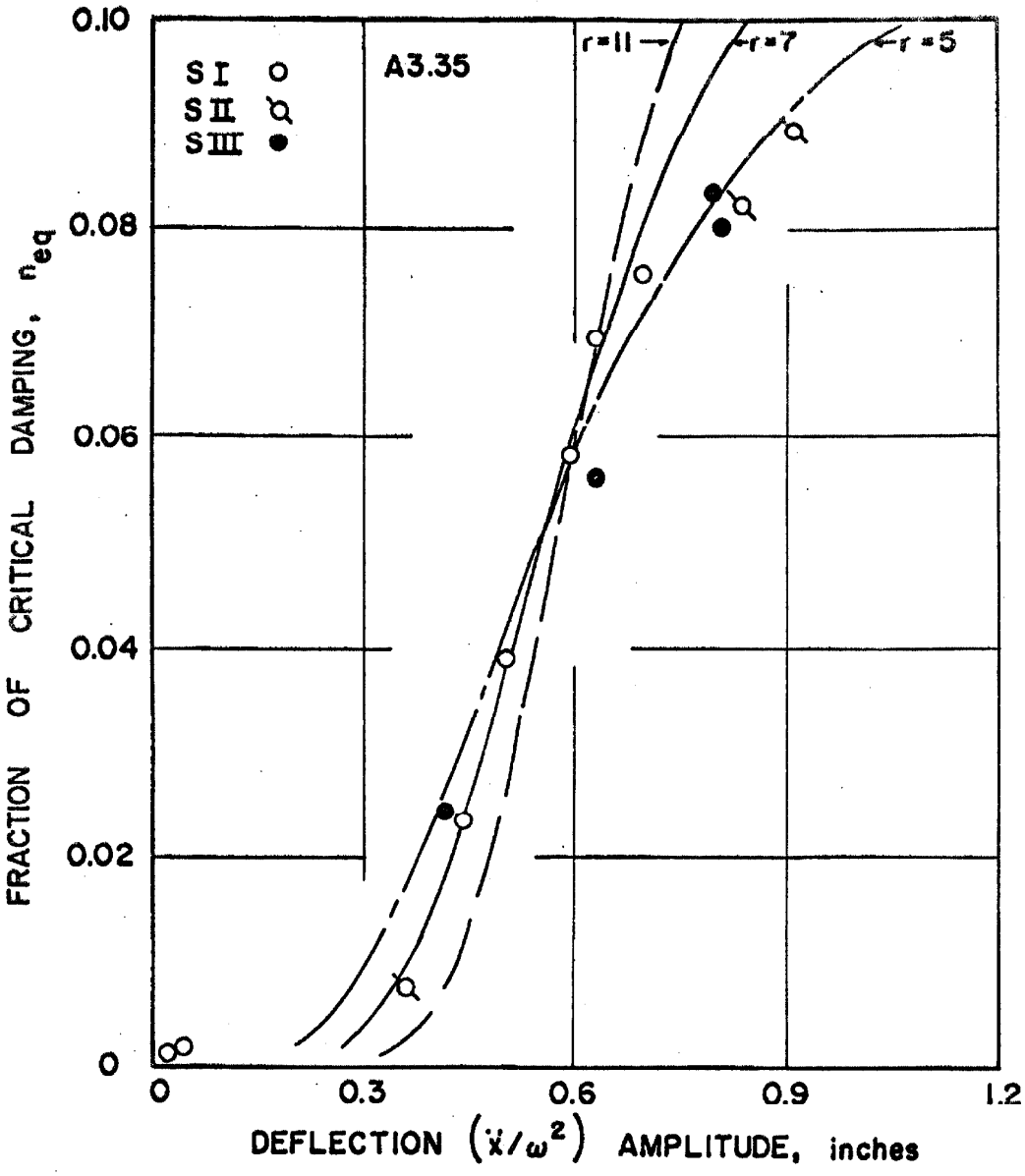

FIG. 5.36 COMPARISON OF EXPERIMENTAL AND PREDICTED EQUIVALENT VISCOUS DAMPING FOR SI, SII, AND SIII

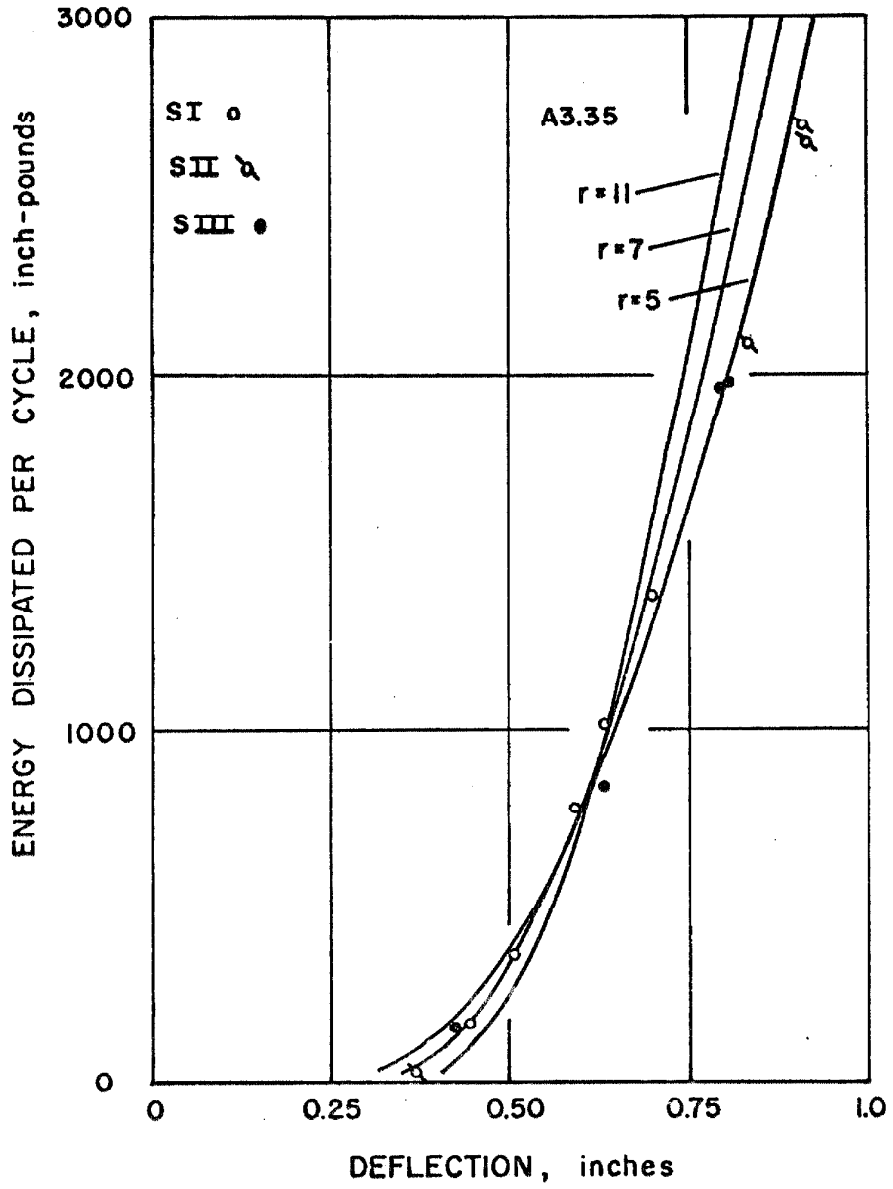

FIG. 5.37 COMPARISON OF EXPERIMENTAL AND PREDICTED ENERGY DISSIPATED PER CYCLE FOR SI, SII, AND SIII

accurate within 5% near the same deflection amplitude as the loop, i.e., A3.31 about 0.40 inches and A3.22 about 0.26 inches. However, this accuracy does not extend to the prediction of the shift in frequency at resonance.

The problem of predicting dynamic response will be considered again, near the end of this chapter, utilizing the following discussion.

B. Interpretation of Test Results

1. Static Skeleton

The disagreement between the theoretical virgin force-deflection relationship determined from tensile test data and the virgin force-deflection test curve could be anticipated from previous tests in the yielding range of mild steel. The two outstanding characteristic differences are first, that the actual test yield point occurs before the theoretical yield point and second, that the maximum theoretical yield load is not achieved for the actual test. Both of these characteristics are commonly known and expected.

The first characteristic has been explained and documented by Yang, et al.[43] for the case of WF continuous beams. The reason for early yielding in the test results lies in the initial residual stresses in the beam after being hot rolled and cooled to air temperature. If the beam is annealed before testing, the test results lie much closer to the theoretically determined values. This substantiates that the residual stresses initiate yielding before the theoretical, initial zero stress, yielding begins. The normal stress

on the section caused by the weight of the structure also contributes to this effect. However, these stresses will cause only a minimal decrease in the full plastic moment; usually less than a one percent decrease.

The reason that the static experimental moment at yielding does not reach the theoretical full plastic moment for mild steel is that the tensile test determination of the yield stress was made at a specific strain rate of loading; whereas, the static skeleton curve data was taken at effectively zero strain rate. The increase in strain rate has the effect of raising the yielding stress. Extrapolation of the results presented by Parkes[44] to the strain rate used in the tension tests reported in Appendix II, about 1.5×10^{-5} per second, determines that the full plastic moment based on the tension test should be about 1.05 times the static full plastic moment. This is approximately the difference shown in figure 5.16. Additional evidence of the theoretical overestimation of the yield load can be found in the literature.* The expected fluctuation of the load during this yielding process is shown for the tensile tests in figure A2.2 and for the virgin force-deflection curve in figure 4.28.

2. Static Hysteresis

If the experimental skeleton curve is used to predict the hysteresis portion of the force-deflection relationship by doubling the ordinates, it will be found that the test data give smaller resulting

* For example: Yang, et al.[43]

forces for equal deflections. This phenomena has been noted in the literature.[45] The magnitude of the difference between the anticipated hysteretic force-deflection curve and the experimental data could depend upon the material, temperature, load rate, and other factors which prohibit its prediction. Currently there is not a commonly accepted explanation of the effect.[46] For this reason, any properties of the hysteresis loop based upon the virgin force-deflection curve must be used with caution.

3. Strain Ageing and Deterioration

If a metal is loaded beyond its yield point with a limited amount of plastic deformation occurring before the load is removed, then when the metal is reloaded after a time of no load, the metal will exhibit a higher yield point than before. This is called strain ageing. Examples of this can be seen in figure 4. 28 where the material of test A3. 37 exhibits an initial yield stress higher than the yield stress at the end of test A3. 35 and similarly with test A3. 38 initial yield exceeding the yield stress of test A3. 37.

Material deterioration was observed from the earliest small vibration tests, figures 4. 2 and 4. 3, to the much larger deterioration occurring during the dynamic test A3. 57 as illustrated by the static tests A3. 56 and A3. 58 given in figure 4. 49.

The intermittent testing as carried out here has had the effect of alternatively causing structural deterioration and strain ageing. The effect of intermittent testing upon fatigue life or low endurance life of the material is not known. However, a more rapid

deterioration occurs after large strain ageing strength increases. This is indicated by comparing the rate of deterioration during the first static test cycles at $\pm$ 0.80^{+} inch deflection relative to the strain ageing preceding these tests, see tests A3.66 and A3.68 in figures 4.34 and 4.37. The initial static test at this deflection range, A3.60, exhibits a much slower rate of deterioration, figure 4.33. This seems to indicate that the number of cycles required to reach a previous level of deterioration after strain ageing is substantially smaller than the original number of cycles required to reach this level.

Fatigue Life. It would be of great value to be able to predict when failure would occur in a real structure. Since much work has been done in the area of fatigue life and cumulative fatigue damage, an attempt will be made to compare the life of the experimental specimens to the expected life as predicted by fatigue theory.

Since the sections are stressed primarily in bending, a fatigue S-N curve will be established for the material described in Appendix II. It should be noted here that all the columns except LI were made of this material. However, the material of LI is not expected to be substantially different because of the similarity of the hardness test results. The procedure used to establish this theoretical S-N curve is that as described in reference (47). According to this procedure, the upper stress limit at 10^3 cycles should be 0.9 times the ultimate stress, and in this case it is about 57,000 psi. The lower limit, which is the endurance limit, at 10^6 cycles can be estimated from

figure 11-12 on page 110 of reference (47) knowing that the test section is hot rolled and has a BHN of 134. Applying the size correction factor of 0.95 to the previously obtained endurance limit, the endurance stress for the experimental section is about 21,000 psi. The S-N curve is assumed linear between these two limits when plotted on logarithmic paper and is horizontal at 21,000 psi for all cycles greater than 10^6.

The number of cycles at each deflection was not recorded and can only be estimated by assuming that a certain number of cycles were required to obtain the experimental data. A lower time limit required to obtain each data point would be about 1/2 minute, since this is about the length of time required to obtain a steady-state motion assuming 1% of critical damping. Also, the data would be taken as rapidly as possible after the steady-state condition had been reached. Since the force generators require a finite time to reach a new forcing frequency, an estimate of the maximum average time per data point would be about 2 minutes. For the long columns tested in the north-south direction, the number of cycles per data point is about 200 cycles for an average time of four thirds minutes. For the short columns tested, 240 cycles per data point results for an average time of four thirds minutes.

The data taken is divided into six strain ranges which can be identified as: the strain associated with the endurance limit of 21,000 psi is 0.00073, the initial yield strain associated with the yield stress of 40,000 psi is 0.0014, and the strain which initiated

strain hardening is 0.014. Table V-2 gives the number of data points and the estimated number of cycles in each strain range and the total. Figure 5.11 with strain hardening is used to translate deflection to strain for this determination. The mean maximum stress in the strain range 0.00073 to 0.0010 is 24,000 psi and in the strain range 0.0010 to 0.0014 is 34,000 psi. For strains between 0.0014 and 0.0140, the maximum stress is 40,000 psi. The mean maximum stress for strains above 0.0140 is 50,000 psi.

One cumulative fatigue damage theory[48] states that the sum of the number of cycles at each stress level divided by the number of cycles allowed at that stress level should be equal to one for failure. In mathematical notation

$$\sum \frac{n}{N} = 1 \tag{5.116}$$

where n is the actual number of cycles at a given stress level and N is the predicted number of cycles required for failure at that stress level. The values of N as obtained by using the mean maximum stresses previously noted and the numerical values of equation 5.116 are also included in Table V-2. As can be seen from Table V-2, the $\sum$ n/N results for the short columns are reasonable and the differences may be partially explained by the variance of the actual number of cycles to the assumed average per data point. The effect of strain ageing on fatigue life may be a possible explanation for the larger difference of the LI column result. It should be noted that the intermittent dynamic experiments were performed over 110, 8, and

TABLE V-2

Cummulative Fatigue Damage

Column Item	Strain Range						Total	$\sum \frac{n}{N}$
	Below 0.00073	0.00073 to 0.0010	0.0010 to 0.0014	0.0014 to 0.0027	0.0027 to 0.0140	over 0.0140		
LI extra cycles			10,000	2800				
No. of points	219	80	229	103			631	3.51
No. of cycles	43,800	16,000	55,800	23,400			139,000	
SI								
No. of points	56	8	19	47	14		144	1.350
No. of cycles	13,440	1920	4560	11,280	3360		34,560	
SII								
No. of points	67	16	18	12	13	3	129	0.918
No. of cycles	15,280	3840	4320	2880	3120	720	30,960	
N	∞	300,000	37,000	12,000	12,000	2500		

16 day intervals for the LI, SI, and SII columns respectively.

4. Strain Rates for Static-Dynamic Comparisons.

Numerous investigators have considered the problem of determining the material properties of tensile loading at various rates and temperatures. In general, most investigators have determined that at room temperature for mild steel, the yield stress increases with increasing loading rates.[49] Wood and Clark[50] have determined that the delay time between the initiation of plastic deformation and the application of stress decreases with increasing stresses in an exponential manner. The lower limit for this approach appears to be the upper yield stress determined in static tensile tests. Nadai and Manjoine[51] have found for a low-carbon steel at room temperature that the ultimate tensile stress remains practically constant over a range of change of strain rate from 10^{-5} to 10^{-1} sec^{-1}.

An increase in the yield point of the material will have the effect of increasing the restoring force component of the force-deflection curves for the same deflections. A strain rate increase in yield stress does occur in these tests as can be seen in figure 4. 50 where the structure has reached a relatively stable deteriorated position, static tests A3. 60 and 3. 66, and the dynamic test A3. 63 results in a larger restoring force for approximately the same maximum deflections. A less positive demonstration of the strain rate increase in the yield stress caused by the dynamic tests can be seen in figures 4. 49 and 4. 51. In these cases the structure has not

reached a stable deterioration position relative to the test deflections used. However, the dynamic test results do indicate an increase in the restoring force above the expected static test result corresponding to the same testing history.

Table IV-4 shows that a decrease in the area of the hysteresis loop accompanies the increase in restoring force level caused by the increase in strain rate for these cases. Again, this is much more obvious in the case of results plotted in figure 4. 50 than in the other two cases. Table IV-4 also shows that the area of the hysteresis loop increases with deterioration.

Since the published strain rate results have dealt primarily with tension and with a few compression tests, the application of the strain rates for predicting increases in yield stress in bending cannot be made accurately. By using the dynamic test frequencies and deflection points as plotted in figures 4. 42 to 4. 46 and the maximum strain-deflection relationship given in figure 5. 11, an estimate of the maximum strain rates for the various tests could be made.

5. Dynamic Theoretical Prediction

It was noted previously that the experimental static skeleton curve could be used to predict dynamic response within a reasonable degree of accuracy. Figures 5. 34, 5. 36 and 5. 37 indicate that appropriate values of r to use for dynamic prediction, are r=5 and 7. However, it was noted from figure 5. 33 that the higher r values, i. e., r=11, 13, etc., would give a better polynomial approximation to the

experimental static skeleton data. A reasonable explanation of this characteristic lies basically in two different phenomena. First, the hysteresis effect tends to eliminate the prominent yield point and produces a smoother force-deflection curve in the lower yield deflection range. Second, the strain rate effect tends to increase the restoring force above the static restoring force for equal deflections and is more pronounced in the larger yield deflection range. Thus, considering figure 5. 33, the cyclic dynamic force-deflection relationship can be expected to be more closely approximated by r=5 or 7, than by r=11 or 13.

In order to predict the dynamic response of a full scale structure, the recommended approach would be as follows. If the static virgin force-deflection curve for the structure was given, the problem would be to determine the magnitudes of the hysteresis effect and of the strain rate effect required to adjust r. Hopefully these effects could be determined from appropriate material specimens from the full scale structure. Then, using the adjusted r value, the dynamic response could be predicted as above.

This analysis does not take into consideration the structural deterioration. The reason for this is based primarily on comparing the dynamic peak response results, figures 4. 49, 4. 50 and 4. 51, with the initial virgin force-deflection curve of figure 4. 28.

In order to use a theoretical static skeleton curve to predict dynamic response, the theoretical analysis would have to be refined to account for its differences with the experimental skeleton curve.

Once this is accomplished, the procedure outlined above for using the experimental skeleton curve may be utilized with the adjusted theoretical curve.

VI. CONCLUSIONS

The following conclusions were reached on the basis of the experimental dynamic and static results of this investigation and by utilizing existing theoretical analyses.

1. It was shown in the comparisons of figures 4. 49, 4. 50, and 4. 51 that the differences between the dynamic and static hysteretic force-deflection curves were, in general, smaller than changes in the static curves caused by deterioration of the material. The major difference between static and dynamic hysteresis results occurred when the response amplitude was close to the initial yield deflection amplitude. This occurred after the material had reached a relatively stable force-deflection cyclic condition. For the frequencies, about 3 cps, and deflections, up to 2 times the initial yield deflection, of the experimental results presented here, the dynamic hysteresis curves may be assumed to be the same as the static hysteresis curves for most purposes.

2. The softening spring type of nonlinearity and ultraharmonic response associated with a nonlinear system occurred in the dynamic response of the yielding structure. Since the basic shape of the experimental and predicted frequency response curves were similar, only two fundamental characteristics of these curves were compared. The dynamic resonant response amplitude and the shift in resonant frequency with amplitude were compared with analytically predicted results based on a polynomial, equation 5. 110, approximation of the

experimental static virgin force-deflection curve. The predicted resonant frequency matched the experimental resonant frequency with sufficient accuracy, ± 2-1/2%, for all the polynomial approximations tried. The resonant deflection amplitude for a given sinusoidal force was not predicted as accurately. The best polynomial-skeleton curve approximation, r=11, produced the worst estimate of the resonant amplitude for large yielding. For this case at the largest experimental deflection, the predicted deflection was about 20% too small. Lower power polynomials produced a less satisfactory static skeleton curve approximation, but they gave a better estimate of the dynamic resonant amplitude.

3. The reason that the lower power polynomial-skeleton curve approximations gave better dynamic results can be explained by the nature of the hysteresis effect of the material which tends to change the sharp yield knee of the virgin structure to a much smoother force-deflection relationship for subsequent cycles.

4. The dynamic response characteristics were also compared with results predicted on the basis of polynomial approximations to static hysteresis loops and a theoretical static force-deflection curve. Both methods were found to give unsatisfactory dynamic predictions. The hysteresis loop method gave a good force-response amplitude prediction only at deflections close to the amplitude of the hysteresis loop. Thus, the force-response amplitude prediction could be made step wise with a selected series of static hysteresis loops of various amplitudes.

5. The energy absorbed per cycle and the equivalent viscous damping were determined because of their significance in the earthquake resistant design of buildings. The maximum fraction of equivalent viscous damping was found from the dynamic experiments to be 0.089 at a deflection of over 2-1/4 times the initial yield deflection.

6. The theoretical static force-deflection relationship based on actual material properties and assumed plane bending predicts larger forces than obtained in the experimental static force-deflection relationship. The discrepancy lies in two regions. First, the experimental structure initiates yielding before the theoretical curve prediction. The cause for this was determined to be initial residual stresses in the experimental structure and the neglect of the axial stresses in the analysis. Second, the theoretical fully plastic moment was not attained in the experiment. This resulted from the fact that the theoretical yield stress was determined from tension tests performed at a higher strain rate than existed during the static skeleton curve experiment.

7. Structural deterioration and recovery caused by testing and rest periods, respectively, were observed. The deterioration continued at a decreasing rate until a relatively stable hysteretic force-deflection relationship was established. (This corresponds to strain softening in figure 1.2.) If the recovery time was long enough, the structure recovered to a strength greater than its initial strength. However, when resuming the experiments after recovery, the number

of cycles necessary to return the structure to its stable relationship was substantially reduced. The area of the static deflection limited hysteretic force-deflection curve increased with testing.

8. Up to a 20% decrease in the dynamic resonant response was caused by the structural deterioration during the experimentation.

9. When the deflection is caused by flexural yielding of a column, the effect of strain hardening is to distribute the yielding section to more material. The result in the experiments presented here was that the desired deflections were obtained with lower maximum strains than would be predicted by neglecting strain hardening.

10. One means of investigating structural damage is to compare the existing natural frequencies with the original frequencies and to determine any change in the position of the center of stiffness of the structural system. Only small changes in the natural frequency can be expected but these may indicate significant damage. The change in position of the center of stiffness will indicate the location of the damage.

11. The determination of dynamic hysteresis force-deflection curves requires a very close analysis of possible errors in order to obtain valid results.

12. The work presented here points out the need for more information in the following areas: (a) Comparison of static and dynamic hysteresis loops should be extended to additional excitation frequencies, strain ranges, and materials. (b) A method of selecting

the most appropriate theoretical force-deflection relationship will have to be developed before the predicted dynamic results can be accepted with confidence. (c) The work started here should be extended to the experimentation of multistory yielding structures. (d) The effect of intermittent loading on material characteristics such as the low endurance fatigue life and the energy absorption should be investigated.

REFERENCES

1. Suyehiro, K., "Engineering Seismology", Proceedings, ASCE, 58(5):1, (May, 1932).

2. Biot, M. A., "Analytical and Experimental Methods in Engineering Seismology", Transactions, ASCE, 108:365, (1943).

3. Housner, G. W., Martel, R. R., and Alford, J. L., "Spectrum Analysis of Strong-Motion Earthquakes", Bulletin of the Seismological Society of America, 43(2):97, (1953).

4. Hudson, D. E., "Response Spectrum Techniques in Engineering Seismology", Proceedings of the World Conference on Earthquake Engineering, Berkeley, (1956).

5. Housner, G. W., "Behaviour of Structures During Earthquakes", Journal of Engr. Mech. Div., ASCE, vol 85, No. EM4, (October, 1959), pp. 109-129.

6. Housner, G. W., "Limit Design of Structures to Resist Earthquakes", Proceedings of the World Conference on Earthquake Engineering, Berkeley, (1956).

7. Housner, G. W., "The Plastic Failure of Frames During Earthquakes", Proceedings, Second World Conference on Earthquake Engineering, Tokyo and Kyoto, (1960), p. 997.

8. Blume, J. A., "A Reserve Energy Technique for the Earthquake Design and Rating of Structures in the Inelastic Range", Proceedings, Second World Conference on Earthquake Engineering, Tokyo and Kyoto, (1960), p. 1061.

9. Berg, G. V., "Analysis of Structural Response to Earthquake Forces", Report IP-291, Univ. of Michigan: Engineering College Industry Program, (May, 1958).

10. Veletsos, A. S., and N. M. Newmark, "Effect of Inelastic Behavior on the Response of Simple Systems to Earthquake Motions", Proceedings, Second World Conference on Earthquake Engineering, Tokyo and Kyoto, (1960), pp. 895-912.

11. Hudson, D. E., "Equivalent Viscous Friction for Hysteretic Systems with Earthquake-Like Excitations", Proceedings, Third World Conference on Earthquake Engineering, New Zealand, (1965).

12. Benham, P. P., and Ford, H., "Low Endurance Fatigue of a Mild Steel and an Aluminum Alloy", Journal of Mechanical Engineering Science, Vol. 3, No. 2, (1961).

13. Pardue, T. E., Melcher, J. L., and Wood, W. B., "Energy Losses and Fracture of some Metals Resulting from a Small Number of Cycles of Strain", Proceedings, Society for Experimental Stress Analysis, Vol. 7, No. 2,(1950), pp. 27-39.

14. Low, A. C., "Short Endurance Fatigue", Proceedings, International Conference on Fatigue of Metals, Institution of Mechanical Engineers, London, 1956, pp. 206-211.

15. Bertero, V. V., and Popov, E. P., "Effect of Large Alternating Strains on Steel Beams", Journal of the Structural Division, ASCE, Vol. 91, No. ST1, (February, 1965), pp. 1-12.

16. Commentary on Plastic Design in Steel, Welding Research Council and the American Society of Civil Engineers, 1961. (ASCE Manual of Engineering Practice, No. 41).

17. Jacobsen, L. S., "Friction Effects in Composite Structures Subjected to Earthquake Vibrations", Technical Report, Dept. of Mechanical Engineering, Stanford University, (March, 1959).

18. Medearis, K. and Young, D. H., "Energy Absorption of Structures under Cyclic Loading", Journal of the Structural Div., ASCE, Vol. 90, No. ST1, (Feb., 1964).

19. Caughey, T. K., and O'Kelly, M. E. J., "General Theory of Vibration of Damped Linear Dynamic Systems", Dynamics Laboratory Report, California Institute of Technology, (June, 1963).

20. O'Kelly, M. E. J., "Vibration of Viscously Damped Linear Dynamic Systems", Dynamics Laboratory Report, Ph. D. Thesis, California Institute of Technology, (May, 1964).

21. Crandall, S. H., and Mark, W. D., Random Vibration in Mechanical Systems, Academic Press, New York, 1963.

22. Bendat, J. S., Principles and Applications of Random Noise Theory, John Wiley and Sons, New York, 1958.

23. Hudson, D. E., "Some Problems in the Application of Spectrum Techniques to Strong-Motion Earthquake Analysis", Bulletin of the Seismological Society of America, Vol. 52, No. 2, (April, 1962), pp. 417-430.

24. Housner, G. W., and Jennings, P. C., "Generation of Artificial Earthquakes", Journal of the Engr. Mech. Div., ASCE, Vol. 90, No. EM1, (Feb., 1964), pp. 113-150.

25. Merchant, H. C., "Mode Superposition Methods Applied to Linear Mechanical Systems under Earthquake Type Excitation", Earthquake Engineering Research Laboratory Report, California Institute of Technology, (March, 1961).

26. Caughey, T. K., "The Existence and Stability of Ultraharmonics and Subharmonics in Forced Nonlinear Oscillations", Journal of Applied Mechanics, Vol. 21, No. 4, (December, 1954), pp. 327-35.

27. Caughey, T. K., "Sinusoidal Excitation of a System With Bilinear Hysteresis", Journal of Applied Mechanics, Vol. 27, No. 4, (December, 1960), pp. 640-643.

28. Jennings, P. C., "Periodic Response of a General Yielding Structure", Journal of the Engr. Mech. Div., ASCE, Vol. 90, No. EM2, (April, 1964), pp. 131-166.

29. Iwan, W. D., 'Steady-State Response of a Double Bilinear Hysteretic Model", to be published in the Journal of Applied Mechanics, ASME.

30. Iwan, W. D., 'The Dynamic Response of Bilinear Hysteretic Systems", Earthquake Engineering Research Laboratory Report, California Institute of Technology, (July, 1961).

31. Hudson, D. E., "Synchronized Vibration Generators for Dynamic Tests of Full-Scale Structures", Earthquake Engineering Research Laboratory Report, California Institute of Technology, (November, 1962).

32. Hudson, D. E., "Resonance Testing of Full-Scale Structures", Journal of the Engineering Mechanics Division, ASCE, Vol. 90, No. EM3, (June, 1964), pp. 1-19.

33. Lewis, F. M., "Vibration During Acceleration Through a Critical Speed", Transactions, ASME, APM-54-24, (1932), pp. 253-261.

34. Timoshenko, S. and Young, D. H., Vibration Problems in Engineering, D. Van Nostrand Company, Inc., Princeton, New Jersey, 1955, 3rd Ed., pp. 104-111.

35. Nielsen, N. N., "Steady-State Versus Run-Down Tests of Structures", Journal of the Structural Division, ASCE, Vol. 90, No. ST6, (December, 1964), pp. 51-64.

36. Kimball, A. L., 'Friction and Damping in Vibrations, Parts IV and V of Vibration Problems Design Data", Journal of Applied Mechanics, ASME, Vol. 8, (March, 1941 and September, 1941).

37. Jacobsen, L. S., "Frictional Effects in Composite Structures Subjected to Earthquake Vibrations", Department of Mechanical Engineering, Stanford University, Stanford, (1959).

38. N. H. Nautical Almanac Office, Interpolation and Allied Tables, Her Majesty's Stationery Office, London, (1956), p. 70.

39. Freudenthal, A. M., The Inelastic Behavior of Engineering Materials and Structures, John Wiley & Sons, New York, 1950 .

40. Neal, B. G., The Plastic Methods of Structural Analysis, John Wiley & Sons, Inc., New York, 1963, 2nd. Edition.

41. Timoshenko, S. and Goodier, J. N., Theory of Elasticity, McGraw-Hill Book Co., New York, 1951, 2nd Edition.

42. Jennings, P. C., "Response of Simple Yielding Structures to Earthquake Excitation", Earthquake Engineering Research Laboratory Report, California Institute of Technology, (June, 1963).

43. Yang, C. H., Beedle, L. S. and Johnston, B. G., "Residual Stress and Yield Strength of Steel Beams", Welding Journal, Research Supplement, (April, 1952), pp. 205-s to 229-s.

44. Parkes, E. W., "The Permanent Deformation of a Cantilever", Proceedings of the Royal Society, Series A, Vol. 228, (1955), pp. 462-476.

45. Moore, H. F., and Kommers, J. B., The Fatigue of Metals, McGraw-Hill Book Co., New York, 1927.

46. Lubahn, J. D. and Felgar, R. P., Plasticity and Creep of Metals, John Wiley & Sons, New York, 1961.

47. Lipson, Charles and Juvinall, R. C., Handbook of Stress and Strength, Design and Material Applications, Macmillan Company, New York, 1963.

48. Miner, M. A., "Cummulative Damage in Fatigue", Journal of Applied Mechanics, Vol. 12, Trans., ASME, Vol. 67, (1945), pp. 159-164.

49. Manjoine, M. J., "Influence of Rate of Strain and Temperature on Yield Stresses of Mild Steel", Journal of Applied Mechanics, Vol. 11, Trans., ASME, Vol. 66, (1944), pp. A211-18.

50. Wood, D. S. and Clark, D. S., "The Influence of Temperature upon the Time Delay for Yielding in Annealed Mild Steel", Trans. Amer. Soc. for Metals, Vol. 43, (1951), pp. 571-86.

51. Nadai, A. and Manjoine, M. J., "High-Speed Tension Tests at Elevated Temperatures, Parts II & III", Journal of Applied Mechanics, Vol. 8, Trans., ASME, Vol. 63, (1941), pp. A77-91.

52. Lysaght, Vincent E., Indentation Hardness Testing, Reinhold Publ. Corp., New York, 1949.

APPENDIX I: INSTRUMENTATION AND FORCE GENERATORS

In reporting the results of any experimental study, it is important to give a detailed description of the experimental subject and the instrumentation used. This is, of course, so that the reader may be able to judge the accuracy, reliability and applicability of the results for his purpose based on his own experience.

Familiarity with the experiment and instruments is required for the experimenter, but this familiarity also encourages omission of common details necessary for the reader to receive the proper perspective. Since a favorable judgement of the reliability of the results is necessary for the results to be acceptable, the writer will make a special effort to give enough information for this judgement to be made.

A. Instrumentation for Dynamic Experiments

It has been the good fortune of the writer that much effort has previously been made by the Faculty and students at the California Institute of Technology to establish a dynamic measurement system for the dynamic response of full-scale civil engineering structures. This eliminated the time-consuming task of gathering the needed equipment together and checking the suitability of the composite measurement system to the specific measurement problems encountered. However, in order to meet individual requirements and desires, the given measurement systems had to be modified and supplemented.

1. Accelerometers

Two completely independent measurement systems were tried before selecting and adapting the system used for most of the experimental dynamic measurements. The accelerometers used with both systems were Statham ± 2g accelerometers type A5-2-350, serial numbers 12133, 12134 and 12122. These accelerometers have an undamped natural frequency of 100 cps with a liquid damping of 0.7 ± 0.1 fraction of critical damping and, therefore, are effectively linear at least up to 30 cps. The accelerometers were not frequency calibrated by the writer absolutely, but were cross calibrated in the frequency range used with a maximum disagreement of about 2 percent at an acceleration of 0.165 gravity. The static ± 1g method of calibration was used before and after each test. At an excitation frequency of 5 cps, the possible error in the phase of the acceleration caused by the 0.7 ± 0.1 damping range is ± 0.6 degrees. For a frequency of 2 cps, it is ± 0.24 degrees.

2. Linear Variable Differential Transformer

The deflection was measured with a Shaevitz LVDT type 1000-SL which has a range of ± one inch. When a calibration curve for this LVDT was made, it was found that the linear range was $\pm \frac{1}{2}$ inch and that near the deflection of 0.9 inch there was almost no increase in output voltage for an increase in deflection. For this reason and because of the critical need for the exact phase relationship between acceleration and deflection, the LVDT was only used for small deflections as a check of the acceleration results. The

accuracy of the deflection was about ± 0.002 inch in the range of 0.200 to 0.300 inch deflections. The acceleration and deflection results agreed within the stated accuracy.

3. Strain Gages

Two similar strain gates were mounted on opposite sides of one of the column end sections 1.88 inches from the column end and were connected in the adjoining legs of a resistance bridge so that the sum of the flexural strains would be recorded. Two different types of post-elastic strain gages were used. The first was a Baldwin-Lima-Hamilton SR4 Type PA-3 gage with a gage factor of 1.95 and a resistance of 120 ohms. The second was a miniature Micro-Measurements precision strain gage Type EP-03-125CA-120 which had a gage factor of 2.01 and a resistance of 120 ohms. The other two legs of the resistance bridge consisted of one 120 ohm resistor and an 84 ohm resistor in series with a variable resistor of 54 ohms maximum resistance. The variable resistor was needed to balance the bridge because the balance resistor of the Miller carrier-amplifier did not have a large enough resistance range. The strain was calibrated by either connecting a known amplifier resistance in parallel across one leg of the bridge or by externally adding a known resistance in parallel across one of the strain gage legs.

4. Amplifiers and Recorders

The first system used consisted of two Sanborn dual channel carrier-amplifier recorders, Model No. 321-406368, for recording

three accelerations and one strain. The Brush Universal Amplifier, Model No. RD-5612-11, together with a Brush Pen Motor Recording Oscillograph, Model No. RD-2321-00, was used for deflection records. The reading error for the Sanborn and the Brush systems was 1/4 mm. in 20 mm. or 1-1/4 per cent. This system has been used extensively for the dynamic testing of multistory reinforced concrete and structural steel buildings with excellent results. One of the major advantages, in addition to its easy transportability, is that the records obtained withstand a great deal of rough handling without any impairment and also the records can be easily reproduced. Some of the disadvantages for using this system for these experiments are: i) three separate paper records were required for one set of data, thus, requiring an accurate method of establishing an identical time base for each record; ii) the natural frequency of the amplifier-recorder was high enough to transmit the noise generated by the chain driven force generators. This made any low acceleration readings very hard to use and relatively inaccurate; and the major reason for not using this system, iii) the time or external event marker uses a 60 cps carrier frequency, which is inadequate when the phase angle between deflection and force is desired. For example, if the force generator is operating at 3 cps, the phase could be determined within approximately ± 18 degrees. Rather than modifying the internal electrical system of the Sanborn carrier-amplifier recorder, a different system was tried.

The second system which was used for a majority of the

experimental work was originally used for testing a reinforced concrete reservoir intake tower. Because of the low amplifier noise generation, it was also used with more sensitive accelerometers for dynamic testing of earth dams. This system consisted of the William Miller Type C-3 carrier-amplifiers with the Consolidated Electrodynamics Recording Oscillograph, Model 5-124. The amplifier provides a 3000 cps carrier bridge excitation adjustable up to 10 volts. The accelerometers and LVDT were balanced very easily with this amplifier, but the resistance balance range was not large enough to balance the strain gage bridge without adding a variable resistor as one of the legs of the bridge. Six carrier-amplifiers with one power supply were in one unit, which was sufficient for this experiment. The amplifiers were remarkably stable for long periods of time.

The Brush Universal Amplifiers have also been used occasionly by replacing one or two of the Miller channels with satisfactory results. The advantage of using a group of amplifiers tied to the same time base and recording simultaneously on one sheet of paper is obvious. Also by putting the phase pulse directly into a galvanometer, a possible phase lag caused by the carrier frequency is eliminated and the time response of the pulse is dependent only upon the rise time of the galvanometer and the time of the pulse.

The CEC Recording Oscillograph is a light beam galvanometer type which records on light sensitive paper. The 7-351 type galvanometers, 20 cps natural frequency, were used for most of the data recording with 7-341 type, 100 cps natural frequency, and 7-315 type,

150 cps natural frequency, galvanometers used for some data and the external force pulse.

Phase Shift. The need for an accurate determination of the phase difference between force and deflection has been noted previously. Since the force pulse was recorded instantaneously, the accuracy of the measured phase difference was dependent upon an accurate determination of the phase shift of the recorded acceleration. Remember that the deflection was obtained by numerical integration of the acceleration. The time lag (phase shift) between the occurrence and the recording of a sinusoidal motion is a characteristic of the recording system and the frequency of the motion. This characteristic is dependent primarily on the damping and natural frequency of the instrumentation, see equation 2. 29.

Since the natural frequencies of the instruments are recorded above, the following discussion will be restricted to a consideration of the damping. The damping of each amplifier-galvanometer system was determined by measuring the overshoot of a step function generated by an instantaneous change in a resistance of the bridge. After the amplifier was balanced with the standard bridge in the position normally occupied by the transducer, the oscillograph was started and a series of steps, 8 or more, were recorded.

The equation of the resulting deflection of a viscously damped single-degree-of-freedom system

$$m\ddot{x} + c\dot{x} + kx = F \qquad \text{(A1. 1)}$$

to a constant force F step function is

$$x = \frac{F}{K}\left[1 - e^{-n\omega_n t}\left(\cos\sqrt{1-n^2}\,\omega_n t + \frac{n}{\sqrt{1-n^2}}\sin\sqrt{1-n^2}\,\omega_n t\right)\right] \quad \text{(Al. 2)}$$

where $\omega_n = \sqrt{K/m}$ and the fraction of critical damping is $n = c/c_c = c/2\sqrt{Km}$. The overshoot ratio is equal to

$$-e^{-n\omega_n t}\left(\cos\sqrt{1-n^2}\,\omega_n t + \frac{n}{\sqrt{1-n^2}}\sin\sqrt{1-n^2}\,\omega_n t\right) \quad \text{(Al. 3)}$$

divided by one when equation Al. 3 reaches its first positive maximum value.

The mean damping value and the range of values for the series of step functions for each amplifier-galvanometer were obtained from equation Al. 3. The phase shifts for the amplifier-recorder system used for most of the data reduction is plotted in figure Al. 1. The experimentally determined damping for this 20 cps system was 0.705 ± 0.010. The phase shifts of the accelerometers are also plotted in figure Al. 1. The 100 cps amplifier-recorder system has a phase shift relation almost identical with the accelerometer. At an excitation frequency of 3 cps, the phase shift of the 20 cps recorder and 100 cps accelerometer would total about 15 degrees. Similarly, for the 100 cps recorder and 100 cps accelerometer, it would total 5 degrees. The maximum error associated with the changes in the damping factor is less than $\pm$ 1 degree. The galvanometer output is linear within one per cent for the recording deflection range of $\pm$ 20 lines from the balanced position.

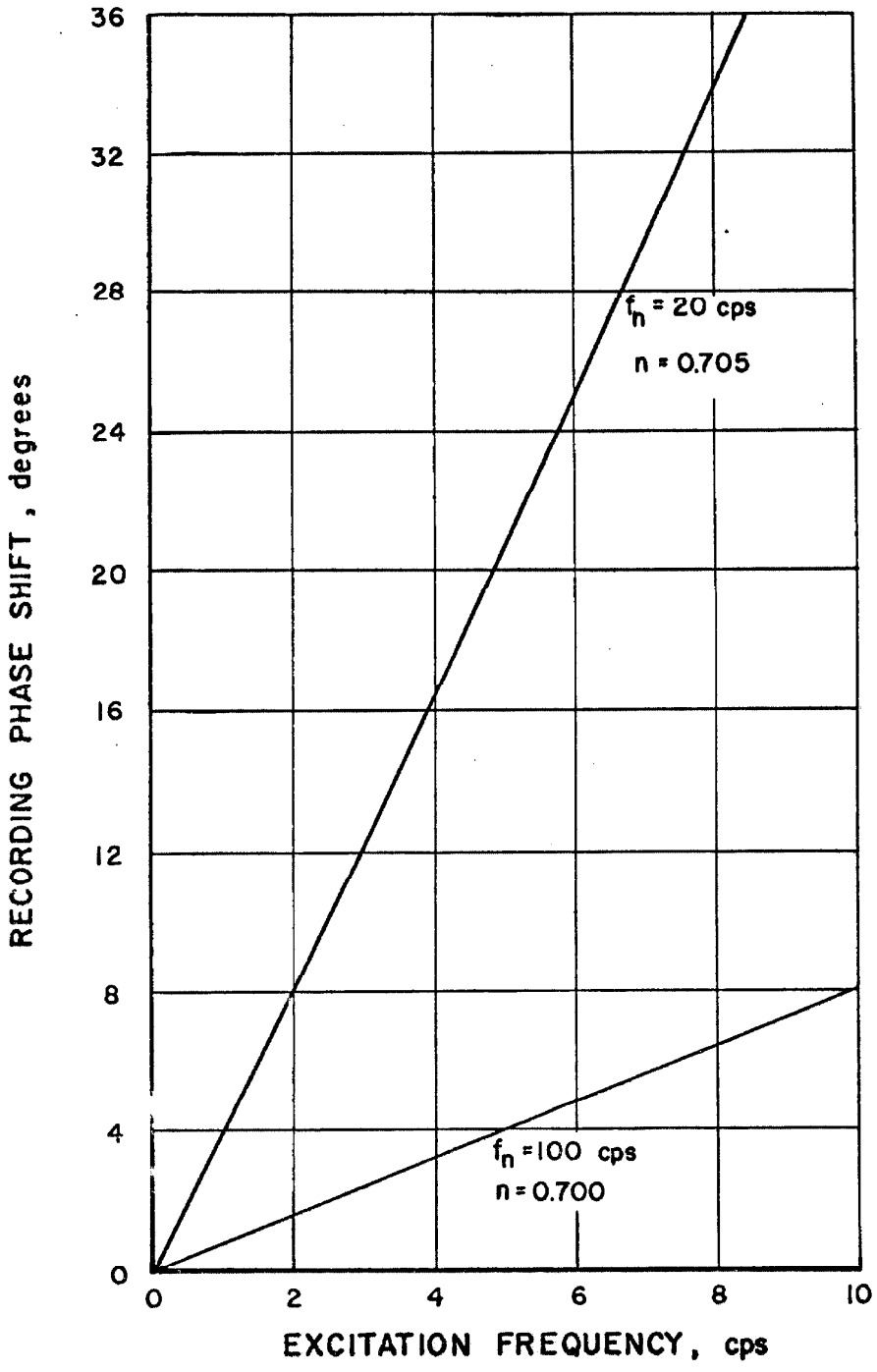

FIG. A1.1 PHASE SHIFT IN RECORDING SINUSOIDAL MOTION

The major disadvantage of this system is that the records are taken on light sensitive paper which requires special handling to preserve the results while analyzing them. This problem is not quite as serious working indoors under artificial light as it is in sunlight. The records are also very difficult to reproduce.

Errors. Since the second system was used for recording almost all the dynamic data, only this system will be considered further. The maximum reading error of the oscillograph records was ± 0.1 line in 20 lines or ± $\frac{1}{2}$ percent of the reading. For example, a 0.200 g acceleration would have a maximum reading error of ± 0.001 g. The concern with the drift of the zero position expressed for the static measuring system was not necessary for the dynamic system unless a specific base line was desired. Thus, for all dynamic measurements an arbitrary base line was used.

The static ± 1 g calibration of the accelerometers consisted of balancing the amplifier with the accelerometer mounted in its recording position and then rotating 90 degrees in the sensitive direction for a 1 g reading and back 180 degrees for a minus 1 g reading. Since the amplitudes measured for each 1 g calibration are not exactly equal, the average of the double amplitude or 2 g reading was used. The accelerometers are mounted in milled rectangular steel blocks to simplify the calibration process. The reason for the difference in calibration in the + 1 g and -1 g directions can be accounted for by a slight slope from the horizontal of the accelerometer in its balanced position of about $\frac{1}{2}$ degree. Whether this was the slope of the local top flange of

the rigid floor or an error in placing the accelerometer in its steel block is not important because it does not affect the resulting dynamic output of the accelerometer.

The amount of error associated with assuming that the deflection amplitude x_o equals minus one-half of the acceleration double amplitude divided by the circular frequency ω squared, i.e.,

$$x_o = -\frac{2\ddot{x}_o}{2\omega^2} \qquad \text{(A1. 4)}$$

has been determined for several of the acceleration records varying the most from sinusoids by numerical integration of the actual acceleration with the Burroughs 220 Datatron digital computer. For dynamic test A3. 64 the deflection calculated from equation A1. 4 was 0. 816 inch and the deflection by double integration of the acceleration was 0. 810 inch. Similarly for A3. 69 (100 cps), the deflection values were 0. 791 and 0. 790 inch respectively. The deflection differences caused by the approximate calculation, equation A1. 4, will be neglected.

In certain instances the 2g calibration of an accelerometer had changed during the time required to run the test as much as 0. 4 line in 40 lines, but the usual change was less than 0. 2 line in 40. The maximum possible error associated with using the average calibration value is $\pm \frac{1}{2}$ percent. Adding this calibration error to the reading error gives a maximum error due to these two causes of ± 1 percent. It is reasonable from this analysis to expect that the accelerations are valid within ± 2 percent for the maximum combination of errors. For example, this would amount to a maximum error of ± 0. 004 g for

an acceleration reading of 0. 200 g.

5. Force Pulse

The force pulse was generated by fixing a small bolt on the top rim of the upper basket of the force generator and locating an induction pickup so that the induction pickup and the bolt were together when the force reached either a maximum or a zero amplitude. The current induced as the bolt passed the pickup at a constant velocity was read directly by a galvanometer in the CEC recording oscillograph. The maximum total length of the recorded pulse for the frequency range used in the tests was about 4 degrees of rotation. By using the center of the pulse for measurements, the probable error in the force-phase pulse was ± 1 degree. Including possible reading errors of the location of the acceleration record, the maximum error in the measured phase position should be expected to be in the range of ± 3 degrees.

B. Instrumentation for Static Experiments

Static force-deflection curves for the structure were obtained by measuring the force required to impose a prescribed deflection of the structure. A frame bolted to the foundation supported a gear system which drove a threaded rod horizontally. The force gage was connected between the experimental structure and the threaded rod. One revolution of the external drive of the gear system corresponded to 0. 025 inch of horizontal motion of the structure. The advantage of this system was that very small increments of deflection could be

imposed on the structure.

The deflections were measured with Starrett® dial indicators having a maximum travel of one inch and marked subdivisions of 0.001 inch. The dial indicators could have been read within 0.1 of the smallest subdivision, i.e., ± 0.0001 inch, but this accuracy was not required so the dial indicators were usually read to the nearest 0.001 inch. Two dial indicators were placed symmetrically with respect to the center line of the structure about mid-height of the rigid floor. The average deflection was rounded to the nearest 0.001 inch for plotting.*

For the preliminary static studies in the weak direction (East-West) of column LI, a low capacity force gage with noticeable non-linearities (see figure A1.2 for the tension calibration curve) was used in connection with a Baldwin SR4 Dial Indicator. After these few preliminary curves were obtained, a new load cell, Allegany Instrument Company, Model No. 35-133-BCF, Serial No. 27149, with a 3000 pound tension-compression capacity was obtained for this work. The maximum combined error of this load cell is 2.1 pounds. The Brush Universal Amplifier was originally intended for use with this load cell, but the D.C. drift could not be eliminated or sufficiently diminished. Therefore, the Miller Type C-3 Amplifier was used with the Consolidated Electrodynamics, Model No. 5-124, recording oscillograph with a 7.351 type galvanometer. A dead load calibration

*In the original loading system a slight eccentricity in the gear system caused a cork screw type of deflection of the structure. The two deflections varied by a maximum of 0.016 inch when the distance between the dial indicators was 64.25 inches, or about 0.00025 radians of rotation.

FIG. A1. 2 CALIBRATION OF OLD FORCE GAGE

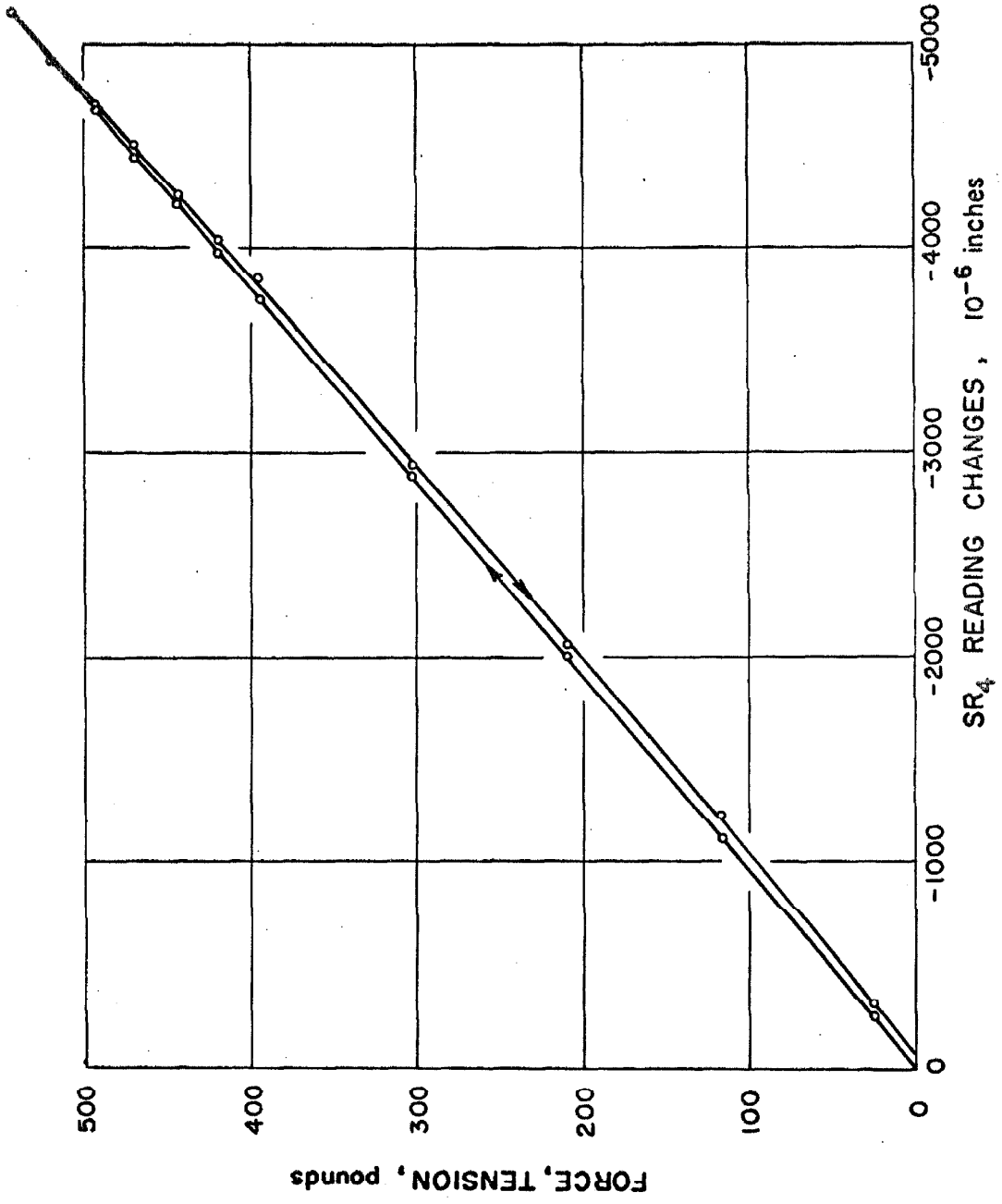

of the load cell with the Miller amplifier, channel no. 76, and CEC recorder was made in approximately 100 pound increments to 488.1 pounds. A full range factory calibration was furnished with the load cell. The maximum expected error of about ± 0.4 percent is associated with reading accuracies of the recorder and assumes that the small amount of drift, which is basically a drift in zero position with the Miller amplifier, was linear between positions of drift check. This drift check was obtained simply by turning the amplifier to zero gain and recording the drifted position of the base line. Although the amount of the drift (about 1/15 of the unreduced reading per hour) was small compared with the Brush amplifier, it could correspond to approximately 15 times the maximum reading error if neglected.

Measurements of the strain at the specific sections noted previously were taken simultaneously with the load and deflection in most of the static studies.

Summarizing the possible maximum errors in the static experiments by neglecting any rotation of the rigid floor, they are: ± 0.0005 inch for deflections and ± 1 percent for forces.

C. Possible Errors in Dynamic Hysteresis Loops

Assuming that no errors are accumulated in the integration procedures, that the effective structural weight was 4200 pounds, and that the accelerometer calibration was about 20 lines per gravity, the possible range in error in R(x) caused by ± 0.1 line reading error of data taken at a frequency of 3 cps with the same amplifier gain as

with the calibration can be found from the $m\ddot{x}$ term of R(x) to be

$$m\ddot{x} = \pm \frac{0.1}{20} (4200) = \pm 21 \text{ pounds} \qquad \text{(A1. 5)}$$

In certain cases where the slope of the acceleration record is great, the error may be twice the amount given in equation A1. 5.

D. The Force Generators[31]

1. General

The mechanical generator itself consists of a pair of counter-rotating eccentric counter-balanced baskets located on a common vertical shaft and driven in opposite directions by a chain drive system. When the baskets have equally distributed additional weights, a rectilinear sinusoidally varying horizontal inertia force is generated. The direction of the sinusoidal force is not limited by the mounting position of the force generator. The weights for normal full-scale structural testing have been made of lead, but for the work reported here wood, aluminum and steel weights have also been used.

The force amplitude generated is

$$\text{Inertia force (pounds)} = F_o = 0.102\, wR\, f^2 \qquad \text{(A1. 6)}$$

where w is the weight added to the baskets in pounds, R is the distance from the centroid of the weights to the axis of rotation in inches and f is the excitation frequency in cps. Using only the small size weight, equation A1. 6 reduces to

$$F_o = B\, f^2 \qquad \text{(A1. 7)}$$

where

$$B = 1.02w \qquad \text{(A1. 8)}$$

because $R \approx 10$ inches. In equation A1. 8 w is the total weight added to both baskets. The maximum value of F_o is 5000 pounds per generator which is the limit based on the mechanical strength of the generators.

The chain drive system is driven by a 1-1/2 horsepower D. C. motor through a timing belt which has a 3:1 speed reduction. The drive motor and the tachometer assembly can be disconnected from the generator for easier handling, transportation and installation.

The requirements of the electrical drive-control system are particularly stringent because of the variable torques imposed on the system and the necessity of insuring the stability of the whole vibrating system when operating near the resonance of lightly damped structures. The ability to hold an accurate speed control at and near the resonance peak requires that the speed-torque curve of the drive system be unusually steep with essentially a constant speed maintained at relatively large torque variations. The requirements of speed control also require a speed variation over a relatively large speed range (up to 10 cps). The 1-1/2 H. P. D. C. motor with a servo-controlled electronic amplidyne system was used to meet these requirements.

2. Torque Limitation

The torque limitation of the force generator was observed while testing columns SII. Since this was the first time that this opportunity has occurred, an analysis of this limitation is presented.

The shunt wound D. C. motor is rated at 1-1/2 horsepower at

1750 rpm which corresponds to a rated motor torque of 54 pound-inches. Since the motor speed is varied by changing the impressed voltage and the air gap flux is relatively constant, the motor torque is proportional to the armature current. This means that the motor draws enough current to overcome the resisting torques and is independent of the motor speed. Therefore, with the 3:1 gear reduction, the rated force generator torque for all test speeds is 162 pound-inches.

The torque requirements due to all factors other than motion of the force generator will be initially disregarded in this discussion although they are not negligible. The experiment in which a torque limit was reached is reported in Appendix III as test A3.46. With the notation as given in Chapter II and figure A1.3, the resisting torque due to a sinusoidal displacement of the force generator

$$x = x_o \sin(\omega t - \phi) \tag{A1.9}$$

is

$$\text{Torque} = -2m\,\omega^2 x_o \sin(\omega t - \phi)\, R \cos \omega t \tag{A1.10}$$

where ϕ is the phase lag of the deflection relative to the exciting force, m is the eccentric mass and R is the radius to the eccentric mass. The average torque required is

$$\begin{aligned} \text{Ave. Torque} &= \frac{1}{2\pi} \int_0^{2\pi} -2m\omega^2 x_o R \sin(\omega t - \phi)\cos \omega t \, d(\omega t) \\ &= \frac{1}{2\pi} (2m\,\omega^2 x_o R)\, \frac{2\pi}{2} \sin \phi \\ &= mR\,\omega^2 x_o \sin \phi \end{aligned} \tag{A1.11}$$

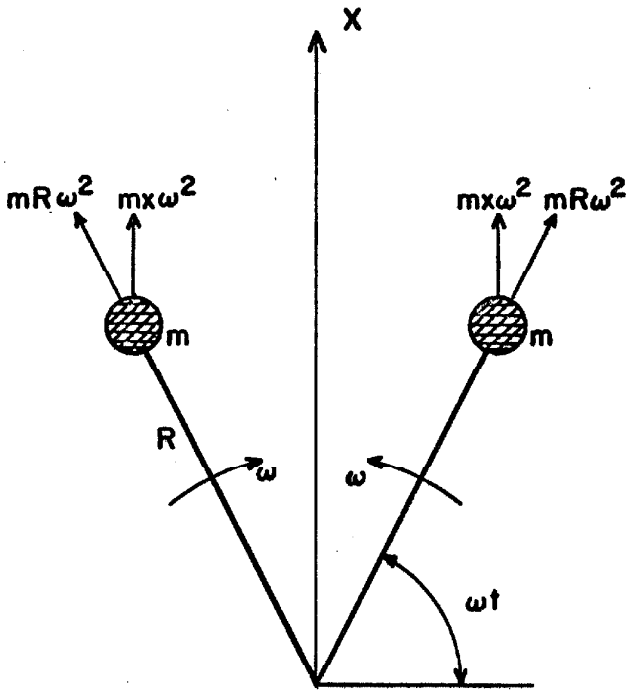

FIG. A1. 3 COUNTER ROTATING ECCENTRIC WEIGHTS

From test A3.46, mR = 403.7/g, $\omega^2 x_o$ = 0.715 g and ϕ = 60 degrees at 3 cps. Substitution into equation A1.11 gives the average torque to be 250 pound inches.

If it is now assumed that the torque requirements for friction and wind losses increase as the square of the speed to the rated torque limit at 10 cps with no base motion, then the sum of the actual torque available from the motor (friction and wind and motion) is 265 pound-inches. This is 164 percent of the rated torque supplied.

APPENDIX II: MATERIAL PROPERTIES

Introduction

In order for the dynamic and static experimental results reported in this paper to have maximum significance, it is necessary that the material be identified more specifically than "a mild structural steel". The easiest way to establish the material classification, without knowledge of its manufacturing history, is to determine its hardness and mechanical properties by a standard tensile test. A chemical determination and a metallographic examination are also included.

Since it is the material of the column end "I" sections which is of interest, the question arises of where the appropriate sample specimen should be taken. In the dynamic and static experiments the web of the "I" section is in a state of flexure in the flange to flange direction, thus, the appropriate specimen would seem to be a section of the web with tensile loads applied at the opposite flanges. The possibility of taking a longitudinal specimen of the web rather than a short transverse specimen was considered, but since the cost of the two types of specimen were the same, the transverse specimen was selected.

The question of different material properties in different directions due to rolling effects does not occur in translating these results for use in the structural analysis because the material properties being tested are the same as desired for the dynamic and static tests.

Material Tested

The short column sets 1, 2 and 3 were made at the same time with material from two 5 I 14. 75 beams believed to be of the same heat. A short section of each beam was taken for testing. Rockwell Hardness Tests were run on each piece, numbered #1 and #2, after one tensile specimen, No. 1, was taken from piece #1 and two tensile specimens, No. 2 and No. 3, were taken from piece #2. Figure A2. 1 shows the tensile specimen in relation to the "I" section. The material was believed to be a mild structural steel.

The material of column set LI has no direct relation to the material of the other columns and this material was subjected to only the Rockwell Hardness Test. This specimen has been designated as #L.

Rockwell Hardness Test

The standard Rockwell B100 Test with a 1/16 inch diameter ball was used. The testing machine calibration was checked with a standard block of 37. 7 ± 1. 5 hardness with the B100 test. The value obtained was 36. 7, which is within the tolerance, so the hardness test values were accepted as read.

With the web surfaces prepared only by polishing with a steel wire brush, the resulting hardness values are given in Table AII-1. After carefully hand grinding the surface of piece #2, the hardness values changed to those also given in Table AII-1. Converting the average value of the Rockwell Hardness Number (RHN) to a corresponding Brinell Hardness Number (BHN) by

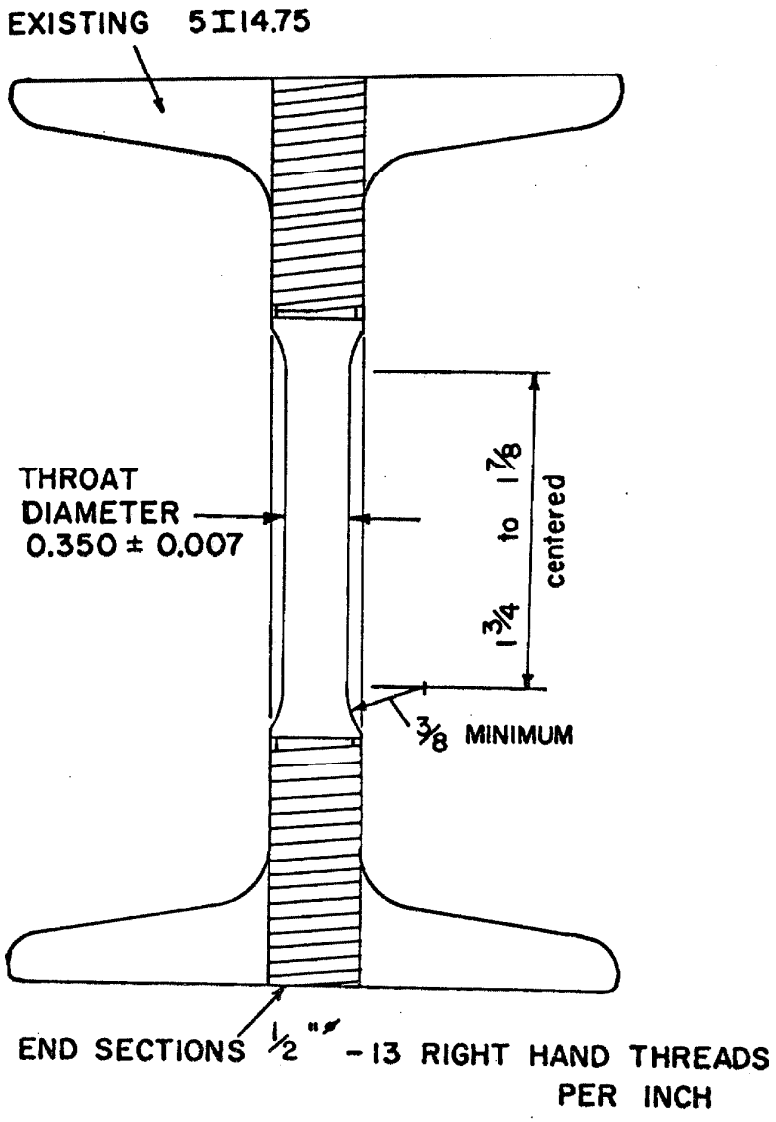

FIG. A2. 1 TENSILE SPECIMENS

TABLE AII-1

Rockwell Hardness Numbers

Specimen	No. of Readings	Ave. Value	Mean Value	Range
# 1	Wire Brushed Surface			
Side 1	7	74.9	75	-3, +2
Side 2	8	77.6	78	-8, +6
# 2				
Side 1	9	72.8	72.5	-2.5, +4.5
Side 2	4	78.2	78	-1, +2
# 2	Hand Ground Surface			
Side 1	13	75.9	76.0	-1.8, +2.0
Side 2	10	79.0	79.0	-1.4, +1.8
# L				
Side 1	10	76.7	76.5	-2.2, +2.0
Side 2	10	75.1	75.2	-1.7, +1.3

$$BHN = \frac{7300}{130-(RHN)} \qquad (A2.\ 1)$$

which is valid for $40 \leq RHN \leq 100$. The estimated ultimate tensile strength in psi is found by

$$f_u = 515(BHN) \qquad (A2.\ 2)$$

for $BHN < 175$, see reference (52). Equation (A2. 2) gives the ultimate tensile strength to be about 69, 000 psi.

Tensile Tests

A standard tensile test was performed with a Tinius Olsen Testing Machine on three specimens as shown in figure A2. 1. The round specimens conform to ASTM (E8-57T) specifications. Two post yield strain gages applied with Eastman 910 cement on opposite sides of the specimen were used to determine small strain values and a dial gage measuring the testing machine head movement was used to determine the average large strain values. The strain gages were used for strains up to 0. 012 in./in. The strain was continuously recorded with the Sanborn amplifier-recorder system and the load was read directly from the Olsen Testing machine. At the instant the load was read, a pulse was recorded on the strain record. The strain rate of loading was about 1.5×10^{-5} per second.

The results of the three tests are summarized in Table AII-2, where the yield stress for specimen No. 3 is omitted because the specimen had an accidental initial loading beyond its yield point. The residual strain after this accidental load was recorded so that the

subsequent tensile test could be strain related to the zero strain condition. Figure A2. 2(a) shows the typical stress-small strain relationship for the tensile specimens and figure A2. 2(b) shows the stress-large strain curves for all three specimens. The similarity of the stress-strain curves indicates that the results are valid.

TABLE II-2

Tensile Test Results

Specimen	Min. Diameter inch	Yield Stress psi	Tensile Stress psi	Elongation %
No. 1	0. 3482	40, 000	63, 500	31
No. 2	0. 348	41, 300	63, 600	28
No. 3	0. 3474	--	60, 600	28
Note: The gage length for elongation was 1. 400 inch.				

The average values for use in the structural yielding analysis will be $E = 28.6 \times 10^6$ psi, the yield stress equal to 40, 000 psi which results in a yield strain of 0. 00142 inch/inch and the strain which initiates strain hardening will be taken as 0. 0142 inch/inch. The average ultimate tensile stress is taken as 63, 400 psi.

The linear yield strain projection is 0. 00138 inch/inch but as can be seen from figure A2. 2 the actual yield strain is 0. 00146 inch/inch. Therefore, the above values are averages.

Metallographic and Chemical Analysis

A $\frac{1}{2} \times \frac{1}{2} \times 5$ inch transverse piece of the same "I" beam section as was used for tensile specimens No. 2 and No. 3 was sent to an

FIG. A2.2 TENSILE TESTS

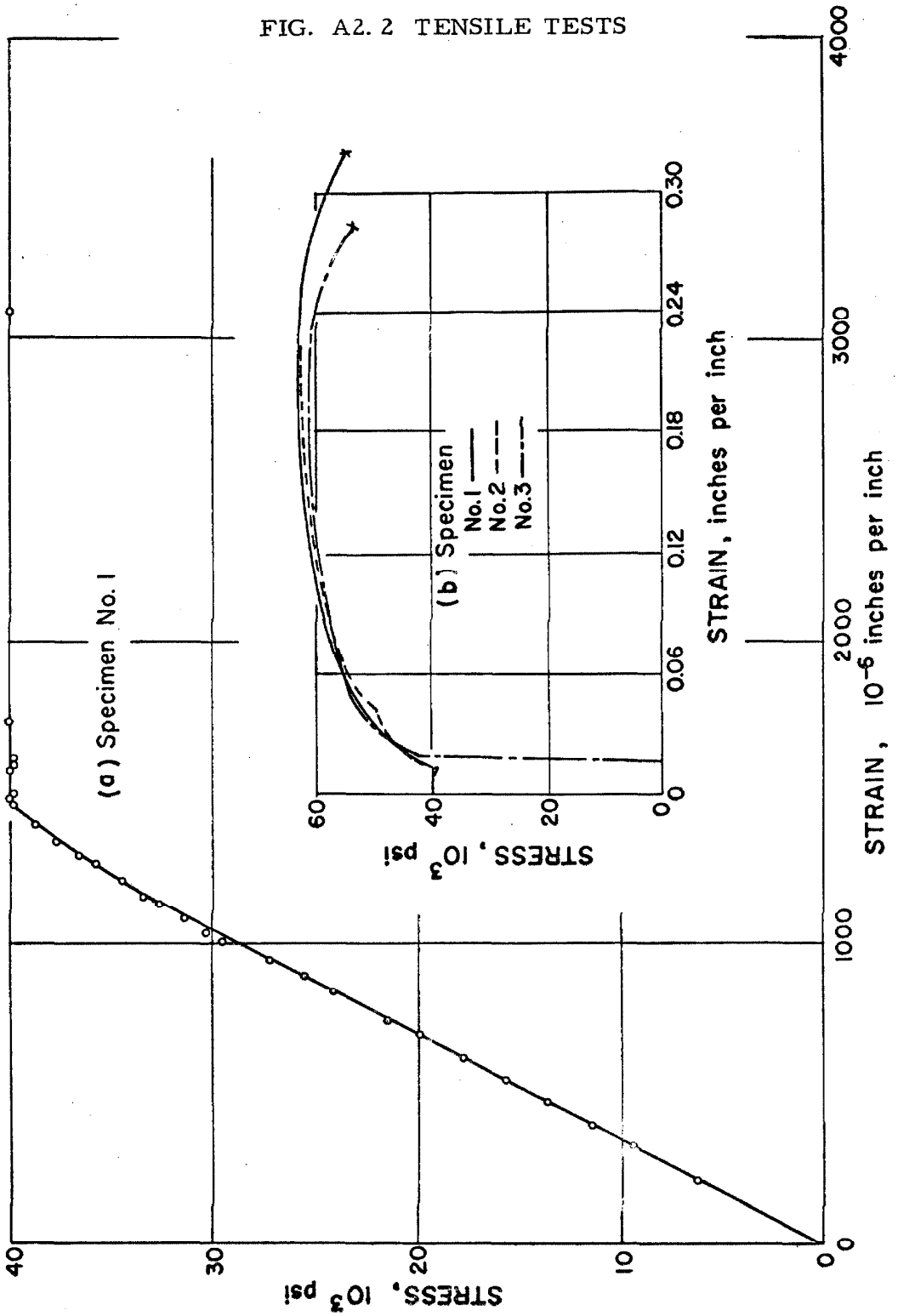

independent testing laboratory for a chemical analysis and a metallographic examination. The section of the web just below the fillet was marked as the area for examination. The entire report of the laboratory analysis follows:

"Chemical Determinations

Carbon (C)	0.22%
Manganese (Mn)	0.47%
Silicon (Si)	0.018%
Sulfur (S)	0.049%
Phosphorus (P)	0.02%
Copper (Cu)	0.30%

Metallographic Examination

The Microstructure indicated a fine grained ferrite and pearlite with areas of severe cold working. The cold working bands appeared most prominent in the area leading to the flange as indicated by the curvature of the bands.

Grain Size, ASTM E 112-63	No. 8
Average grain diameter	0.834×10^{-3} inches

Respectfully submitted,
SMITH-EMERY COMPANY"

APPENDIX III: EXPERIMENTAL HISTORY

During this investigation, it was found that the structure was in a continual process of change. Primarily this consisted of damage during testing and recovery during periods of rest. Therefore, it is important to know the past history of the structure for each experiment when attempting to compare or contrast several results. The static and dynamic studies did not follow a rigidly prescribed sequence, but followed a general testing plan which could be modified at will. For this reason, the history will be described in chronological order and numbered so that the data presented can be referred directly to this account.

The experimentation started with long column set 1, LI, and then went to short column sets 1, 2 and 3, SI, SII, and SIII, respectively. The reference number in the test of this paper shall be indicated, for example, by A3.10 for item 10 in the following list. The type of test and the date the test was made plus other pertinent information will be included. All deflections are given in inches with all initial free deflections assumed to be zero. Static deflections are assumed positive in the East and North directions. The force amplitude F_o in pounds equals $B f^2$, where f is the excitation frequency in cps.

The notation used here is: W is the effective weight of the structure for that test, n is the fraction of critical damping according to equation 4.13 or 4.14, u is the frequency ratio ω_p / ω_n and ϕ is the measured phase lag in degrees.

Long column set 1, LI:

1. East-West static test Sept. 4, 1963. Deflections 0 to -0. 228 to 0. 228 to -0. 036 with a residual deflection of 0. 012; W = 3238;

2. Free vibration test in both directions Sept. 5, 1963. W = 3238; E-W, n=. 00072 at x=0. 029; E-W, n=. 00104 at x=0. 177; N-S, n=0. 0013 at x=0. 044;

3. E-W static test Sept. 9, 1963. W= 3238; Deflections 0 to 0. 477 to -0. 483 to 0. 472 to -0. 085 with a residual deflection of 0. 018;

4. E-W static test Sept. 10, 1963. W=3238; Deflections 0 to -0. 701 to 0. 702 to 0. 061 with a residual deflection of 0. 112;

5. Free vibration test Sept. 11, 1963. W=3238; E-W, n=0. 0017 at x=0. 126; N-S, n=0. 0019 at x=0. 027;

6. Free vibration test Sept. 12, 1963. W=4220; E-W, n=0. 0019 at x=0. 131; N-S, n=0. 0013 at x=0. 032;

7. Free vibration test Sept. 16, 1963. W=4220; N-S, n=0. 0013 at x=0. 034;

8. E-W static test Sept. 17, 1963. W=4220; Deflections 0 to -0. 799 to 0. 701 to -0. 790 to -0. 172 which is the residual deflection;

9. Free vibration test Sept. 17, 1963. W=4220; E-W, n=0. 0018 at x=0. 075; N-S, n=0. 0013 at x=0. 029;

10. E-W static test Sept. 25, 1963. W=4220; Deflections 0 to 0. 856 to -0. 667 to 0. 858 to -0. 676 to -0. 038 which is the residual deflection;

11. N-S forced vibration test Sept. 26, 1963. W=4220; B=0; A run down test with no force other than the slight error in the counter balance of vibration generator No. 1;

12. N-S forced vibration test Sept. 27, 1963. W=4221; B=1.39; Increasing frequency only with a maximum displacement about 0.234;

13. N-S forced vibration test Sept. 29, 1963. W=4221; B=1.38; Increasing frequency only and then rerun resonant range with increasing and decreasing frequency; max. x=0.210;

14. N-S forced vibration test Oct. 1, 1963. W=4223; B=2.73; Increasing and decreasing frequency; max. x=0.224;

15. N-S forced vibration test Oct. 5, 1963. W=4224; B=4.11; Increasing and decreasing frequency; max. x=0.232;

16. N-S forced vibration test Oct. 11, 1963. W=4225; B=5.46; Increasing and decreasing frequency; max. x=0.248;

17. N-S forced vibration test Oct. 17, 1963. W=4225; B=5.46; Increasing, decreasing and increasing frequency primarily in the resonant range; max. x=0.244;

18. N-S forced vibration test Oct. 17, 1963. W=4224; B=4.11; Resonant range, increasing and decreasing frequency; max. x=0.217;

19. N-S forced vibration test Oct. 17, 1963. W=4223; B=2.73; Resonant range, increasing frequency only; max. x=0.196;

20. N-S forced vibration test Oct. 17, 1963. W=4221; B=1.39; Resonant range, increasing frequency only; max. x=0.164;

All following static tests use the Alinco Load Cell and all forced dynamic tests use the Miller system.

21. N-S static test Oct. 22, 1963. W=4220; Deflections 0 to 0.164 to -0.164 to 0.163 to -0.196 to 0.196 to -0.196 to 0.215 to -0.215 to 0.091;

22. N-S static test Oct. 24, 1963. W=4220; Deflections -0.002 to 0.240 to -0.240 to 0.241 to -0.261 to 0.260 to -0.260 to -0.028;

23. N-S forced vibration test Nov. 1, 1963. W=4225; B=5.46; Decreasing frequency sweep for possible comparison with steady state tests.

24. N-S forced vibration test Nov. 2, 1963. W=4225; B=5.46; Data taken after exciting the structure at resonance. Increasing freq. with several checks with decreasing freq. max. x=0.244; u=0.956, x=0.244, ϕ = 86, n=0.024;

25. N-S forced vibration test Nov. 10, 1963. W=4227; B=7.04; Increasing and decreasing frequency; max. x=0.253; u=0.946, x=0.252, ϕ = 86, n=0.029;

26. N-S forced vibration test Dec. 9, 1963. W=4224; B=4.09; Three hysteresis loop data points were taken before and after exciting the structure for 10,000 cycles near resonance; the 10,000 cycles gave approximately a 3% decrease in the acceleration amplitude.

max. x=0. 226;

27. N-S forced vibration test Jan. 6, 1964. W=4225; B=5. 45; Decrease and increase frequency; u=0. 957, max. x=0. 244; x=0. 244, ϕ = 88, n=0. 024; ω / ω_p = 1. 008, x=0. 242, ϕ = 104, n=0. 023;

28. N-S forced vibration test Jan. 6, 1964. W=4229; B=9. 34; Increase and decrease freq. ; max. x=0. 281, u=0. 939, x=0. 281, ϕ = 95, n=0. 035;

29. N-S forced vibration test Jan. 7, 1964. W=4232; B=12. 70; After about 800 cycles at 0. 282 inch, increase and decrease freq. ; max. x-0. 299, u=0. 930, x=0. 299, ϕ =100, n=0. 042;

30. N-S forced vibration test Jan. 8, 1964. W=4238; B=18. 07; After about 800 cycles at 0. 310 inch, increase and decrease freq. ; max. x=0. 326, inc. u=0. 906, x=0. 326, ϕ = 92, n=0. 052; dec. u=0. 908, x=0. 319, ϕ =95, n=0. 054;

31. N-S static test Jan. 11, 1964. W=4238; Deflections ± 0. 320, ±0. 320 ±0. 400 before data taken as 0. 002 to -0. 320 to 0. 320 to -0. 400 to 0. 400 to -0. 400 to -0. 084 which is the residual deflection;

32. N-S forced vibration test Jan. 13, 1964. W=4250; B=30. 80; After about 1200 cycles at 0. 357 inch, increase freq. until fatigue fracture at bottom of the northeast column; max. x=0. 383; u=0. 874, x=0. 383, ϕ = 103, n=0. 069;

33. E-W forced vibration test Jan. 18, 1964. B=1. 39, 5. 46, 9. 34, 12. 73, 18. 07, 36. 09, 46. 29, 88. 60 and 134. 95. Since the

structure failed during the previous test, this test was used to check the stability of the vibration generator during large motions and to note the characteristics of the structure as it collapsed ; max. x=0. 895;

Short column set 1, SI: The testing direction is East-West unless otherwise noted.

34. Free vibration test for damping, March 7, 1964. W=4038; n=0. 0020 at x=0. 049;

35. Static test March 7, 1964. W=4038; Deflections 0 to 0. 343 to 0. 007 to 0. 997 to 0. 206 with a residual deflection of 0. 355; gives the skeleton curve;

36. Free vibration test for damping March 7, 1964. W=4038; n=0. 0016 at x=0. 052;

37. Static test March 9, 1964. W=4038; Deflections 0. 355 to -0. 353 to 0. 498 to -0. 375 to 0. 138 which is the residual deflection;

38. Static test March 10, 1964. W=4038; Deflections 0. 138 to -0. 494 to 0. 084 which is the residual deflection;

39. Forced vibration test March 11, 1964. W=4229; B=9. 34; The Floor mass was not wedged properly, therefore, the results of this test are not reported except in the fatigue considerations;

40. Forced vibration test March 12, 1964. W=4229 ; B=9. 34; increasing freq. ; max. x=0. 444; u=0. 990, x=0. 444, ϕ=86, n=0. 024;

41. Forced vibration test March 14, 1964. W=4238; B=18.07; resonance range, increase freq.; max. x=0.505; u=0.975, x=0.505, ϕ=92, n=0.039;

42. Forced vibration test March 14, 1964. W=4255; B=36.08; resonance range, increase freq.; max. x=0.595; u=0.928, x=0.595, ϕ=84, n=0.059;

43. Forced vibration test March 15, 1964. W=4220; B=46.23; resonance range, increase freq.; max. x=0.631; Damaged; u=0.909, x=0.630, ϕ=90, n=0.069;

44. Forced vibration test March 16, 1964. W=4238; B=64.33; increase freq.; the bottom of NE column fractured and the top of NW column had a crack; max. x=0.699; u=0.846, x=0.699, ϕ=86;

Short column set 2, SII: The testing direction is East-West unless otherwise noted.

45. Free vibration test March 20, 1964. W=4220; n=0.0016 at x=0.027;

46. Forced vibration test March 20, 1964. W=4255; B=82.34; torque limit of vibration generator # 1 was reached before the complete test could be run; max. x=0.715;

47. Forced vibration test March 20, 1964. W=4220; B=46.26; to investigate the torque limitation, no limitation at this level;

48. Forced vibration test March 20, 1964. W=4238; B=64. 33; no torque limitation; max. x=0. 737;

49. Free vibration test March 20, 1964. W=4238; n=0. 0032 at x=0. 032;

50. Forced vibration test April 8, 1964. W=4041; B=2. 75; increase freq. ; max. x=0. 371;

The following forced vibration tests were made with two force generators.

51. Forced vibration test April 25, 1964. W=4686; B=2. 76; increase freq. ; max. x=0. 366; u=0. 998, x=0. 366, ϕ =99; n=0. 0077;

52. Free vibration test May 4, 1964. W-4683; n=0. 0027 at x=0. 048;

53. Forced vibration test May 4, 1964. W=4774; B=92. 40; increase freq. ; max. x=0. 835; u=0. 854, x=0. 835, ϕ =89, n=0. 083;

54. Forced vibration test May 6, 1964. W=4809; B=128. 5; increase freq. ; max. x=0. 919; this test fractured the SW and SE column tops, almost cracked through the NW column top, and started the crack in NE column top; u=0. 791, x=0. 910, ϕ =93, n=0. 089;

Short column set 3, SIII: All tests are in the East-West direction unless noted otherwise.

55. Free vibration test June 22, 1964. W=4683; n=0. 0012 at x=0. 0056;

56. Static test June 22, 1964. W=4683; Deflections 0 to 0. 631 to

-0. 631 to 0. 629 to -0. 604 to 0. 609 to 0. 072 which is the residual deflection;

57. Forced vibration test for hysteresis determination only, June 23, 1964 W=4725; B=42. 68; Deflections about 0. 640;

58. Static test June 25, 1964. W=4683; Deflections 0 to -0. 450 to 0. 450 to -0. 450 to 0. 451 to -0. 641 to 0. 644 to -0. 640 to 0. 490 to 0. 052 which is the residual deflection;

59. Forced vibration test for hysteresis determination only, June 30, 1964, W=4694; B=10. 88; Ten data points taken with deflections about 0. 420;

60. Static test June 30, 1964. W=4683; Deflections 0 to 0. 450 to -0. 420 to 0. 420 to -0. 421 to 0. 824 to -0. 825 to 0. 824 to -0. 592 to -0. 078 which is the residual deflection;

61. Free vibration test July 2, 1964. W=4683; n=0. 0020;

62. Forced vibration test for hysteresis determination only, July 6, 1964. W=4684; B=1. 39; one data point with x=0. 120;

63. Forced vibration test for hysteresis determination only, July 7, 1964. W=4694; B=10. 88; one data point with x=0. 420;

64. Forced vibration test for hysteresis determination only, July 7, 1964. W=4774; B=92. 41; six data points with x about 0. 816;

65. Free vibration test July 7, 1964. W=4683; n=0. 0020 at x=0. 011;

66. Static test July 8, 1964. W=4683; Deflections 0 to 0. 812 to -0. 815 to 0. 815 to -0. 420 to 0. 419 to -0. 421 to 0. 120 to -0. 120 to 0. 120 to 0. 00 with a residual deflection of 0. 006;

67. Free vibration test August 17, 1964. W=4683; n=0. 0015 at x=0. 016;

68. Static test August 17, 1964. W=4683; Deflections 0 to 0. 814 to -0. 815 to 0. 815 to -0. 815 to 0. 815 to -0. 416 to 0. 007 which is the residual deflection;

69. Forced vibration test for hysteresis determination, August 18, 1964. W=4774; B=92. 41; one data point with x=0. 794;

70. Free vibration test August 18, 1964. W=4683; n=0. 0016 at x=0. 019;

Appendix IV: Notation

The symbols used in this thesis are defined as follows for Chapter II:

A, B	constants of deflection amplitude
$[C]$	viscous damping matrix
$[C^*]$	$= [M]^{-1/2} [C] [M]^{-1/2}$
c	viscous damping coefficient of a single degree of freedom system
$\bar{c}$	linearized viscous damping
$[D]$	$= [\Psi]^T [C] [\Psi]$, diagonal matrix
d_i	major diagonal element of the i^{th} row of $[D]$
$E[x]$	mean or expected value of x
$E[x^2]$	mean square value of x
e	base of the Napierian logarithm
F	force applied to the mass as a function of time
$\{F\}$	vector of the forces acting on the masses
$F(\omega)$	Fourier transform
$[I]$	matrix with all zeros except for unit values elements along the major diagonal
$[K]$	stiffness matrix
$[K^*]$	$= [M]^{-1/2} [K] [M]^{-1/2}$
k	spring stiffness of a single degree of freedom system
$[M]$	mass matrix for multiple-degree-of-freedom system
m	mass of a single-degree-of-freedom system

n	$= \frac{c}{2\sqrt{km}}$, fraction of critical viscous damping
P_i	element of the i^{th} row of $\left[\Psi\right]^T \left(F\right)$
$p(x)$	first order probability density
$R(x)$	restoring force
$R(\tau)$	autocorrelation function
S_o	uniform power spectral density
S_v	maximum velocity response spectrum (equation 2.42)
$S(\omega)$	power spectral density
t	time in seconds
$x, \dot{x}, \ddot{x}$	deflection, velocity, and acceleration of the mass relative to the base of the system, respectively
x_i	deflection of the i^{th} mass relative to the base
y	displacement of the base
$\left(\ddot{y}\right)$	acceleration of the base times a vector whose elements are all unity
ϵ_i	element of the i^{th} row of $\left(\epsilon\right)$
$\left(\epsilon\right)$	defined by equation 2.13
$\left[\theta\right]$	orthogonal transformation matrix
$\left(\xi\right)$	defined by equation 2.9
σ^2	variance of x defined by equation 2.35
ϕ	deflection-force phase lag defined by equation 2.29
$\left[\Psi\right]$	defined by equation 2.15
$\left(\psi^i\right)$	i^{th} column of $\left[\Psi\right]$
ω	excitation circular frequency
$\omega_d = \sqrt{1-n^2}\,\omega_n$	damped natural frequency of vibration

ω_i^2	major diagonal element of the i^{th} row of (square of the i^{th} mode natural frequency) $\left[\sim\omega^2\sim\right]$
$\omega_n = \sqrt{k/m}$	undamped natural frequency of vibration
ω_p	resonant frequency of the nonlinear system
ω_{rd}	damped natural frequency of the r^{th} mode
	and for Chapter III where different from above:
a_1, b_1, c_1	dimensions of the experimental section
a_2, b_2, c_2	dimensions of the experimental section
LI	long column set No. 1 structure
SI	short column set No. 1 structure
SII	short column set No. 2 structure
SIII	short column set No. 3 structure
γ , δ	defined by equation 3. 5
κ	$= (1 + k_2/k_1)$
λ	characteristic complex frequency
$\omega_1 = \sqrt{k_1/m_1}$	
	and for Chapter IV where different than above:
A_m	constant, amplitude of the m^{th} term of expansion
B	constant defined by equation Al. 8
C(A)	$= (\omega_p / \omega_n)^2$ shift of nonlinear resonant frequency
c_{eq}	equivalent viscous damping
(E-W)	East-West direction
F_o	sinusoidal force amplitude, pounds
f	excitation frequency in cps

f_n	undamped natural frequency of the structure in cps
f_{nt}	undamped natural frequency of structure to be used for normalization, equation 4. 4
g	acceleration of gravity, 386 inches per second squared
H	constant defined by equation 4. 3
K	small deflection stiffness of the structure
m	variable integer coefficient; mass of the structure
(N-S)	North-South direction
n	fraction of viscous damping
n_{eq}	fraction of equivalent viscous damping
Δt	time interval between data points
W	effective weight of the structure during the experiments, pounds
W_n	effective weight of the structure when f_n was determined, pounds
X_o	deflection amplitude of linear system
X_p	peak deflection of experimental structure
Δx	change in the deflection amplitude between two points
ϕ_m	phase lag of the m^{th} term of the expansion
ψ	measuring phase error between acceleration and deflection
ω_n	initial small vibration natural frequency
ω_p	frequency at which X_p occurs

and for Chapter V:

A	constant to define location of initial strain hardening; point of reference
A_s	cross sectional area of the beam
a	distance defined by figure 5.12
B	constant to define location of a change in rate of strain hardening; point of reference
b	width of the rectangular beam
$C(x_o)$	defined by equation 5.101, equals C(A) of Chapter IV
c	distance from neutral axis to extreme fiber
c*	half the depth of a variable depth section
$d=\frac{1}{K}=\frac{p_y}{x_y}$	see equation 5.110
E	Young's modulus of elasticity
E_1, E_2	average Young's modulus of elasticity used for column sections I_1 and I_2 respectively
$e=\left(\frac{\alpha x_y}{p_y}^r\right)$	see equation 5.110
F	shear force on the section
F_o	amplitude of sinusoidal force
F_p	area of the section times one half the yield stress
f_n	undamped natural frequency of the structure, cps
G	strain hardening slope factor, see figure 5.3
g	acceleration of gravity
H	strain hardening slope factor, see figure 5.3
I	moment of inertia of the cross section

I_1, I_2	column moments of inertia, see figure 5.9
I_2'	second stress invariant expressed in terms of distortional stresses only
K	stiffness of the structure; initial stiffness of the structure
K'	stiffness of the structure corrected for the effect of the weight of the structure
K_1	stiffness of one column of the structure
L	effective length of the column
ℓ_1, ℓ_2	column dimensions, see figure 5.9
M	static bending moment
$M_{e\ell}$	static moment at a section where the extreme fibers start to yield
$M^*_{e\ell}$	increased maximum elastic moment due to variable depth section
M_F	fully plastic yield moment corrected for shear stress effects
M_N	fully plastic yield moment corrected for normal stress effects
M_{max}	maximum value of M_1
M_p	fully plastic yield moment
M_s	static bending moment at a section
M_{SHA}	increase in moment due to strain hardening
M_{SHB}	decreasing in moment due to decrease in strain hardening rate

M_{SII}	moment at the section for elasto-plastic stress-strain only
M_1	bending moment at the column ends
M_2	reverse bending moment
N	normal force on the section; predicted number of cycles required for failure at a given stress level
N_p	area of section times the yield stress
n	number of cycles at a given stress level
n_{eq}	fraction of equivalent viscous damping
P	concentrated load acting along the y axis; horizontal load
P*	portion of total P which is resisted by a particular column
P'	horizontal force corrected for the effect of the weight of the structure
P_{el}	horizontal force required to initiate yielding
P_i, X_i	data force and deflection terms
p(x)	restoring force
p_o	maximum hysteretic force
p_y	characteristic force
q	ratio of the first coefficient of the Fourier series expansion of the displacement to X_o
r	positive odd integer, see equation 5.89
S	column spacing in the direction of P
$S(x_o)$	defined by equation 5.101

V	vertical column load due to deflection and horizontal load P
v	linear value from 1.0 to 1.5
W	effective weight of the structure
X	deflection of rigid floor relative to the base
X_{el}	deflection at which yielding begins
X_{max}	maximum deflection
X_2	deflection associated with M_2
x, y, z	axes along which distances are measured; also these distances
x_o	maximum hysteretic displacement
x_y	characteristic displacement
Y_1, Y_2	deflections of the column between two sections
y	distance from the neutral axis
y_{el}	distance to initial yield strain position
z_{el}	distance from origin to section with $M=M_{el}$
α	positive constant, see equation 5.89
ϵ	strain
ϵ_c	strain at the extreme fiber, i.e. at y=c
ϵ_{el}	the elastic strain limit, initiates plastic yielding
ϵ_{max}	maximum strain associated with M_{max}
ϵ_2	strain associated with M_2
$\eta =$	ω / ω_n
θ	change in slope per unit length $\left(\text{curvature}\right)$
θ_{el}	curvature at which the extreme fibers begin to yield

$\theta_1, \theta_2, \theta_3$ rotations of the column between two sections

υ Poisson's ratio

σ normal stress at a section

σ_{el} yield stress, begins at ϵ_{el}

σ_{SHA} strain hardening stress increase = $(\sigma - \sigma_{el})$

σ_{SHB} decrease in strain hardening stress = $(\sigma - \sigma_{SHA})$

$\sigma_x, \sigma_y, \sigma_z$ normal stresses

$\tau_{xy}, \tau_{yz}, \tau_{zx}$ shearing stresses

$\phi_1 = \phi$ phase angle of the first term in the Fourier series

ω_n undamped natural frequency of the structure = $2\pi f_n$

$\omega_n^2 = \frac{p_y}{x_y m}$ small vibration natural frequency squared

and for Appendix I, the same as Chapter II with the addition of:

B constant defined by equation A1. 8

F_o sinusoidal force amplitude

f excitation frequency in cps

f_n undamped natural frequency in cps

m mass of eccentric weight of force generator for equations A1. 10 and A1. 11 only

R radius from the eccentric weight center to the axis of rotation

x_o deflection amplitude

w total eccentric weight added to force generator baskets, pounds

and for Appendix III, the same as Chapter IV with the addition of:

u $= \omega_p / \omega_n$